© Copyright 2019

Alexander Scott Ditter

Using advanced x-ray spectroscopic methods to probe actinide 5f electronic structure

Alexander Scott Ditter

A dissertation

submitted in partial fulfillment of the

requirements for the degree of

Doctor of Philosophy

University of Washington

2019

Reading Committee:

Gerald Seidler, Chair

Marjorie Olmstead

Andreas Karch

Program Authorized to Offer Degree:

Physics

University of Washington

Abstract

Using advanced x-ray spectroscopic methods to probe actinide 5f electronic structure

Alexander Scott Ditter

Chair of the Supervisory Committee:
Gerald Seidler
Physics

X-ray absorption spectroscopy (XAS) and x-ray emission spectroscopy (XES) are element specific, bulk sensitive measures of local electronic structure. As such, they make an ideal probe of actinide 5f electrons, and are situated to answer important questions about actinide covalency. To this end, I have performed resonant inelastic x-ray scattering measurements on uranium 4+ and 5+ hexachlorides to show that $U^{V}Cl_6^{1-}$ is the more covalent of the two compounds due to the energy degeneracy between the uranium and chlorine atomic orbitals. Also discussed here is the work I did to make these measurements possible using a compact, dispersive Rowland circle monochromator at the Stanford Synchrotron Radiation Lightsource. I also discuss my contributions to the goal of expanding access to XAS and XES, and in particular the development of the Clean Energy Institute X-ray Absorption Near-Edge Spectrometer, CEI-

XANES, where I lead a project to create the world's first modern laboratory mail-in XAS user facility.

TABLE OF CONTENTS

LIST OF FIGURES

LIST OF TABLES

ACKNOWLEDGEMENTS

This work would only be possible with the help of many people. First and foremost, I'd like to thank my advisor, Gerald Seidler. His guidance and support have made me the scientist I am today, and he has been a great help in all of my academic pursuits. I'd also like to thank my colleagues in the group, in particular Evan and Will. Without them, this work would not have been possible.

I'd also like to thank Stosh Kozimor, my advisor at Los Alamos National Lab. His support was critical in achieving my goals during my two years there, and his friendship made the experience very enjoyable. I also would like to thank the entire group, and in particular Veronika, Maryline and Sam for all their help.

I'd also like to thank my parents, without whose love and support I would not have been able to even begin down the path to this achievement. I owe a great deal to them and greatly appreciate their care and understanding. And finally, I would also like to thank my friends at the University of Washington who helped me a great deal and kept me grounded during the PhD process.

Chapter 1. INTRODUCTION TO X-RAY ABSORPTION SPECTROSCOPY, X-RAY EMISSION SPECTROSCOPY, AND RESONANT INELASTIC X-RAY SCATTERING

X-ray absorption spectroscopy (XAS), x-ray emission spectroscopy (XES) and associated techniques have become important, widely used spectroscopic tools for determining structural and electronic information. These techniques and the instrumentation necessary to perform them are a major focus of this thesis. This section outlines the basics of XAS and XES, describing the theory and giving several applications of each technique.

1.1 X-RAY ABSORPTION SPECTROSCOPY

1.1.1 *Description and Theoretical Underpinnings of X-ray Absorption Spectroscopy*

X-rays with energy below the pair-production threshold interact with matter in three ways: the photoelectric effect, coherent scattering (x-ray diffraction), and Compton scattering. The x-ray scattering cross section of Cu as a function of energy is shown in Figure 1.1. X-ray absorption spectroscopy (also called x-ray absorption fine structure, XAFS) is a consequence of the photoelectric effect: an incident x-ray is absorbed by an atom and an electron is ejected. There is an overall decreasing trend in absorption as the energy of the incident x-ray increases (up to 1 MeV) indicating that the x-rays become more penetrating as their energy increases. Also evident in this spectrum is that at the binding energy of electrons, a new absorption channel becomes available and there is a jump in the absorption.

If we enlarge the energy region at one of these discontinuities (near 9 keV, Figure 1.2), there is a "fine structure" of peaks and oscillations in the absorption spectrum. It is these features that are the primary concern of XAS.

The XAS spectrum of Figure 1.2 can be split into two distinct regions: the area immediately surrounding the edge-step (appx 8990 to 9010 eV in Figure 1.2), which is also known as the x-ray absorption near edge structure (XANES), and the region far above the edge-step, which is known as the extend x-ray absorption fine-structure (EXAFS). XANES and EXAFS are distinguished because the lifetime effects in the two regimes are sufficiently different as to require different theoretical treatments. In the XANES region, the photoelectron energy is insufficient to generate so-called extrinsic losses, such as plasmon generation, and consequently coherence of the combined wavefunction of corehole and photoelectron is limited mainly by the photoelectron lifetime. Consequently, best theoretical treatment must address the long spatial range of the photoelectron, such as in a full-multiple scattering formalism.[1,2] On the other hand, in the EXAFS regime the photoelectron energy is high enough to spawn plasmons, giving a strong inelastic interaction with the environment that rapidly destroys coherence and prevents longer scattering paths from participating in interference.[3] Best theoretical treatment in this case instead focuses on enumerating the dominant low-order scattering paths and carefully calculating the associated phase shifts.[4] In the next sections, a brief outline of each technique is presented and several examples in actinide science are presented.

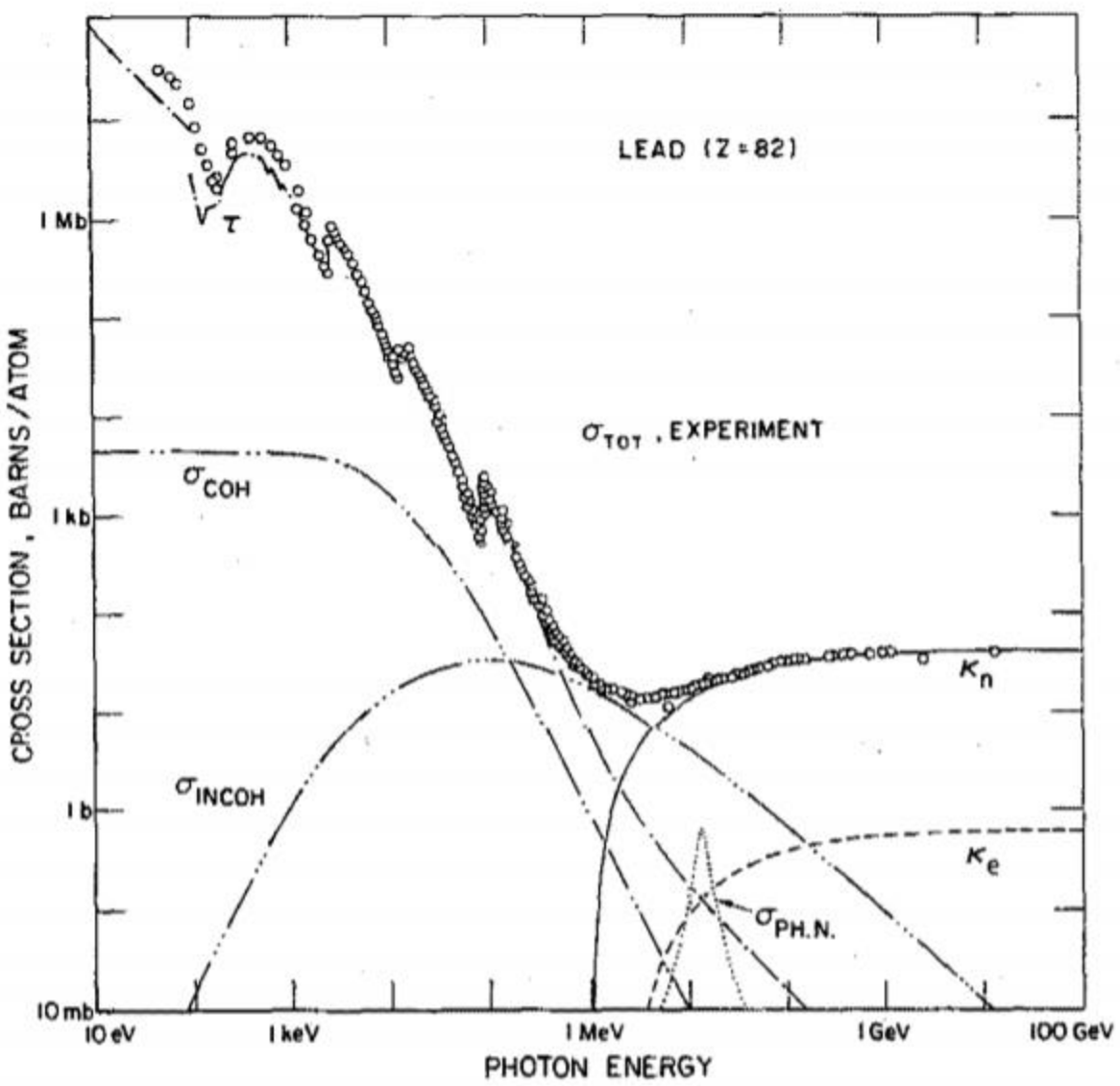

Figure 1.1. Cross section as a function of energy for copper. For energies less than 500 keV, this is broken down into coherent and incoherent scattering as well as the photoelectric effect. Figure from Hubbell et al.[5]

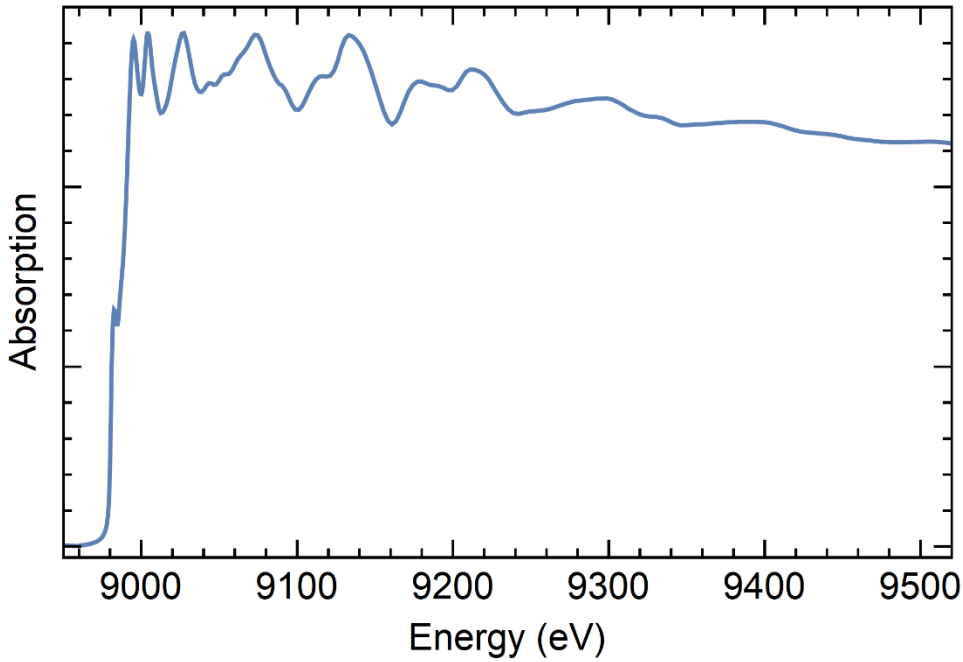

Figure 1.2. Cu Foil XAFS spectrum. Absorption as a function of incident photon energy. Data from the GSE-CARS EXAFS Library[6]

Because EXAFS is not a focus of the remainder of this thesis, we only give the most basic outline of the technique, but several excellent books and tutorials go into more details.[7–9] The ideas behind EXAFS are quite simple: an x-ray is absorbed, leading to a photoelectron being emitted in a spherical wave (ignoring polarization effects, for simplicity). This spherical wave scatters off neighboring atoms, resulting in constructive or destructive interference depending on the energy of the photoelectron and the local scattering environment, in both distances and phase shifts. This is summarized in the EXAFS equation, developed by Stern, Lytle and Sayers in the 1970's [10–12],

$$\chi(k) = \sum_j \frac{N_j S_0^2}{kR_j^2} F_j(k) e^{-2R_j/\lambda_j(k)} e^{-2k^2/\sigma_j^2} \sin\left(2kR_j + \phi_j(k)\right). \quad (1.1)$$

Here, $\chi(k)$ is the spectrum where the edge-step and atomic background from an isolated atom has been subtracted, expressed in terms of the wavenumber of the photoelectron ($k \propto \sqrt{E - E_0}$; E_0 is the edge energy). Not every component of this equation is discussed here, but the main parts are

that the signal is proportional to the coordination number, N_j, and that the sinusoidal dependence on the bond length (R_j) allows this information to be extracted via Fourier transform. In this way, EXAFS is often used to extract bond lengths and coordination number. To perform a quantitative analysis, a number of analysis tools and calculation packages are available for modelling spectra.[13,14]

The region below and just above the absorption edge is called X-ray Absorption Near-Edge Structure (XANES) and this region is often described as containing information on the local electronic structure of the material under study, although the electronic structure is itself of course a consequence of the atomic configuration. Figure 1.3 shows an example of several different iron compounds, each with very different spectra. As we will see in the examples, XANES can be used to determine oxidation state, for fingerprinting, and for determining components of mixtures.

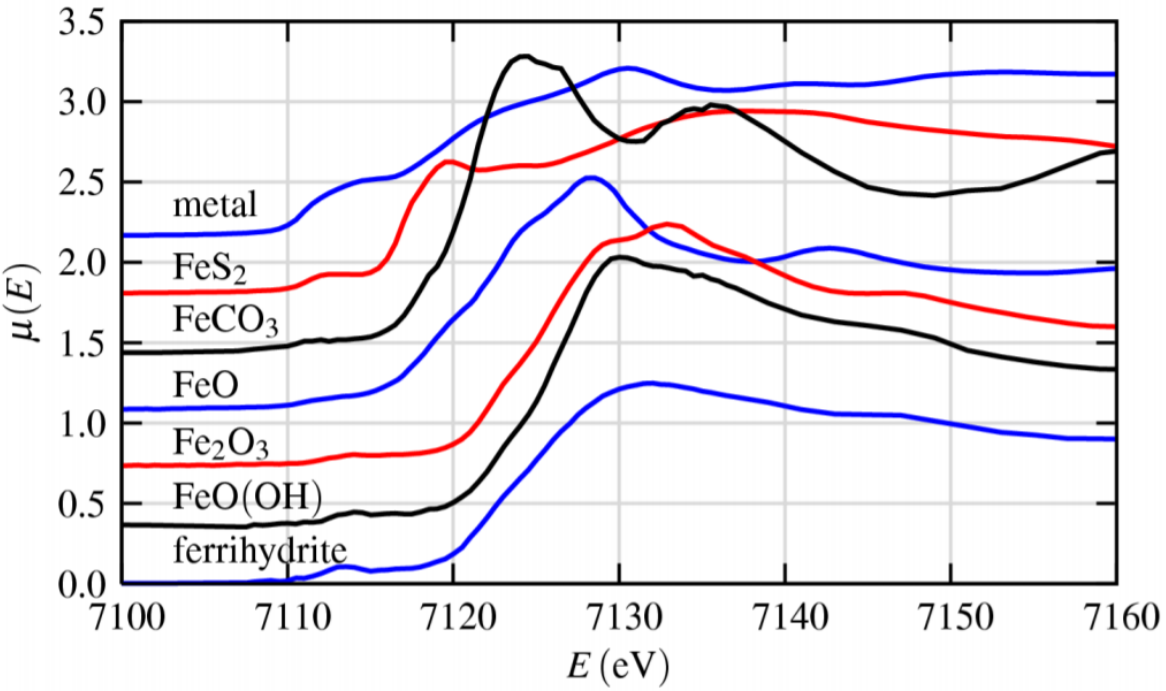

Figure 1.3. XANES of several different iron compounds. Figure from Newville.[9]

These transitions are broadened due to the core-hole lifetime. The finite lifetime of the core-hole state translates to an energy broadening via the uncertainty principle. These lifetimes are collected in Krause and Oliver and for example, are less than 1 eV for the 1s electron of sulfur but nearly 10 eV for the L (2^{nd} shell) and ~3 eV for the M (3^{rd} shell) edges of actinides.[15] However, underlying features of interest in the unoccupied density of states captured by the XANES are often only split by an eV or less, and hence are not directly observable in the XANES.

In the context of this dissertation, this leads to several paths forward. First, if the sample of interest contains a ligand with a much longer core-hole lifetime and hence less energy broadening, one can often better learn about the electronic structure by looking at the XANES of the ligand. This technique was pioneered by Solomon et al. where they examined pre-edge features in a chlorine spectrum for several transition metal compounds.[16] In Figure 1.4, spectra for several MCl_4^{x-} compounds (M = Cu^{2+}, Ni^{2+}, Co^{2+}, Fe^{2+}, and Fe^{3+}) are shown, as well as the transition that the pre-edge feature corresponds to for $CuCl_4^{2-}$. In that paper, the authors show that the probability of this transition is directly related to the covalency of the orbital, which is a critically important measurement for actinide 5f orbitals, as is explained in section 3.3, and is a central focus of the paper in Chapter 5.

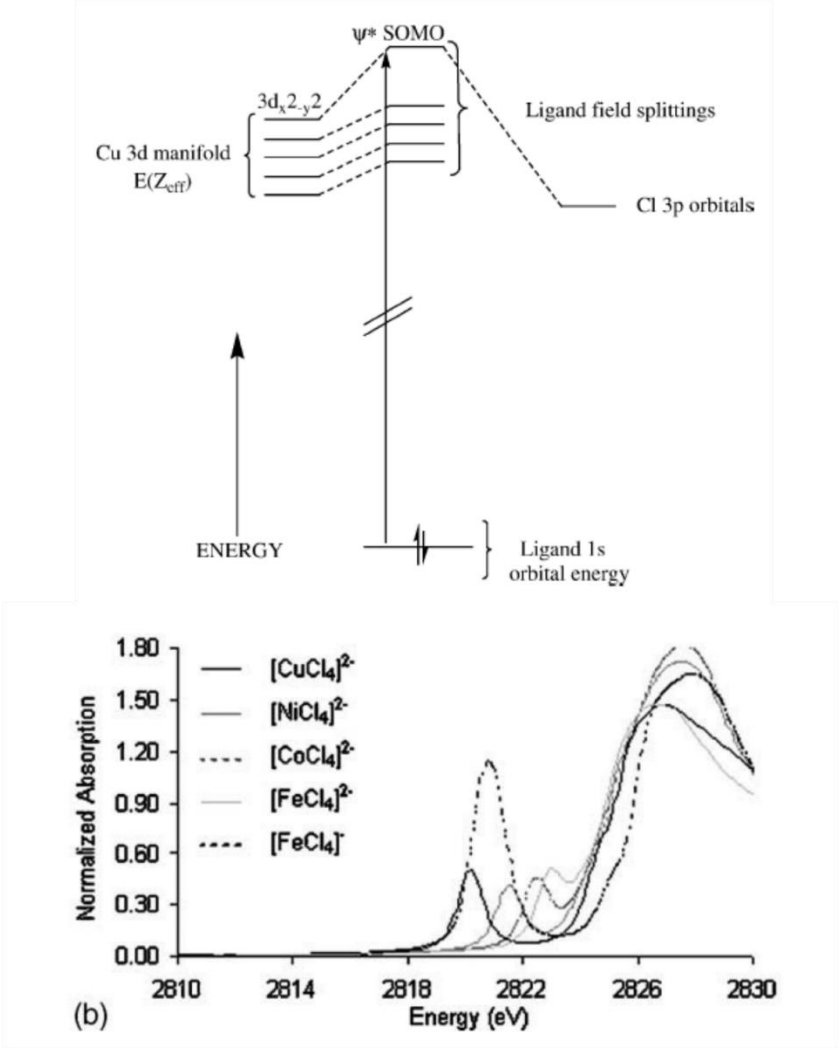

Figure 1.4. Energy level diagram showing the transition for $CuCl_4^{2-}$ from the Cl 1s electron into the singly occupied molecular orbital (bonding orbital) and XANES spectra for several other transition metal tetrachlorides.[16]

1.1.2 *Examples of X-ray Absorption Spectroscopy*

XAS has become an important method to determine the local electronic structure of materials, and so there are thousands of studies per year in fields like basic physics and chemistry[17–19], biology[20,21], environmental studies[22–24], catalysis[25–28], energy storage[29,30], materials science[31], nanomaterials[32,33], astrophysics[34], and solar energy[35]. To give an idea of how this technique is used, several examples from literature showing the use of XAS are presented here,

with a particular focus on actinides as these have the most relevance to the later parts of this dissertation.

One of the more common applications of XANES is to use the edge position as a proxy for oxidation state. The basic idea is that for a more oxidized atom, less valence electrons are present to shield the nuclear charge, and the energy needed to remove the core-shell electron increases. As an example of this, XANES spectra from Denecke et al. are presented in Figure 1.5 for several different uranium compounds of differing oxidation states.[36] The edge position is measured as the zero of the first derivative (the inflection point) at the edge, which is a common way to determine the edge position. Although this general trend of higher oxidation state corresponding to a higher edge energy tends to hold generally in XANES experiments, there are exceptions, especially when the two samples being compared are not chemically similar.

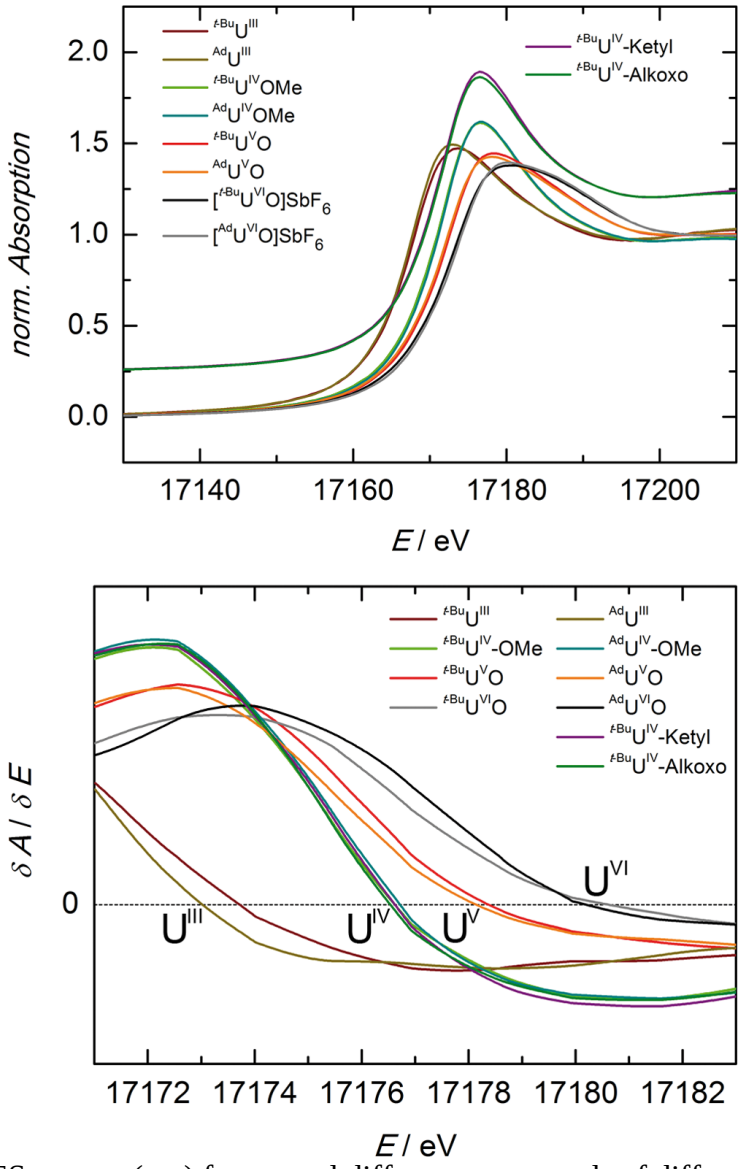

Figure 1.5. XANES spectra (top) for several different compounds of different oxidation states and coordinating atoms. Bottom shows the first derivative of the spectra, showing that the edge position (where the first derivative crosses the x-axis) is grouped by oxidation state, with a clear trend.

On the other hand, the relation between oxidation state and edge position is often not so straightforward, as is the case for PuO_{2+x}. Figure 1.6 shows XANES spectra for several plutonium oxides derived from PuO_2 in data collected by Conradson *et al.*[37] PuO_{2+x} systems have to do with the aging of PuO_2 and are therefore are highly relevant to nuclear forensics as well as studies of

nuclear waste. These spectra show that while each has a similar edge position, there is no clear trend with oxidation state. The reason given for this by Conradson *et al.* is that there are competing effects, one being the change in Pu valence, and the other being an increase in disorder due to oxygen or hydroxide ions disrupting the PuO_2 fluorite structure, essentially causing a broadening of the edge. This highlights the importance of understanding the chemistry of the system before drawing conclusions from a XANES spectrum.

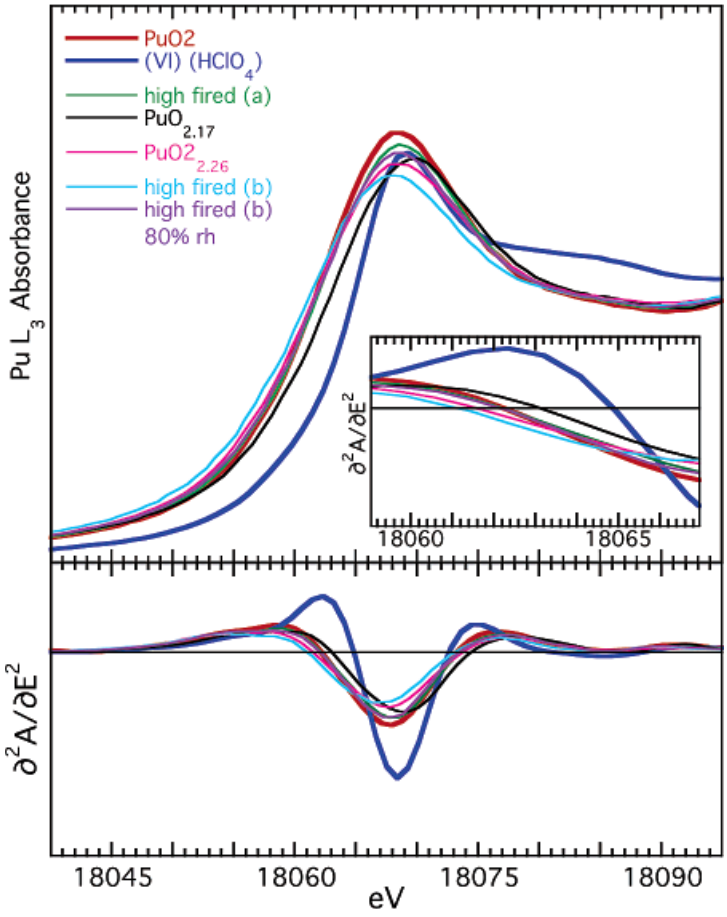

Figure 1.6. XANES spectra (top) for several different PuO_{2+x} states. Note that the edge position does not show a clear trend with oxidation state for the multivalent PuO_{2+x}.

Despite the complications of identifying the exact oxidation state for these plutonium compounds, it is still relatively easy to distinguish between say Pu(VI) and Pu(IV). This is critical in environmental applications where the oxidation state of plutonium determines its transport

through the geological system (see, for example, section 3.4.4). Hence, there have been many XANES studies of plutonium environmental samples.[38–41] As one example, consider particles from a crash of a B52 bomber over Spain, which resulted in Pu being dispersed in a wide area.[42] These particles were studied by Lind et al., who found that the particles collected had very similar XANES spectra to those collected in a similar incident over Greenland.[43] In addition, x-ray fluorescence and mass spectrometry also showed these samples to be identical. These Pu particles were from the same source, and so the authors concluded that even though both were the result from different crashes, the measurements of these samples were only dependent on the source material, which has important implications for nuclear forensics work.

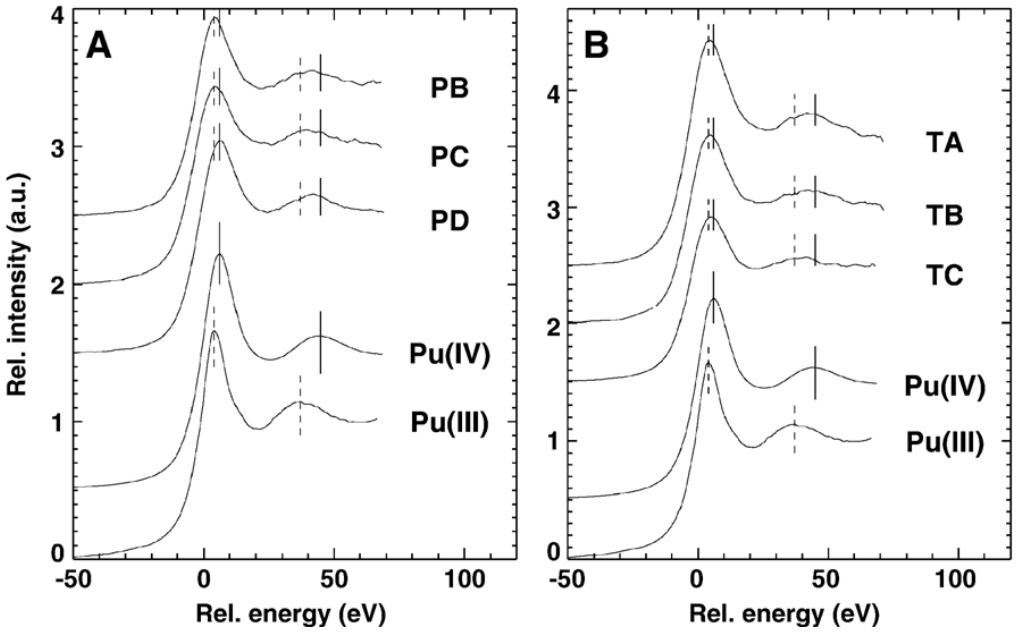

Figure 1.7. XANES spectra for several different microparticles recovered from the collision of a B-52 bomber over Spain (A). These are compared to particles from a similar incident over Greenland (B) with no difference being found between the two samples.[42]

Finally, we look at the study of actinides from a purely chemical perspective in order to gain understanding of the nature of the bonds made with ligands and address the issue of covalency

which is a central focus of this dissertation. A study by Su *et al.* looked at XANES of $AnCl_6^{2-}$ (An = Th, U, Np, Pu). As mentioned before, the degree of covalency can be extracted by looking at the strength of pre-edge features in the ligand. Figure 1.8 shows XANES spectra and shows that the Pu bond has the greatest degree of 5*f* covalency. Because both overlap between the metal and orbital ligand, as well as the difference in energy between those orbitals affect the degree of covalency,[44] we can conclude that as Pu has the smallest An 5*f* – Cl 3*p* overlap, the covalency is driven by the energy degeneracy of these orbitals. This idea of energy-degeneracy driven covalency is also the main focus of chapter 5.

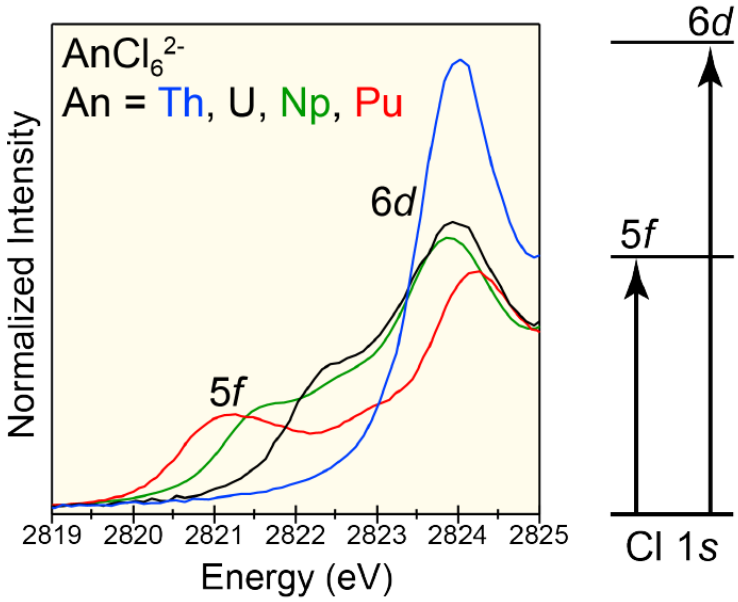

Figure 1.8. XANES spectra of $AnCl_6^{2-}$ (An = Th, U, Np, Pu) showing that the degree of 5*f* covalency is greatest for Pu despite having the smallest orbital overlap. Figure from Su et al.[45]

1.2 X-RAY EMISSION SPECTROSCOPY AND RESONANT INELASTIC X-RAY SCATTERING

1.2.1 *Description and Theoretical Underpinnings of X-ray Emission Spectroscopy and Resonant Inelastic X-ray Scattering*

X-ray emission fluorescence occurs when an incident photon removes a core electron, and then another electron falls into the core-hole and emits a photon. X-ray emission spectroscopy (XES) refers to very high resolutions studies of the x-ray fluorescence. The information yielded by this technique is similar to XANES except that the electrons are coming from the occupied density of states, and so the emitted spectra yield information on the occupied states rather than the unoccupied ones. In this section, we will separate this phenomenon based on the energy of the incident photon. When that photon's energy is far above the edge energy, we are in the non-resonant regime, and the emitted electron can be ignored. However, in the regime where the incident energy is near the binding energy, there are resonant effects, and the technique is also known as Resonant inelastic x-ray spectroscopy (RIXS). An excellent review by Glatzel and Bergmann (from which some of this information is synthesized) is a good resource for further reading on the topic.[46]

Non-resonant x-ray emission spectroscopy is useful to separate from the resonant case for a couple of reasons. First, in a laboratory instrument (described in section 2.3.1), the majority of photons are far above the binding energy and so only non-resonant XES is possible, but at the synchrotron, the incident energy can be tuned to perform resonant experiments. Second, non-resonant XES is treated differently theoretically than resonant XES. In non-resonant XES, we assume that the primary phototelectron has very high energy and the resulting spectrum is a measure of the occupied density of states without any spectator effects. A typical XES spectrum

measures the intensity of emitted x-rays as a function of their energy, leading to a spectrum like that of Figure 1.9. Here we can see transitions into the 1s hole of Cr from the 2p, 3p and valence electrons. Similar to XANES, non-resonant XES contains information on oxidation state and local electronic structure, and is often paired with theoretical calculations to explain the spectra.

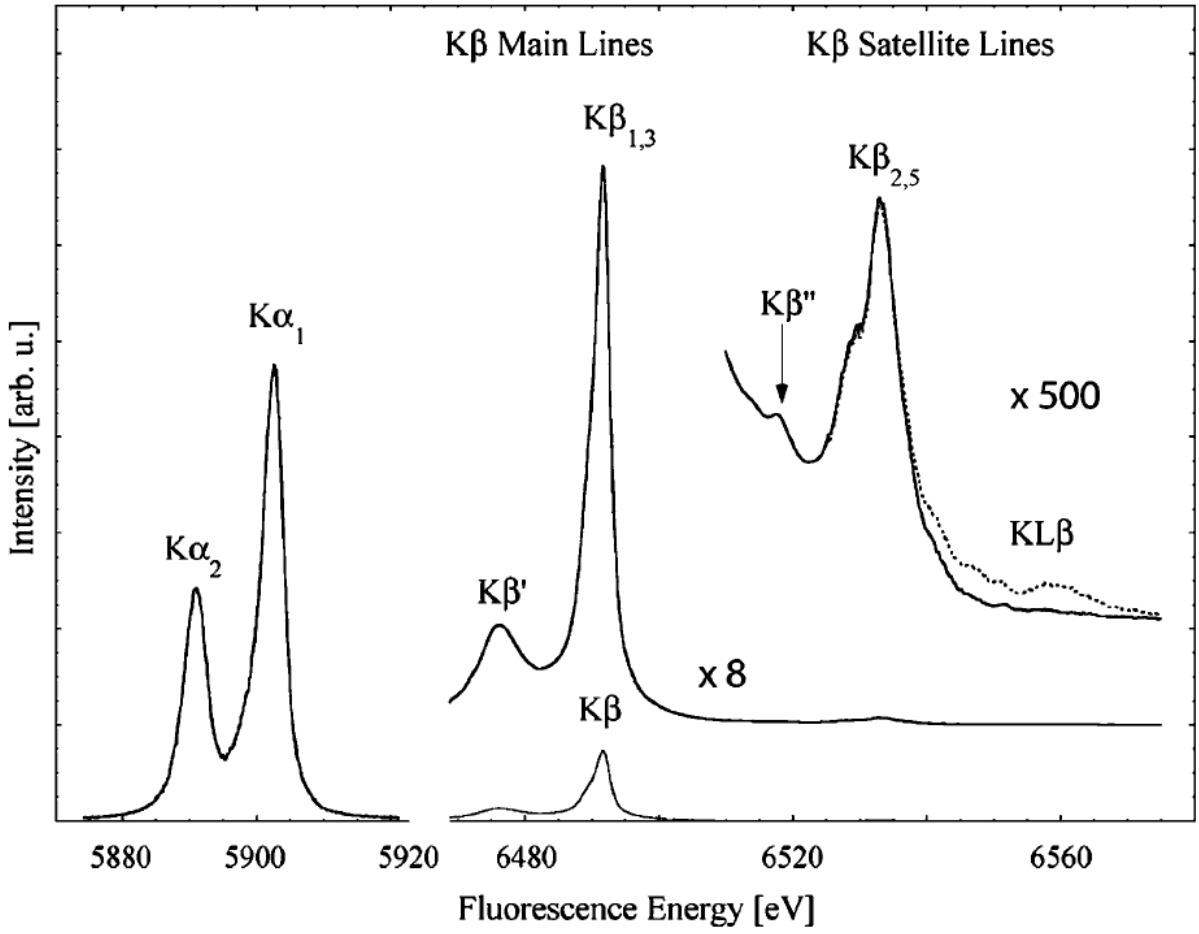

Figure 1.9. V K-shell (1*s*) emission lines. These are split into Kα (2*p* → 1*s*) and Kβ (3*p* → 1*s*). Figure from Glatzel and Bergmann.[46]

1.2.1.1 Resonant Inelastic X-ray Scattering

When the incident x-ray energy can also be varied, it is also possible to do resonant inelastic x-ray scattering measurements. Here, the incident energy is varied around the binding energy of a core electron and the emission spectrum is measured at each point. This results in the central atom

in an excited state (core-hole state), with subsequent relaxation filling the core hole and emitting a photon to conserve energy. These transitions are shown in Figure 1.10, along with the emitted and absorbed photons. At the end of the RIXS experiment, we have the emitted intensity as a function of incident and emitted x-ray energy.

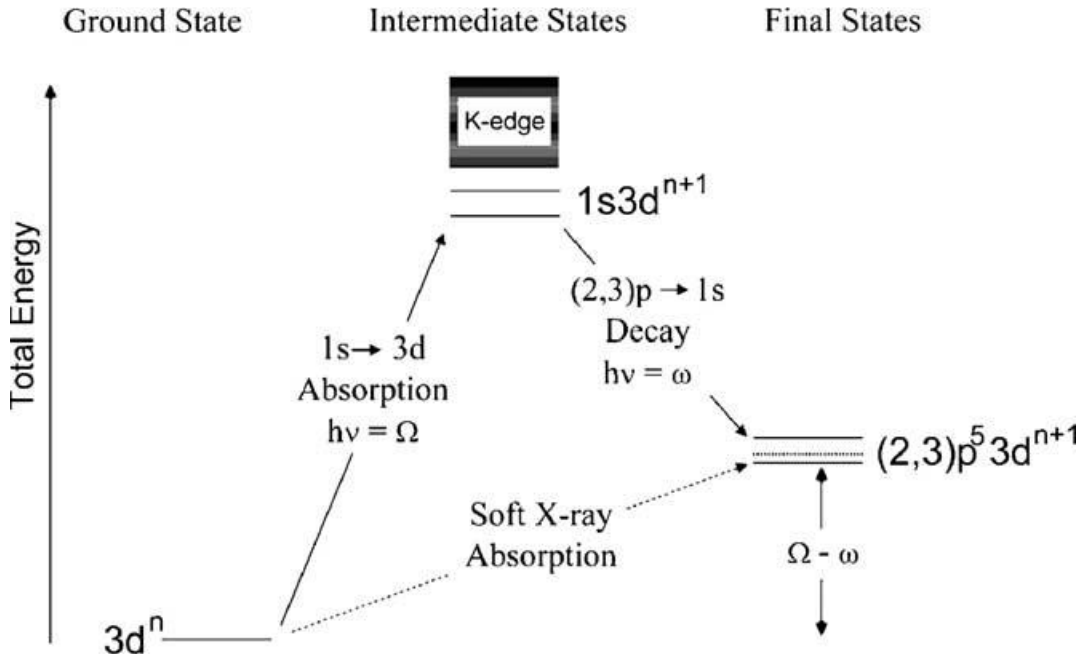

Figure 1.10. Energy levels involved in K-shell (1s) RIXS on a 3d transition metal. The incident photon energy (Ω) and emitted photon energy (ω) are the difference between the ground and intermediate and intermediate and final states respectively. Figure from Glatzel and Bergmann.[46]

These plots are sometimes better shown as a function of energy transfer, which is the incident minus the emitted energy and corresponds to the energy of the final state (Figure 1.11). Thisis useful because we can see the intermediate state energy – equal to the incident photon energy – has broadening due to the core-hole lifetime, and the final state is broadened from the lifetime of the final hole. This final state where the core-hole is filled often has a much longer lifetime and so the energy broadening is reduced. As a result, if we take a diagonal cut as shown in Figure 1.11, top-right, we can get a High Energy Resolution Fluorescence Detection (HERFD)

spectrum, which is similar to a XANES measurement, but the core-hole lifetime is suppressed. The energy resolution improvement can be estimated as demonstrated in De Groot *et al.*[47]

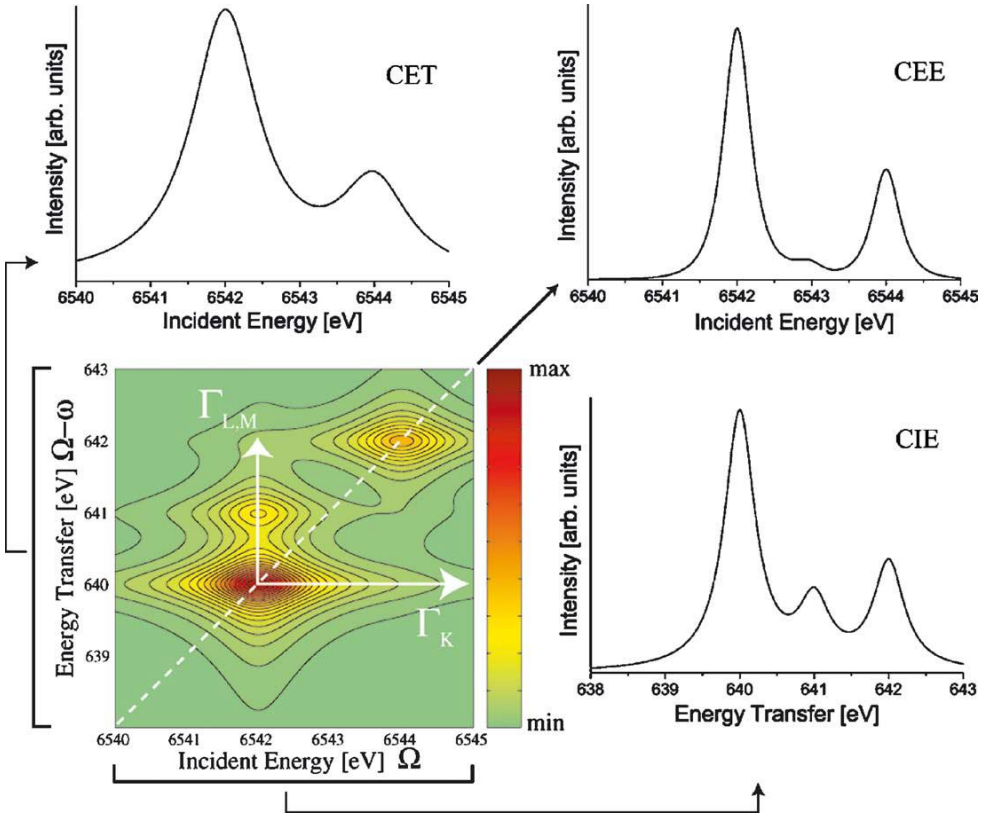

Figure 1.11. A simulated RIXS plane (bottom left) and a constant emission energy, or HERFD cut (top right), a constant incident energy cut, and a constant energy transfer cut. Note that the broadening due to the 1s electron, Γ_K, is suppressed in the CIE and CEE cuts. Figure from Glatzel and Bergmann.[46]

1.2.2 *Examples*

Although XES and RIXS have not been around as long as XAS, in recent years, these techniques have seen increased use, with applications in biology,[48,49] batteries,[50,51] environmental studies,[52] and many other fields. In this section, I will again give several examples of the technique's use with a particular focus on actinide studies.

As mentioned previously, XES is often sensitive to oxidation state change, with the core-hole energy changing as the nucleus charge becomes less screened with missing valence electrons. This is particularly obvious in the study of Kα ($2p \rightarrow 1s$) emission of sulfur and phosphorous, examples shown in Figure 1.12. Here, we can see that the shape of the emission line remains largely the same and simply shifts up or down in energy depending on the oxidation state. This means the emission line does not contain as much information as others (Kβ) about the local electronic structure, but this insensitivity to chemical state can be a benefit when trying to deduce oxidation state. For example, work from our group showed that InP quantum dots consisted of an oxidized outer layer and a reduced inner shell, and in sulfur speciation in biochars[53,54]. This analysis was greatly simplified due to the unchanging nature of the lineshape, allowing for the proportion of reduced and oxidized components to be estimated accurately. This also simplified the analysis of the sulfur RIXS spectra in Chapter 6.

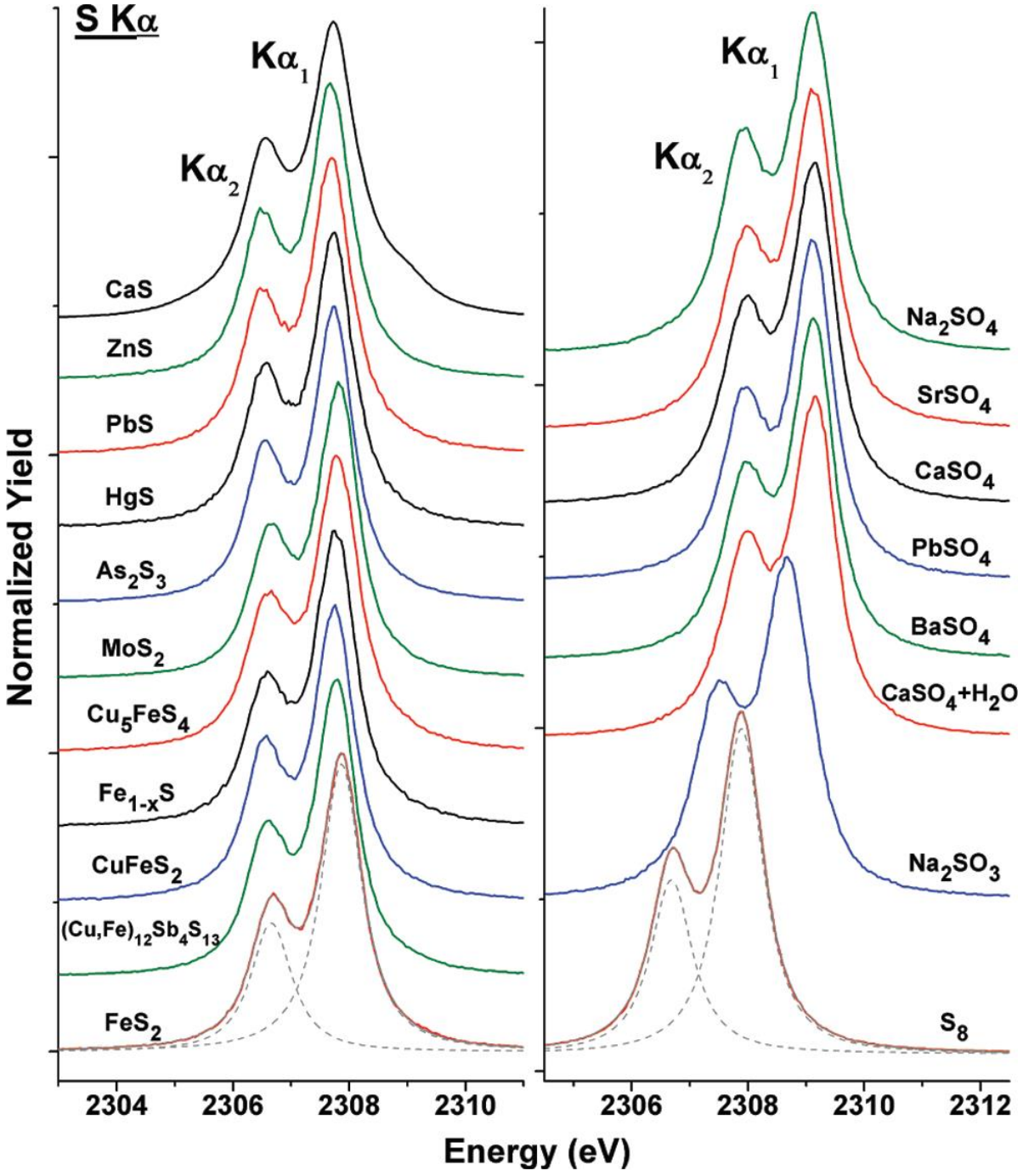

Figure 1.12. Sulfur Ka spectra for several compounds. Note that there is essentially no difference in lineshape between different species, only a shift in energy corresponding to oxidation state change. Figure from Mori et al.[55]

In contrast with the sulfur and phosphorous Kα, valence to core emissions typically contain much more information. For example, valence to core XES on transition metals includes a satellite due to charge transfer from the ligand, and so the position of this peak identifies the ligand[56]. The example discussed here is valence-to-core on several iron compounds, collected by the DeBeer group, shown below in Figure 1.13 [57]. This transition is from the valence bonding electrons to the 1*s* core hole. Because of this, the Kβ spectra offer a good test of electronic structure models (like the DFT models, discussed in section 4.3), and we can see here that the models produced in Pollock et al. successfully reproduce the major features of the XES spectra.

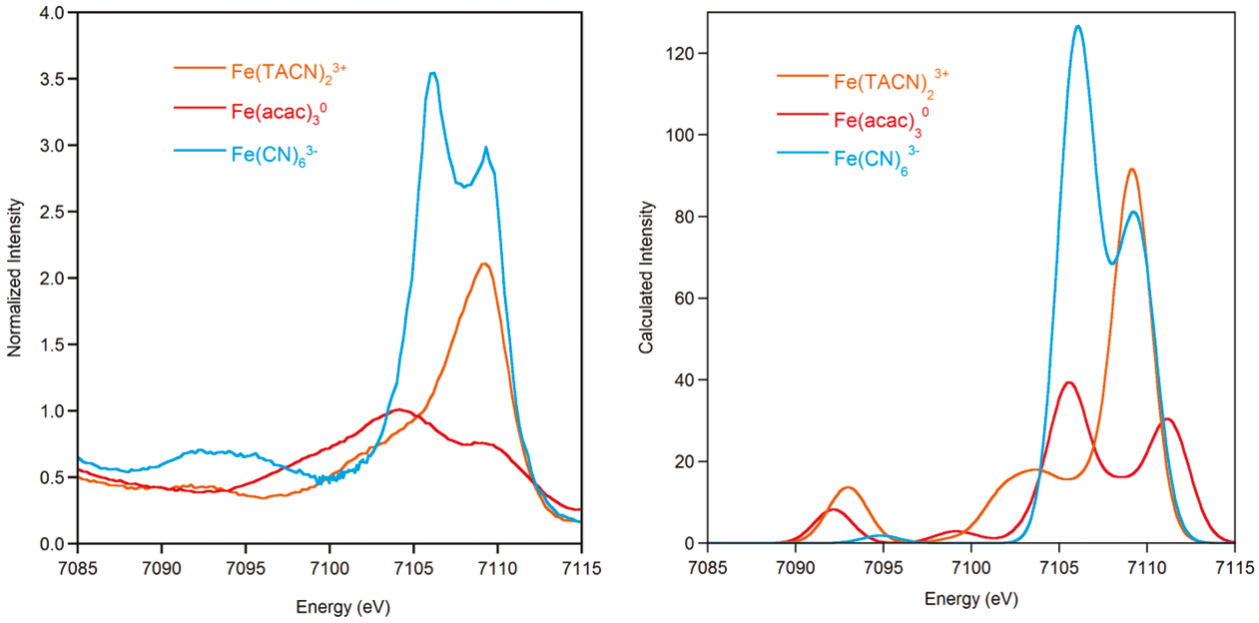

Figure 1.13. Valence to core x-ray emission on several iron compounds (left) and calculations (right). Figure from Pollock *et al.*[57]

Moving to RIXS, a few studies at the synchrotron have been done on uranium intermetallics[58,59]. Here, the primary concern is the degree to which the f electrons are delocalized. Through theoretical calculations and fitting the RIXS plane, Soderland et al. were able to calculate the contribution from f^2, f^3 and f^4 configurations from UF_4, UCd_{11}, UO_2, α-U, and URu_2Si_2 [59]. URu_2Si_2 is an interesting material due to the possibility of a "hidden order" transition. Some of the

theories have posited a solely f^2 configuration for uranium, but the RIXS results show that there is substantial evidence for a f^3 configuration with 3 U f-electrons delocalized, and fairly consistently rule out a solely f^2 configuration.

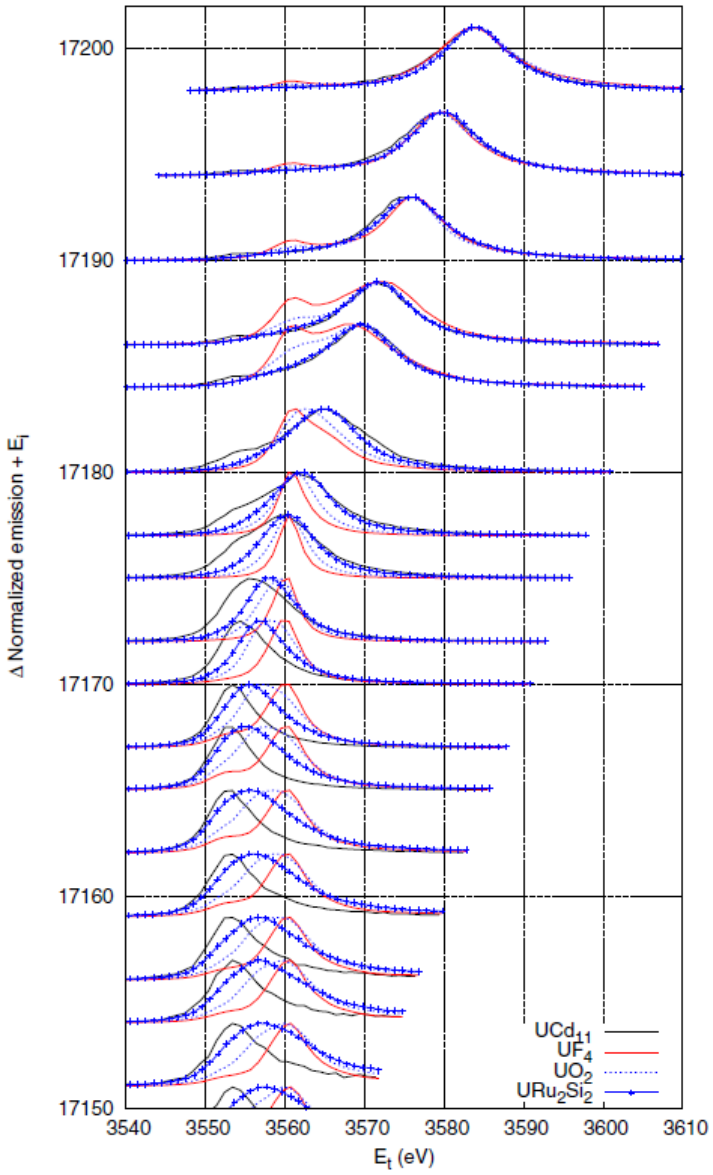

Figure 1.14. Many resonant XES cuts of UCd_{11}, UF_4, UO_2 and URu_2Si_2 at different incident energies. Comparison with standards shows that URu_2Si_2 does not exist in a f^2 configuration as was previously expected[58,59].

One reason why RIXS is an attractive measurement for actinide M-edges is due to the suppression of the core-hole lifetime, as described above. For actinides, the core-hole lifetime is around 7 eV at the L_3 edge and 3-4 eV at the M_4 or M_5 edge,[15] resulting in considerable lost information because of the much smaller energy splitting (~1 eV) for underlying features in the frontier orbitals. Consequently, lifetime-broadening suppression by HERFD can be very useful for recovering the scientifically important detail. One example here shows HERFD spectra measured by Vitova et al. on AnO_2^{2+} (An = U, Np, Pu), see Figure 1.15 with three distinct transitions corresponding to the U 5*f* antibonding orbital splits into δ/φ non-bonding orbitals and σ and π antibonding orbitals (see section 4.2 for an explanation of this terminology). These features are not resolved in a normal XANES measurement due to the lifetime-induced broadening, but they provide central information on the covalency of the An-O bond: in a completely ionic bonding model there would be no energy splitting of the 5*f* orbitals.

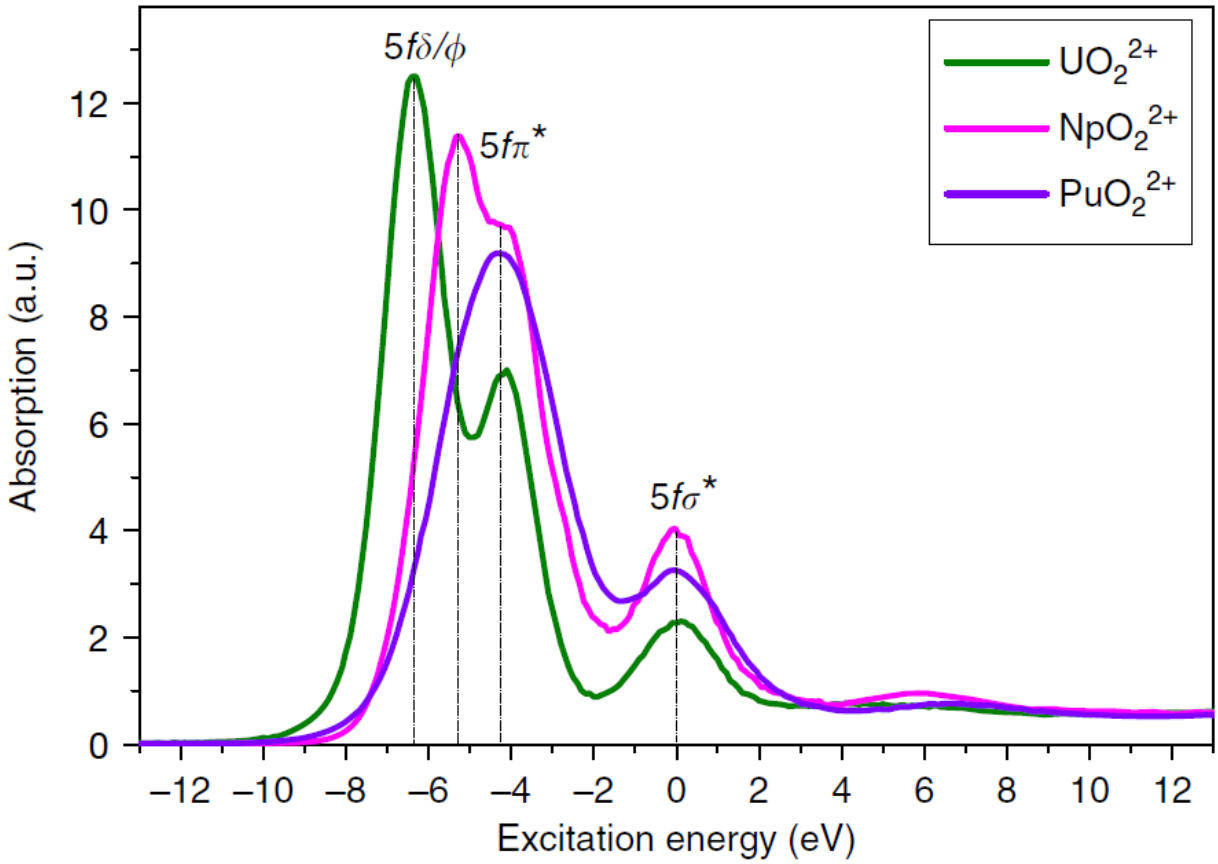

Figure 1.15. Kvashnina et al. study of AnO_2^{2+}. This splitting indicates a degree of covalency in bonding as the ionic model would have degenerate 5*f* electron levels.

A number of studies have also looked at resonant XES at the M-edge, looking at the valence-to-core emission of compounds. These are transitions from the occupied 5*f* electrons into the 3*d* core-hole. Again, we make use here of the lifetime broadening suppression, but instead of taking a diagonal cut in Figure 1.11, we make a vertical one. Again, there is no broadening due to the metal 3*d* core-hole lifetime, whereas in the non-resonant case, there is. Figure 1.16 shows the valence x-ray emission of several different uranium oxides with an excitation energy at the white line of the M5 edge (exciting the $3d_{5/2}$ electron). The spectra show a clear difference between several of the oxidation states. Here the main peak is elastic scatter off of the sample. The next peak contains both charge-transfer transitions (O 2*p* to U 3*d*) and U 5*f* to U 3*d* transitions. The

primary use of these spectra is to test theoretical models, similar to the ones described in section 4.3. Once the validity of these models is established, interpretation of the spectra and statements about the electronic structure of these compounds (including covalency) can be made with more certainty.

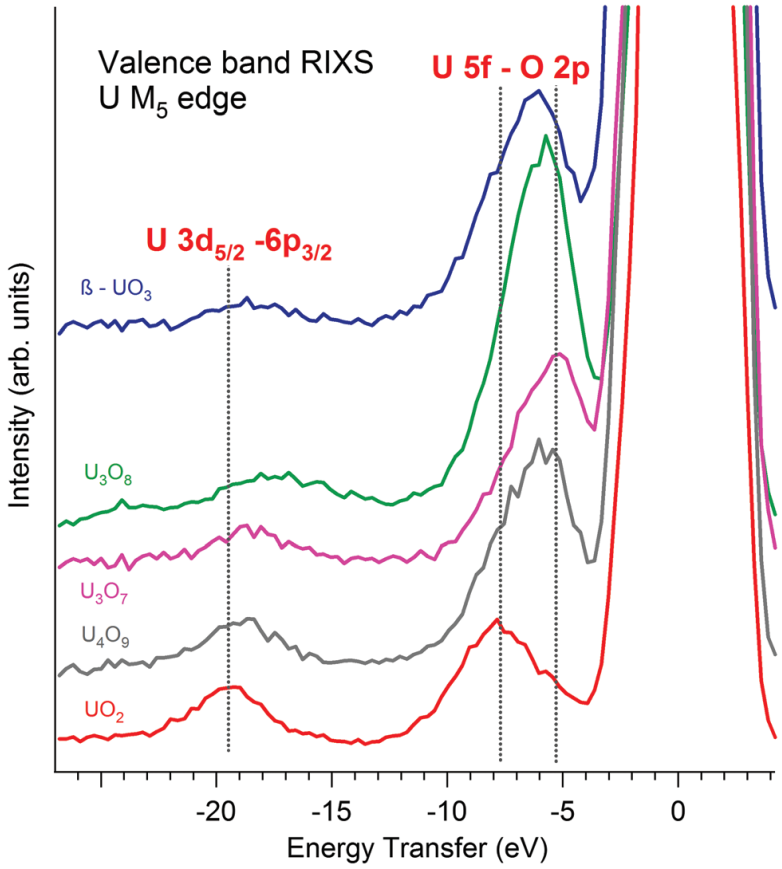

Figure 1.16. Valence RXES at the M5 ($3d_{5/2}$) edge on several uranium oxides. The spectra here show sensitivity to the uranium species with different oxidation states. The main peak at 0 eV energy transfer is the elastic scatter.

1.2.3 *Conclusion*

X-ray emission and X-ray absorption spectroscopies are commonly utilized techniques with broad applicability to a number of fields, and here we have demonstrated their utility in particular in actinide science. In the following sections, I discuss the instrumentation involved in

bringing these techniques to the lab (section 2.3, chapters 6, 7, 9) and the use of both synchrotron-based and lab-based instruments applied to the question of actinide covalency (Chapter 5).

1.3 REFERENCES

1. Rehr, J. J., Albers, R. C. & Zabinsky, S. I. High-order multiple-scattering calculations of x-ray-absorption fine structure. *Phys. Rev. Lett.* **69**, 3397–3400 (1992).

2. Ankudinov, A. L. & Rehr, J. J. Relativistic calculations of spin-dependent x-ray-absorption spectra. *Phys. Rev. B* **56**, R1712–R1716 (1997).

3. Rehr, J. J. *et al.* Inelastic Losses and Multi-Electron Excitations in X-Ray Spectra. in *AIP Conference Proceedings* **882**, 85–88 (AIP, 2007).

4. Rehr, J. J. & Albers, R. C. Theoretical approaches to x-ray absorption fine structure. *Rev. Mod. Phys.* **72**, 621–654 (2000).

5. Hubbell, J. H., Gimm, H. A. & O/verbo/, I. Pair, Triplet, and Total Atomic Cross Sections (and Mass Attenuation Coefficients) for 1 MeV-100 GeV Photons in Elements *Z* =1 to 100. *J. Phys. Chem. Ref. Data* **9**, 1023–1148 (1980).

6. GSE-CARS XAFS Spectra Library (beta). Available at: http://cars.uchicago.edu/xaslib/search. (Accessed: 28th May 2019)

7. Agarwal, B. K. *X-Ray Spectroscopy*. (Springer-Verlag New York, 1989).

8. Stöhr, J. *NEXAFS Spectroscopy*. **25**, (Springer Berlin Heidelberg, 1992).

9. Newville, M. Fundamentals of XAFS. *Rev. Mineral. Geochemistry* **78**, 33–74 (2014).

10. Lytle, F. W., Sayers, D. E. & Stern, E. A. Extended x-ray-absorption fine-structure technique. II. Experimental practice and selected results. *Phys. Rev. B* **11**, 4825–4835 (1975).

11. Stern, E. A. Theory of the extended x-ray-absorption fine structure. *Phys. Rev. B* **10**, 3027–3037 (1974).

12. Sayers, D. E., Stern, E. A. & Lytle, F. W. New Technique for Investigating Noncrystalline Structures: Fourier Analysis of the Extended X-Ray—Absorption Fine Structure. *Phys. Rev. Lett.* **27**, 1204–1207 (1971).

13. Ravel, B. & Newville, M. ATHENA , ARTEMIS , HEPHAESTUS : data analysis for X-ray absorption spectroscopy using IFEFFIT. *J. Synchrotron Radiat.* **12**, 537–541 (2005).

14. Newville, M. & IUCr. EXAFS analysis using *FEFF* and *FEFFIT*. *J. Synchrotron Radiat.*

8, 96–100 (2001).

15. Krause, M. O. & Oliver, J. H. Natural widths of atomic K and L levels, Kα X-ray lines and several K L L Auger lines Relative transition probabilities for the x-ray lines from the K level Natural Widths of Atomic K and L Levels, Ka X . . . Ray Lines and Several Kit Auger Lines. *J. Phys. Chem. Ref. Data* **8**, 431–6138 (1979).

16. Solomon, E. I., Hedman, B., Hodgson, K. O., Dey, A. & Szilagyi, R. K. Ligand K-edge X-ray absorption spectroscopy: Covalency of ligand-metal bonds. *Coord. Chem. Rev.* **249**, 97–129 (2005).

17. Young, N. A. The application of synchrotron radiation and in particular X-ray absorption spectroscopy to matrix isolated species. *Coord. Chem. Rev.* **277**–**278**, 224–274 (2014).

18. Hardacre, C. APPLICATION OF EXAFS TO MOLTEN SALTS AND IONIC LIQUID TECHNOLOGY. *Annu. Rev. Mater. Res.* **35**, 29–49 (2005).

19. KURISAKI, T., MATSUO, S., TÓTH, I. & WAKITA, H. Recent Development of the XANES Spectral Analysis Methods for the Structure Characterization of Metal Complexes in Solution. *Anal. Sci.* **24**, 1385–1392 (2008).

20. Strange, R. W., Ellis, M. & Hasnain, S. S. Atomic resolution crystallography and XAFS. *Coord. Chem. Rev.* **249**, 197–208 (2005).

21. Levina, A., Armstrong, R. S. & Lay, P. A. Three-dimensional structure determination using multiple-scattering analysis of XAFS: applications to metalloproteins and coordination chemistry. *Coord. Chem. Rev.* **249**, 141–160 (2005).

22. Brown, G. E. & Sturchio, N. C. An Overview of Synchrotron Radiation Applications to Low Temperature Geochemistry and Environmental Science. *Rev. Mineral. Geochemistry* **49**, 1–115 (2002).

23. Fandeur, D. *et al.* XANES Evidence for Oxidation of Cr(III) to Cr(VI) by Mn-Oxides in a Lateritic Regolith Developed on Serpentinized Ultramafic Rocks of New Caledonia. *Environ. Sci. Technol.* **43**, 7384–7390 (2009).

24. TAKAHASHI, Y., OHTAKU, N., MITSUNOBU, S., YUITA, K. & NOMURA, M. Determination of the As(III)/As(V) Ratio in Soil by X-ray Absorption Near-edge Structure (XANES) and Its Application to the Arsenic Distribution between Soil and Water. *Anal. Sci.* **19**, 891–896 (2003).

25. Bare, S. R. & Ressler, T. Chapter 6 Characterization of Catalysts in Reactive Atmospheres by X-ray Absorption Spectroscopy. in 339–465 (2009). doi:10.1016/S0360-0564(08)00006-0

26. Iino, K. & Anpo, M. Atomic level characterization by synchrotron radiation for the design of high performance catalysts. *Res. Chem. Intermed.* **29**, 773–782 (2003).

27. Yamamoto, T. X-ray Absorption Spectroscopic Characterization of Solid Acid-base Catalysts. *J. Japan Pet. Inst.* **57**, 261–270 (2014).

28. John Meurig Thomas*, †,‡ and & Gopinathan Sankar*, †. The Role of Synchrotron-Based Studies in the Elucidation and Design of Active Sites in Titanium−Silica Epoxidation Catalysts. (2001). doi:10.1021/AR010003W

29. Li, W. *et al.* Synchrotron-Based X-ray Absorption Fine Structures, X-ray Diffraction, and X-ray Microscopy Techniques Applied in the Study of Lithium Secondary Batteries. *Small Methods* **2**, 1700341 (2018).

30. Cheng, H. *et al.* Synchrotron radiation X-ray powder diffraction techniques applied in hydrogen storage materials - A review. *Prog. Nat. Sci. Mater. Int.* **27**, 66–73 (2017).

31. Fuentes-Cobas, L., Montero-Cabrera, M., Pardo, L. & Fuentes-Montero, L. Ferroelectrics under the Synchrotron Light: A Review. *Materials (Basel).* **9**, 14 (2015).

32. Sham, T. K. Nanoparticles and nanowires: synchrotron spectroscopy studies. *Int. J. Nanotechnol.* **5**, 1194 (2008).

33. Sun, Z., Liu, Q., Yao, T., Yan, W. & Wei, S. X-ray absorption fine structure spectroscopy in nanomaterials. *Sci. China Mater.* **58**, 313–341 (2015).

34. Lee, J. C. X-ray Spectroscopy of Astrophysical Dust. *Space Sci. Rev.* **157**, 93–101 (2010).

35. Yun, S. *et al.* New-generation integrated devices based on dye-sensitized and perovskite solar cells. *Energy Environ. Sci.* **11**, 476–526 (2018).

36. Kosog, B., La Pierre, H. S., Denecke, M. A., Heinemann, F. W. & Meyer, K. Oxidation State Delineation via U L_{III} -Edge XANES in a Series of Isostructural Uranium Coordination Complexes. *Inorg. Chem.* **51**, 7940–7944 (2012).

37. Conradson, S. D. *et al.* Speciation and unusual reactivity in PuO2+x. *Inorg. Chem.* **42**, 3715–3717 (2003).

38. Um, W. *et al.* Characterization of uranium-contaminated sediments from beneath a nuclear waste storage tank from Hanford, Washington: Implications for contaminant transport and fate. *Geochim. Cosmochim. Acta* **74**, 1363–1380 (2010).

39. Eugene S. Ilton, *,†, Steve M. Heald, †, Steven C. Smith, †, David Elbert, ‡ and & Liu†, C. Reduction of Uranyl in the Interlayer Region of Low Iron Micas under Anoxic and Aerobic Conditions. (2006). doi:10.1021/ES0522478

40. Shi, W.-Q. *et al.* Exploring Actinide Materials Through Synchrotron Radiation Techniques. *Adv. Mater.* **26**, 7807–7848 (2014).

41. Hess, N. J., Weber, W. J. & Conradson, S. D. X-ray absorption fine structure of aged, Pu-

doped glass and ceramic waste forms. *J. Nucl. Mater.* **254**, 175–184 (1998).

42. Lind, O. C. *et al.* Characterization of U/Pu particles originating from the nuclear weapon accidents at Palomares, Spain, 1966 and Thule, Greenland, 1968. *Sci. Total Environ.* **376**, 294–305 (2007).

43. Lind, O. C., Salbu, B., Janssens, K., Proost, K. & Dahlgaard, H. Characterization of uranium and plutonium containing particles originating from the nuclear weapons accident in Thule, Greenland, 1968. *J. Environ. Radioact.* **81**, 21–32 (2005).

44. Neidig, M. L., Clark, D. L. & Martin, R. L. Covalency in f-element complexes. *Coord. Chem. Rev.* **257**, 394–406 (2013).

45. Su, J. *et al.* Energy-Degeneracy-Driven Covalency in Actinide Bonding. *J. Am. Chem. Soc.* **140**, 17977–17984 (2018).

46. Glatzel, P. & Bergmann, U. High resolution 1s core hole X-ray spectroscopy in 3d transition metal complexes—electronic and structural information. *Coord. Chem. Rev.* **249**, 65–95 (2005).

47. De Groot, F. M. F., Krisch, M. H. & Vogel, J. Spectral sharpening of the Pt L edges by high-resolution x-ray emission. *Phys. Rev. B - Condens. Matter Mater. Phys.* **66**, 1–7 (2002).

48. Kern, J. *et al.* Simultaneous Femtosecond X-ray Spectroscopy and Diffraction of Photosystem II at Room Temperature. 491–496 (2013). doi:10.1126/science.1234273

49. Lancaster, K. M. *et al.* X-ray emission spectroscopy evidences a central carbon in the nitrogenase iron-molybdenum cofactor. *Science* **334**, 974–7 (2011).

50. Kavčič, M. *et al.* Operando Resonant Inelastic X-ray Scattering: An Appropriate Tool to Characterize Sulfur in Li-S Batteries. *J. Phys. Chem. C* **120**, 24568–24576 (2016).

51. Robba, A. *et al.* Mechanistic Study of Magnesium-Sulfur Batteries. *Chem. Mater.* **29**, 9555–9564 (2017).

52. Jahrman, E. P., Seidler, G. T. & Sieber, J. R. Determination of Hexavalent Chromium Fractions in Plastics Using Laboratory-Based, High-Resolution X-ray Emission Spectroscopy. *Anal. Chem.* **90**, 6587–6593 (2018).

53. Holden, W. M., Seidler, G. T. & Cheah, S. Sulfur Speciation in Biochars by Very High Resolution Benchtop Kα X-ray Emission Spectroscopy. *J. Phys. Chem. A* **122**, 5153–5161 (2018).

54. Stein, J. L. *et al.* Probing Surface Defects of InP Quantum Dots Using Phosphorus Kα and Kβ X-ray Emission Spectroscopy. *Chem. Mater.* **30**, 6377–6388 (2018).

55. Alonso-Mori, R. *et al.* Electronic Structure of Sulfur Studied by X-ray Absorption and Emission Spectroscopy. *Anal. Chem.* **81**, 6516–6525 (2009).

56. Bergmann, U., Horne, C. R., Collins, T. J., Workman, J. M. & Cramer, S. P. Chemical dependence of interatomic X-ray transition energies and intensities – a study of Mn Kβ″ and Kβ2, 5 spectra. *Chem. Phys. Lett.* **302**, 119–124 (1999).

57. Pollock, C. J. & DeBeer, S. Valence-to-Core X-ray Emission Spectroscopy: A Sensitive Probe of the Nature of a Bound Ligand. *J. Am. Chem. Soc.* **133**, 5594–5601 (2011).

58. Booth, C. H. *et al.* Probing 5 f -state configurations in URu2Si2 with U LIII-edge resonant x-ray emission spectroscopy. *Phys. Rev. B* **94**, 045121 (2016).

59. Söderlind, P. *et al.* On the valence fluctuation in the early actinide metals. *J. Electron Spectros. Relat. Phenomena* **207**, 14–18 (2016).

Chapter 2. X-RAY SPECTROSCOPY INSTRUMENTATION

2.1 INTRODUCTION

Historically, x-ray absorption fine structure (XAFS) measurements started in the lab using systems having limited flux and energy resolution, and then greatly expanded in both quality and access with the advent of synchrotron x-ray light sources and dedicated XAFS beamlines in the 1970's and 1980's. This trend became acute with the development of the third-generation synchrotrons in the 1990's, and laboratory-based XAFS became quite infrequent. Synchrotron facilities are expensive to construct, equip, and operate, with about 50 in construction or operating globally, including six in the United States (APS, ALS, SSRL, NSLS II, CHESS, CAMD). Beamtime requests are consequently very competitive, and beamtime allocation heavily favors cutting-edge science over, e.g., routine industrial or research measurements, new user recruiting and training, or University-level instruction. Contrast this experimental landscape to that of x-ray diffraction (XRD), where lab instruments are plentiful, and all scientists have an opportunity for hands on training, routine measurement capability, and preliminary sample testing.

Due to the previously mentioned factors, the development of laboratory XAS and XES instruments has been a primary focus of the Seidler group for several years,[1–5] including my own research. In this section, I lay out the general operation of both synchrotron light sources (section 2.2) as well as Rowland circle monochromators (section 2.3), which helps provide the background knowledge necessary to understand the construction of the first modern mail-in XAFS user facility (Chapter 6), the use of a portable instrument designed by our group[3] to do resonant inelastic x-ray

scattering (Chapter 7), and the results obtained with these instruments relating to actinide covalency (Chapter 5).

2.2 Synchrotron Light Sources

A brief overview of synchrotron lightsources is provided here both as reference for later discussion of RIXS measurements as well as a point of comparison for laboratory instruments.[6] Synchrotron 'rings' in fact have the electron take a polygonal path consisting of bends (where 'bending magnets' cause a transition between two straight edges of the polygon) and straight sections that often themselves have arrays of magnets to 'wiggle' or 'undulate' the electron beam without changing its overall trajectory. Recalling that when an electron is accelerated it radiates, it is clear that strong radiation should be emitted in the forward direction (due to relativistic effects) at the bending magnet locations and also along the straight sections due to the so-called wigglers or undulators, collectively called insertion devices.

This is shown in Figure 2.1. Each oscillation produces radiation, so insertion devices produce a much larger flux of x-rays. The bending magnet produces an extremely spectrally broad 'white beam' of x-rays, whereas the insertion devices make a somewhat 'pink' beam with harmonics 500-2000eV wide in the hard x-ray range. However, usual hard x-ray energy-scanning XAFS requires a monochromatic beam where the most common monochromators works via a double bounce off two single crystals of silicon and typically has a resolving power ($\Delta E/E$) of about 1/10,000. For reference, a sulfur spectrum (edge energy 2472 eV) has an inherent core-hole lifetime broadening of approximately 0.5 eV, and so the sharpness of features in final measured spectra are generally dominated by intrinsic effects.

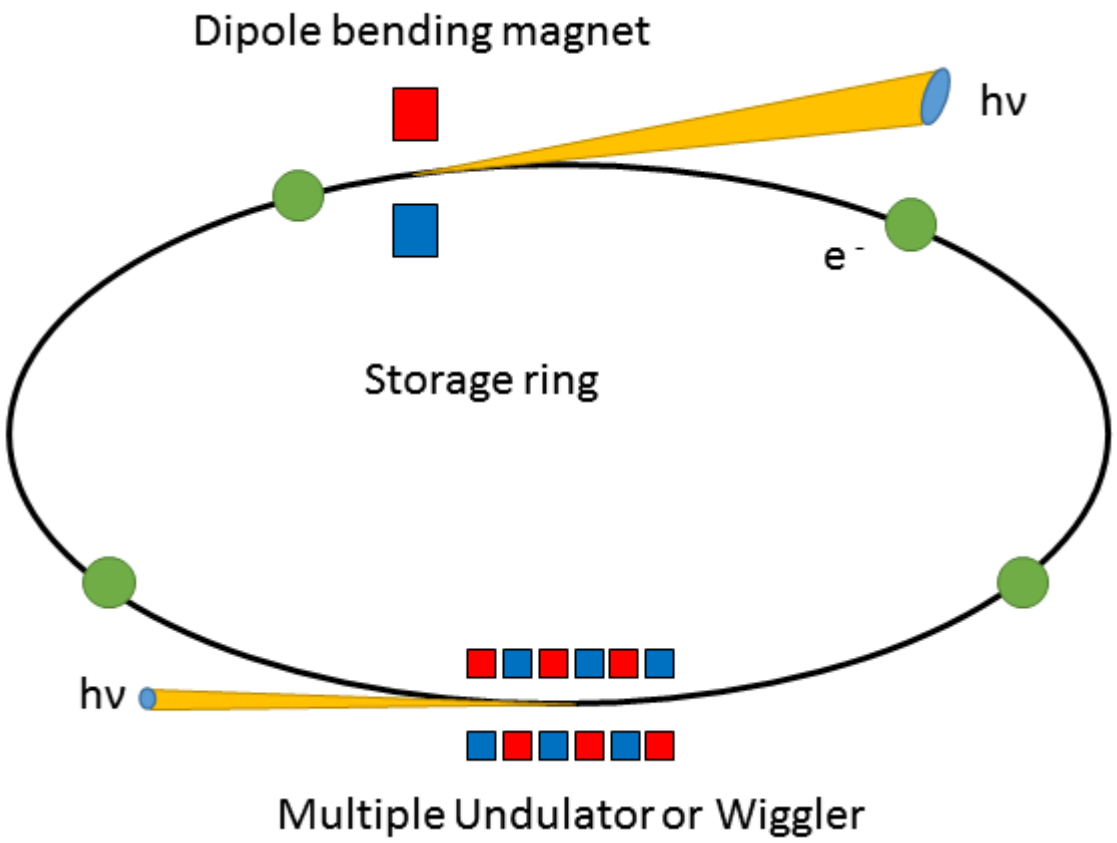

Figure 2.1. Illustration of how synchrotron's produce x-rays in a bending magnet or an insertion device. Figure from Rankovic (2016).[7]

In an XAFS measurement, the desired quantity is the absorption coefficient $\mu(E)$, and this is typically done in either transmission mode or fluorescence mode. Starting with transmission-mode studies, consider the Beer-Lambert Law,

$$I_T(E) = I_0(E)e^{-\mu(E)x}, \tag{2.1}$$

where I_T is the transmitted x-ray flux, I_0 is the incident x-ray flux, μ is the absorption, and x is the thickness of the sample. The absorption spectrum is typically background-subtracted to remove energy dependent absorption from electrons not in the element and electronic shell of interest, and then normalized to an edge-step (called $\Delta\mu x$) of 1. These intensities are commonly measured by gas ionization chambers that generate a current proportional to the x-ray intensity. Figure 2.2

shows the beamline configuration for a transmission mode setup. First the x-rays are transmitted through an ion chamber (I_0) to measure the incident flux, then the sample, then another ion chamber (I_T) to measure the transmitted flux, and finally through a reference sample and a final ion chamber (I_{Ref}). In this way, the incident and transmitted flux on both the sample of interest and the reference sample can be measured simultaneously.

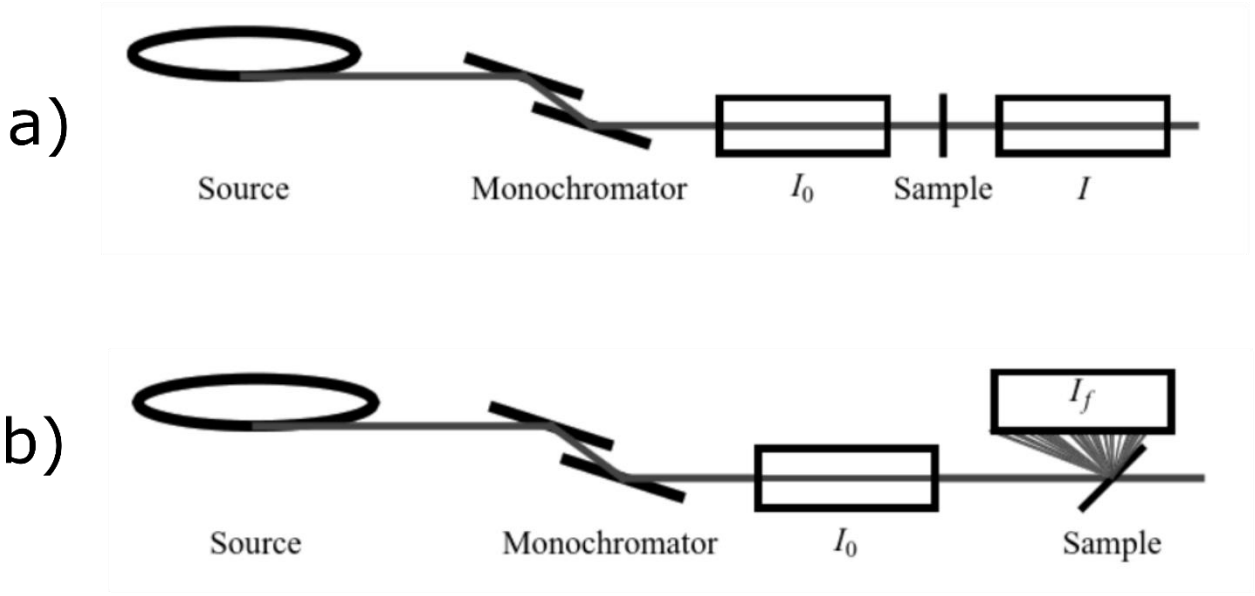

Figure 2.2. Diagram of a typical beamline set up to measure XAS in transmission mode (a) and fluorescence mode (b). Figures from *Introduction to XAFS: A Practical Guide to X-ray Absorption Fine-Structure Spectroscopy*.[6]

However, this approach only works well for sufficiently thick samples. The signal being measured is much smaller for a thin sample, but the noise (proportional to the square root of the count rate) is not.[8] For this reason, very thin or dilute samples are measured in fluorescence mode (sometimes also called total fluorescence yield (TFY)). In this case, the incident x-ray flux as a function of monochromator energy is still measured, but instead of measuring the transmitted flux the experiment instead watches the intensity of the fluorescence due to the core-hole being filled, i.e., a consequence of the element-specfific absorption process. An energy-resolving detector like

a silicon drift detector (SDD) or germanium detector is used to select the fluorescence from the element of interest. The intensity of this fluorescence is proportional to the likelihood of generating that core-hole, which is itself proportional to the element-specific x-ray beam absorption. In the limit where $\mu x \ll 1$, we then have the following equation to relate μ to the incident and fluorescence intensity,

$$I_F \propto I_0 * \mu * x\,. \tag{2.1}$$

However, if the sample is too thick, the linear relation breaks down due to self-absorption.[9,10]

2.3 Rowland Circle Monochromators

Energy resolving detectors, like an SDD or germanium detector have an energy resolution on the order of 100 eV and so are insufficient for the high-resolution measurements of XES. As described in section 2, synchrotron monochromators are a double-bounce type monochromator off of flat silicon crystals. This is sufficient for a strongly collimated synchrotron beam, however for XES, x-rays are emitted in all directions, so that flat crystal monochromators are inefficient at energy resolving narrow energy bands in fluorescence. There are a few other options suitable for XES, such as a von Hamos spectrometer[11,12] or a TES array[13], but we focus here on the Rowland circle spectrometer, as it is currently the most prevalent in XES measurements currently, as well as being highly relevant for work in this dissertation where laboratory XAFS is either developed or used..

2.3.1 *Focusing Rowland Circle Monochromators*

The Rowland circle was developed in 1896 by Henry Rowland in order to make high resolution studies at optical wavelengths, famously starting with the solar spectrum.[14] Those optical-wavelength monochromators used curved diffraction gratings, but a similar optical

geometry applies x-rays when instead using Bragg reflection off a bent single crystal as the dispersing element. Figure 2.3 shows a diagram of the Rowland circle with an x-ray source (point S), an optic (points P), and a detector (point D). Each sit on a circle of radius R. For the moment, we are only concerned with light in the plane shown. Photons emitted from the x-ray source move toward the optic and are reflected back to the detector. Because the source and detector lie on the circle, the angle $\angle SPD$ is half the angular distance from S to D, regardless of which point P on the Rowland circle the x-ray reflects off of. Because these angles are the same, the Bragg condition dictates that only a certain energy is refocused back onto the detector. In addition, we know that for specular reflection the incident angle equals the reflected angle, so the crystal plane of the optic is perpendicular to the bisector of this angle $\angle SPD$. However, this means the perpendicular bisector intersects the point that bisects the arc SD, point B, and so the crystal planes of the optic are perpendicular to the line from P to B. This means that the crystal planes form a circle centered at point B with radius 2R. Changing the energy simply means moving the source and detector along the circle to change the incident and reflected angles.

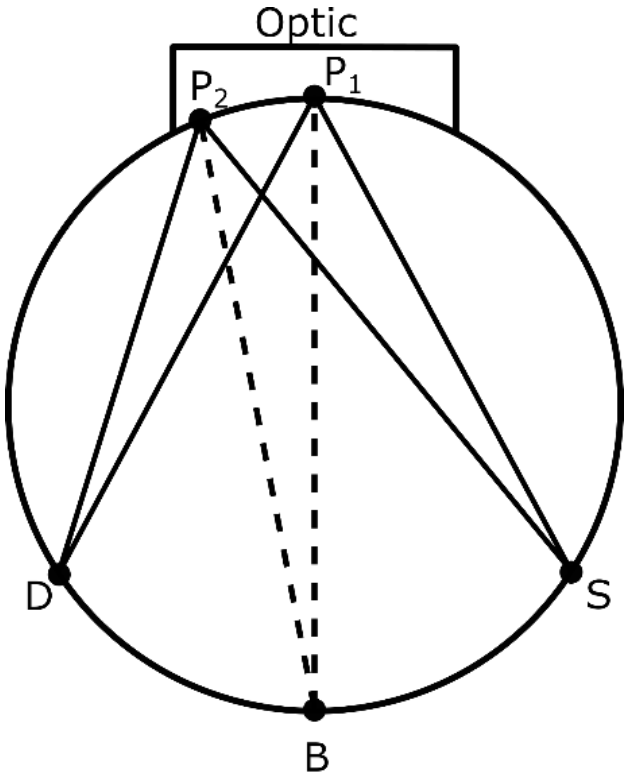

$$\angle SP_1D = \angle SP_2D = \widehat{SBD}$$

$$\angle SP_1B = \angle BP_1D = \widehat{SB}$$

Figure 2.3. Diagram of the Rowland circle showing how each ray from the source (S) is reflected to the detector (D). The two relations at the bottom show that each point on the optic reflects only the same energy

These optics are made by bending single crystals of silicon, germanium, or other semiconductors with high Debye temperatures, and so the optic of figure 2.3 has a bend radius of 2R (the radius of the crystal planes) but sits on a circle of radius R, so it must be ground before or after bending. Such an optic is called a Johansson optic, and its fabrication is notoriously difficult due to, among other factors, the likelihood of surface damage from the grinding process. An approximation which is much easier and less expensive to manufacture is the Johann optic, where the optic is not ground and the crystal planes no longer sit tangent to the Rowland circle. Figure 2.4 illustrates how the Johann optic introduces error (called Johann error) which has both a spectral

component because of errors in the angle of incidence and also spatial error from broadening of the focus on the detector.

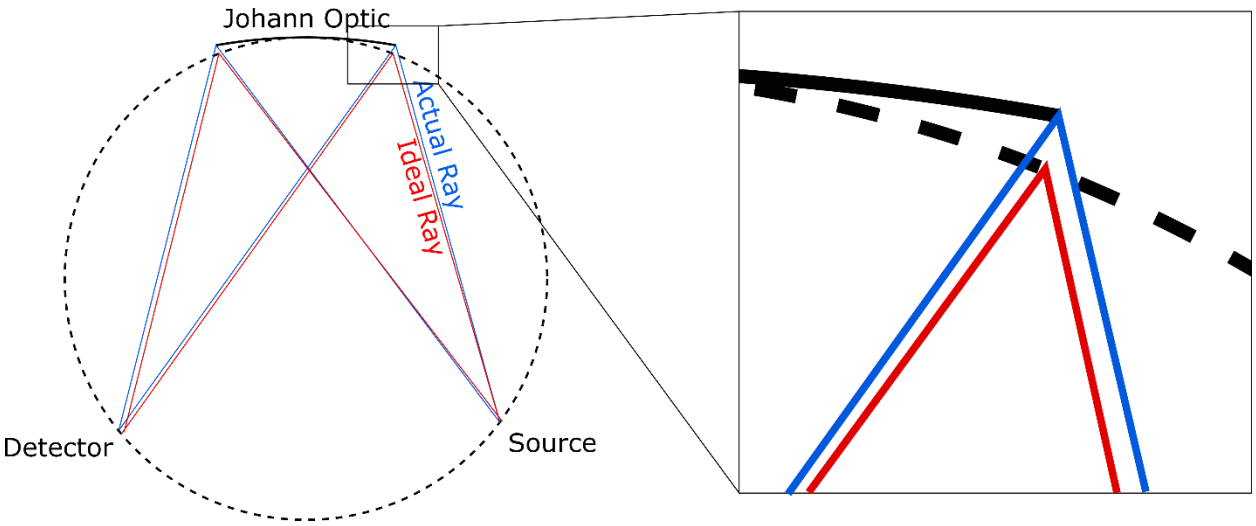

Figure 2.4. Difference between Johan and Johannson geometry showing how Johan error occurs. Both the refocusing position and the Bragg angle are changed from the ideal Johannson optic.

So far, we have only considered two dimensions. To extend this to 3 dimensions, we need to consider how to modify the optic. The simplest extension is to use a cylindrical crystal, and this is how measurements were done for many years. The benefits for the cylindrical crystal are that these optics are easier to bend and so larger optics, Johannson optics and smaller bend radii are more feasible compared to the other options. However, this yields dispersive behavior (like a flat crystal) out of the Rowland plane, and so either a slit must be put up to collimate in the vertical direction, resulting in reduced flux, or energy resolution is sacrificed. To refocus the out of plane dimension, the ideal optic can be found from rotating the Rowland plane about the line through the source and detector. However, this is only point-to-point focusing at that particular Bragg angle. For example, at backscatter the source and detector are close to each other and the optimum-focusing x-ray analyzer is then a spherically bent crystal analyzer (SBCA). As the Bragg angle

moves further from backscatter, sagittal error becomes steadily larger and the optic becomes effectively point-to-line focusing. The vertical (out of plane) stretching of the focused beam on the detector becomes important when the height becomes larger than the size of the detector and signal is lost. However, for studies that have to be performed at some known range of Bragg angles far from backscatter, it is possible to fabricate a toroidal optic so that the point-to-point focusing is recovered. This is discussed more in Chapter 8 on vacuum-formed optics with both spherical and toroidal shapes.

Other factors like source-size and the displacement of the source or detector off the Rowland circle can contribute to the energy resolution. These factors are discussed in detail in Bergmann and Cramer[15], but for reference, the resolution of the instruments discussed in later chapters is primarily due to Johann error and the source size.

Rowland circle monochromators had seen use in the early days of XAFS experimentation, but suffered from limited performance due to the cylindrical optics of the era and detector limitations, especially in their inability to reject harmonic from the analyzer optic and stray fluorescence. This resulted in poor energy resolution (compared to intrinsic limitations from core-hole lifetimes) and also systematic errors that distorted the relative intensities of the experimentally-determined $\mu(E)$.[16–21] However, with the advent of spherically bent crystal analyzers and solid-state detectors, these problems became solvable and resulted in an increase in XES and RIXS measurements at synchrotrons. These instruments use the synchrotron x-ray beam to excite sample fluorescence, where the sample acts as the source on the Rowland circle and the Rowland circle spectrometer itself provides a high resolution characterization of the energy spectrum of the fluorescence, i.e., we perform x-ray emission spectroscopy (XES). These experiments can be count-rate limited for dilute samples of contemporary interest, such as

metaloproteins,[22] and several overlapping Rowland spectrometers can be used to increase the solid angle collected. An example of this is Figure 2.5, which shows the optical configuration for an XES endstation at SSRL beamline 6-2.[23]

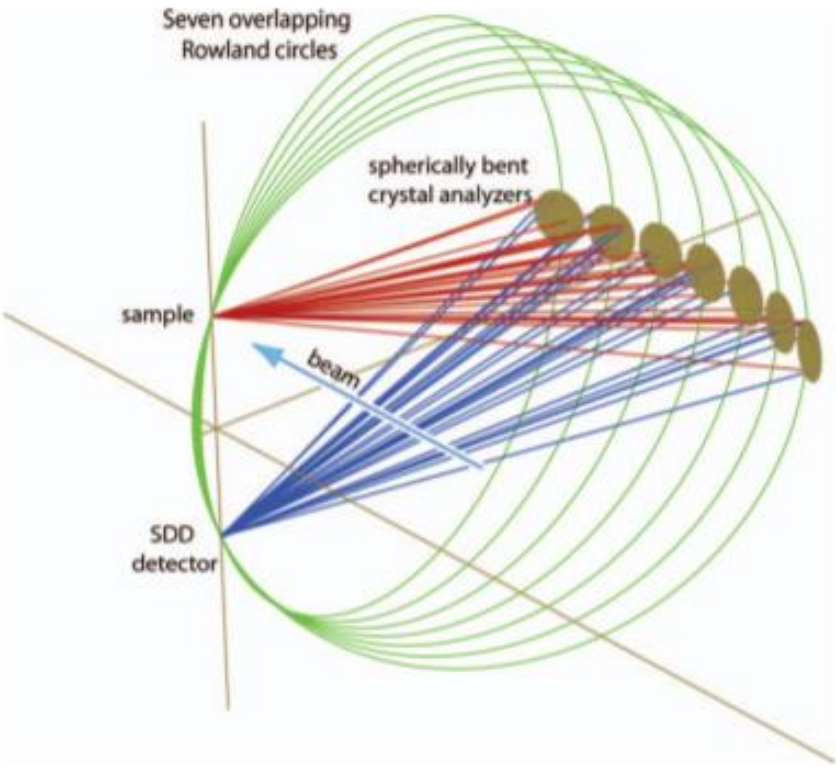

Figure 2.5. Diagram of Rowland circle spectrometer at beamline 6-2 of SSRL. The incident beam is a focused beam of x-rays from the synchrotron.[23]

Those same improvements in optic and detector also allow for a much better laboratory XAS/XES instrument, as first shown by Seidler, et al., in 2014.[1] A schematic of that instrument is shown in Fig. 2.6. In these instruments the Bremsstrahlung radiation from a conventional x-ray tube is used as a broadband x-ray source. In x-ray absorption mode, the x-ray source is pointed directly at the optic and the monochromator produces a monochromatic beam of light incident on the detector. An I_0 scan is taken with no sample present, and then I_T is measured with the sample

in front of the detector. The same instrument can also be used for XES. In that case, the x-ray source points directly at the sample, and then sample fluorescence is monochromatized and refocused at the detector. In both cases, symmetric scanning of the source and detector on the Rowland circle results in an energy spectrum, whether for the transmitted intensity in the case of XAFS or for the emission spectrum, in the case of XES. Several spectrometers of this design have been produced[1,2,24,25], including the work presented in Chapters 5 and 7, and more detail about the design and performance of these instruments is available in those references.

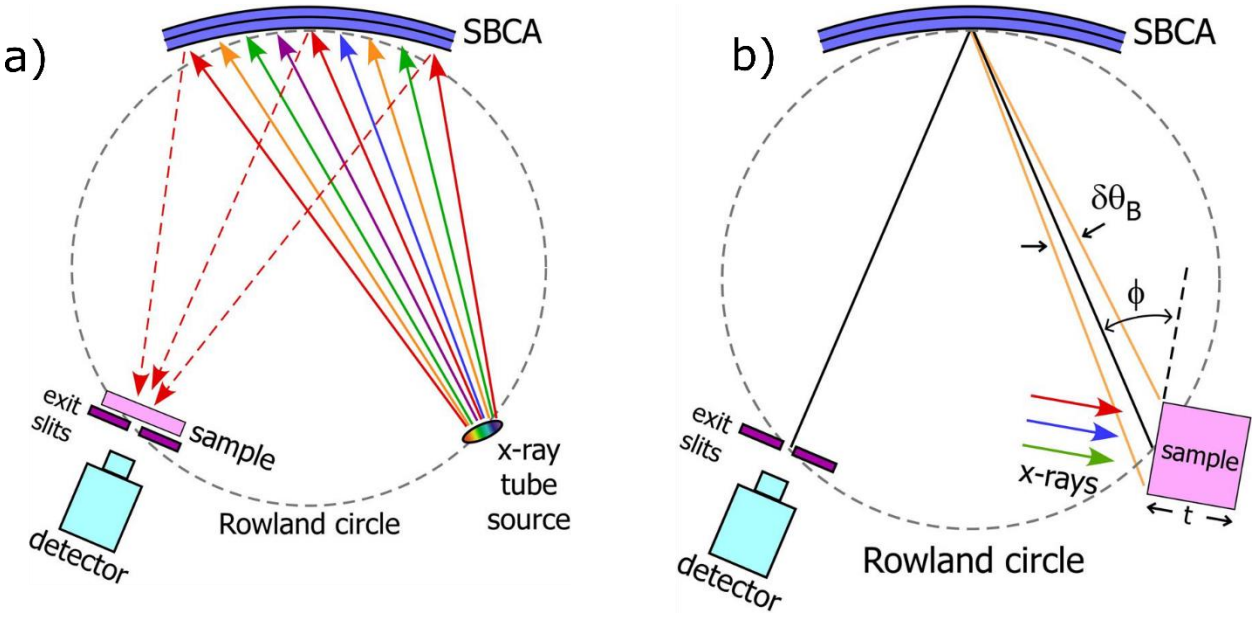

Figure 2.6. Laboratory instruments for XAFS (a) and non-resonant XES (b). Figures from Seidler et al.[1]

One main difference between these laboratory instruments and the synchrotron for XAFS is the monochromatic x-ray flux. Lab instruments produce up to 10^6 photons/second for ~1 kW of x-ray tube power, whereas synchrotrons produce 10^9 to 10^{13} photons/second depending on the use of a bend magnet or insertion device. However, for concentrated samples, laboratory instruments can produce high quality transmission-mode XAFS spectra on scientifically useful measurement

times. Figure 2.7 shows simulations of a cobalt foil spectrum to give an idea of what flux rates are required to get good quality statistics for a concentrated sample. We see that even counting tens of seconds per point can give publication quality results at quite modest incident flux. As a further example, we will see that the system described in Chapter 7 is capable of doing measurements of an absorption edge on a timescale of minutes (e.g. Figure 6.5), so long as one is only concerned about the edge position for measuring, e.g., the oxidation state.

On the other hand, in XES mode, laboratory instruments generate core-holes at a similar rate to a synchrotron.[3] The main difference is that the incident x-rays are not monochromatic in the lab, meaning resonant x-ray emission is impossible. Another difference between the laboratory instruments and the synchrotron are that synchrotron experiments have more control over polarization as well as focusing of the beam, while the same is not true about current laboratory instruments. However, when spatial resolution and resonant effects are not needed, laboratory-based XES can be extremely powerful, such as for speciation of some elements even at trace-level concentrations.[26,27]

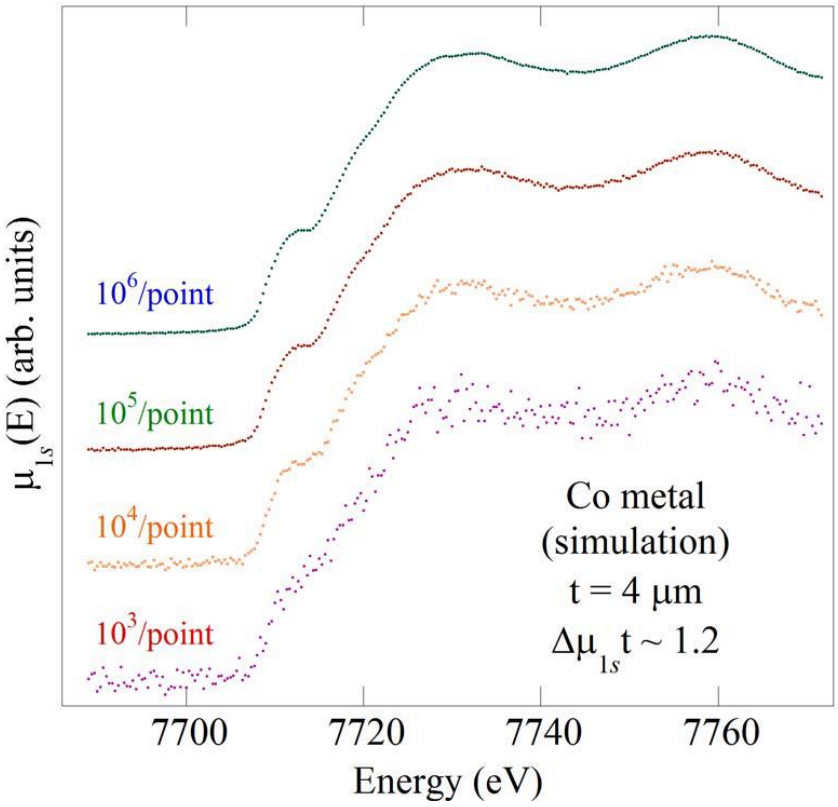

Figure 2.7. Simulated XAFS spectra of a cobalt foil for several different incident fluxes. Figure from Seidler et al.[1]

2.3.2 *Dispersive Rowland Circle Monochromators*

Holden *et al.* discusses several different spectrometer designs that produce a dispersive spectrum.[3] First, consider instead a point source in the interior of the circle, as in Figure 2.8 (a). The light from the source is emitted towards the optic and by creating virtual point sources (as in the figure) in order to determine where that light is reflected. The reflected spectrum is collected by a position-sensitive detector, and in this way an entire spectrum can be measured at once. This dispersive design has been utilized in synchrotron measurements.[21,28] In a similar setup, one could imagine a source along one arc of the Rowland circle, and a position sensitive detector along the opposite arc (Figure 2.8 (b)). Here sample uniformity is important, as each part of the sample

contributes to a different part of the spectrum. This approach has seen use in XES studies in plasma physics[29–42]. Finally, for a finite source off the Rowland circle (Figure 2.8 (c)), a similar dispersive spectrum is obtained. Unlike the example of the large source on the circle, the entire sample contributes for each energy, and as a result concerns over sample inhomogeneity are lessened. The Holden et al. spectrometer used in this work utilizes this off circle, large source design.

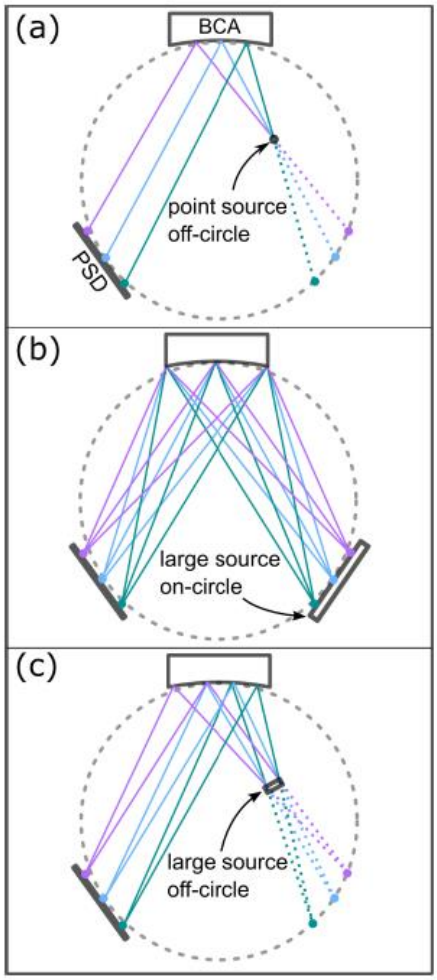

Figure 2.8. Dispersive Rowland circle spectrometer arrangements for a point source off the Rowland circle (a), a large source on the circle (b), and a large source off the circle (c). The bent crystal analyzer (BCA) and position sensitive detector (PSD) are also labelled. Figure from Holden *et al.*[3]

It is worth discussing some specifics of the Holden et al. spectrometer used in later chapters. The optic used is a cylindrical bent crystal analyzer with a radius of 10 cm and the spectrometer can be used with a laboratory source[26,43] or with the synchrotron x-ray beam (see Chapter 7). Other, similar designs in use at ESRF[44] and SSRL[45] utilize a 25-cm radius optic and are mainly used with a focused synchrotron x-ray beam as the source. This distinction becomes very important for measurements of sulfur where radiation damage is a special concern. A defocused beam allows the same incident flux to provide a dose rate tens to hundreds of times smaller without needing to raster the sample.

One important aspect of the Holden *et al*. spectrometer design is that the source size affects the energy resolution in a different way than for a point-to-point focusing spectrometer. Imagining a point source from the detector at a single energy, we get a single arc on the camera due to the cylindrical optic (Figure 2.9, left). If we ignore Johann error, moving the point source in the Rowland plane changes which part of the optic is used, but does not change the image on the camera. However, moving the point source in and out of the plane moves the image on the camera up and down. Because the image on the camera from a point source is an arc, the finite size of the source out of the plane corresponds to an asymmetric broadening of the spectrum towards lower energies. This affect is visible in data where we can control the source size. Using the setup in Figure 2.9, the horizontal size of the beam controls the size of the illuminated spot in the sample, and in Figure 2.10 there is a clear difference in the valence emission of $UO_2Cl_4^{2-}$ and the asymmetric broadening is evident between two measurements with different source sizes. This is a useful thing to keep in mind in Chapter 7 where during the HERFD measurements, the spot size was not limited and so there could be some distortion towards the lower energy side.

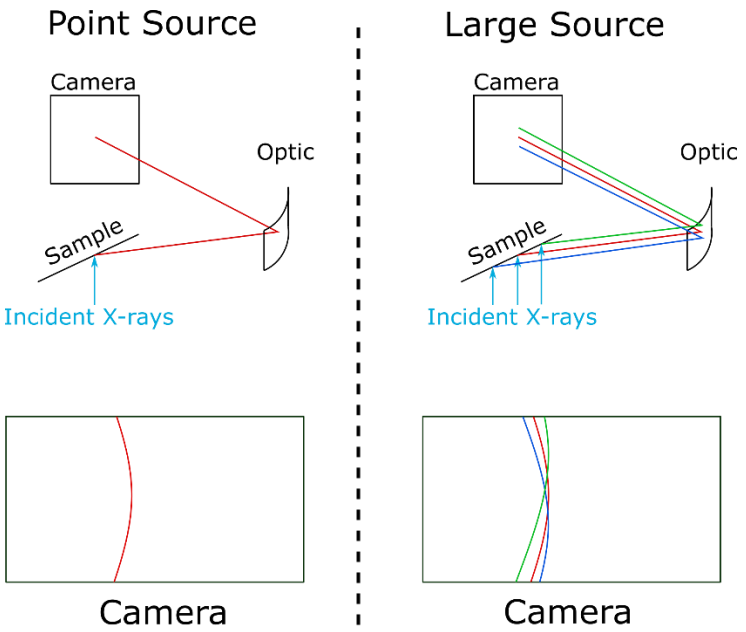

Figure 2.9. Camera image for a point source emitting a single energy (left) and a source of finite size, still emitting a single energy (right). Broadening occurs due to the finite size, with a tail extending towards lower energy.

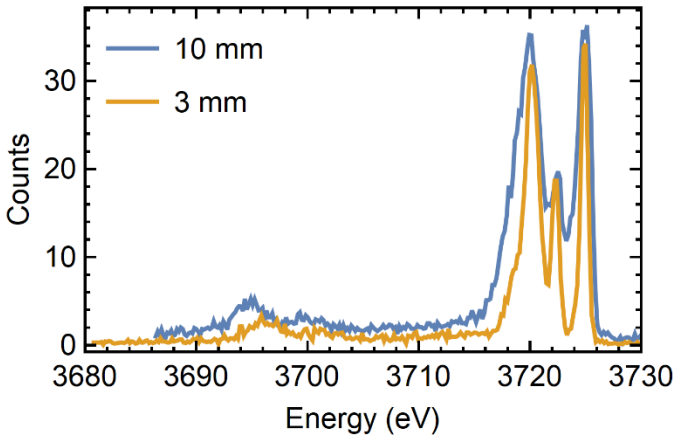

Figure 2.10. Comparison of resonant X-ray emission on $UO_2Cl_4^{2-}$ with two different slit sizes, 10 mm (blue) and 3 mm (yellow). The smaller slit means the illuminated sample has a smaller extent out of the Rowland plane and therefore has a better energy resolution. Note the improved energy resolution for the smaller slit size..

2.4 CONCLUSION

X-ray spectroscopies have greatly benefitted from the use of synchrotron radiation as a monochromatic, high-intensity x-ray source. However, for many measurements, such high monochromatic flux is not necessary. Recent innovations in laboratory x-ray spectroscopy therefore provide increased access to XAS and XES which can benefit the field as a whole. These instruments show the promise to revamp the whole of x-ray spectroscopy

2.5 REFERENCES

1. Seidler, G. T. *et al.* A laboratory-based hard x-ray monochromator for high-resolution x-ray emission spectroscopy and x-ray absorption near edge structure measurements. *Rev. Sci. Instrum.* **85**, 113906 (2014).

2. Seidler, G., Mortensen, D., Ditter, A., Ball, N. & Remesnik, A. A Modern Laboratory XAFS Cookbook. *J. Phys. Conf. Ser.* **712**, 012015 (2016).

3. Holden, W. M. *et al.* A compact dispersive refocusing Rowland circle X-ray emission spectrometer for laboratory, synchrotron, and XFEL applications. *Rev. Sci. Instrum.* **88**, 073904 (2017).

4. Jahrman, E. P. *et al.* An improved laboratory-based x-ray absorption fine structure and x-ray emission spectrometer for analytical applications in materials chemistry research. *Rev. Sci. Instrum.* **90**, 024106 (2019).

5. Jahrman, E. P. *et al.* Vacuum formed temporary spherically and toroidally bent crystal analyzers for x-ray absorption and x-ray emission spectroscopy. *Rev. Sci. Instrum.* **90**, 013106 (2019).

6. Bunker, G. *Introduction to XAFS:* (Cambridge University Press, 2010). doi:10.1017/CBO9780511809194

7. Rankovic, M. L. Photon and Electron Action Spectroscopy of Trapped Biomolecular Ions - From Isolated to Nanosolvated Species. (University of Belgrad, 2016). doi:10.1103/PhysRev.65.343

8. Lee, P. A., Citrin, P. H., Eisenberger, P. & Kincaid, B. M. *Extended x-ray absorption fine structure and lir-~citations as a structural tool its strengths*.

9. Goulon, J., Goulon-Ginet, C., Cortes, R. & Dubois, J. M. On experimental attenuation

factors of the amplitude of the EXAFS oscillations in absorption, reflectivity and luminescence measurements. *J. Phys.* **43**, 539–548 (1982).

10. Pompa, M., Flank, A.-M., Delaunay, R., Bianconi, A. & Lagarde, P. Self-absorption effect in fluorescence XAS of polarization dependent white lines. *Phys. B Condens. Matter* **208**–**209**, 143–144 (1995).

11. Anklamm, L. *et al.* A novel von Hamos spectrometer for efficient X-ray emission spectroscopy in the laboratory. *Rev. Sci. Instrum.* **85**, 053110 (2014).

12. Malzer, W. *et al.* A laboratory spectrometer for high throughput X-ray emission spectroscopy in catalysis research. *Rev. Sci. Instrum.* **89**, 113111 (2018).

13. Doriese, W. B. *et al.* A practical superconducting-microcalorimeter X-ray spectrometer for beamline and laboratory science. *Rev. Sci. Instrum.* **88**, 053108 (2017).

14. Rowland, H. A. On a Table of Standard Wave Lengths of the Spectral Lines. *Mem. Am. Acad. Arts Sci.* **12**, 101 (1896).

15. Bergmann, U. & Cramer, S. P. High-resolution large-acceptance analyzer for x-ray fluorescence and Raman spectroscopy. in (eds. Macrander, A. T., Freund, A. K., Ishikawa, T. & Mills, D. M.) **3448**, 198 (International Society for Optics and Photonics, 1998).

16. Knapp, G. S., Chen, H. & Klippert, T. E. Development of a laboratory EXAFS facility. *Rev. Sci. Instrum.* **49**, 1658–1666 (1978).

17. Cohen, G. G., Fischer, D. A., Colbert, J. & Shevchik, N. J. Tunable laboratory extended x-ray absorption fine structure system. *Rev. Sci. Instrum.* **51**, 273–277 (1980).

18. Thulke, W., Haensel, R. & Rabe, P. Versatile curved crystal spectrometer for laboratory extended x-ray absorption fine structure measurements. *Rev. Sci. Instrum.* **54**, 277–283 (1983).

19. Tohji, K., Udagawa, Y., Kawasaki, T. & Masuda, K. Laboratory EXAFS spectrometer with a bent crystal, a solid-state detector, and a fast detection system. *Rev. Sci. Instrum.* **54**, 1482–1487 (1983).

20. Williams, A. Laboratory x-ray spectrometer for EXAFS and XANES measurements. *Rev. Sci. Instrum.* **54**, 193–197 (1983).

21. Brennan, S. *et al.* Performance of a tuneable secondary x-ray spectrometer. *Rev. Sci. Instrum.* **60**, 2243–2246 (1989).

22. Lancaster, K. M. *et al.* X-ray emission spectroscopy evidences a central carbon in the nitrogenase iron-molybdenum cofactor. *Science* **334**, 974–7 (2011).

23. Sokaras, D. *et al.* A seven-crystal Johann-type hard x-ray spectrometer at the Stanford

Synchrotron Radiation Lightsource. *Rev. Sci. Instrum.* **84**, 053102 (2013).

24. Jahrman, E. P. *et al.* An Improved Laboratory-Based XAFS and XES Spectrometer for Analytical Applications in Materials Chemistry Research. (2018).

25. Honkanen, A.-P. *et al.* Johann-type laboratory-scale x-ray absorption spectrometer with versatile detection modes. *Rev. Sci. Instrum.* **90**, 033107 (2019).

26. Holden, W. M., Seidler, G. T. & Cheah, S. Sulfur Speciation in Biochars by Very High Resolution Benchtop Kα X-ray Emission Spectroscopy. *J. Phys. Chem. A* **122**, 5153–5161 (2018).

27. Jahrman, E. P., Seidler, G. T. & Sieber, J. R. Determination of Hexavalent Chromium Fractions in Plastics Using Laboratory-Based, High-Resolution X-ray Emission Spectroscopy. *Anal. Chem.* **90**, 6587–6593 (2018).

28. Huotari, S., Albergamo, F., Vankó, G., Verbeni, R. & Monaco, G. Resonant inelastic hard x-ray scattering with diced analyzer crystals and position-sensitive detectors. *Rev. Sci. Instrum* **77**, 53102 (2006).

29. Glenzer, S. H. *et al.* Demonstration of Spectrally Resolved X-Ray Scattering in Dense Plasmas. *Phys. Rev. Lett.* **90**, 175002 (2003).

30. Glenzer, S. H. & Redmer, R. X-ray Thomson scattering in high energy density plasmas. *Rev. Mod. Phys.* **81**, 1625–1663 (2009).

31. Kritcher, A. L. *et al.* Development of X-ray Thomson scattering for implosion target characterization. *High Energy Density Phys.* **7**, 271–276 (2011).

32. Hudson, L. T. *et al.* A high-energy x-ray spectrometer diagnostic for the OMEGA laser. *Rev. Sci. Instrum.* **73**, 2270–2275 (2002).

33. Hoidn, O. R. & Seidler, G. T. Photometric study of single-shot energy-dispersive x-ray diffraction at a laser plasma facility. *Phys. Plasmas* **21**, 012707 (2014).

34. Gamboa, E. J. *et al.* Imaging x-ray Thomson scattering spectrometer design and demonstration (invited). *Rev. Sci. Instrum.* **83**, 10E108 (2012).

35. Woolsey, N. C. *et al.* Precision X-ray spectroscopy of intense laser-plasma interactions. *High Energy Density Phys.* **7**, 105–109 (2011).

36. Valdivia, M. P. *et al.* Talbot–Lau x-ray deflectometry phase-retrieval methods for electron density diagnostics in high-energy density experiments. *Appl. Opt.* **57**, 138 (2018).

37. Valdivia, M. P., Stutman, D. & Finkenthal, M. Single-shot Z_eff dense plasma diagnostic through simultaneous refraction and attenuation measurements with a Talbot–Lau x-ray moiré deflectometer. *Appl. Opt.* **54**, 2577 (2015).

38. Suggit, M. *et al.* Nanosecond x-ray Laue diffraction apparatus suitable for laser shock compression experiments. *Rev. Sci. Instrum.* **81**, 083902 (2010).

39. Plateau, G. R. *et al.* Low-Emittance Electron Bunches from a Laser-Plasma Accelerator Measured using Single-Shot X-Ray Spectroscopy. *Phys. Rev. Lett.* **109**, 064802 (2012).

40. Matlis, N. H. *et al.* Snapshots of laser wakefields. *Nat. Phys.* **2**, 749–753 (2006).

41. Mao, J. Y. *et al.* Application of a transmission crystal x-ray spectrometer to moderate-intensity laser driven sources. *Rev. Sci. Instrum.* **83**, 043104 (2012).

42. Labate, L., Köster, P., Levato, T. & Gizzi, L. A. A novel technique for single-shot energy-resolved 2D x-ray imaging of plasmas relevant for the inertial confinement fusion. *Rev. Sci. Instrum.* **83**, 103504 (2012).

43. Stein, J. L. *et al.* Probing Surface Defects of InP Quantum Dots Using Phosphorus Kα and Kβ X-ray Emission Spectroscopy. *Chem. Mater.* **30**, 6377–6388 (2018).

44. Kavčič, M. *et al.* Design and performance of a versatile curved-crystal spectrometer for high-resolution spectroscopy in the tender x-ray range. *Rev. Sci. Instrum.* **83**, (2012).

45. Tobin, J. G. *et al.* Separate measurement of the 5f5/2 and 5f7/2 unoccupied density of states of UO2. *J. Electron Spectros. Relat. Phenomena* **232**, 100–104 (2019).

Chapter 3. ACTINIDE F-ELECTRON CHEMISTRY

Actinide are an important part of everyday life, with applications from nuclear power and national security, to spaceflight and advanced medical treatments. Unfortunately, the rarity of the actinides and the hazards involved in handling them has tempered progress in understanding their chemistry. In section 3.1, I briefly describe the discovery and history of actinides. Next, in section 3.2, I will discuss the unique properties of f-electrons that influence actinide chemistry and how this compares to the other elements with a partially filled f-orbital, the lanthanides. Finally, I will conclude with an overview of the importance of actinides in real world problems and how f-electron chemistry and in particular, f-electron covalency, is related to those issues.

3.1 HISTORY

The actinides are the group of elements just below the rare-earths (lanthanides) on the periodic table and include elements actinium (89) to lawrencium (103). The vast majority of these elements have no stable isotopes, and only the first four are found in appreciable quantities in nature, mainly from uranium (92) and thorium (90) and their decay products.[1] Uranium was first discovered in 1789 in pitchblende and thorium was discovered in 1828.[2,3] Actinium (89) was discovered in 1902 by Giesel through separating radium and this new "emanation" producing material from pitchblende. Protactinium (91) was discovered in 1918 by Soddy and Cranston and simultaneously Hahn and Meitner while trying to explain the occurrence of Ac with U, even though Ac is not part of the U decay chain. For the heavier actinides, there are no appreciable natural sources, and so these were not discovered until the advent of cyclotrons that allowed researchers

to bombard nuclei with neutrons and other particles. In this way, neptunium (93) and plutonium (94) were discovered in 1940, by bombarding uranium and neptunium with neutrons and deuterons respectively.

During World War II and with the advent of nuclear weapons, there was an increased focus on producing large quantities of plutonium and other actinides for the war effort. Through cyclotron experiments, americium (95) and curium (96) were first discovered in 1945, and by 1946 enough of these elements were being produced in research reactors to enable a more serious chemical study of elements 93-96. Seaborg gives an account of this period in "The Transuranium Elements"[4] and also lays out the case for the actinides being a series of elements with unfilled f orbitals belonging below the lanthanides on the periodic table. Prior to this development, the actinides were assumed to be 6d transition metals. This "actinide concept" helped guide chemical experiments on separating and identifying the remainder of the actinide elements which, after plutonium, are increasingly difficult to produce, radioactive, and short lived. The next elements, berkelium (97) and californium (98) were discovered through cyclotron bombardment of americium in 1950, and the elements einsteinium (99) and fermium (100) were discovered in debris from a nuclear weapon test in 1952. Rounding out the series, the elements mendelevium (101), nobelium (102) and lawrencium (103) were produced at cyclotrons with Am or Cm targets. For a more complete description of the discovery of each element, the reader is directed to the individual chapters for each element in *The Chemistry of the Actinide and Transactinide Elements*.[3]

3.2 Atomic and Chemical Perspective on F-Orbitals

The lanthanides (elements 57 – 71) are unique in that they have a partially filled 4f-band. Because the 4f electrons do not extend radially past the core, they do not participate in covalent bonding. As a result, the lanthanides are very similar chemically and all form predominantly +3 compounds in solution. Chemically separating lanthanides from each other is difficult as the main difference between the members of each species is their ionic radius.[5] The 4f electrons only partially shield the nuclear charge, so as one moves to higher Z across the series, the lanthanide ionic radius decreases. This is shown in figure 3.2, where D'Angelo *et al.* measured the ionic radii for actinide and lanthanide ions in the +3 oxidation state in solution and found them to be remarkably similar.[6]

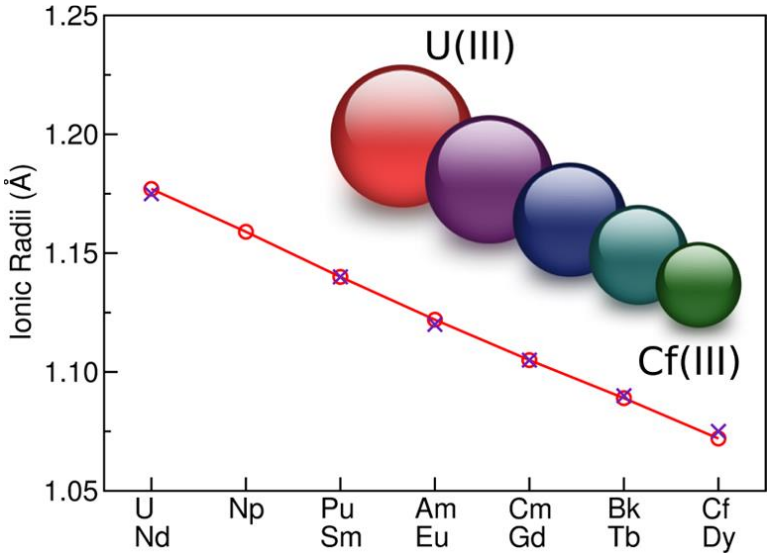

Figure 3.1. Ionic radii of An(III) and Ln(III) ions in solution. Almost no difference between Ln and An means separations are very difficult. Figure from D'Angelo *et al.*[6]

The actinides are chemically similar to the lanthanides, especially later in the series. As one moves across the series, the 5f band fills, and similar to the lanthanides, the ionic radius decreases. In fact, the similarity is so strong that lanthanides are often used as stand-ins for their

more radioactive counterparts (e.g. Ce for Pu). However, this similarity also causes problems when trying to separate acutely radioactive lanthanides in radioactive waste from the longer-lived actinides, as is discussed more in section 3.4.3.

The main difference between the lanthanides and actindes is that the 5f orbitals of the actinides extend beyond the core and are available to participate in bonding seen in the radial distribution functions of Figure 3.2. This results in some of the most complicated chemistry on the periodic table, particularly in the early actinides. For example, in solution, Pu can exist in four different oxidation states simultaneously and therefore the redox chemistry of plutonium in solutions is particularly complicated.[7] For the heavier actinides (Am and heavier specifically), the f-orbitals begin to contract, leading to very similar chemistry as that of the lanthanides. It is for this reason, that the actinides are sometimes thought of in two groups, the early ones being more transition metal-like and the later ones being lanthanide-like.[4]

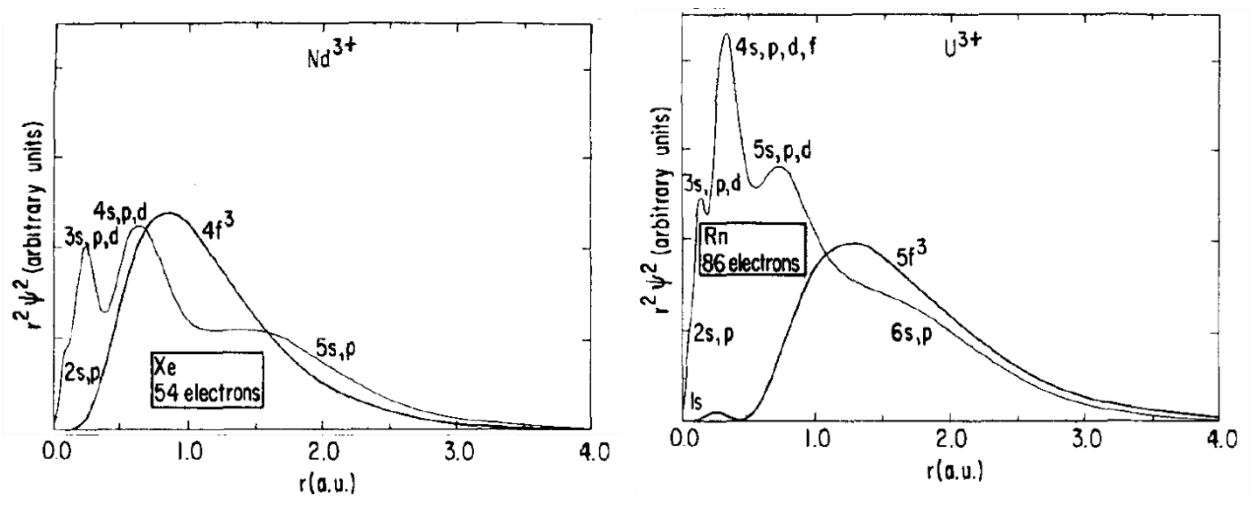

Figure 3.2. Difference in radial extent of 5f and 4f orbitals showing that 5f orbitals are slightly more available for bonding and hence the early actinides have a much more complex chemistry than that of the actinides. Figure from Crosswhite *et al.*[8]

3.3 Covalency in 5f Electrons

In designing an extractant for separating actinides from lanthanides, the nature of the bond between the metal and the extractant is key in determining how effective the separations technique will be.[9] To this end, we return to the main point of Figure 3.2, i.e., that the 4f electrons for the lanthanides are deep while the actinides extend past the core electrons. Lanthanides consequently almost always bond ionically.[10] Actinides, on the other hand, have at least the potential to have bonding with a significant covalent character. This gives fair hope for schemes for strong separation of lanthanides and actinides, but begs the question: how can we quantify the extent of 5f electrons' involvement in covalent bonding.

In addition to potentially being useful in a separations context, covalency is used to rationalize reactivity and physical properties of elements across the periodic table. The lack of knowledge about whether actinides participate in covalent bonds is a major stumbling block in understanding their behavior in real-world systems. As such, the question of 5f electrons' participation in covalent bonds has seen much study over the past several decades.[11–17]

Covalency, as defined by Heitler and London,[18] is when electrons are shared among atoms. On the other hand, a perfectly ionic bond is when electrons are completely transferred from one atom to another. With the use of molecular orbital theory, we can make this more quantitative. The degree of covalency in a bond between a metal and a ligand can be measured by the mixing coefficient of two orbitals, $\lambda_{ML} = \frac{H_{ML}}{E_M - E_L}$, where H_{ML} is the overlap of the two orbitals and E_M is the energy of the metal orbital and E_L is the energy of the ligand orbital.[19] However, there is some discussion of whether λ_{ML} is a suitable measurement of covalency as it doesn't necessarily say anything about the electron density between the two atoms and may not have an effect on the

energy of those bonds.[20] It's up for debate whether decreasing the energy difference between the metal and ligand orbitals actually makes for a more covalent bond in any practical sense of the word.

The first evidence in favor of covalent bonding was given by Diamond, Street and Seaborg in 1954.[12] Those authors looked at elution rates from ion exchange columns in both lanthanides and actinides. Ion exchange columns use a resin with a tendency to attract positive ions (usually H+ initially) through which a solution is flowed. Cations (like An^{3+} in water) displace the hydrogen ions and stick to the resin. This is useful in separations because different ions stick to the resin preferentially, based on factors like ion charge and ionic radius.

In Seaborg's experiment, Solutions of $^{241}Am^{3+}$ and $^{147}Pm^{3+}$ were loaded onto the column in solutions of varying HCl concentration and then centrifuged. The eluted volume and resin were each counted in an α or β counter for ^{241}Am and ^{147}Pm respectively. The comparison of the count rates with the volume and weight of resin give the equilibrium distribution coefficient. This is proportional to the amount of solution required to achieve the peak elution (measured elsewhere in that paper). The results were very similar for low acid concentrations but the distribution coefficient for Pm began to rise at higher acid concentrations and that of Am continued to fall (Figure 3.3). Seaborg argued that because the ionic radii are so similar for the two, the difference in behavior between the two must be because the Am3+ must be forming a covalent complex with Cl in solution.

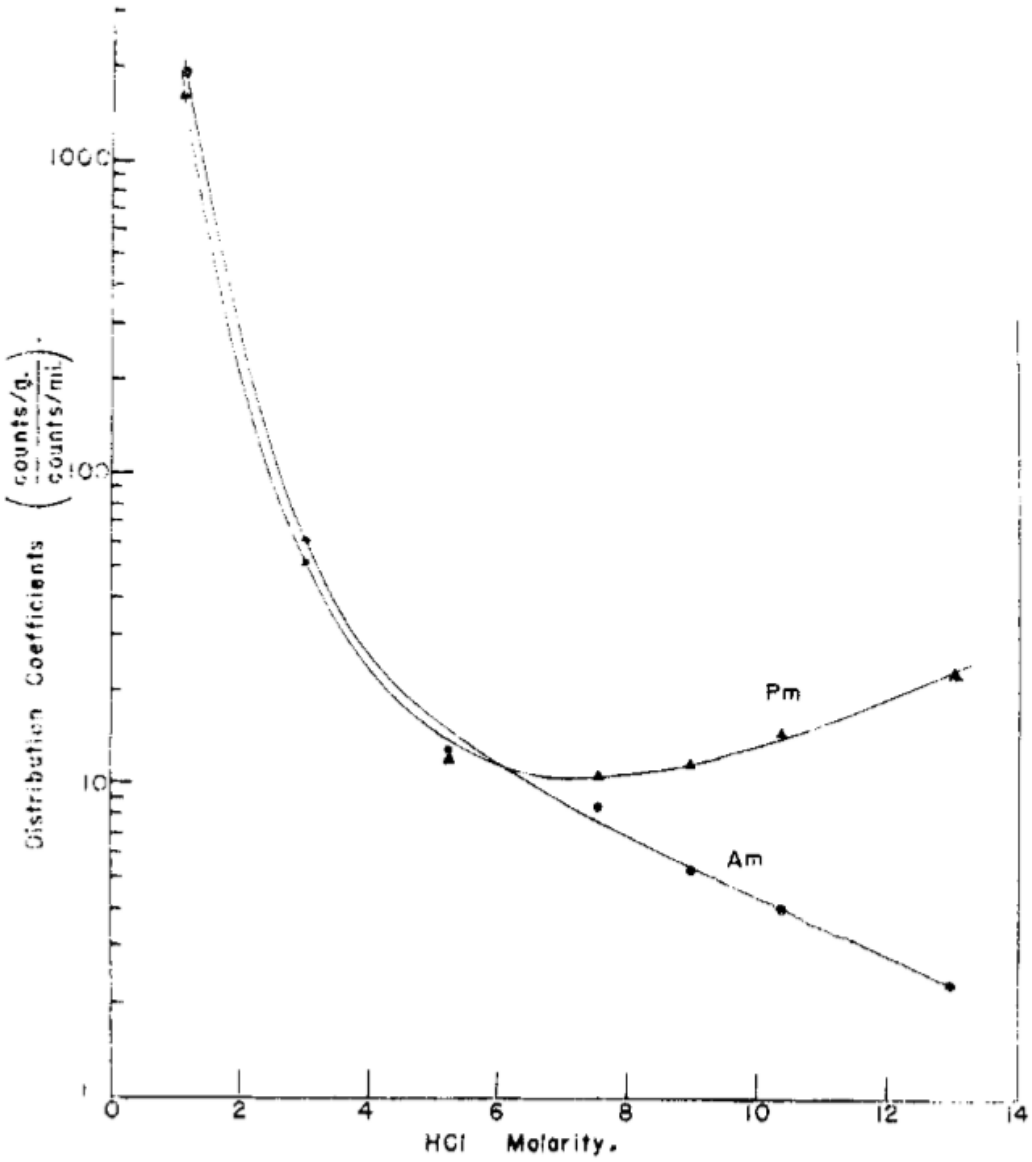

Figure 3.3. Equilibrium distribution coefficients for Pm and Am on a cation exchange column. Seaborg argues that the difference in behavior between Am and Pm is due to Am forming covalent complexes with Cl at higher HCl concentrations.[12]

Section 1.1.1 covered ligand spectroscopy and how the technique can be used to explore the electronic structure of the metal the ligands are bound to, and some of the more convincing evidence for actinide covalency comes from these ligand x-ray spectroscopy studies. The primary benefit of ligand spectroscopy in the actinides is that you can still probe the unoccupied electronic

structure, but avoid the large lifetime broadening of the core-hole states of actinides. This builds on work by Solomon et al. who showed that the intensity of features below the edge are directly proportional to the covalency of the bond.[19] Work by the Kozimor group at Los Alamos National Laboratory has found a number of actinide compounds for which this mixing coefficient is non-zero, resulting in visible pre-edge features in Cl and C K-edge spectra, corresponding to transitions into unoccupied orbitals of 5f character.[16,21,22] Figure 3.4 shows a variety of actinide hexachlroides measured at the Cl K-edge by Su *et al.*[16] The first pre-edge peak is due to the 1s electron transitioning into an anti-bonding orbital with 5f character (as determined by TD-DFT). We can see this peak is largest for Pu, despite the fact that the Pu 5f orbital has the smallest spatial overlap with the Cl 2p orbital. This is because the Pu 5f orbital is closest in energy to the Cl 3p orbital. This phenomenon is also the focus of Chapter 5, Covalency in Pentavalent Uranium, where changing the energy of the uranium 5f orbitals (by changing the oxidation state) increases the covalency by bringing the U 5f and Cl 2p orbitals closer together in energy.

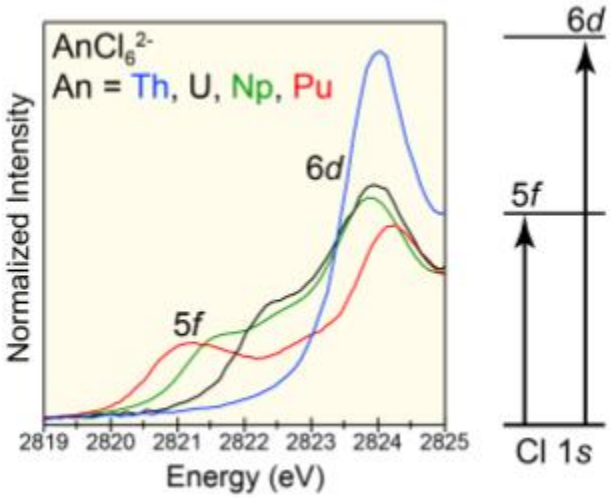

Figure 3.4. Cl K-edge measurements of $AnCl_6^{2-}$ for An = Th, U, Np, Pu[16]

On the other hand, there is also some evidence to suggest the interaction of actinides with ligands is a purely ionic one. Perhaps the most intuitive evidence comes from crystallographic and EXAFS measurements of bond distances in actinide compounds. Figure 3.5 reproduces data collected from several references on bond length vs. ionic radius for a number of MCl_6^{x-} compounds (M = Th, U, Sm, … , x = 2,1).[23–25] In an ionic bond, the bond length is the sum of the metal and ligand ionic radii, so we would expect a linear relationship between the metal ionic radius and bond distance with a slope of 1. Further, the intercept should be the ionic radius of Cl^-. This is exactly what is shown in Figure 3.5, which is suggestive of ionic bonding in these U^{IV} and U^{V} hexachloride compounds. It should be noted that while this is suggestive of ionic bonding, it does not rule out covalent bonding in these compounds.

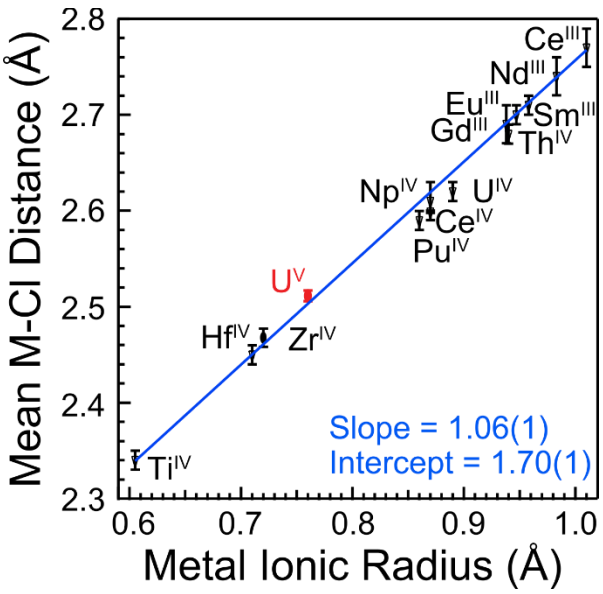

Figure 3.5. M-Cl distance as a function of Metal Ionic Radius for a number of metal hexachlorides. The straight line is a fit and lines up with the expectation for an ionic bonding model.

Further evidence that the bond between actinide and ligand is entirely ionic comes from optical spectroscopy of actinides. A typical optical light measurement excites a valence electron, directly observing the transition between the ground and excited state, giving an effective

measurement of f-electron energy levels. The effects of the ligand environment can also be measured by comparing the transition lines of different actinides species (or an actinide compound with a free ion). For actinides, this crystal field effect is typically on the order of 10^2 cm^{-1}, which is very small compared to the crystal field effect on other elements (transition metals ~ 10^4 cm^{-1}).[26,27] Because this suggests that the energy levels of the bonded f-electrons are so similar to those of the free ion,[28] it's been suggested that this implies the actinide must be essentially in an ionic state.[14]

Kaltsoyannis also argues that a bond can only really be called covalent if there is a buildup of charge between the two atoms.[20] The orbital mixing term λ_{ML} described above doesn't necessarily have anything to do with how the charge is distributed because it depends not only on the orbital overlap, but also the energy difference of the two orbitals. In theoretical calculations, they found that some of the An-Cp bonds they looked at did not have much covalency in the sense of charge between the atoms, but there was substantial covalency in An–N bonds in 2,6-bis(triazinyl)pyridines (BTP), which are notable for their preferential bonding to actinides over lanthanides.[20]

Because covalency in actinides remains an active area of research, and that covalency is easily probed by x-ray spectroscopy, studying it is an ideal way to explore 5f electronic structure. Covalency of actinides has an impact on several of the applications for actinides discussed in the next section, and in particular discussions of separations.

3.4 Importance and Applications

3.4.1 *Nuclear Weapons*

As briefly mentioned before, the advent of nuclear weapons jump-started the field of actinide science. The development of these weapons in the US was known as the Manhattan Project and was led by Oppenheimer. This took place in the utmost secrecy during World War II, culminating in the first and only uses of atomic weapons on Hiroshima and Nagasaki in 1945. In an atomic bomb, a large quantity of fissile material (typically highly-enriched uranium or plutonium) is brought together, creating a critical, runaway fission reaction. These weapons are drastically more powerful than conventional explosives and in addition, spread vast amounts of radioactive by-products in the surrounding area.

With the rise of nuclear weapons, the field of nuclear forensics was developed as a means to police the spread of nuclear weapons and identify the source of nuclear materials.[29] This is a key aspect of the nuclear deterrent. The isotopic composition of materials can often be used to determine the age of a plutonium sample, and help identify the source of nuclear material. In particular, the Pu^{241}/Am^{241} ratio (measured by gamma radiation detection) is commonly used to determine the age of a plutonium sample.[30] However, additional fingerprinting techniques are always helpful, and there has been increased interest in using chemical identification in addition to isotopic information. For example, tracking the composition of uranium materials could trace back where those materials were mined or processed.[31,32] In this regard, understanding the basic chemistry of actinides is critical.

3.4.2 *Nuclear Energy*

Although early actinide research was primarily focused on nuclear reactions, as early as 1939, it was demonstrated that a controlled nuclear reaction was possible. Nuclear reactors were already a critical component of plutonium production during the Manhattan project, and starting in 1946 in the USSR and in 1953 in the US with Eisenhower's "Atoms for Peace" program, significant resources were focused on nuclear energy research, both for use in civilian power plants as well as naval applications.[33] The world's first nuclear power plant began operation in 1954 in Obninsk and produced electricity for several years. The first commercial plant was a 250 MW power plant built by Westinghouse in 1962. Today, around 20% of the world's electrical power is generated by nuclear plants,[34] and nuclear energy is likely to stay as an important part of the world's energy generation in the foreseeable future.

At its most basic, a nuclear power plant is a continuous fission reaction. A fissionable atom, typically ^{235}U, absorbs a neutron and fissions, giving off several neutrons and a large quantity of heat. If enough fissile material is present, this reaction can run continuously. Fuel is organized in fuel rods, typically in the form of UO_2. Neutrons emitted by a fissioning nucleus have a fairly high energy (2 MeV) and so the reactor can be made more efficient by introducing a moderator (typically water) which slows the fast neutrons to energies where the ^{235}U neutron cross section is much higher. The water also serves as the coolant used to generate electricity.

Natural uranium is typically found as an oxide (U_3O_8, pitchblende) and needs substantial processing before it can be used as uranium fuel. First the ore is concentrated into a purified U_3O_8, also known as yellowcake. Naturally occurring uranium is 0.7% ^{235}U, 99.3% ^{238}U, and <0.1% ^{234}U, but for a nuclear reactor to be feasible, the percentage of ^{235}U needs to be between 3 and 5 % (what is called Low Enriched Uranium or LEU). Before it can be enriched, the yellowcake needs to be

converted to UF_6 which is better for centrifuging. UF_6 is used because it exists as a gas at low temperature and fluorine has only one naturally occurring isotope so only the weight of the uranium atom affects the weight of the molecule. In the US, enrichment is done by gas centrifuge, spinning the UF_6 gas at high speed so the heavier molecules move to the outside of the centrifuge. The enriched uranium is collected and then processed into uranium fuel as pellets of UO_2. The unused ^{238}U is referred to as depleted uranium and is useful in some military and industrial applications due to its high density. These steps are laid out in Figure 3.6, which shows the basic process of refining nuclear fuel. Further details of how nuclear reactors work and how uranium is processed into fuel are available at the USNRC.[35]

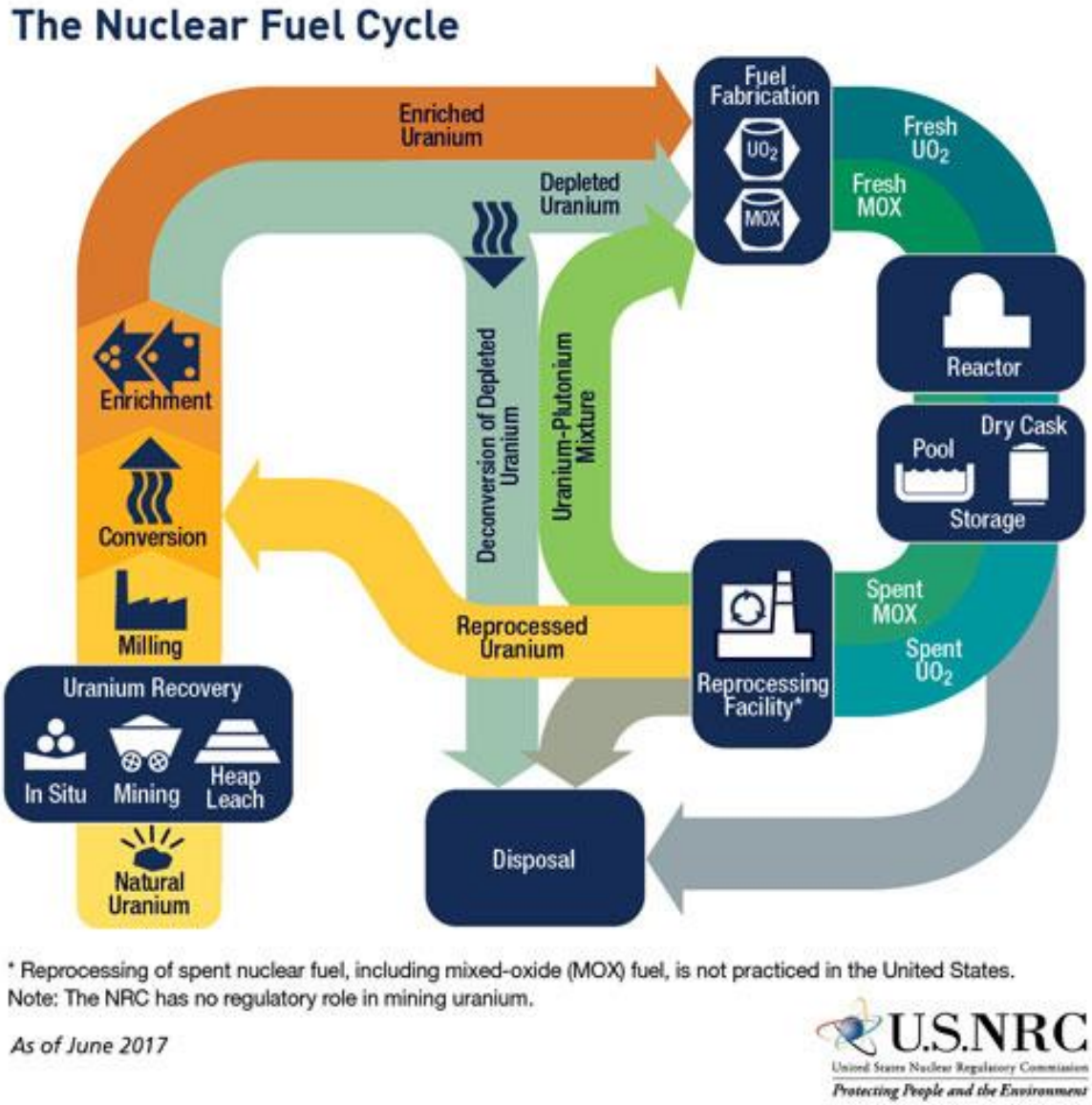

Figure 3.6. Nuclear Fuel cycle, showing the steps in processing nuclear fuel from mining to disposal. From the USNRC.[35]

During operation, ^{235}U fissions and produces fission products like ^{135}Xe and ^{149}Sm which are very strong neutron absorbers (neutron poisons). Because of these neutron poisons, the nuclear fuel becomes inactive far before the ^{235}U is used up and must be replaced. Figure 3.7 shows a breakdown of nuclear waste and the major radiation producing isotopes by volume[36] and Figure 3.8 is a breakdown of nuclear waste by activity.[37] In the short term, the activity of nuclear fuel is

dominated by the short-lived fission products. In the longer term, the minor actinides (Am, Cm, Np) produce the majority of the radiation. This longer-term storage has no solution currently and so separating the hotter, short term products as well as the less-active or stable parts of the waste would drastically reduce the volume of the stored waste and greatly simplify the process.

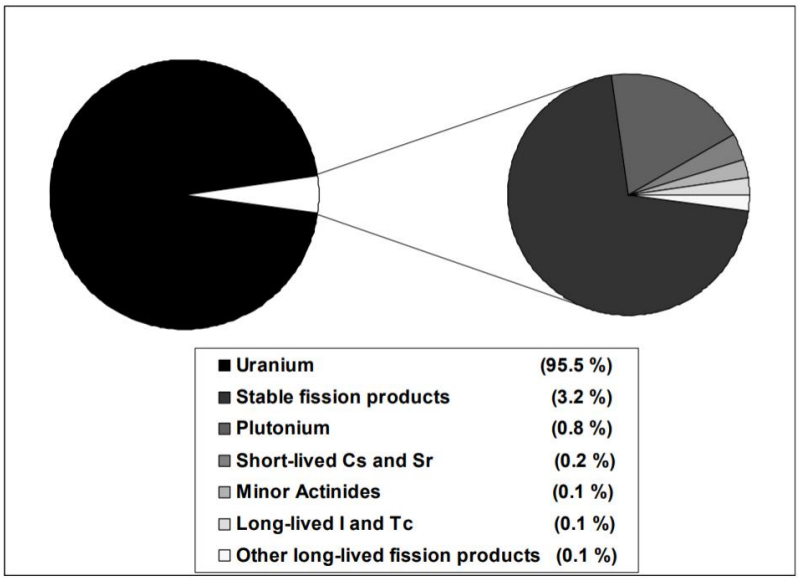

1 tonne of SNF contains:
955.4 kg U
8.5 kg Pu

Minor actinides (MAs)
0.5 kg ^{237}Np
0.6 kg Am
0.02 kg Cm

Long-lived fission products (LLFPs)
0.2 kg ^{129}I
0.8 kg ^{99}Tc
0.7 kg ^{93}Zr
0.3 kg ^{135}Cs

Short-lived fission products (SLFPs)
1 kg ^{137}Cs
0.7 kg ^{90}Sr

Stable isotopes
10.1 kg lanthanides
21.8 kg other stable

Figure 3.7. Breakdown of spent nuclear fuel by weight. From NEA 2006 report on transmutation.[36]

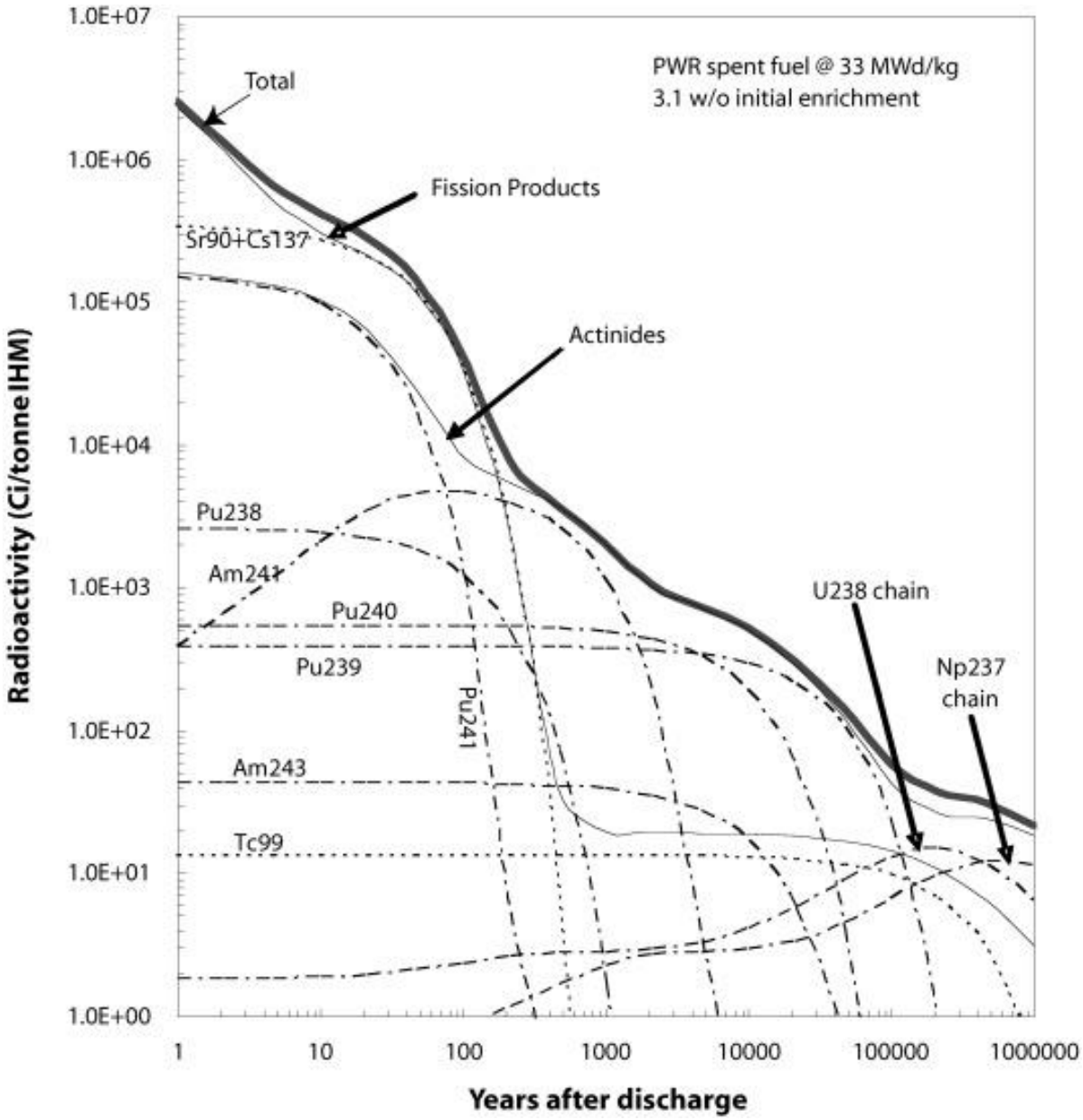

Figure 3.8. Breakdown of spent nuclear fuel by activity. Reproduced from Xu et al.[37]

Taking this one step further, the required storage time could be additionally reduced by transmuting the minor actinides. In this process, the actinides are bombarded by neutrons, typically from another reactor, causing them to change to fissionable isotopes whose fission products have much shorter lifetimes. However, the spent fuel contains some neutron poisons, including lanthanides, so An/Ln separations are necessary to achieve transmutation.[36]

3.4.3 *Separations*

One critical component of a wide variety of chemistry processes, either in the laboratory or on an industrial scale is the separation of a compound of interest from the rest of a mixture. This can be as simple as burning off organic compounds, but in the case of separating very chemically similar elements, this process can be exceedingly difficult. This can be further compounded when one species in a mixture is very dilute. For example, in nuclear waste, minor actinides make up < 1% of the volume, but 99% of the radioactivity after 200 years,[37] so it is desirable to separate those components from the remainder of the waste. However, the fact that the highly radioactive components are only present in small quantities makes the separation difficult. In fact, some separations techniques would not be nearly so widely developed if not for the need of large amounts of plutonium for atomic weapons.[38] Further, without these actinide separations procedures, laboratory work on actinides would be impossible as, aside from uranium and thorium, actinides are produced either in a reactor or by a particle beam hitting a target. In either case, other actinides and chemically similar lanthanide fission products are present and need to be separated.

For actinides in particular, one major motivation is to remove uranium and plutonium from the spent fuel, both to re-use as new fuel, but also so that the highly radioactive component of the waste is greatly reduced in volume (and is therefore easier to store). The predominant method of doing this currently is the PUREX process, first developed in 1949.[39] The PUREX process has a lot of variations which depend on the reactor the fuel was processed in, so we will only outline the basics of the process as described in *Advanced Separations Techniques for Nuclear Fuel Processing.*[40] A general schematic (Figure 3.9) shows that the process removes the Pu and U from solution by changing their oxidation state. The PUREX process relies on the oxidation state selectivity of tri-butyl phosphonate (TBP) which has a large affinity for coordinating with metals

in the +4 or +6 oxidation state, but not in +3 or +5. Because the uranyl $(U^{6+}O_2)^{2+}$ and Pu^{4+} ions are easily achievable oxidation states in solution, TBP can separate those elements from the rest of the nuclear waste. Because the two solvents are non-polar (TBP, diluted in kerosene) and polar (nitric acid), they are immiscible and so a liquid-liquid extraction can be performed. Liquid-liquid extraction is preferred here because the extraction can be done continuously rather than in batches and so a large amount of material can be processed at once.

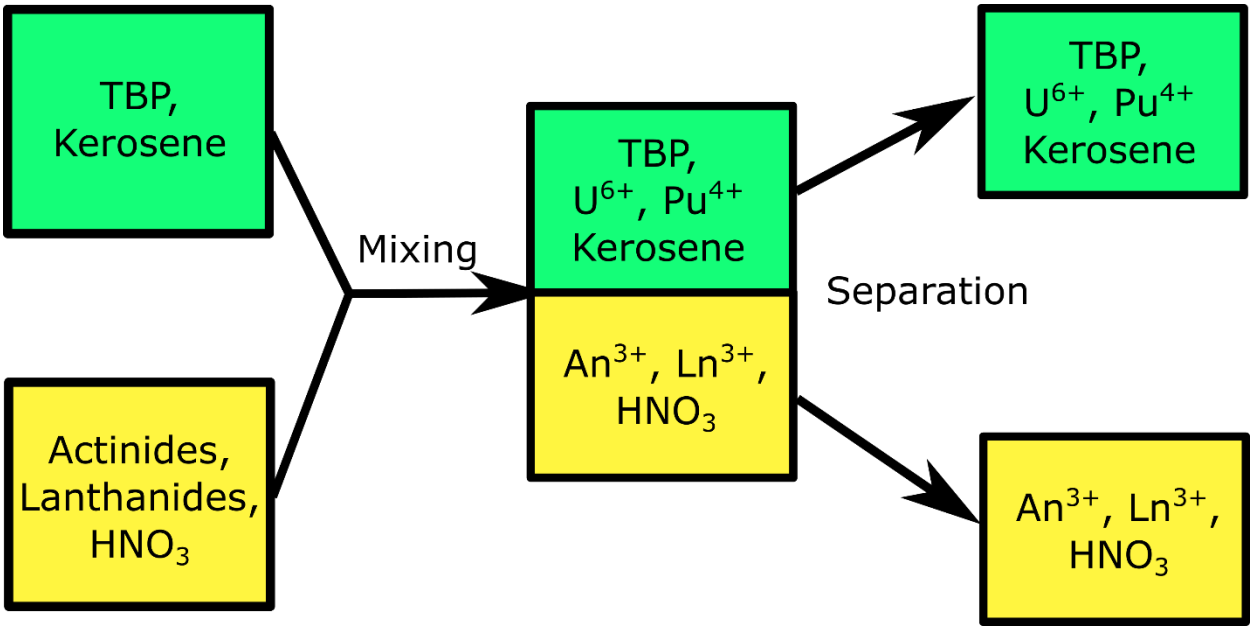

Figure 3.9. Diagram illustrating the PUREX process.

However, separating the minor actinides from the remainder of the PUREX raffinate (leftover materials) is much more difficult than separating the uranium and plutonium. This is because changing the oxidation state of the minor actinides in solution is much more challenging, so a similar process is not available. Instead, Ln/An separations make use of "soft donor" ligands containing elements like S and N which act as Lewis acids, donating electrons to bond with the actinide of interest, but are not so electronegative (like O) that electron density in the An-L bond is only on the ligand end of the bond. The thought behind these ligands is that the 5f orbitals of the

actinide will be available for covalent bonding, but the lanthinde 4f orbitals will not, and therefore the ligand will show a much greater affinity for bonding with actinides.[41,42]

This hypothesis is supported by spectroscopic measurements of actinides, showing a higher affinity for actinides in ligands when the An-ligand bond is more covalent. For example, one particularly effective An/Ln extractant is dithiophosphonate.[43] The dithiophophonate (Figure 3.10, left) bonds to the actinide at the sulfur site. For this compound, the selection factor (how much the compound preferentially bonds to An over Ln) can be as high as 10,000 (quite high for An/Ln applications) depending on the functional group attached to the sulfur. X-ray absorption measurements of the sulfur K-edge, in concert with density functional theory (DFT), show that for a dithiophosphonate with ortho-substituted functional groups (red), the sulfur is made less electronegative, allowing for more covalent bonds to be formed. As nuclear waste remains one of the largest issues with nuclear power, insight into how these extractants work could have wide-reaching effects in the design of future separations techniques.

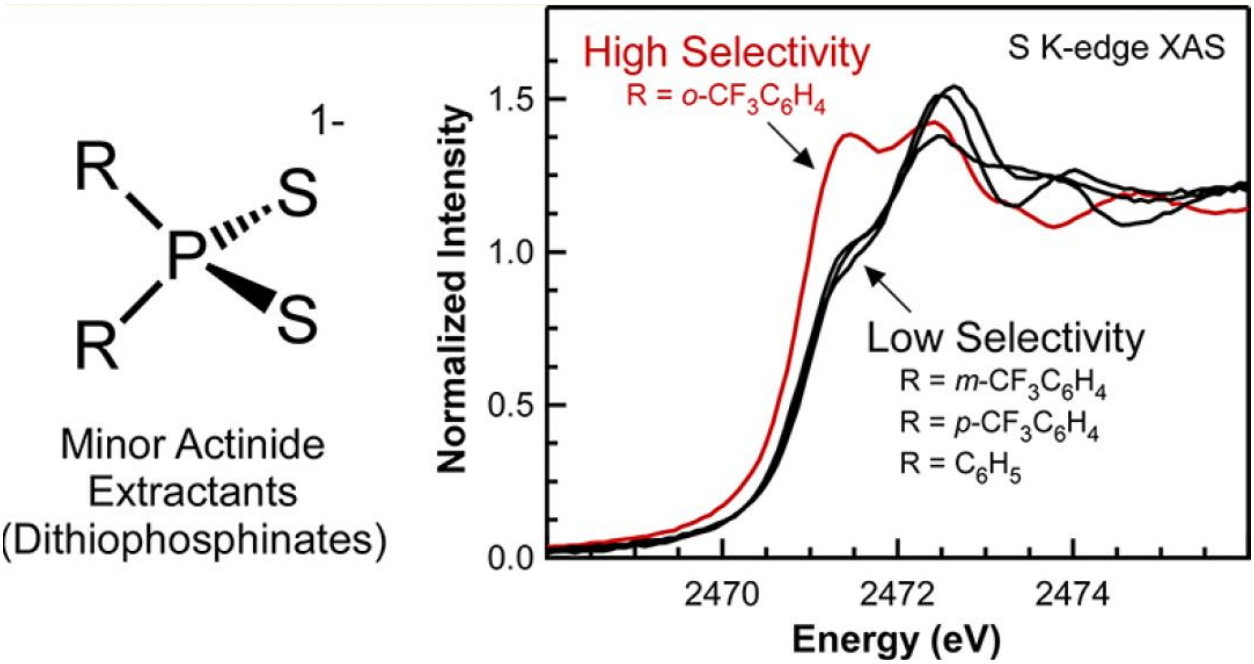

Figure 3.10. Dithiophosphinate structure (left) and corresponding XAS spectra for different functional groups. The high-selectivity compound has a large pre-edge feature, indicating a higher degree of covalency. Figure from Daly et al.[44]

3.4.4 *Environmental Concerns and Legacy Waste*

The nuclear waste generated by the Manhattan project and subsequent reactors as well as spent nuclear fuel remains a problem to this day. Hanford, WA was a site of plutonium production and processing during the cold war, and after decommissioning of the reactors there was almost 1,000,000 m^3 of solid waste stored in casks. Other sites like Oak Ridge and Savannah River contain large amounts of legacy waste, but Hanford has the majority of waste handled by the DOE. It has been known for some time that the liquid waste stored in single-shelled casks at the Hanford site had begun to leak into the groundwater. This problem emphasizes some of the issues with storing nuclear waste for thousands of years.

Currently, the US government stores transuranic waste at the Waste Isolation Pilot Plant (WIPP) in New Mexico.[45] The site is a salt bed, several hundred feet underground in a geologically

stable region. This means it is a secure, water-free storage area, not susceptible to earthquakes, which makes it suitable for storage on the scale of hundreds to thousands of years. Yucca Mountain in Nevada is a similar site that has been proposed as a long-term storage site for both legacy waste and commercial spent nuclear fuel. However, due to concerns with the safety of long term storage, the Yucca Mountain project has proven politically difficult. As a result, all commercial spent nuclear fuel has been kept onsite, temporary storage at nuclear reactors.[35]

The interaction of both man-made and natural actinides with the environment is of critical concern in first being able to design effective storage, as well as being able to develop tests for actinide contamination. In the environment, only uranium and thorium are present in large quantities naturally, and the transuranic element present mostly from manmade sources. These are legacy waste from weapons programs, uranium mining tailings, unintended releases from incidents with nuclear reactors or weapons carrying planes, and some other minor sources like Cf and Am in oil well exploration.[46]

Near the source, where the actinide concentration is highest, radiolysis, complexation, and solubility are the primary concerns in discerning their fate.[46] However, the behavior of actinides in solution are particularly complicated, evidenced in the plot of Figure 3.11, which shows the primary species of Pu in solution as a function of pH and redox potential.[47] In addition, the local environment has a large impact on the solubility of actinides. For example, it has been shown that actinides are much more likely to form solids in the presence of Cl^- ions, which has implications for storage in salt beds like WIPP or Yucca Mountain.[48] Far from the source, the fate of actinides is dominated by the possibility of adsorption onto geological layers, where the actinide can become fixed. EXAFS has been key to understanding the solution chemistry of actinides, which is critical to these environmental concerns.[49]

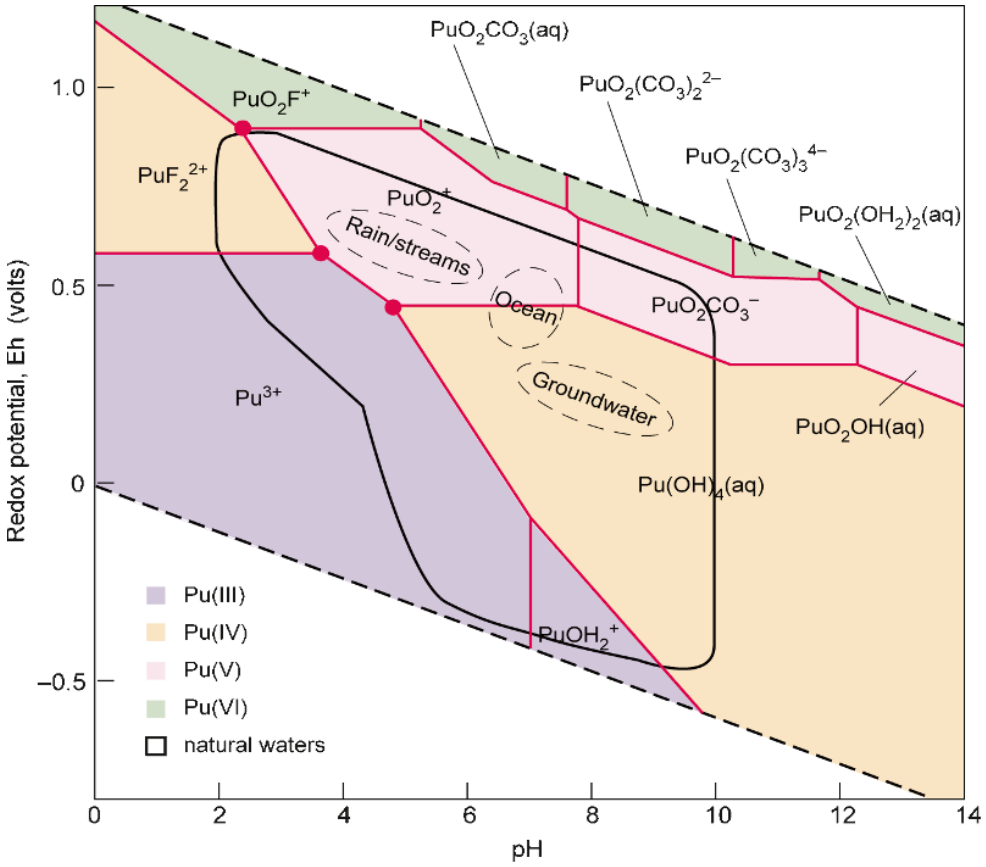

Figure 3.11. Plutonium oxidation state and coordinating environment as a function of pH and redox potential. Note that Pu exists in 3 oxidation states in naturally occurring conditions.[47]

3.4.5 *Radiation Utilizing Applications*

Although it is primarily thought of as a hazard, the radioactivity of actinides can be useful in certain applications. For example, satellites and spacecraft can use the heat generated by radioactive materials to generate power. In what is known as a Radioisotope Thermoelectric Generator (RTG), a quantity of radioactive material decays, generating heat which is then used in some sort of heat engine. Most commonly, the radioisotope is ^{238}Pu, which has a half-life of 87.7 years and has low neutron and gamma radiation levels, reducing the shielding necessary to protect

other components.[50] As an example, the voyager probes each carry with them an RTG containing approximately 4.5 kg of ^{238}Pu, providing 157 W of power.

Another example of useful radioactivity is that of smoke detectors. Typical smoke detectors use a small quantity of ^{241}Am to ionize air, causing an electric current to flow between an anode and a cathode. If smoke enters the chamber, it bonds to the ionized air and that change in current is detected, causing the system to alarm. These types of smoke detectors have been in use in homes since the 1970's and are most likely the closest interaction most people have with actinides in their everyday life.

Finally, we will briefly explore the use of actinides in medicine. Radioisotopes have proven to be a useful tool in imaging, particularly Positron Emitting Tomography (PET) and Single Photon Emission Computed Tomogrophy (SPECT), which have seen widespread use. In the most common example (SPECT), $^{99\text{-m}}$Tc is used as a low energy (140 keV) gamma emitter in combination with a computed tomography technique to construct a 3D image of where the Tc is in the body.[51] Depending on the drug containing the Tc, this technique has broad applications to many areas of medicine (e.g. blood flow or brain activity). The Tc is derived ultimately from fission products of ^{235}U.

Similar to the application of radioisotopes in imaging, actinides have been proposed as radiotherapeutic drug. In targeted alpha therapy, the goal is to get an alpha emitting radioisotope close to a tumor or bacteria and use the alpha emission of the isotope to kill it.[52] Alpha emission is ideal for this because it deposits the maximum amount of energy in the neighboring cells, compared to beta or gamma radiation which penetrates further and disperses the radiation over a wide area. This is key to achieving the double strand break that is necessary to prevent the regeneration of DNA.[52] ^{225}Ac is a promising candidate for this technology because it has four

alpha decays on its way to isotopically stable ^{209}Bi, which is also bio-stable, and so has roughly 4 times the killing power as an isotope with a single emission.

The design of radiotherapeutic drugs is similar in most cases, consisting of a targeting vector and a way of binding the actinide to that targeting vector. In the case of a recent ^{225}Ac study, prostate-specific membrane antigen (PMSA) was used as a targeting agent for prostate cancer.[53] This combination proved to be exceptionally effective in targeting even metastasized cancer (see Figure 3.12). On the other hand, for the first FDA approved alpha therapy drug, "Xofigo", the radioisotope ^{223}R is itself the targeting vector. Xofigo treats bone cancer, and radium in the body is chemically similar to calcium and is preferentially taken up in bones. Results for Xofigo showed a marked increase in survival among patients with metastasized bone cancer.[54]

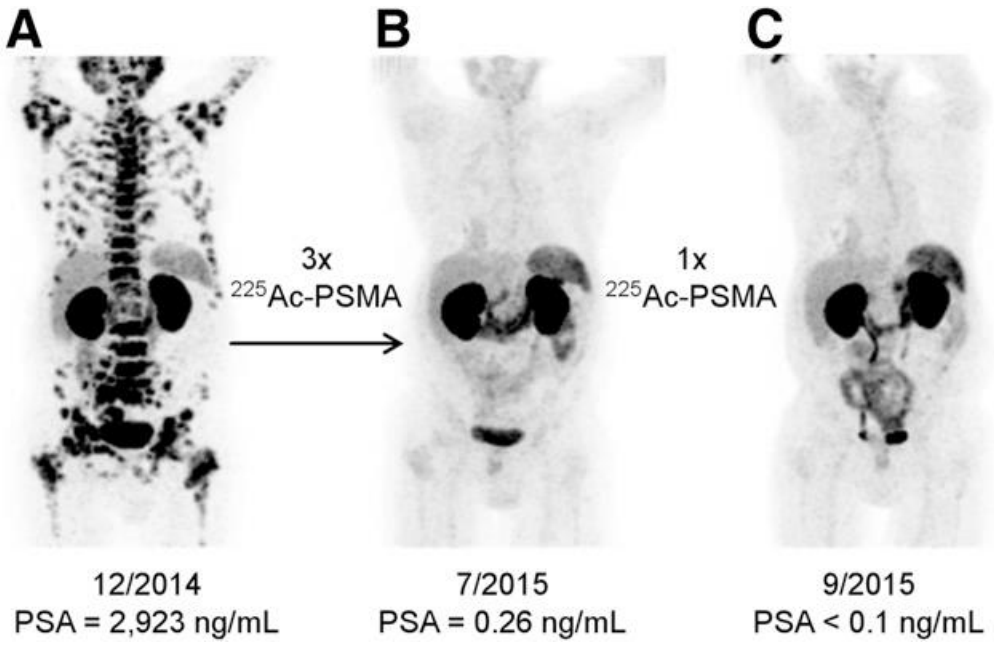

Figure 3.12. PET scan of metastasized prostate cancer after 3 treatments of ^{225}Ac-PSMA and one follow up, showing that the cancer is completely removed. Figure from Kratochwil *et al.*[53]

However, for actinides to be effective in medical applications, a strong chelator is often required to attach the actinide to the linker.[52] One commonly used chelator is DOTA, which holds

the actinide in the center of a ring with phosphorous capped arms (used in the PMMA study above).[55] This chelator design is attractive because it is biologically safe, but some concerns have been raised on how well it contains the actinide in a biological environment, due to the large size of the actinide cation.[52] If the chelator fails to bind the actinide, the toxicity of the treatment to the rest of the body is increased and the effectiveness of the treatment decreases. Study of these systems is an active area of research and furthering the basic understanding of actinide chemistry will have a large impact on future chelator designs.

3.5 Conclusion

Actinides are an important part of life with primary applications in nuclear weapons and energy. Active research is still being done in basic chemistry areas, and in particular, the question of whether 5*f* orbitals participate in covalent bonding has been debated for decades. This question directly affects lanthanide/actinide separations, which could have a large impact on the long-term storage or transmutation of spent nuclear fuel. Actinide 5*f* covalency could also have a direct impact on the behavior of actinides in the environment as well as the design of chelators for medical applications. It is these reasons that motivate the study of actinide covalency in the following chapters of this dissertation.

3.6 References

1. IAEA. Chart of the Nuclides. (2019). Available at: https://www-nds.iaea.org/relnsd/vcharthtml/VChartHTML.html. (Accessed: 18th May 2019)

2. Klaproth, M. H. Chemische Untersuchung des Uranits, einer neuentdeckten metallische Substanz. *Chem. Ann.* **2**, 387–403 (1789).

3. Morss, L. R., Edelstein, N. M., Fuger, J. & Katz, J. J. (Joseph J. *The chemistry of the actinide and transactinide elements.* (Springer, 2006).

4. Seaborg, G. T. The Transuranium Elements. *Science (80-.).* **104**, 379–386 (1946).

5. Cotton, A. F. & Wilkinson, G. The Lanthanides; also Scandium and Yttrium. in *Advanced Inorganic Chemistry* 981 (1980).

6. D'angelo, P., Martelli, F., Spezia, R., Filipponi, A. & Denecke, M. A. Hydration Properties and Ionic Radii of Actinide(III) Ions in Aqueous Solution. (2013). doi:10.1021/ic400678u

7. Clark, D. L., Hecker, S. S., Jarvinen, G. D. & Neu, M. P. Plutonium. in *The Chemistry of the Actinide and Transactinide Elements* 813–1264 (Springer Netherlands). doi:10.1007/1-4020-3598-5_7

8. Crosswhite, H. M., Crosswhite, H., Carnall, W. T. & Paszek, A. P. Spectrum analysis of U^{3+}:$LaCl_3$. *J. Chem. Phys.* **72**, 5103–5117 (1980).

9. Nash, K. L. The Chemistry of TALSPEAK: A Review of the Science. *Solvent Extr. Ion Exch.* **33**, (2015).

10. Burns, C. J. & Bursten, B. E. Covalency in f-Element Organometallic Complexes: Theory and Experiment. *Comments Inorg. Chem.* **9**, 61–93 (1989).

11. Tatsumi, K. & Hoffmann, R. Bent cis d0 MoO22+ vs. linear trans d0f0 UO22+: a significant role for nonvalence 6p orbitals in uranyl. *Inorg. Chem.* **19**, 2656–2658 (1980).

12. Diamond, R. M., Street, K. & Seaborg, G. T. An Ion-exchange Study of Possible Hybridized 5f Bonding in the Actinides. *J. Am. Chem. Soc.* **76**, 1461–1469 (1954).

13. Pepper, M. & Bursten, B. E. The electronic structure of actinide-containing molecules: a challenge to applied quantum chemistry. *Chem. Rev.* **91**, 719–741 (1991).

14. Choppin, G. R. Covalency in f-element bonds. *J. Alloys Compd.* **344**, 55–59 (2002).

15. Denning†, R. G. Electronic Structure and Bonding in Actinyl Ions and their Analogs. (2007). doi:10.1021/JP071061N

16. Su, J. *et al.* Energy-Degeneracy-Driven Covalency in Actinide Bonding. *J. Am. Chem. Soc.* **140**, 17977–17984 (2018).

17. Kelley, M. P. *et al.* On the Origin of Covalent Bonding in Heavy Actinides. *J. Am. Chem. Soc.* **139**, 9901–9908 (2017).

18. Heitler, W. & London, F. Wechselwirkung neutraler Atome und homöopolare Bindung nach der Quantenmechanik. **44**, 455–472 (1927).

19. Neidig, M. L., Clark, D. L. & Martin, R. L. Covalency in f-element complexes. *Coord. Chem. Rev.* **257**, 394–406 (2013).

20. Kaltsoyannis, N. Does covalency increase or decrease across the actinide series? Implications for minor actinide partitioning. *Inorg. Chem.* **52**, 3407–3413 (2013).

21. Daly, S. R. *et al.* Sulfur K-edge X-ray Absorption Spectroscopy and Time-Dependent Density Functional Theory of Dithiophosphinate Extractants: Minor Actinide Selectivity and Electronic Structure Correlations. *J. Am. Chem. Soc.* **134**, 14408–14422 (2012).

22. Minasian, S. G. *et al.* Determining Relative f and d Orbital Contributions to M–Cl Covalency in MCl_6^{2-} (M = Ti, Zr, Hf, U) and $UOCl_5^-$ Using Cl K-Edge X-ray Absorption Spectroscopy and Time-Dependent Density Functional Theory. *J. Am. Chem. Soc.* **134**, 5586–5597 (2012).

23. Shannon, R. D. & IUCr. Revised effective ionic radii and systematic studies of interatomic distances in halides and chalcogenides. *Acta Crystallogr. Sect. A* **32**, 751–767 (1976).

24. Minasian, S. G. *et al.* Synthesis and Structure of $(Ph_4P)_2MCl_6$ (M = Ti, Zr, Hf, Th, U, Np, Pu). *Inorg. Chem.* **51**, 5728–5736 (2012).

25. Minasian, S. G. *et al.* Determining Relative f and d Orbital Contributions to M–Cl Covalency in MCl_6^{2-} (M = Ti, Zr, Hf, U) and $UOCl_5^-$ Using Cl K-Edge X-ray Absorption Spectroscopy and Time-Dependent Density Functional Theory. *J. Am. Chem. Soc.* **134**, 5586–5597 (2012).

26. Cotton, A. F. & Wilkinson, G. Transition Elements and the Electronic Structures of Their Compounds. in *Advanced Inorganic Chemistry* 611–688 (1980).

27. Liu, G. & Beitz, J. V. Optical Spectra and Electronic Structure. in *Chemistry of the Actinide and Transactinide Elements* 2013–2089 (2010).

28. Crosswhite, H. M. & Crosswhite, H. Parametric model for f-shell configurations I The effective-operator Hamiltonian. *J. Opt. Soc. Am. B* **1**, 246 (1984).

29. Mayer, K. *et al.* Nuclear Forensics: A Methodology Applicable to Nuclear Security and to Non-Proliferation. *J. Phys. Conf. Ser.* **312**, 062003 (2011).

30. Fitzgerald, R., Inn, K. G. W. & Horgan, C. HOW OLD IS IT? - 241PU/241AM NUCLEAR FORENSIC CHRONOLOGY REFERENCE MATERIALS. *J. Radioanal. Nucl. Chem.* **307**, 2521–2528 (2016).

31. Mayer, K., Wallenius, M. & Varga, Z. Nuclear Forensic Science: Correlating Measurable Material Parameters to the History of Nuclear Material. *Chem. Rev.* **113**, 884–900 (2013).

32. Crean, D. E. *et al.* Expanding the nuclear forensic toolkit: chemical profiling of uranium ore concentrate particles by synchrotron X-ray microanalysis. *RSC Adv.* **5**, 87908–87918 (2015).

33. Helwett, R. G. & Holl, J. M. *Atoms for Peace and War*. (University of California Press,

1989).

34. International Atomic Energy Agency. Nuclear Power Reactors in the World | IAEA. *Ref. Data Ser. No. 2* (2018).

35. Spent Fuel Storage. Available at: https://www.nrc.gov/waste/spent-fuel-storage.html. (Accessed: 12th June 2019)

36. Salvatores, M. Nuclear fuel cycle strategies including Partitioning and Transmutation. *Nucl. Eng. Des.* **235**, 805–816 (2005).

37. Xu, Z., Kazimi, M. S. & Driscoll, M. J. Impact of High Burnup on PWR Spent Fuel Characteristics. *Nucl. Sci. Eng.* **151**, 261–273 (2005).

38. Nash, K. L., Madic, C., Mathur, J. N. & Lacquement, J. Actinide Separation Science and Technology. in *The Chemistry of the Actinide and Transactinide Elements* 2622–2798 (Springer Netherlands). doi:10.1007/1-4020-3598-5_24

39. Lanham, W. B. & Runion, T. C. *PUREX PROCESS FOR PLUTONIUM AND URANIUM RECOVERY*. (1949). doi:10.2172/4165457

40. Herbst, R. S., Baron, P. & Nilsson, M. Standard and Advanced Separation: PUREX Processes for Nuclear Fuel Reprocessing. in *Advanced separation techniques for nuclear fuel reprocessing* 141–175 (Woodhead Publishing Ltd., 2011).

41. Lewis, F. W., Hudson, M. J. & Harwood, L. M. Development of highly selective ligands for separations of actinides from lanthanides in the nuclear fuel cycle. *Synlett* 2609–2632 (2011). doi:10.1055/s-0030-1289557

42. Kolarik, Z. Complexation and Separation of Lanthanides(III) and Actinides(III) by Heterocyclic N-Donors in Solutions. *Chem. Rev.* **108**, 4208–4252 (2008).

43. Klaehn, J. R. *et al.* Synthesis of symmetric dithiophosphinic acids for “minor actinide” extraction. *Inorganica Chim. Acta* **361**, 2522–2532 (2008).

44. Olson, A. C. *et al.* Using solution- and solid-state S K-edge X-ray absorption spectroscopy with density functional theory to evaluate M–S bonding for MS_4^{2-} (M = Cr, Mo, W) dianions. *Dalt. Trans.* **43**, 17283–17295 (2014).

45. WIPP Geological Disposal Safety Case. Available at: https://wipp.energy.gov/geologic-disposal-safety-case.asp. (Accessed: 12th June 2019)

46. Runde, W. & Neu, M. P. Actinides in the Geosphere. in *Chemistry of the Actinide and Transactinide Elements* 3475–3575 (2000).

47. Runde, W. The Chemical Interactions of Actinides in the Environment. *Los Alamos Sci.* **26**, 392–411 (2000).

48. Kelm, M., Pashalidis, I. & Kim, J. . Spectroscopic investigation on the formation of hypochlorite by alpha radiolysis in concentrated NaCl solutions. *Appl. Radiat. Isot.* **51**, 637–642 (1999).

49. Ferrier, M. G. *et al.* The coordination chemistry of Cm^{III}, Am^{III}, and Ac^{III} in nitrate solutions: an actinide L_3-edge EXAFS study. *Chem. Sci.* **9**, 7078–7090 (2018).

50. Blanke, B. C., Birden, J. H., Jordan, K. C. & Murphy, E. L. *NUCLEAR BATTERY-THERMOCOUPLE TYPE SUMMARY REPORT*. (1960). doi:10.2172/4807049

51. Schwochau, K. *Technetium : chemistry and radiopharmaceutical applications*. (Wiley-VCH, 2000).

52. Birnbaum, E. R., Fassbender, M. E., Ferrier, M. G., John, K. D. & Mastren, T. Actinides in Medicine. in *Encyclopedia of Inorganic and Bioinorganic Chemistry* 1–21 (John Wiley & Sons, Ltd, 2018). doi:10.1002/9781119951438.eibc2563

53. Kratochwil, C. *et al.* 225Ac-PSMA-617 for PSMA-Targeted -Radiation Therapy of Metastatic Castration-Resistant Prostate Cancer. *J. Nucl. Med.* **57**, 1941–1944 (2016).

54. Sartor, A. O. *et al.* Radium-223 chloride impact on skeletal-related events in patients with castration-resistant prostate cancer (CRPC) with bone metastases: A phase III randomized trial (ALSYMPCA). *J. Clin. Oncol.* **30**, 9–9 (2012).

55. Scheinberg, D. A. & McDevitt, M. R. Actinium-225 in targeted alpha-particle therapeutic applications. *Curr. Radiopharm.* **4**, 306–20 (2011).

Chapter 4. MOLECULAR ORBITALS AND THEORETICAL CALCULATIONS

4.1 OVERVIEW

Theoretical chemistry, including its connection with spectroscopy, is a rich field where strong progress is being made in a wide variety of contemporary programs. In the context of f-electron chemistry, the complexities introduced by the involvement of the f-orbitals challenge fundamental approaches using full wavefunction calculations, and instead more approximate techniques must be used. In this chapter, I briefly survey the dominant qualitative and quantitative approaches to conceptualizing chemical bonding, spectroscopic observables, and function and properties of actinides. First, in section II, I will discuss molecular orbitals (MO's). This will include the steady development of more and more complex MO's until we reach the point of describing the specific uranium compounds of interest in this dissertation. Second, in section III, I briefly address density functional theory (DFT). After a summary of the fundamentals, I explore some specialized characteristics that DFT treatments must have to best address actinide chemistry.

4.2 MOLECULAR ORBITALS

Molecular orbitals are an intuitive way to talk about chemical bonding, particularly in simple molecules. In the most general sense, molecular orbitals are analogous to atomic orbitals (e.g. 2*d*, 3*p* etc.) in that they are the single-electron energy eigenstates for a given molecule. For the qualitative discussions in this section, we will talk about molecular orbitals as a linear combination of atomic orbitals (LCAO), but molecular orbitals can still be discussed in a more

general sense, i.e. the orbitals that result from DFT calculations. The discussion of this section is synthesized from several books,[1–4] which are useful resources for a more in-depth look at these topics.

4.2.1 *Diatomic Molecules*

Under the linear combination of atomic orbitals model, the wavefunction for an atomic orbital is expressed as $\psi = \sum_i c_i \phi_i$, where the sum goes over all possible atomic orbitals ϕ_i. To illustrate how this works, we start here with the simplest example, that of the hydrogen molecule, H_2. We'll label the two hydrogen atoms A and B. For these two atoms, the occupied atomic orbital of the A atom, $\phi_{A,1s}$, can be in phase or out of phase with that of the B atom, $\phi_{B,1s}$. This leads to two distinct combinations, $\psi_1 = 1/\sqrt{2}\left(\phi_{A,1s} + \phi_{B,1s}\right)$ and $\psi_2 = 1/\sqrt{2}\left(\phi_{A,1s} - \phi_{B,1s}\right)$. If the two hydrogen atoms are far from each other, the electron density (proportional to $|\psi^2|$) for these two orbitals looks very similar to what you would get from adding the electron density for the individual wavefunctions. However, as the two atoms are brought together, the atomic orbitals begin to overlap and the shape of the molecular orbital changes. For ψ_1, this results in substantial electron density between the two atoms. For ψ_2, the atomic orbitals cancel out, creating a node between the two atoms. The number of nodes in a molecular orbital is important because it is qualitatively related to the energy of a bond. As a rule of thumb, a molecular orbital with more nodes has a larger kinetic energy associated with it because the kinetic energy term of the Hamiltonian is $-\frac{\hbar}{2m}\nabla^2$, which is larger for a wavefunction with a larger gradient. By analogy with atomic orbitals, a wavefunction with a higher number of nodes is also represented by a higher order Hermite polynomial, and therefore has a higher energy. Figure 4.1 is a molecular orbital diagram of H_2, which encapsulates many of the topics covered here. In a molecular orbital diagram

for two atoms, the individual atoms are on either side and the molecular orbitals are between. Dashed lines from the atomic orbitals to the molecular orbitals show which atomic orbitals contribute to each molecular orbital. For H_2 we see ψ_1 is lower in energy than both ψ_2 and the individual atomic orbitals. It is occupied by two electrons and so the resulting H_2 molecule is more stable than the individual H molecules. We call any molecular orbitals with energy lower than their constituent atomic orbitals bonding and any with higher energy antibonding. Antibonding orbitals are denoted by a star. When the two atomic orbitals point towards each other, they form a sigma bond which has no nodes that include the entire bond axis. Putting it all together, ψ_1 is a sigma bonding orbital, denoted by σ, and has lower energy than ψ_2, which is a sigma antibonding orbital, denoted by σ^*.

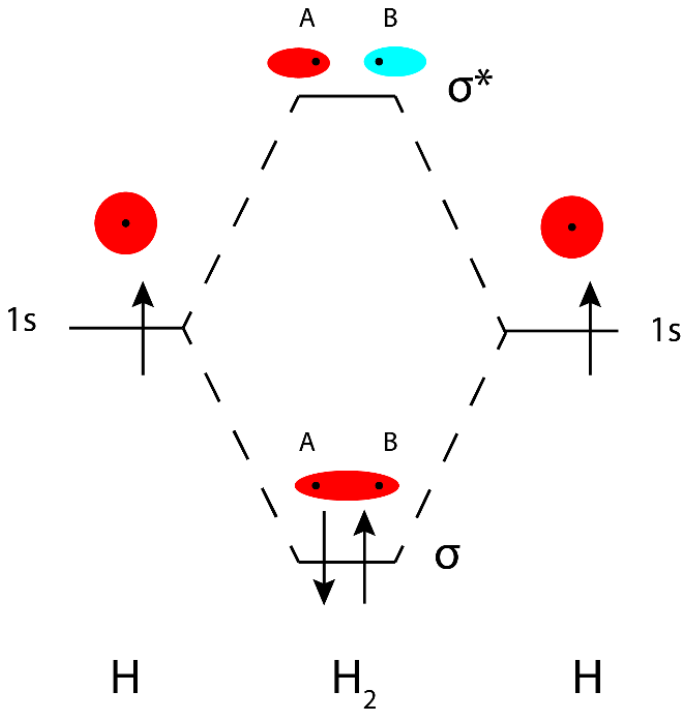

Figure 4.1. Molecular Orbital diagram showing the linear combinations for a symmetric (σ) and anti-symmetric (σ*) combination of two hydrogen atoms. Red and blue are used to indicate different phases.

To introduce a little more complexity, we will now look at the molecular orbital diagram of O_2. O_2 has 2*p* atomic orbitals, which introduce a new type of bond, the π bond. The O 1*s* and 2*s* have a much smaller radial extent than the O 2*p* orbitals, so the effect of the other O atom on them is small and we can ignore those orbitals when speaking of bonding. Note that we're ignoring the possibility of sp hybridization, which can be important, particularly for molecules containing carbon. The 2*p* orbitals are substantially more interesting. If we let the z-axis be the bond axis, the p_z orbitals can form σ and σ^* orbitals. The p_x and p_y orbitals form π bonds that have one node in the axis of the bond. Each oxygen atom has 4 electrons in its p orbitals, so each of the bonding orbitals are filled and one electron goes into each π^* orbital.

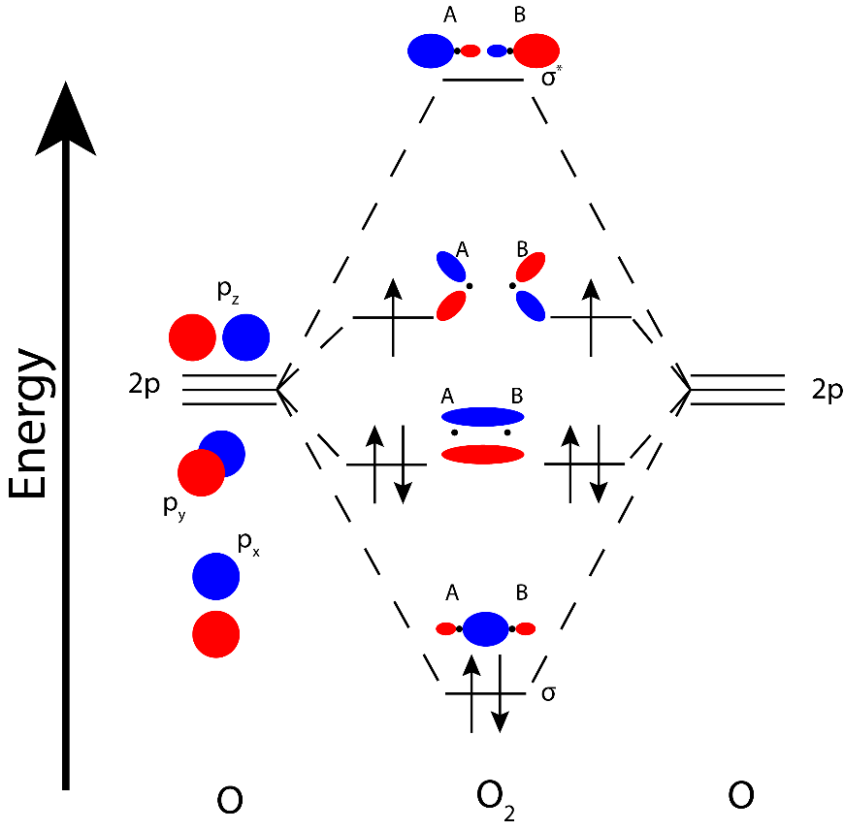

Figure 4.2. Molecular orbital diagram for oxygen. Energy levels are meant to be qualitative and are not reflective of actual energy values.

4.2.2 *Polyatomic Molecules*

When working with more than two atoms, our molecular orbitals are potentially made up of several different atomic orbitals, and so the complexity of molecular orbitals increases quickly as more atoms are added. However, we can get around this by making an appeal to the symmetry of the system by using concepts from group theory. In this section, these group theory concepts are only briefly covered, and a fuller treatment of the topic is available in several excellent textbooks on the topic.[1–3]

We start with the CO_2 molecule, containing a central carbon atom and two "ligand" oxygen atoms. In general, I will be considering molecular compounds which have a central atom and is surrounded by ligand atoms. In the case of CO_2, we first need to classify the symmetry operations which leave the molecule unchanged. For example, a rotation of any angle about the axis passing through all three atoms leaves the molecule unchanged. This and the remaining symmetry operations form a group (known as a point group) with the designation $D_{\infty h}$. The D indicates a central axis of rotation that is dihedral (that is, there are 180 degree rotations perpendicular to this central axis which also leave the molecule unchanged), the subscript ∞ refers to the period of this central axis (how many distinct rotations about this axis are allowed), and the subscript h indicates a reflection plane perpendicular to the central axis. Both H_2 and O_2 also fall into this symmetry group. For another example, ethylene (C_2H_4) is a planar molecule which has a central axis with period 2 and belongs to the group D_{2h}.

One useful way to describe the symmetry of a molecule is to use a character table (e.g. from http://symmetry.jacobs-university.de/). The full meaning of the character table is outside the scope of this dissertation, but the important parts for our discussion are the Mulliken symbols used to describe each irreducible representation and which orbitals (of the central atom) belong to which

irreducible representation. The Mulliken symbols indicate the degeneracy (a, b = 1, e = 2, t = 3) and behavior under inversion (g = even, u = odd) of the irreducible representation. In other words, the orbitals of each irreducible representation behave differently under the set of symmetry operations belonging to the point group and the character table helps in determining the Mulliken label of each orbital. In the case of CO_2, the central carbon atom's p_x and p_y orbitals belong to the e_u representation and the p_z orbital belongs to the a_u representation. The carbon s orbital also participates in bonding and belongs to the a_g representation. To construct molecular orbitals, we need to find combinations of the two oxygen ligands with the same symmetry as those orbitals. These combinations are known as symmetry adapted linear combinations (SALCs). These combinations are shown in Figure 4.3, and we see that the six oxygen p-orbitals make up e_g, e_u, a_u and a_g SALCs. The SALCs that share the same symmetry as the central carbon atom's orbitals (e_u, a_u and a_g) will participate in bonding, and the remaining oxygen electrons (e_g) remain in nonbonding orbitals. The resulting molecular orbital diagram for CO_2 is shown in Figure 4.4.

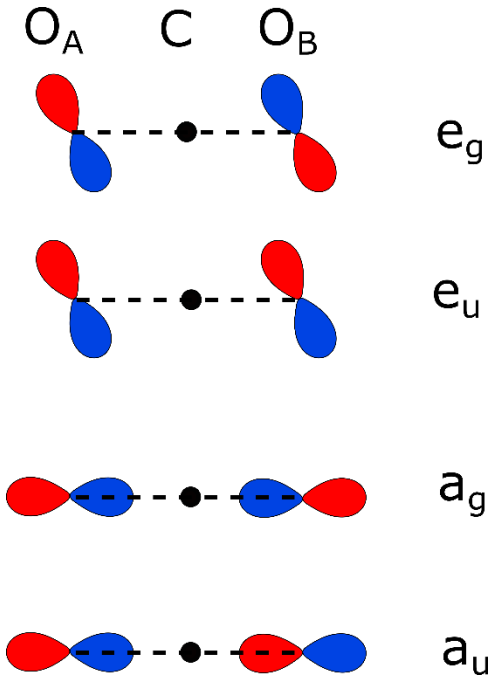

Figure 4.3. SALCs of the oxygen ligands (O_A and O_B) and their Mulliken symbols.

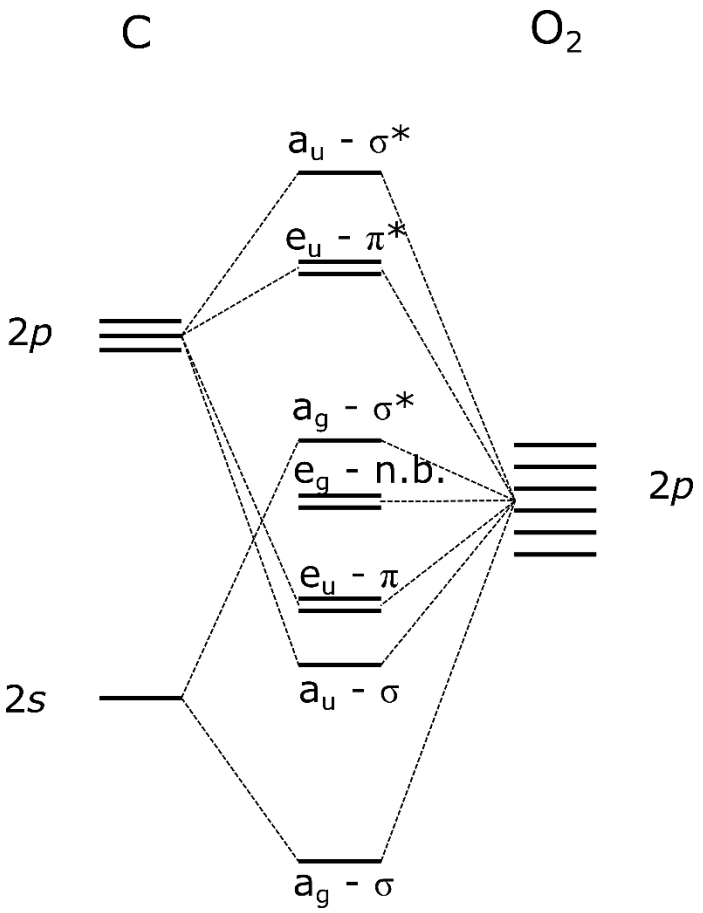

Figure 4.4. Molecular orbital diagram for CO_2. The molecular orbitals are labelled by their Mulliken label as well as the type of bond formed.

Next, it is no longer a large jump to consider one of the uranium compounds of interest, UCl_6^{2-}. Here there is a central U atom surrounded by Cl ligands in octahedral (O_h point group) symmetry. The d orbitals are the primary bonding orbitals, so we again look to a character table for the symmetry of these orbitals in an octahedral environment. These orbitals split into two different Mulliken symbols: e_g and t_{2g}, a well-known splitting for transition metals in octahedral environments. However, the primary orbitals of interest are the f-orbitals. These belong to the representation a_{2u}, t_{1u} and t_{2u} in an octahedral environment (UCl_6^{2-}). A simplified molecular orbital diagram of UCl_6^{2-} is shown in Figure 4.5 below, which shows these splittings. The a_{2u} orbital is non-bonding and the other two are available for bonding with Cl electrons.

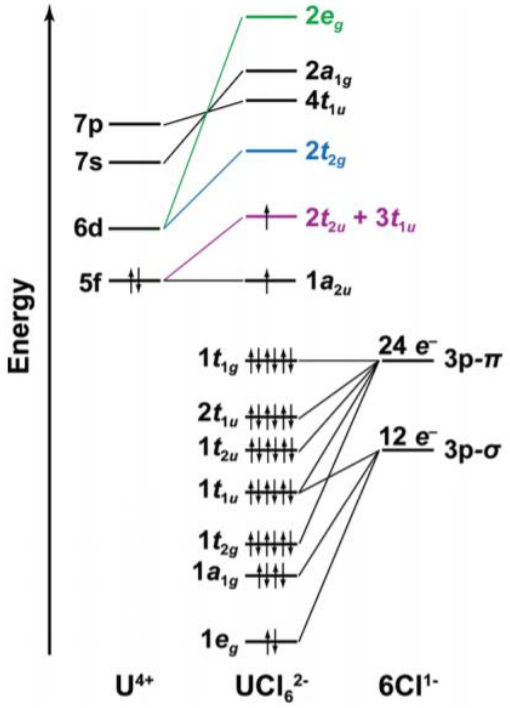

Figure 4.5. Molecular orbital diagram for UCl_6^{2-}. The molecular orbitals are labelled by their Mulliken label. Figure reproduced from Minasian et al.[5]

Molecular orbitals are often used in actinide spectroscopy to help label spectral features and interpret spectra.[6–8] As an example, we look at the bonding of actinyl ions (AnO_2^{2+}, AnO_2^{1+}) and specifically uranyl in Figure 4.6. Denning finds that to fully explain the oxygen x-ray absorption spectra and optical spectra that are measured, the uranium 6*d*, 5*f*, 6*p*, and 6*s* orbitals all need to be considered, but once they are, the experimental spectra are well explained by the molecular orbital model. To get more quantitative than this (and explore questions of covalency and electron distribution), a more sophisticated model, such as DFT, is needed.

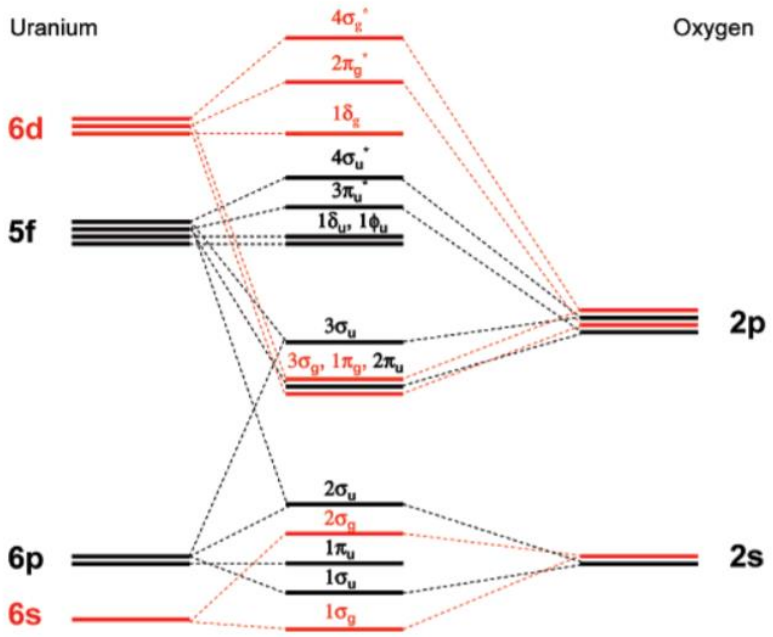

Figure 4.6. Uranyl molecular orbital diagram. Figure from Denning.[8]

4.3 Density Functional Theory

Density functional theory (DFT) is a rich field that would be outside of the scope of this work to cover completely. In this section, I synthesize information gleaned from a number of excellent reviews on the topic[9,10] which should be referenced for further details. Density Functional Theory is an alternative to conventional wavefunction analysis methods. The idea is that instead of using the wavefunction, Ψ, we rewrite the energy as a function of the electron density, $n(\vec{r})$. This method was first developed by Kohn and Hohenberg.[11] In this formulation, the wavefunction is written as a functional of the density,

$$\Psi = \Psi[n(\vec{r})] \tag{4.1}$$

A simple proof that the resulting solutions are valid for the ground state is given in Levy et. al.[12], but it should be noted that this approximation is only valid for the ground state wavefunction. We

can then write any observable in terms of the density by using this formulation of the wavefunction. In particular, the energy can be written as

$$E[n] = T[n] + V_{ext}[n] + V_{ee}[n] \tag{4.2}$$

Under the assumptions of Kohn and Hoenberg, this can be written as

$$E = \int v(\vec{r})n(\vec{r})d\vec{r} + \frac{1}{2}\iint \frac{n(\vec{r})n(\vec{r}')}{|\vec{r}-\vec{r}'|}d\vec{r}d\vec{r}' + G[n] \tag{4.3}$$

where the first term is $V_{ext}[n]$, the external potential, the second is the classical Coulomb energy, and the third is a functional of the density encompassing the kinetic energy and non-classical electron-electron interactions. Kohn and Sham further separated the remaining functional into two terms,

$$G[n] = T_s[n] + E_{XC}[n] \tag{4.4}$$

where $T_s[n]$ is the kinetic energy of a non-interacting group of electrons (not the same as $T[n]$ above), and E_{XC} is known as the exchange-correlation energy.[13] Of all of these terms, only E_{XC} does not have a closed-form expression. This reformulation allows the Schrodinger equation to be written in terms of single-electron wavefunctions

$$\left[-\frac{\hbar^2}{2m}\nabla^2 + V_{ext}(\vec{r}) + V_H(\vec{r}) + V_{XC}(\vec{r})\right]\psi_i(\vec{r}) = \epsilon_i\psi_i(\vec{r}), \tag{4.5}$$

$$V_H(\vec{r}) = e^2\int \frac{n(\vec{r}')}{|\vec{r}-\vec{r}'|}d\vec{r}' \tag{4.6}$$

$$V_{XC}(\vec{r}) = \frac{\delta E_{XC}[n]}{\delta n(\vec{r})} \tag{4.7}$$

These Kohn-Sham equations can be solved self-consistently by iterating and finding solutions that minimize the energy.

In practice, an approximation for the density is used in the exchange-correlation functional. Perhaps the most common is the Local Density Approximation.[13] In this, the exchange-correlation functional is approximated as being entirely local and this allows calculations of the exchange-

correlation energy of a homogenous electron gas to be used.[14,15] Corrections to this local density approximation can be made at the cost of computational complexity. The single-electron wavefunctions are expanded in terms of a basis of orthogonal wavefunctions to reduce this differential equation to a matrix problem. These orthogonal wavefunctions constitute a basis set and can have a large impact on how accurately and quickly the calculation can be done. The basis set needs to be large enough to express the solution accurately, but small enough that calculations don't take forever. These basis set functions can be tuned for the specific problem, but some general sets are fairly popular.[16,17]

Because the calculations quickly become unreasonably expensive with increased number of electrons, often only the valence electrons are allowed to vary in what is known as the frozen core approximation. For actinides in particular, the choice of size of this core is critical. Batista et. al. showed that a 78 e^- frozen core (which keeps frozen the 5s, 5p and 5d electrons) has a significantly different shape of the 5f, 6d and 7s electrons than a 60 e^- core.[18] Further, the difference in energy between UF_6 and UF_5+F (bond breaking) was significantly more accurate in the 60 e^- core. The reason given for this was that the inclusion of the 5d orbitals enforced a node in the 6d orbital near the maximum of the 5f orbitals (see Figure 4.7) and so the interaction between the 5f and 6d electrons was not properly described in the larger core model.

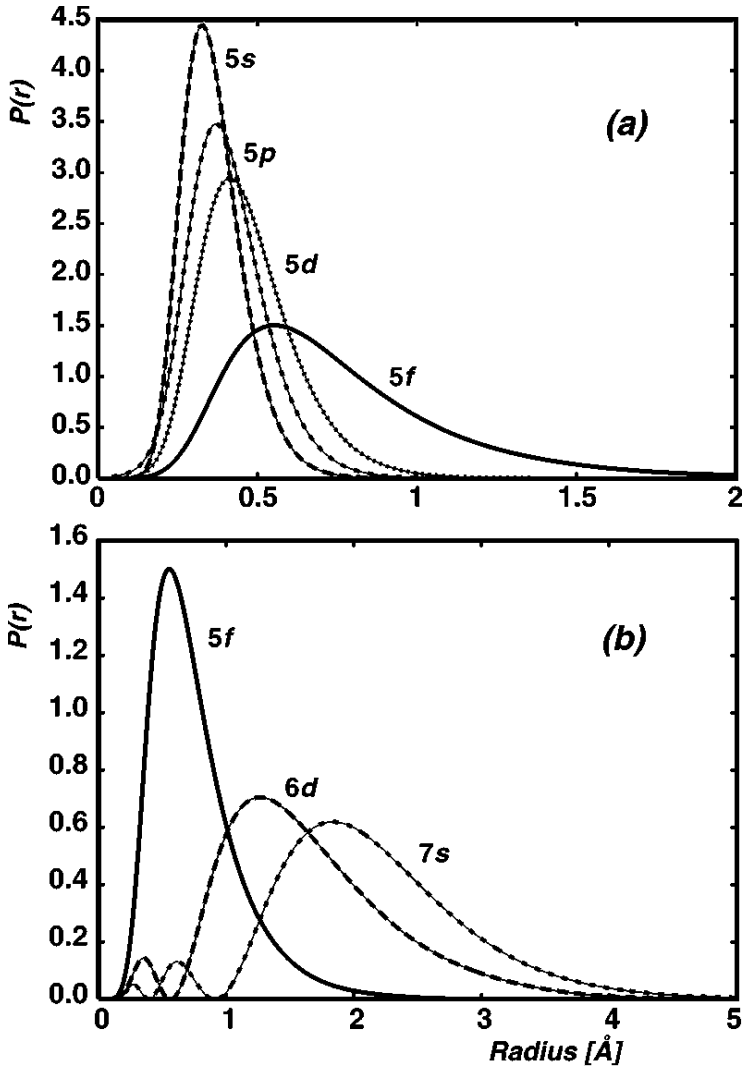

Figure 4.7. Radial wavefunctions with a 60 electron frozen core approximation.

For large atoms like actinides, relativistic effects become important. The correction due to relativistic effects is on the order of $(Z\alpha)^2$ and so when $Z\sim137$, this correction becomes important for the 1s electrons. However, due to orthogonality, the valence orbitals are also substantially affected, as shown in Figure 4.8. This effect is explained in Barends et. al.[19] where they examine whether the valence orbitals are affected more by orthogonality with the innermost orbitals or by mixing with perturbed unoccupied states. The radial extent is particularly important in determining which electrons are available for bonding, so using relativistic corrections is particularly important

for studies of 5f participation. Relativistic corrections are implemented by using a relativistic effective core potential (RECP). This effective core potential is created by first doing a relativistic full-electron calculation of the atomic orbitals. The core potential is then created by finding the potential that has the calculated valence wavefunctions as solutions.[20]

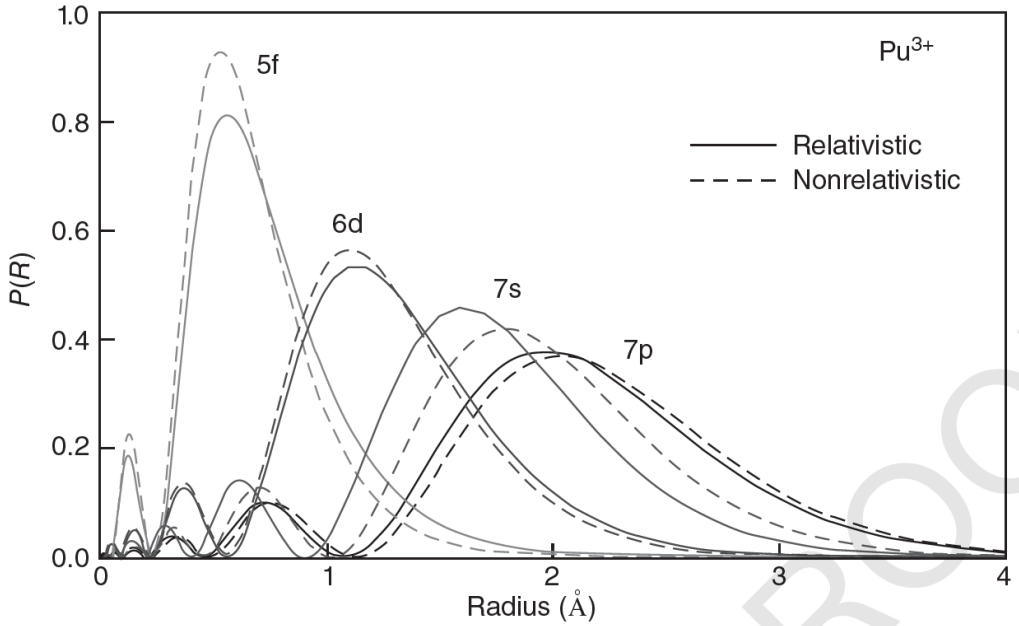

Figure 4.8. Radial wavefunctions for frontier orbitals in a relativistic and non-relativistic calculation. Note that the extent of the 5f orbitals changes appreciably, which has important implications for covalency.

The specific relativistic corrections made to calculate the RECP used in this code are outlined in the paper by Van Lenthe et. al. in what has become known as the zero order regular approximation (ZORA).[21] I reproduce part of their argument here in order to illustrate how this expansion works and why it is used. The relativistic energy of an electron in a potential V is

$$E = \sqrt{m^2c^4 + p^2c^2} - mc^2 + V$$

This can be rewritten similar to the non-relativistic energy as

$$\frac{p^2}{2m}\left(\frac{1}{1+\frac{E-V}{2mc^2}}\right)+V \tag{4.8}$$

And the relativistic component can be expanded in terms of

$$\frac{E-V}{2mc^2} \approx \frac{p^2}{4mc^2} \tag{4.9}$$

However, for electrons in a coulomb potential, this term diverges near the nucleus, so any expansion in it is invalid. Van Lenthe et. al. instead rewrote the energy as

$$E = \frac{p^2c^2}{(2mc^2-V)\left(1+\frac{E}{2mc^2-V}\right)}+V \tag{4.10}$$

And expanded in terms of

$$\frac{E}{2mc^2-V} \tag{4.11}$$

which is not divergent near the nucleus. This leads to a zeroth order approximation for the energy of

$$E_0 = \frac{p^2c^2}{2mc^2-V}+V \tag{4.12}$$

which is already different than the non-relativistic energy. They then use this zeroth order approximation to produce wavefunctions very similar to those of the full Dirac equation (Figure 4.9).

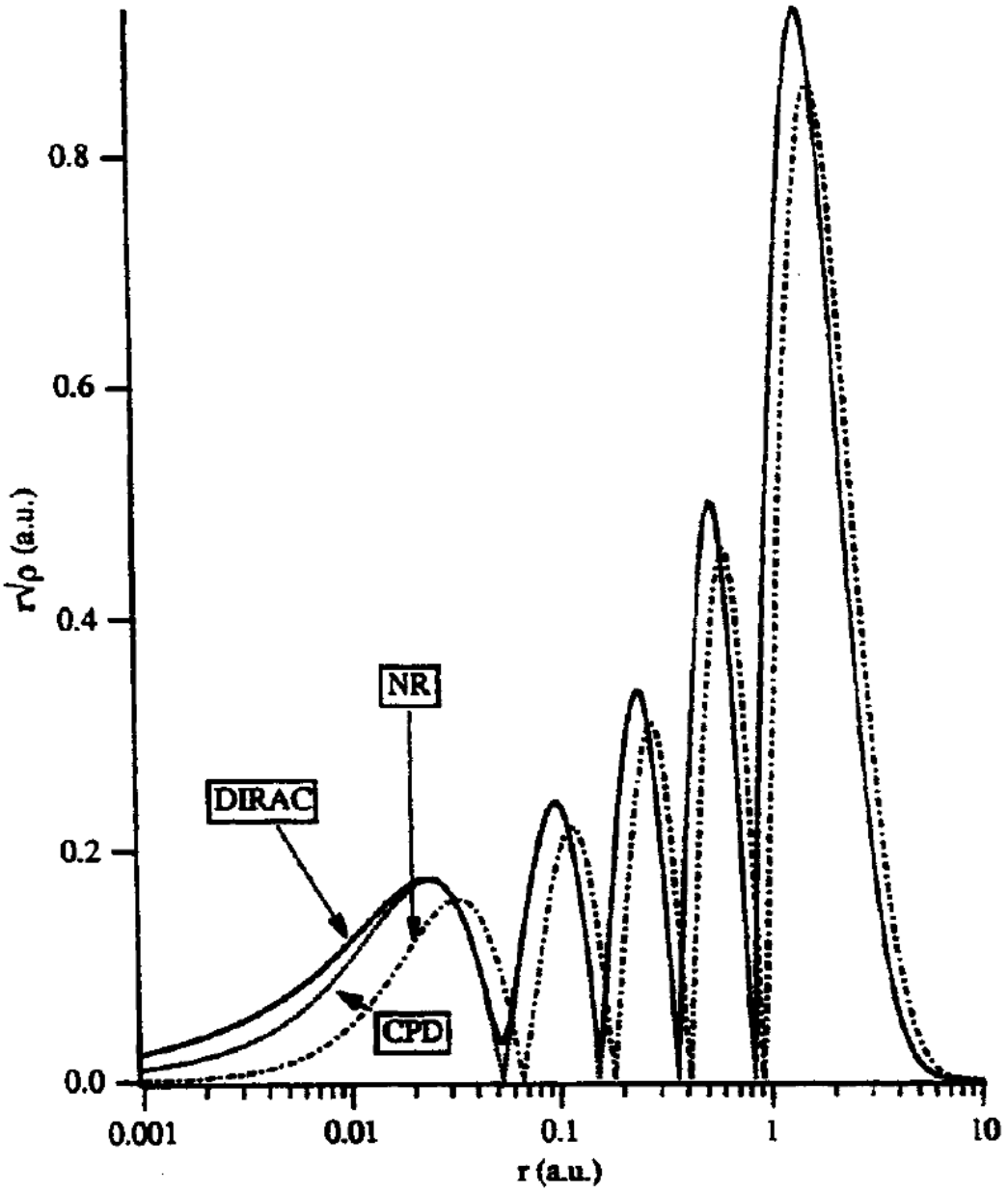

Figure 4.9. Comparison of radial wavefunction calculated with full dirac Hamiltonian, non-relativistic and the zeroth order relativistic approximation.

Spin-orbit corrections also become important as the spin orbit term in the Hamiltonian also scales like $(Z\alpha)^2$. In the same calculations of UF_6 dissociation energy, Batista et. al. also looked at the effects of including spin-orbit coupling. In these calculations, the central U atom changes

from a $5f^0$ to a $5f^1$ state, and the energy of the UF_5 fragment was found to decrease due to this spin orbit interaction, bringing it more in line with experimental results.[22]

One final concern specific to actinides is that of unpaired spin. The main issue is that unpaired electrons result in multiplet states which aren't treated well by DFT. The 5f orbitals are degenerate and when a number of electrons are placed in the 5f states, instead of each electron occupying one of the degenerate orbitals, the total spin of the electrons must be considered, yielding a multiplet of states very close in energy. The problem enters because DFT assumes the orbitals are either fully occupied or unoccupied and the true wavefunction has instead partial occupation of the multiplet states. This creates a great deal of calculation complexity. The effect of unpaired electrons is shown in calculations of UF_n and UCl_n (n= 1, … 6) molecules (Figure 4.10).[23] Here, the best agreement with experimental results is demonstrated for n=5 and 6 where the uranium atom is in a $5f^0$ or $5f^1$ state.

With these considerations there is opportunity for variation in specifics in DFT calculations and further details are provided in chapter 5 about the particular calculations performed. Once DFT calculations are complete, XES spectra can be predicted simply by taking differences in energy levels, as is done in Chapter 5.[24] Typically, a single shift in energy is needed to align the predicted and experimental spectra. X-ray absorption is calculated similarly, by taking the difference between the ground state energy and an excited "virtual" molecular orbital (again, see section 5.4.8 for details). A usual central goal of x-ray absorption or x-ray emission experiments is to test these theoretical applications by comparing to predicted spectra.[25–31] This is key in providing confidence for other predictions made by DFT, such as covalency, and is the main way that covalency is explored in chapter 5.

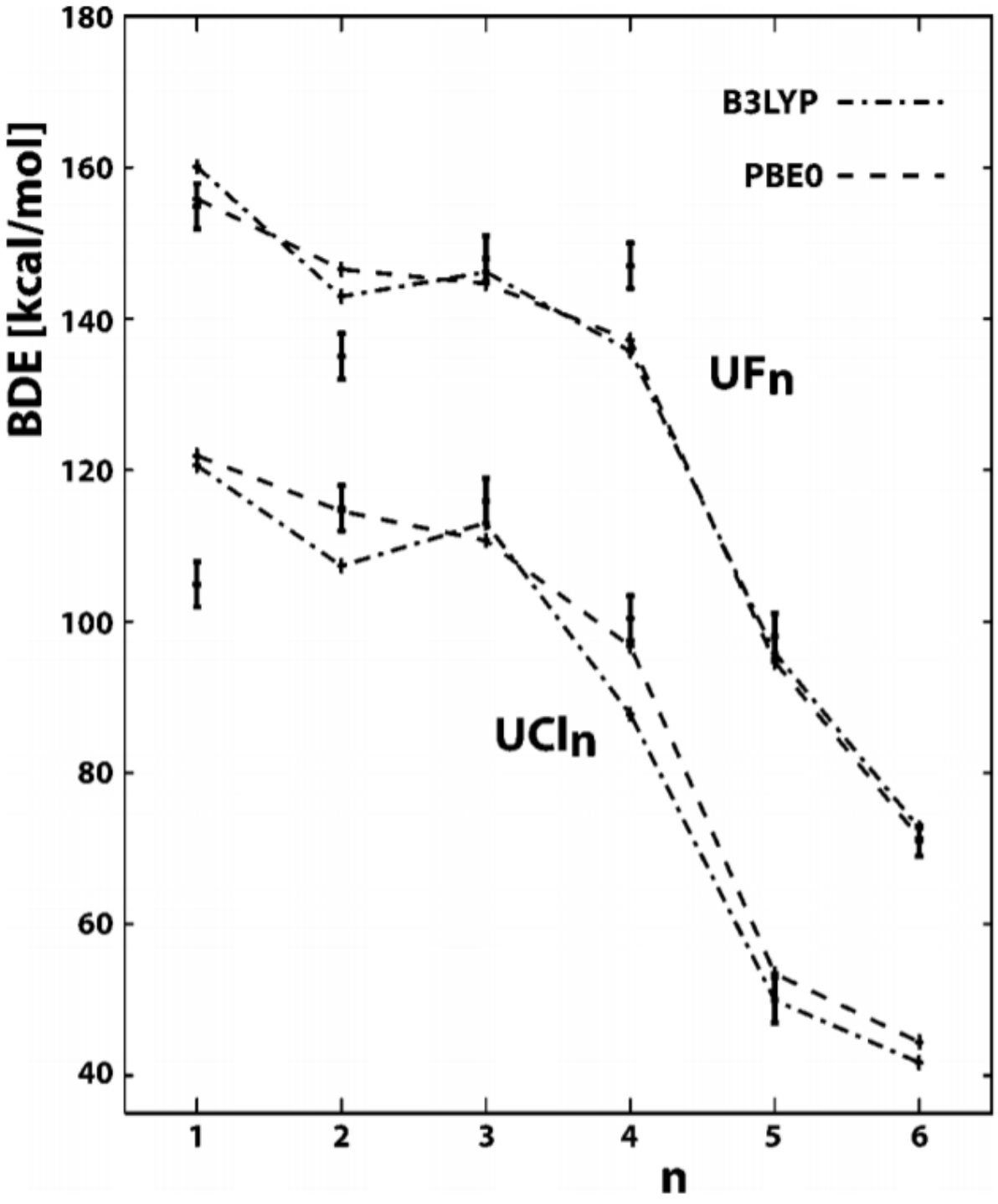

Figure 4.10. Bond-dissociation Energies calculated for UCl_n and UF_n. The larger the number of unpaired electrons (smaller n), the worse the agreement with experimental data.[23]

4.4 CONCLUSION

We've discussed here both the qualitative method of molecular orbitals and group theory as well as the more quantitative DFT calculations, and these techniques will play a critical role in the interpretation of x-ray absorption and x-ray emission spectra. In turn, carefully chosen experimental results can help refine DFT calculations by providing benchmark results on model systems.

4.5 REFERENCES

1. Dresselhaus, M. S., Dresselhaus, G. & Jorio, A. *Group Theory: Application to the Physics of Condensed Matter*. (Springer-Verlag Berlin Heidelberg, 2008).

2. Jones, H. F. (Hugh F. . *Groups, representations, and physics*. (Insitute of Physics Pub, 1998).

3. Hamermesh, M. (Morton). *Group theory and its application to physical problems*. (Dover Publications, 1989).

4. Jean, Y., Volatron, F. & Burdett, J. K. *An introduction to molecular orbitals*. (Oxford University Press, 1993).

5. Minasian, S. G. *et al.* Determining Relative f and d Orbital Contributions to M–Cl Covalency in MCl_6^{2-} (M = Ti, Zr, Hf, U) and $UOCl_5^-$ Using Cl K-Edge X-ray Absorption Spectroscopy and Time-Dependent Density Functional Theory. *J. Am. Chem. Soc.* **134**, 5586–5597 (2012).

6. Liu, G. & Beitz, J. V. Optical Spectra and Electronic Structure. in *Chemistry of the Actinide and Transactinide Elements* 2013–2089 (2010).

7. Butorin, S. M., Kvashnina, K. O., Vegelius, J. R., Meyer, D. & Shuh, D. K. High-resolution X-ray absorption spectroscopy as a probe of crystal-field and covalency effects in actinide compounds. *Proc. Natl. Acad. Sci. U. S. A.* **113**, 8093–7 (2016).

8. Denning†, R. G. Electronic Structure and Bonding in Actinyl Ions and their Analogs. (2007). doi:10.1021/JP071061N

9. Barth, U. Von. Basic Density-Functional Theory — an Overview. *Phys. Scripta.* **T109**, 9–39 (2004).

10. Batista, E. R., Martin, R. L. & Yang, P. Computational Studies of Bonding and Reactivity

in Actinide Molecular Complexes. in *Computational Methods in Lanthanide and Actinide Chemistry* 375–400 (John Wiley & Sons Ltd, 2015). doi:10.1002/9781118688304.ch14

11. Hohenberg, P. & Kohn, W. Inhomogeneous Electron Gas. *Phys. Rev.* **136**, 864 (1964).

12. Levy, M. Universal variational functionals of electron densities, first-order density matrices, and natural spin-orbitals and solution of the v-representability problem. *Proc. Natl. Acad. Sci. U. S. A.* **76**, 6062–5 (1979).

13. Kohn, W. & Sham, L. J. Self-Consistent Equations Including Exchange and Correlation Effects. *Phys. Rev.* **140**, 1133 (1965).

14. Gunnarsson, O., Jonson, M. & Lundqvist, B. I. Descriptions of exchange and correlation effects in inhomogeneous electron systems. *Phys. Rev. B* **20**, 3136–3164 (1979).

15. Engel, E. & Vosko, S. H. Wave-vector dependence of the exchange contribution to the electron-gas response functions: An analytic derivation. *Phys. Rev. B* **42**, 4940–4953 (1990).

16. Becke, A. D. Density-functional exchange-energy approximation with correct asymptotic behavior. *Phys. Rev. A* **38**, 3098–3100 (1988).

17. Lee, C., Yang, W. & Parr, R. G. Development of the Colle-Salvetti correlation-energy formula into a functional of the electron density. *Phys. Rev. B* **37**, 785 (1988).

18. Batista, E. R., Martin, R. L., Hay, P. J., Peralta, J. E. & Scuseria, G. E. Density functional investigations of the properties and thermochemistry of UF 6 and UF 5 using valence-electron and all-electron approaches. *J. Chem. Phys.* **121**, 2144–2150 (2004).

19. Barends, E. J., Schwarz, W. H. E., Schwerdtfeger, P. & Snijders, J. G. Relativistic atomic orbital contractions and expansions: Magnitudes and explanations. *J. Phys. B At. Mol. Opt. Phys.* **23**, 3225–3240 (1990).

20. Van Lenthe, E., Van Leeuwen, R., Baerends, E. J. & Snijders, J. G. Relativistic Regular Two-Component Hamiltonians. **57**, 281–293 (1996).

21. DeBeer George, S. & Neese, F. Calibration of Scalar Relativistic Density Functional Theory for the Calculation of Sulfur K-Edge X-ray Absorption Spectra. *Inorg. Chem.* **49**, 1849–1853 (2010).

22. Olson, A. C. *et al.* Using solution- and solid-state S K-edge X-ray absorption spectroscopy with density functional theory to evaluate M–S bonding for MS_4^{2-} (M = Cr, Mo, W) dianions. *Dalt. Trans.* **43**, 17283–17295 (2014).

23. Batista, E. R., Martin, R. L. & Hay, P. J. Density functional investigations of the properties and thermochemistry of UFn and UCln (n=1,...,6). *J. Chem. Phys.* **121**, 11104–11 (2004).

24. Lee, N., Petrenko, T., Bergmann, U., Neese, F. & DeBeer, S. Probing Valence Orbital Composition with Iron Kβ X-ray Emission Spectroscopy. *J. Am. Chem. Soc.* **132**, 9715–9727 (2010).

25. Cross, J. N. *et al.* Covalency in Americium(III) Hexachloride. *J. Am. Chem. Soc.* **139**, 8667–8677 (2017).

26. Minasian, S. G. *et al.* Determining Relative f and d Orbital Contributions to M–Cl Covalency in MCl_6^{2-} (M = Ti, Zr, Hf, U) and $UOCl_5^-$ Using Cl K-Edge X-ray Absorption Spectroscopy and Time-Dependent Density Functional Theory. *J. Am. Chem. Soc.* **134**, 5586–5597 (2012).

27. Minasian, S. G. *et al.* New evidence for 5f covalency in actinocenes determined from carbon K-edge XAS and electronic structure theory. *Chem. Sci.* **5**, 351–359 (2014).

28. Löble, M. W. *et al.* Covalency in Lanthanides. An X-ray Absorption Spectroscopy and Density Functional Theory Study of $LnCl_6^{x-}$ (x = 3, 2). *J. Am. Chem. Soc.* **137**, 2506–2523 (2015).

29. Minasian, S. G. *et al.* Carbon K-Edge X-ray Absorption Spectroscopy and Time-Dependent Density Functional Theory Examination of Metal–Carbon Bonding in Metallocene Dichlorides. *J. Am. Chem. Soc.* **135**, 14731–14740 (2013).

30. Su, J. *et al.* Energy-Degeneracy-Driven Covalency in Actinide Bonding. *J. Am. Chem. Soc.* **140**, 17977–17984 (2018).

31. Fieser, M. E. *et al.* Evaluating the electronic structure of formal LnII ions in LnII(C5H4SiMe3)31- using XANES spectroscopy and DFT calculations. *Chem. Sci.* **8**, 6076–6091 (2017).

Chapter 5. USING X-RAY EMISSION AND ABSORPTION SPECTROSCOPY TO CHARACTERIZE COVALENCY IN THE URANIUM(V)–CHLORIDE BOND

5.1 PREFACE

This chapter is the results of work that I led at SSRL and is going to be submitted to JACS in the very near future. My contributions to this work were the RIXS and HERFD measurements (everything from the beamline proposal to sample prep to integration with beamline facilities) as well as data analysis and writing. I am joint first author on this paper with Jing Su, who did the theoretical calculations. The synthesis and other measurements were done by other members of the Kozimor group at LANL.

Authors:

Jing Su,[1,†] Alex S. Ditter,[1,2,†] Enrique Batista,[1,*] David L. Clark,[1] Justin N. Cross,[1] Stosh A. Kozimor, [1,*], Gerald T. Seidler,[2] Matthias W. Löble,[1] Stefan G. Minasian,[3] Richard L. Martin,[1] Angela C. Olson,[1] Brian L. Scott,[1] David K. Shuh,[2] Chantal E. Stieber,[1] Benjamin Stein,[1] Ping Yang.[1,*]

[1] Los Alamos National Laboratory (LANL), P.O. Box 1663, Los Alamos, New Mexico, 87545, USA

[2] University of Washington, Seattle, Washington 98195, United States

[3] Lawrence Berkeley National Laboratory, 1 Cyclotron Road, Berkeley, California, 94720, United States

[†] Su and Ditter contributed equally to this manuscript.

5.2 ABSTRACT

Pentavalent uranium is of particular interest not only because it is an unusual uranium oxidation state, but also because it has seen increased importance in environmental fate and transport schemes. Here, we study the electronic structure of $(PPh_4)UCl_6$ and associated compounds with single crystal X-ray diffraction, cyclic voltammetery, Cl K-edge, and U $M_{5,4}$-edge x-ray absorption spectroscopy (XAS), U M_4-edge x-ray emission spectroscopy (XES) and high energy-resolution fluorescence detection XAS (HERFD-XAS) and relativistic density functional theory (DFT). Results of Cl K-edge spectroscopy showed increased U 5*f* – Cl 3*p* mixing for pentavalent UCl_6^{1-} as opposed to tetravalent UCl_6^{2-} which is a result of both increased orbital overlap and improved energy matching between the uranium and ligand orbitals.

5.3 INTRODUCTION

Recent creative synthetic advances have identified methods for stabilizing uranium in exotic oxidation states.[1–6] Other than U^{III}, U^{IV}, and U^{VI} (which are typical in uranium chemistry) there have been surprising observations of complexes containing U^{II} and U^{V}. Complexes containing U^{II} are intriguing because they are highly reducing and because they have been proposed to contain unusually split electronic configurations, with one valence electron in the 6*d*-orbitals and four electrons in the U 5*f*-orbitals. Compounds containing U^{V} have received equal (if not more) attention, primarily owing to potential relevance in numerous applied areas of actinide science. This includes, but is not limited to, the emergence of U^{V} in environmental fate and transport models[7–12] and as key intermediates[13,14] in catalysis schemes.

In terms of electronic structure and bonding, the U^{V} ion is attractive in comparison to other actinide systems because of its $5f^1\ 6d^0$ electronic configuration. Having only a single 5*f*-electron

facilitates interpreting numerous physical properties associated with uranium. It also simplifies computational efforts to a certain degree – which historically for uranium have been challenged by the large spin-orbit coupling, the emergence the *f*-manifold, significant relativistic effects, and the large number of unpaired valence electrons. Conveniences associated with this $5f^1$ electronic configuration – especially when associated with highly symmetric coordination environments – have been exploited to provide foundational information regarding chemical bonding in actinide complexes. In many cases, spectroscopic and computational results implied that there was considerable uranium–ligand orbital mixing, where orbital mixing is defined as synonym for covalency in the sense of Heitler and London.[15–17]

Ligand K-edge X-ray absorption spectroscopy (XAS) offers opportunity to test propositions that U^V forms highly covalent bonds. As described previously, the experiment involves quantifying intensities of bound-state electronic transitions between ligand 1*s*-electrons into virtual (unoccupied) orbitals that contain some degree of ligand *p*-character.[18] Because the experiment generates a core hole localized on the ligand, the intensity of the dipole allowed transition is proportional to the amount of ligand *p*-character in the final state. Hence, the ligand K-edge XAS method provides a quantitative measure of the orbital mixing and provides a direct measure of metal−ligand covalency. Resonant inelastic X-ray scattering (RIXS) has emerged as a powerful tool to probe metal-ligand covalency in d- and f-block metal compounds.[19–23] This technique combines XAS with X-ray emission spectroscopy (XES). Specifically, RIXS is a two-photon process that starts with exciting a core electron into an unoccupied valence orbital like in XAS, followed by detecting photon emission by the decay of an electron from a differen orbital filling the core hole like in XES.[24,25] As RIXS measurements obey a different selection rule for

spectral intensity from XAS and XES and can provide detailed electronic structure information, making it a complementary method to the other two in the study of metal-ligand bonding.

Reported here is the first ligand K-edge XAS and DFT study focused on characterizing U^{V} covalent bonding. For these studies, tetraphenyl phosphonium uranium hexahalide, $(PPh_4)UCl_6$, was prepared as single crystals and characterized by single crystal X-ray diffraction, cyclic voltammetery, Cl K-edge, U $M_{5,4}$- and U $N_{5,4}$-edge XAS, and U Mβ XES. The UCl_6^{1-} anion was exceptionally suited for the ligand K-edge XAS, XES, and DFT experiments, as there is no symmetry allowed *f*- and *d*-orbital mixing in O_h-symmetry. Hence, U^{V} 5*f*- and 6*d*- covalency could be probed independently. Analysis of UCl_6^{1-} provided a basis for characterizing the magnitude of *f*-element multiplet and spin-orbit contributions to the ligand K-edge XAS spectra. Our results have been presented in the context of previous actinide covalency studies and collectively provide insight into how spatial overlap vs. energy degeneracy between the metal and ligand valence orbitals influence covalency in actinide bonding.

5.4 Experimental Details

5.4.1 *General Considerations*

Caution! The ^{238}U isotope is a low specific-activity α-emitting radionucleotide and its use presents a hazard to human health. This research was conducted in a radiological facility with appropriate analyses of these hazards and implementation of controls for the safe handling and manipulation of these toxic and radioactive materials. All procedures were performed with rigorous exclusion of air and moisture using Schlenk and glovebox techniques under an atmosphere of argon. All glassware was dried at 150 °C for at least 12 hr. Acetonitrile (anhydrous, Fischer) was dried over CaH_2, degassed by three freeze-pump-thaw cycles, and vacuum transferred

before use. The UCl_4 was prepared as previously described from UO_3 and hexachloropropene.[26] Elemental analyses were carried out by the Midwest M*croLab, LLC in Indianapolis, IN.

5.4.2 *Synthesis of Tetraphenylphosphonium Uranium(V) Hexachloride, $(PPh_4)UCl_6$*

On a Schlenk line under argon, $UO_2Cl_2 \cdot H_2O$ (0.900 g, 2.51 mmol) was dissolved in thionyl chloride (5 mL) and stirred, followed by the addition of PPh_4Cl (0.942 g, 2.51 mmol) dissolved in thionyl chloride (5 mL). The orange solution was heated to reflux at 90 °C overnight, over which time a color change to dark red/orange, and finally, a lighter orange was observed. After cooling to room temperature, the solvent was removed en vacuo yielding an orange solid, and the flask was sealed and transferred to a glove box. The solid was taken into 5 mL of acetonitrile, transferred to a scintillation vial, heated to 50 °C to dissolve all of the solid, and allowed to recrystallize at ambient temperature. After 5 days, orange crystals were present and could be isolated in 73% yield as $(PPh_4)UCl_6$.

In an argon filled glovebox, PPh_4Cl (0.524 g, 1.40 mmol) was dissolved in thionyl chloride (5 mL) and was added to a 20 mL scintillation vial containing UO_3 (0.400 g, 1.40 mmol) also dissolved in thionyl chloride (5 mL). The solution was allowed to stir for a few minutes, after which a color change to deep red was observed. The solution was allowed to cool to room temperature and dark red crystals grew over the course of several days. The solution was heated to 91 °C and refluxed for 3 days, cooled to 21 °C, and the solvent was removed in vacuo. The resulting yellow powder was washed with diethyl ether and dissolved in acetonitrile heated to 91 °C, followed by slow cooling. After 3 days, orange crystals and green crystals were present in the solution. The orange crystals were picked out with tweezers to yield orange crystals identified as $(PPh_4)UCl_6$ (0.463 g, 0.588 mmol, 42%) that were suitable for single crystal X-ray diffraction measurements. Anal. Calcd. for $C_{24}H_{20}Cl_6UP$: C, 36.59; H 2.56. Found. C, 36.66; H, 2.66.

5.4.3 *Cl K-edge Measurements*

All Cl K-edge XAS data were either collected at the beamlines 4-3 at SSRL or the INE beamline for Actinide Research at ANKA. The Cl K-edge XAS measurements made at SSRL were conducted under dedicated operating conditions (3.0 GeV, 500 mA) at Beamline 4-3. This beamline was equipped with a 20-pole, 2.0 Tesla wiggler, utilized a liquid N_2-cooled double-crystal Si[111] monochromator and employed a flat, bent vertically collimating and focusing mirrors (fwhm beam spot size = 3 x 16 mm). At the ANKA, operating conditions of 2.5 GeV and 120 mA were used. The beamline was equipped with a 1.5 Tesla bending magnet and a water-cooled Si[111] double crystal monochromator. The crystals were detuned by 30% from the rocking curve maximum. Two mirrors were utilized, the first mirror vertically collimating and the second mirror vertically and horizontally focusing.

At both facilities samples were analyzed within a chamber that was separated from the beam pipe by a 4 μm polypropylene window and continually flushed with He gas. An additional window of the same material separated the sample from a Vortex Si fluorescence detector (4 element SSRL; 1 element ANKA) that was positioned at 90° from the incident beam and sufficiently far from the sample to ensure dead times that were less than 3%. Sample fluorescence was measured using the Vortex detector against the incident radiation (I0), which was monitored using an ionization chamber through which He was continually flowed. The ion chamber was isolated from the sample chamber with a 4 μm polypropylene window. Spectra were collected with a dwell times of 1 to 3 s. Dead time corrections to all experimental scans collected at SSRL were achieved by measuring fluorescence intensities of the Vortex elements vs. the total counts and

opening the horizontal slit (starting at 0.1 mm slit width) in steps of 0.1 mm until full saturation was achieved. Detector dead times were evaluated by obtaining a response curve for the single channel analyzer (SCA) vs. the incoming count rate (ICR) of the detector. The SCA to ICR relationship was modeled assuming that $r = kr_1e^{-rt}$ where t is the dead time, r is the SCA count rate, r_1 is the ICR count rate, and k is a constant of proportionality. These analyses showed dead time contributions of less than 3%. Spectra were obtained in triplicate, with unique samples of the hexahalides being analyzed during four different synchrotron scheduling periods to establish reproducibility and evaluate error associated with the measurements.

5.4.4 *Cl K-edge XAS Data Analysis*

Data manipulation and analysis was conducted as previously described by Solomon and co-workers.[18] Energy calibrations were conducted externally using the maxima of the first pre-edge features in Cs_2CuCl_4 (2820.02 eV).[18] Data were analyzed by fitting a line to the pre-edge region, 2702.1−2815.0 eV, which was subsequently subtracted from the experimental data to eliminate the background of the spectrum. The data were normalized by fitting a first-order polynomial to the post-edge region of the spectrum (2836−3030 eV) and setting the edge jump at 2836 eV to an intensity of 1.0. This normalization procedure gave spectra normalized to a single Cl atom or M−Cl bond. A deconvoluted model for the Cl K-edge XAS data was obtained using a modified version of EDG_FIT in IGOR 6.0. The pre-edge regions (<2824.8 eV) were best modeled by two symmetry-constrained pseudo-Voigt line shapes. Approximate peak positions were determined using first- and second-derivatives of each spectrum. The edge regions were modeled with two pseudo-Voigt functions (for the edge peak) and an additional function consisting of a 1:1 ratio of arctangent and error function contributions, which was used to model the absorption threshold. Deconvoluted spectral models were performed over several energy ranges.

To facilitate comparison with previously reported Cl K-edge XAS spectra for $(PPh_4)_2UCl_6$,[27,28] the energy position for the step function was optimized near the value used previously. The areas under the pre-edge peaks (hereafter defined as the intensity) are equal to the fwhm × peak height.[29]

5.4.5 *Uranium $N_{5,4}$-edge Measurements*

Samples were prepared in an argon-filled glovebox by grinding crystals of the analyte into a fine powder with a mortar and pestle and brushing the powder onto a Si_3N_4 membrane (100 nm, Silson). A second membrane was placed over the sample, and the edges were sealed together using using Hardman Double/Bubble® epoxy. STXM methodology was similar to that discussed previously.[28,30–33] Single-energy images and U $N_{5,4}$-edge XAS spectra were acquired using the STXM instrument at the Advanced Light Source-Molecular Environmental Science (ALS-MES) beamline 11.0.2, which is operated in top-off mode at 500 mA, in a ~0.5 atm He filled chamber.[34] An energy calibration was performed at the Ne K-edge for Ne gas (867.30 eV). For these measurements, the X-ray beam was focused with a zone plate onto the sample, and the transmitted light was detected. The spot size and spectral resolution (0.08 eV) were determined from characteristics of the 40 nm zone plate. During the STXM experiment, samples showed no sign of radiation damage and each spectrum was reproduced from multiple independent crystallites and over multiple beam-runs. Areas under the N_5 and N_4 peaks were determined by fitting a cubic spline and two Lorentzian functions to the raw data using the program IGOR 6.0 (Supporting Information).

5.4.6 *Uranium Mβ RIXS and HERFD Measurements*

Samples were finely ground for 2 min in polystyrene canisters with plexiglass pestles using a Wig-L-Bug® grinder to obtain a homogeneous fine powder. Aluminum plates with a 1 mm x 5

mm x 20 mm well were filled with a mixture of 50 mg of analyte and 10 mg of boron nitride. The samples were sealed on the back with 1 mil kapton tape and on the front with 4 μm polypropylene. Another layer of 1 mil kapton tape and 4 μm polypropylene was used to provide a second layer of containment. Measurements were performed at beamline 4-3 of SSRL under dedicated operating conditions (3 GeV, 5%, 500 mA). Measurements of Uranium Mβ x-ray emission were taken in the LANL/UW tender x-ray spectrometer.[35] The spectrometer was connected to the beam pipe via a bellows to a calibration sample chamber where a KCl standard was lowered into the beam to provide energy calibration of the incident beam. The calibration standard was measured in fluorescence mode using a PIPS detector. Upstream of the calibration chamber was an ion chamber for measuring the incident flux. Helium was flown through the spectrometer, bellows, calibration chamber and ion chamber throughout the measurements. Upstream slits were set to 10 mm x 0.5 mm.

The SSRL monochromator was a set of LN_2-cooled Si 111 crystals. Energy was detuned to 50% in order to prevent third harmonic contamination. The energy of the monochromator was calibrated by setting the peak energy of the pre-edge feature of KCl to 3608.4 eV. The emission spectrometer utilized a Ge 220 crystal for energy discrimination. The emission spectrometer simultaneously collected x-ray emission from 3331.4 eV to 3345.6 eV. The emission spectrometer was calibrated by setting the peak of the non-resonant $Cs_2UO_2Cl_4$ uranium Mβ emission to 3339.8 eV.[23] This energy calibration was performed with the incident x-ray energy set to 3900 eV. It is sometimes beneficial to mask part of the cylindrical optic in the LANL-UW x-ray spectrometer. Doing so can improve energy resolution by reducing Johann error. However, we found that masking the optic had little effect as far as resolving additional features was concerned, so we left the optic unmasked in order to maximize count rate.

Uranium Mβ RIXS was collected for 2 hours on each sample. Two scans of incident energy from 3700 to 3800 eV were performed on each sample in steps of 0.35 to 1 eV with dwell times of 40 s per point. There was no indication of radiation damage between the two scans for any sample. Helium was flowed through the spectrometer during all measurements.

5.4.7 *Uranium Mβ RIXS Data Analysis*

HERFD spectra were obtained from the RIXS data by selecting data corresponding to a single emission energy equal to the maximum of the resonant x-ray emission. These energies are 3339.7 eV, 3340.0 eV and 3339.8 eV for $(PPh_4)_2UCl6$, $(PPh_4)UCl6$, and $Cs_2UO_2Cl_4$ respectively. HERFD spectra were normalized so that the average intensity in the post-edge region (3750-3800 eV) was equal to 1. It was not necessary to subtract a pre-edge background. The locations of the maxima were determined by fitting a quadratic polynomial in the excitation energy and the emission energy to the data near the maximum.

The uranium HERFD fits were performed in Mathematica 11 with a Levenberg-Marquardt algorithm. The fit functions were an arc-tangent as an edge step and three pseudo-Voigts with 1:1 Lorentzian to Gaussian character. The resulting fit parameters are given in Table 5.1. The maxima of the RIXS plane were fit to the highest 30% intensity of data with a two dimensional polynomial of order 2. The uncertainty in Figure 5.8 is the 95% confidence level in the vertex of this polynomial.

5.4.8 *Density Functional Calculations*

Ground-state electronic structure calculations were performed on the $UO_2Cl_4^{2-}$, UCl_6^{1-} and UCl_6^{2-} anions using the hybrid functional B3LYP[36,37] as implemented in the Amsterdam Density Functional (ADF 2017.106).[38,39] Given that gas-phase DFT/B3LYP geometry optimization of the

above anions always gives much longer An-Cl distances due to strong Coulomb repulsion between Cl^- ions without inclusion of counterions in the crystal lattice, only single-point DFT/B3LYP calculations were performed at the experimental geometry of the above three anions, and O_h-symmetry geometry of UCl_6^{1-} and UCl_6^{2-} with experimental averaged U-Cl bond distances, and D_{4h}-symmetry geometry of $UO_2Cl_4^{2-}$ with experimental averaged U-O and U-Cl bond distances (Table 5.3). The all electron Slater basis sets with the quality of triple-ζ plus two polarization functions (TZ2P)[40] were used, where the most diffuse 3s basis function with exponent of 1.60 for Cl and 6d basis function with exponent of 0.88 for U were removed to avoid negative Mulliken population of atomic orbitals in the molecular orbitals (MOs). The transition-dipole method (see below) was employed to calculate the core electron excitations at the experimental geometry of $UO_2Cl_4^{2-}$, UCl_6^{1-} and UCl_6^{2-}. The scalar relativistic (SR) effects and spin-orbit (SO) coupling effects were both taken into account by the zero-order regular approximation (ZORA).[41] The molecular orbital overlap matrix is printed using the subkey SFO with the arguments eig and ovl to the EPRINT key. Orbital overlap of the U-Cl bonds was printed using the input keyword TRANSFERINTEGRALS, and the UCl_6^{1-} and UCl_6^{2-} molecules of O_h symmetry were built from two neutral fragments, i.e., U and Cl_6.

5.4.9 *DFT-Simulation of XAS Spectra*

The U $M_{5,4}$- and $N_{5,4}$-edge XAS spectra of the above three anions and Cl K-edge of UCl_6^{1-} and UCl_6^{2-} were simulated as the Kohn-Sham orbital energy differences from SO-DFT/B3LYP calculations, i.e. the energy difference between an occupied orbital and a virtual orbital of the ground state. For a specific core excitation, the oscillator strength was calculated using the transition-dipole approximation between this occupied MO and the virtual MOs. For the U $M_{5,4}$- and $N_{5,4}$-edge spectra, they were respectively simulated by calculating core electron excitation

originating from U 3d and 4d dominated MOs to virtual MOs, respectively, at the experimental crystal structure. All other excitations from orbitals between the U 3d/4d and the highest occupied MOs were excluded by restricting the energy range of the occupied orbitals involved in the excitation, so that only the excitation from U 3d/4d core level to virtual MOs were allowed. Similarly for the Cl K-edge spectra, they were simulated by calculating core electron excitation originating from Cl 1s dominated MOs to virtual MOs. The calculated transition intensities were evenly broadened with a Gaussian function of FWHM of 1.0 eV (i.e., peak width) for U $M_{5,4}$- and $N_{5,4}$-edge XAS spectra and of 0.5 eV for HERFD M_4-edge and Cl K-edge XAS spectra to emulate the experimental spectra. To facilitate the comparisons with experiment, constant shifts were applied to all the calculated XAS spectra, which are 13 eV for U $N_{5,4}$-edge, and 2.3 eV for U M_5-edge, and 0.4 eV for U M_4-edge, and 1.4 eV for HERFD M_4-edge, and 42.93 eV for Cl K-edge. The above DFT transition dipole moment method has been applied successfully in the simulation of ligand XAS and metal L-edge XANES spectra of actinide and lanthanide compounds, giving good agreement with experimental results.[28,42,43]

5.4.10 *DFT-Simulation of XES Spectra*

The Mβ XES spectra were simulated based on the transition-dipole method at the SO-B3LYP level implemented in ORCA 4.0.1 quantum chemistry package.[44] We employed ORCA code rather than ADF software because this function is unavailable in the latter one. Scalar relativistic effects were treated explicitly by employing second-order scalar relativistic Douglas−Kroll−Hess Hamiltonian formalism,[45,46] and spin-orbit coupling effects were accouted for based on effective potential and mean-field approaches invoked by SOMF(1X) operator.[47] The all electron scalar relativistic SARC basis sets[48] SARC-TZVP for U and DEF2-TZVPP basis sets[49,50] for O and Cl were used. In addition, the AUTOAUX feature[51] was used in order to

automatically generate auxiliary basis sets for the resolution of identity approximation.[52] The Mβ XES of $UO_2Cl_4^{2-}$, UCl_6^{1-} and UCl_6^{2-} were simulated as the Kohn-Sham orbital energy differences from SO-DFT/B3LYP calculations, i.e. the energy difference between occupied 4f and 3d orbitals of the ground state.[53] The emission oscillator strength was calculated in the same way as the absorption one.[53,54] All the calculated transition intensities were evenly broadened with a Gaussian function of FWHM of 1.0 eV to emulate the experimental spectra. The calculated spectra were shifted by a constant 34.5 eV, which aligned the experimental and calculated emission peak

5.5 Results and Discussion

5.5.1 UCl_6^{1-} Syntheses

Tetraphenylphosphonium uranium hexachloride $(PPh_4)UCl_6$ – hereafter referred to as UCl_6^{1-} – was freshly prepared and isolated as large orange single crystals prior to XAS analyses. We note that although structures with different counterions have been reported for U^V hexachlorides, our sample preparation contributed the first crystallization methods for PPh_4^{1+} salts of UCl_6^{1-}.[24] Our approach differed in that we isolated UCl_6^{1-} with a crystalline yield of 73% by heating (90 °C) $UO_2Cl_2•H_2O$ (1 equiv.) with PPh_4Cl (1 equiv.) in thionyl chloride ($SOCl_2$) (12 h). The UCl_6^{1-} compound was characterized using electrochemical analyses using cyclic voltammetry (CV). Figure 5.1 compares the electrochemical results from orange UCl_6^{2-} with the blue $(PPh_4)_2UCl_6$ (U^{IV}) in acetonitrile (NCMe). The voltamogram from both compounds were quite similar, showing $E_{1/2}$ values of 0.45 V and 0.43 V for UCl_6^{1-} and UCl_6^{2-}, respectively. The peak potential separations (E_p) for UCl_6^{1-} and UCl_6^{2-} were also quite similar at 0.13 V and 0.12 V. These waves were attributed to the quasireversible $UCl_6^{2-} + 1e^{1-} \rightarrow UCl_6^{1-}$ redox processes.

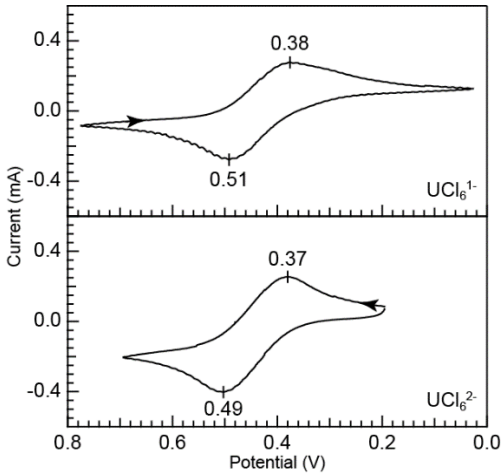

Figure 5.1. Cyclic voltamagram of $(PPh_4)UCl_6$ (*top*) and $(PPh_4)_2(UCl_6)$ (*bottom*). Measurements were performed using a platinum working electrode and a platinum counter electrode at a scan rate of 100 mV s^{-1} with NBu_4PF_6 as the supporting electrolyte. Potentials were referenced to $Fe(C_5H_5)_2/Fe(C_5H_5)_2^{1-}$.

A thermal ellipsoid representation from UCl_6^{1-} was provided in Figure 5.2. In the UCl_6^{1-} structure, there were three nearly equivalent U–Cl distances and the Cl–U–Cl angles deviated only slightly from 90°. The U–Cl distances ranged 2.5146(4) to 2.5048(5) and the angles 90.159(14) to 90.849(17). Given that these distortions were slight, we found it appropriate to describe the UCl_6^{1-} structures using O_h-symmetry. The U–Cl distances increased could be predicted based on the U^V ionic radii. This was depicted graphically by plotting the mean M–Cl bond distance verses the metal ionic radii (Figure 5.3). The data were compared to MCl_6^{x-} (x = 2 for M^{IV} = Ti, Zr, Hf, Ce, Th, U, Np, Pu; x = 3 for M^{III} = Ce, Nd, Sm, Eu, Gd) salts that had been previously characterized by Cl K-edge XAS.[28,55–57] A linear fit to these data has a slope near unity, 1.06(1), and a *y*-intercept, 1.70(1) Å, which was close to the expected anionic radius of chloride (1.81 Å).[58] This structural data incorrectly suggested that the amount of M–Cl orbital mixing was largely ionic and did not appreciably change with metal identity. Inspection of the M–Cl interaction by Cl K-edge XAS and DFT revealed appreciable diversity in bonding within this group (*vide infra*).

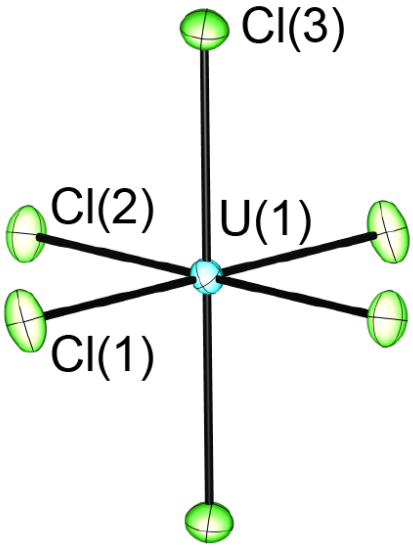

Figure 5.2. A thermal ellipsoid plot of $(PPh_4)UCl_6$ shown at the 50% probability level. The PPh_4^{1+} counterion was omitted.

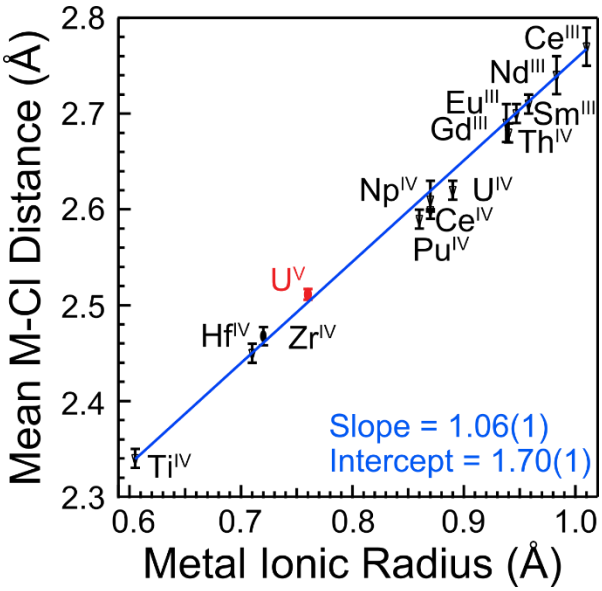

Figure 5.3. Average experimental M–Cl bond distances for metal hexachlorides that have been analyzed by Cl K-edge XAS, versus six-coordinate ionic radii.[58] The $[PPh_4]_x[MCl_6]$ (x = 2 for M = Zr, Nb, Mo; x = 1 for M = U) were shown in black while $[PPh_4]_x[M'Cl_6]$ (x = 3 for M' = Nd,[57] Sm,[57] Eu,[57] Gd;[57] x = 2 for M' = Ti,[56] Hf,[56] Th,[56] Ce,[57] U,[56] Np,[56] Pu[56]) and $[NEt_4]_3CeCl_6$[57] are shown in gray. A linear fit of the data was shown as the blue trace.[a]

[a]With the exception of $CeCl_6^{2-}$, errors for average bond lengths were taken to be the standard deviation of the three experimental values and reported at the 95% confidence level. For $CeCl_6^{2-}$, the error bar associated with the unique Ce–Cl bond distance was included.

5.5.2 *U $N_{4,5}$ XAS*

Given the rarity and sensitive nature of U^{V} [59–61] the UCl_6^{1-} analyte was characterized U $N_{5,4}$-edge XAS spectroscopy alongside common impurities, specifically $UO_2Cl_4^{2-}$ and UCl_6^{2-}. The U $N_{5,4}$-edge experiment directly probes valence 5*f*-orbital occupancy through dipole allowed excitation of core 4*d*-electrons ($4d^{10}\ldots5f^{n} \rightarrow 4d^{9}\ldots5f^{n+1}$).[27,30,62,63] Hence, changes in uranium oxidation state can manifest in the branching ratio for the U N_5 and N_4 peaks.[64–69] Background subtracted U $N_{5,4}$-edge XAS spectra from $UO_2Cl_4^{2-}$, UCl_6^{1-}, and UCl_6^{2-} have been provided in Figure 5.4. Peak positions and intensities were determined from a Lorentzian deconvolution (See SI). The N_5 and N_4 transitions were split by *ca.* 41 eV into two primary N_5 ($4d_{5/2}$) and N_4 ($4d_{3/2}$) edges, owing to spin-orbit coupling of the core-hole. Each of the N_5 and N_4-edge energies decreased from 738.0 and 779.3 eV ($UO_2Cl_4^{2-}$) to 737.5 and 778.8 eV (UCl_6^{1-}) to 736.9 and 778.1 eV (UCl_6^{2-}). The trend toward decreased transition energy with decreased oxidation state was consistent with earlier uranium $N_{5,4}$-edge XANES studies,[30,62,63,69,70] in addition to the general expectation of decreased transition energies with the increased orbital occupation (lower oxidation state) of the absorbing uranium atom.

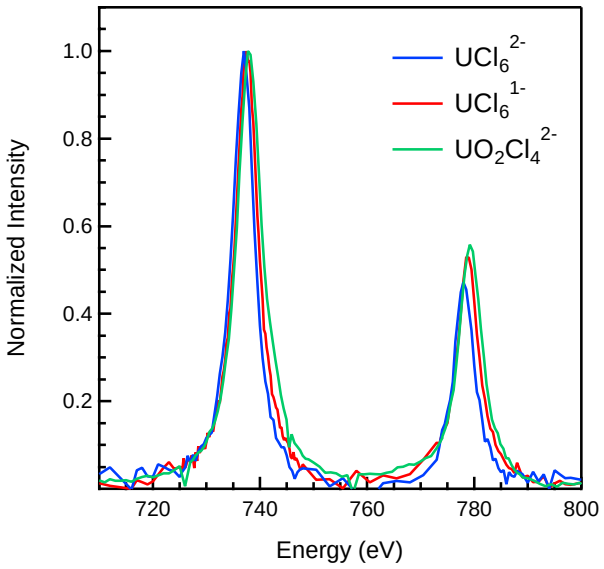

Figure 5.4. Uranium $N_{5,4}$-edge ($4d_{5/2,3/2}$) XAS data obtained in transmission for $(Ph_4P)_2UCl_6$, $(Ph_4P)UCl_6$, and $(Me_4N)_2UO_2Cl_4$. To facilitate comparison, the data have been normalized such that the maximum of each N_5-edge resonance is equal to one.

The branching ratios $A_5/(A_5+A_4)$, where A_5 and A_4 are the areas under the N_5 and N_4 peaks, were 0.64 for $UO_2Cl_4^{2-}$, 0.67 for UCl_6^{1-}, and 0.67 for UCl_6^{2-}. The smaller branching ratio for $UO_2Cl_4^{2-}$ was consistent with previous spectroscopic and theoretical studies that showed a general trend towards smaller branching ratios with smaller formal 5*f*-orbital occupancies. One rationale for understanding this trend is that as the 5*f*-orbital occupancy increases in the initial state, the $5f_{5/2}$ states are filled first and the probability of the $4d_{3/2} \rightarrow 5f_{5/2}$ (N_4) excitation decreases.[64–69] However, the observation of identical $N_{5,4}$-edge branching ratios for UCl_6^{2-} and UCl_6^{1-} contributes to a growing body of literature that suggests that this simple framework may be inadequate in some cases.[66,67] Final state effects, differences in ligand field and spin-orbit coupling, and uncertainty introduced during the measurement and data reduction procedures may also play a role. Hence, additional insights into ligand field strength and effects from covalency were sought using additional X-ray measurements.

5.5.3 *U M_4, M_5 XAS*

As reported previously[71–78] and shown here – uranium $M_{5,4}$-edge XAS has utility in diagnosing uranium oxidation state. From the perspective of the free ion, U $M_{5,4}$-edges originated from dipole-allowed transitions that generate a U 3*d*-core hole and result in U 5*f*-final states.[79–82] In Figure 5.5, the background subtracted and normalized U $M_{5,4}$-edge spectra from UCl_6^{1-} were compared to those of common impurities, specifically $UO_2Cl_4^{2-}$ and UCl_6^{2-}. In each spectrum, there was an immense edge feature superimposed on a step like absorption threshold. As confirmed by calculating the 1st and 2nd derivatives of the data, the spectrum from $UO_2Cl_4^{2-}$ was unique in comparison to the hexachlorides in that it contained numerous post-edge features. This comparison also showed distinct increases (by ~1 eV) for the M_5-edge (3547.0, 3547.9, and 3548.7 eV) and M_4-edge (3721.2, 3722.0, and 3723.2 eV) inflection point energies upon moving from UCl_6^{2-} to UCl_6^{1-} to $UO_2Cl_4^{2-}$, respectively. These values were characterized by the point where the second derivative of the data equaled zero. Similar increases of approximately 1 eV between UCl_6^{2-}, UCl_6^{1-}, and $UO_2Cl_4^{2-}$ were observed for the peak maxima. Other metrics used to evaluate *f*-orbital occupancy included the M_5- and M_4-edge peak intensities (defined as peak areas). For example, increased *f*-orbital occupancy was expected to decreases the intensity of the M-edge features, with the M_4-edge decreasing to a larger extent than that of the M_5-edge (see branching ration in $N_{5,4}$-edge section).[79–82] As such, the normalized intensity at the peak maximum decreased systematically upon moving from the $5f^0$ $Cs_2UO_2Cl_4$ to $5f^1$ $(PPh_4)UCl_6$ to $5f^2$ $(PPh_4)_2(UCl_6)$; e.g. 9.2, 7.5, and 6.0 for the M_5-edge and 9.6, 7.0, and 5.6 at the M_4-edge. To characterize the magnitude of the relative changes of the M_5 vs M_4-edge peak intensities (peak area), peak area branching ratios were determined as described above using a graphical approach based on the integration of the second-derivative of the ratioed data. As expected based on formal 5*f*-electron

count, the results were consistent with the $N_{5,4}$-edge study discussed above. The $M_{5,4}$-edge XAS measurements showed the 0.58 branching ratio from UCl_6^{2-} ($5f^2$) to be similar to the 0.57 value from UCl_6^{1-} ($5f^1$), which in turn was appreciably larger than the 0.48 branching ratio from $UO_2Cl_4^{2-}$ ($5f^0$).

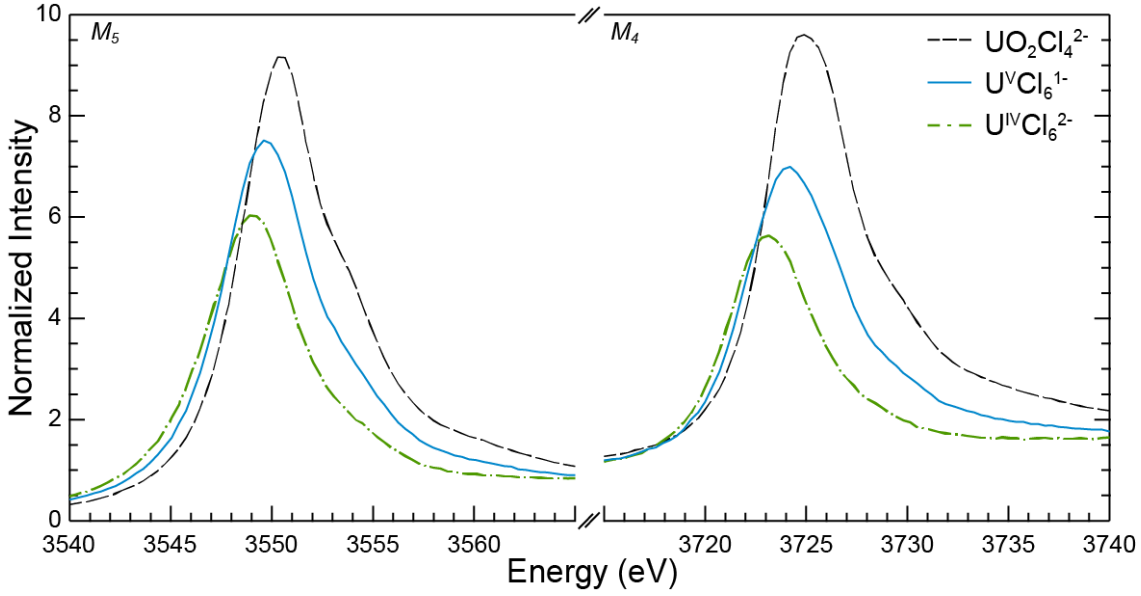

Figure 5.5. U $M_{5,4}$-edge XANES spectra from $(PPh_4)_2UCl_6$ (green double dashed trace), $(PPh_4)UCl_6$ (aqua trace), and $[Me_4N]_2[UO_2Cl_4]$ (blue single dashed trace).

5.5.4 *U Mβ RIXS*

A deeper dive into the X-ray absorption and emission processes that occurred at the U M_4-edge were undertaken using resonant inelastic X-ray scattering (RIXS). Because U M_4-edge RIXS is somewhat of a novelty[23,83,84] a general description is included here. In a RIXS experiment, the X-ray emission spectrum is collected for each excitation energy with high energy resolution. As shown in Figure 5.6, the analyte is excited at the M_4-edge. The resulting 3*d*-core hole is subsequently and rapidly (~ 10^{-16} s) filled by core-to-core electronic relaxations ($4f^{5/2} \rightarrow 3d^{3/2}$; U Mβ emission), which shifts the 3*d*-core hole to the 4*f*-manifold. We expect the anticipated upgrades

at synchrotron facilities, innovation in end-station technologies, and advancement of computational methods for interpreting core-to-core electronic transitions will see continued use of U Mβ-RIXS as a powerful technique for characterizing U–ligand electronic structure.

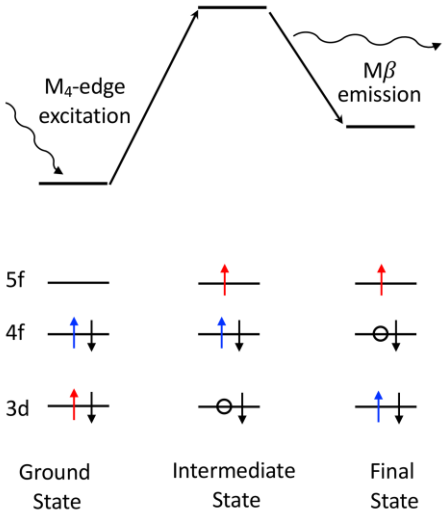

Figure 5.6. A diagram showing (Top) the overall energies for electronic states and (bottom) electronic configurations associated with the excitation and emission processes in U Mβ RIXS.

For $U^{VI}O_2Cl_4^{2-}$, $U^{V}Cl_6^{1-}$, and $U^{IV}Cl_6^{2-}$, Mβ-RIXS were measured with high precision at SSRL's beamline 4-3 using the LANL/UW tender X-ray emission spectrometer.[35] Our approach to Mβ-RIXS offered advantages in terms of characterizing certain analytes, in that the excitation source was unfocused. This feature minimized sample decomposition that can result from radiation damage and expanded compatibility of the RIXS measurement to include sensitive molecular species. The small size of the sample chamber (~10 cm on a side) allowed the spectrometer to be installed at beamline 4-3, despite the crowded nature of this experimental end-station, where the beam comes within ~7 cm from the hutch wall. Furthermore, the portability of the spectrometer greatly simplified concerns involved in transport and installation of the instrument.

The U Mβ-RIXS results from $UO_2Cl_4^{2-}$, UCl_6^{1-}, and UCl_6^{2-} were best captured by the contour plots in Figure 5.7 by plotting the X-ray emission count rate against the emission (*y*-axis)

and excitation energies (*x*-axis). In this scheme each vertical slice of this plot (holding the excitation energy constant) represented a unique X-ray emission spectrum. Similarly, each horizontal slice (holding the emission energy constant) provided a unique absorption spectrum. The U Mβ-RIXS data in Figure 5.7 provided an opportunity to characterize $UO_2Cl_4^{2-}$, UCl_6^{1-}, and UCl_6^{2-} on multiple levels. In terms 5*f*-orbital occupancy, U M_4-edge RIXS seemed uniquely useful for determining uranium oxidation states. For example, plotting the emission maximum versus the absorption maximum in Figure 5.8 showed the expected trend of increasing peak position (in excitation energy) with increased oxidation state. However, the variation of the peak position was interestingly non-monotonic with oxidation state. While the generality of using U Mβ-RIXS to characterize uranium oxidation states has yet to be determined, the 3-dimensional approach presented herein has potential to provide fidelity over more conventional approaches for characterizing 5*f*-orbital occupation, namely using 2-dimentional XAS or XES spectroscopy.

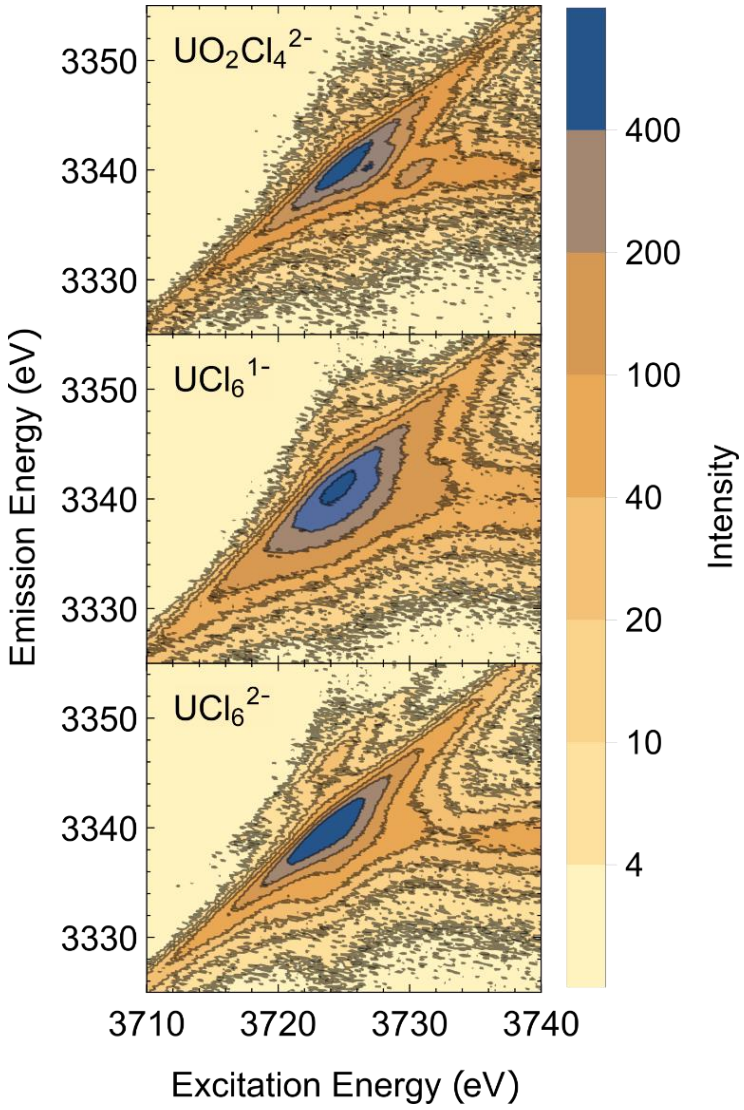

Figure 5.7. U Mβ RIXS spectra from $(PPh_4)_2UCl_6$ (bottom), $(PPh_4)UCl_6$ (middle), and $Cs_2[UO_2Cl_4]$ (top). Here, intensity is plotted on a log scale as a function of absorption energy and emission energy.

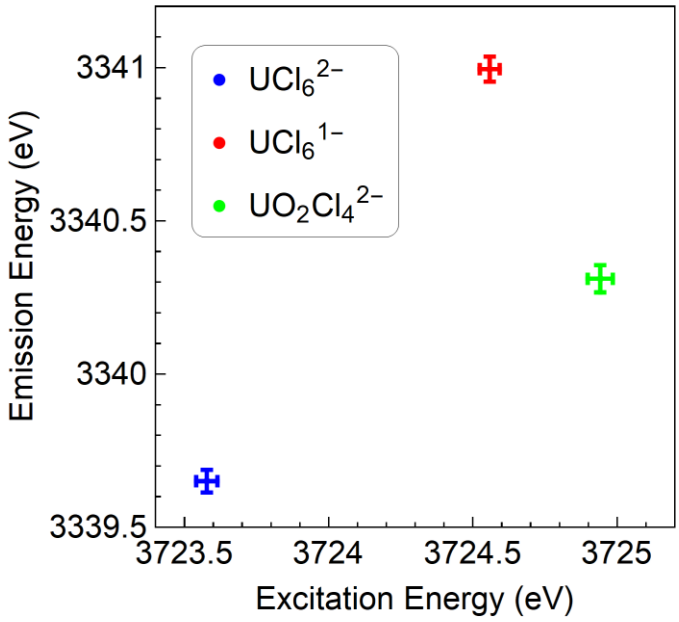

Figure 5.8. Excitation and emission energies of maximum intensity for UCl_6^{2-}, UCl_6^{1-}, and $UO_2Cl_4^{2-}$. Uncertainties shown are 95% confidence level of peak position.

The contour plots were additionally valuable in probing uranium electronic structure and bonding. These data provided clarity for identifying spectral features associated with bound state transitions that would typically go unresolved when using conventional 2-dimentional XAS or XES spectroscopy. For example, electronic transitions with overlapping relaxation (or emission) energies can be resolved so long as their excitation energies are unique. Alternatively, transitions with overlapping excitation energies (or absorptions) can be resolved so long as their emission energies are unique. The $UO_2Cl_4^{2-}$, UCl_6^{1-}, and UCl_6^{2-} data in Figure 5.7 provided a textbook example of using RIXS to reveal obscured X-ray absorption features. For example, RIXS spectra from all three of these uranium compounds were dominated by an emission maximum near 3340 eV and an absorption maximum near 3724 eV, but additional features were present at higher excitation energy. Some of these post-edge absorption features were apparent in the U M_4-edge XAS data described above in Figure 5.5, albeit poorly resolved. Other post-edge absorption

features were not obvious using conventional U M_4-edge XAS or non-resonant U Mβ XES spectroscopy.

To most effectively describe these post-edge XAS features, U M_4-edge absorption spectra from $UO_2Cl_4^{2-}$, UCl_6^{1-}, and UCl_6^{2-} were extracted at constant emission energies (3340.3 eV, 3341 eV and 3339.7 eV, respectively; Figure 5.9). This contour slice is commonly referred to as a high energy-resolution fluorescence detection (HERFD) spectrum. These HERFD data were essentially equivalent to the U M_4-edge XAS data shown above in Figure 5.5. However, unlike the typical U M_4-edge XAS measurements provided above, the HERFD detection method employed only a narrow band of emission energies. As such the dominant factor in the energy broadening – the core-hole lifetime of the $3d_{3/2}$ electron (approximately 3.6 eV) – was (essentially) eliminated and the absorption energy resolution greatly improved. These spectra were modeled with three functions (pseudo-Voigts with 1:1 Lorentzian to Gaussian weight) superimposed on an arctangent step function (gray), Table 5.1. For $UO_2Cl_6^{2-}$, our fit showed an intense feature at low energy (3724.4 eV), an intermediate feature at moderate energy (3726.5 eV), and a weak feature at high energy (3730.4 eV). This spectrum agreed well with that reported previously by VITOVA and COWORKERS[23] in their U M_4-edge HERFD analysis of $UO_2Cl_4^{2-}$. For instance, the relative peak intensities were similar and the absorption energies differed by a constant 2.3 eV, which was associated with variation in the monochromator energy calibration (our data calibrated to KCl at 3808.04 eV and VITOVA'S data calibrated to Ti foil at 4966 eV).

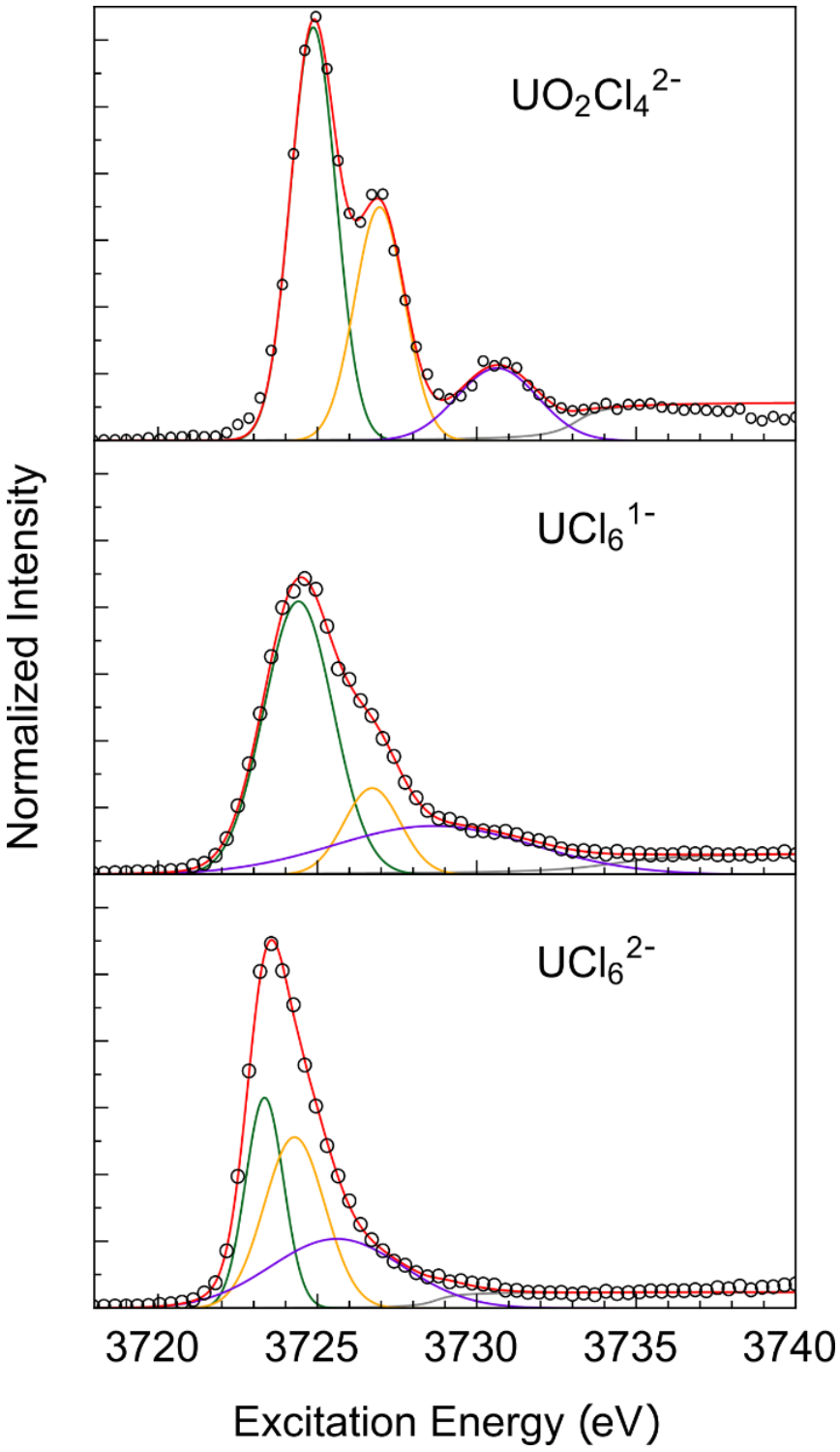

Figure 5.9. U M_4 HERFD spectra of $Cs_2UO_2Cl_4$, $(PPh_4)_2UCl_6$, and $(PPh_4)_2UCl_6$ (○). The least squares fit (red), and individual fit functions (edge-step: gray; peaks: green, orange, and purple) are also shown.

Table 5.1. Fit parameters for U M_4 HERFD fits of UCl_6^{2-}, UCl_6^{1-}, and $UO_2Cl_4^{2-}$.

Parameter	**$(PPh_4)_2UCl_6$**	**$(PPh_4)UCl_6$**	**$Cs_2UO_2Cl_4$**
Edge Position	3728.19	3734.12	3732.07
Edge Amplitude	1	1	1
Edge Width	0.50	1.04	1.25
Gaussian 1 Position	3723.35	3724.38	3724.85
Gaussian 1 Amplitude	7.62	8.20	11.71
Gaussian 1 FWHM	1.40	2.57	1.64
Pseudo-Voigt 2 Position	3724.4	3726.69	3726.91
Pseudo-Voigt 2 Amplitude	5.24	3.45	7.24
Pseudo-Voigt 2 FWHM	1.97	2.43	1.88
Gaussian 3 Position	3725.66	3730.01	3730.70
Gaussian 3 Amplitude	1.82	1.09	1.90
Gaussian 3 FWHM	4.06	5.79	2.06

Reproducing VITOVA's $UO_2Cl_4^{2-}$ U M_4-edge HERFD spectrum – which was recorded using a conventional (point-to-point) X-ray emission spectrometer located at the Institut Für Enstsorgun (INE) beamline at the Angstromquelle Karlsruhe (ANKA) synchrotron – using our LANL/UW tender X-ray spectrometer on an unfocused beam line at SSRL provided credibility to our instrumentation and spectroscopic method. It also provided confidence in subsequent U M_4-edge HERFD data obtained from UCl_6^{1-} and UCl_6^{2-}. The UCl_6^{1-} spectrum was similar to $UO_2Cl_4^{2-}$ in that it also contained three peaks. It differed in that the absorption peaks were lower and much closer in energy. There was a large peak at low energy (3724.4 eV), a moderate peak at intermediate energy (3726.7 eV), and a weak shoulder at high energy (3730.0 eV). Lowering the oxidation state from +5 (in UCl_6^{1-}) to +4 (in UCl_6^{2-}) again moved these peaks lower in energy and

closer together. This agrees with the naïve expectation that increased covalency in the higher oxidation state should lead to a more pronounced ligand field splitting of the 5*f* antibonding orbitals.[85]

Taking vertical cuts from the U Mβ-RIXS contour plots shown in Figure 5.7 generated U Mβ resonant-XES spectra. Because these spectra were obtained at constant excitation energies (3723.6 eV, 3724.6 eV and 3724.9 eV for UCl_6^{2-}, UCl_6^{1-}, and $UO_2Cl_4^{2-}$, respectively; Figure 5.10), they enable spectral features to be identified that would otherwise go unnoticed by U Mβ non-resonant XES. From this perspective, we make the crude analogy that U M_4-edge HERFD is to conventional U M_4-edge XAS as U Mβ resonant-XES is to Mβ non-resonant-XES. Both the resonant and non-resonant emission spectra were dominated by an intense $4f \rightarrow 3d$ transition. The emission peaks in the non-resonant spectra were symmetric. In contrast, each emission line in the resonant spectra were asymmetric and broadened on the low energy side. All three resonant spectra contained a low energy pre-tail that started near 3332 eV and increased in intensity to near 3336 eV until being consumed by the main emission peak. After the peak maximum the emission intensity rapidly dropped. This asymmetric line shape was characteristic of RIXS emission and is typically attributed to energy conservation.[86]

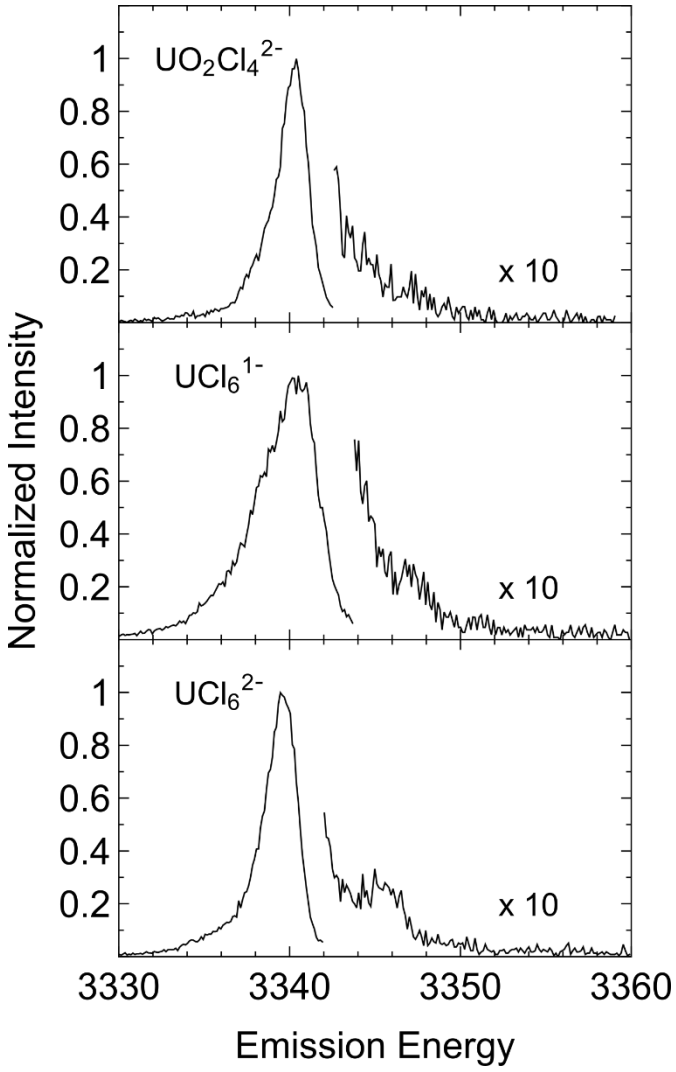

Figure 5.10. Resonant x-ray emission of UCl_6^{2-}, UCl_6^{1-}, and $UO_2Cl_4^{2-}$. The high-energy side is expanded 10 times to highlight the high-energy M beta satellite at 3346 – 3348 eV.

There were a few unexpected observations associated with the U Mβ resonant-XES data. One unusual aspect of the resonant-XES was associated with the peak widths. At the onset we expected the FWHM to be similar for all three compounds. However, for UCl_6^{1-} the width was larger. At this time, it is difficult to justify this observation, especially because the magnitude for peak broadening from UCl_6^{1-} is difficult to rationalize based solely on 3*d*- vs 4*f*-linewidths. Another peculiarity with the resonant XES data was the high-energy emissions near 3346 eV.

These features were emphasized in the expanded section of Figure 5.10. To our knowledge, these measurements represented the first observations of high-energy satellites in Mβ XES, likely owing to the infrequency that these emission lines have been studied. The satellite intensity increased (normalized to the main Mβ line) with decreased uranium oxidation state. The satellite was subtle (bordering on non-existent) for $UO_2Cl_4^{2-}$, had intermediate intensity for UCl_6^{1-}, and was clearly visible for UCl_6^{2-}. At this time, we do not understand the origin of these transitions and limit our discussion as empirical observations. Only by conducting Mβ resonant XES experimentation on a larger suite of uranium compounds and expanding the computational efforts focused on explaining Mβ resonant XES spectra will the electronic transitions responsible for these satellites be revealed.

5.5.5 *Cl K-edge XAS*

The background subtracted and normalized[87] Cl K-edge XAS spectra obtained from UCl_6^{x-} was shown in Figure 5.11. This spectrum was reproduced during multiple scheduling periods at the Stanford Synchrotron Radiation Lightsource (SSRL) on beamline 4-3 as well as at the Institut für Nukleare Entsorgung (INE) beamline at the Angströmquelle Karlsruhe (ANKA). The energy was calibrated to the peak maximum of the first feature in the Cl K-edge XAS spectrum from D_{2d}-Cs_2CuCl_4 at 2820.20 eV.[18] The spectrum contained a strong absorption edge feature near 2827 eV that was preceded by intense pre-edge features between 2820 to 2826 eV. Observation of these intense pre-edge features was exciting, as their oscillator strength is directly related to the orbital mixing coefficient associated with the U–Cl bond. Hence, the presence of these appreciable features suggested significant covalent U^V–Cl bonding. To quantify the amount of orbital mixing within the U–Cl bonds in UCl_6^{1-} the Cl K-edge XAS spectrum was deconvoluted. As described in the experimental section, these curve-fits were obtained with a linear least-squares algorithm using

a minimum number of pseudo-Voigt functions. High quality models of the data (Table 5.2) were only obtained with a minimum of three pre-edge peaks, as evidenced from good correlation coefficients and symmetric residual peaks that were similar in shape to the corresponding pseudo-Voigt functions. There was a low energy feature at 2824.1(1) eV, an intermediate energy peak at 2821.5(1) eV, and a high energy feature at 2820.6(1) eV. We have high confidence in the energy for these peak energies, and have likely overestimated the uncertainty at 0.1 eV. All three peaks displayed appreciable intensity (peak area), such that the intensity for the high energy feature at 0.39(7) was bracketed on the small side by low energy feature at 0.11(2) and on the large side by the intermediate energy feature at 0.47(4). Using the D_{2d}-Cs_2CuCl_4 Cl K-edge intensity standard, which has an intensity of 0.53 corresponding to 7.5% Cl 3*p*-character per Cu–Cl bond, showed the high, intermediate, and low energy peak intensities corresponded to 5.5, 6.7, and 1.6 % Cl 3*p*-character per bond. Note, these intensities were comparable to those reported for many 3*d*-transition metal tetrachlorides. Besides, a comparison of Cl K-edge of UCl_6^{1-} with our previous report of UCl_6^{2-} is shown in Figure 5.12. It is noted that from UCl_6^{2-} to UCl_6^{1-}, pre-edge feature at low energy (<2823 eV) decrease in energy while that at 2824 eV remain unchanged.

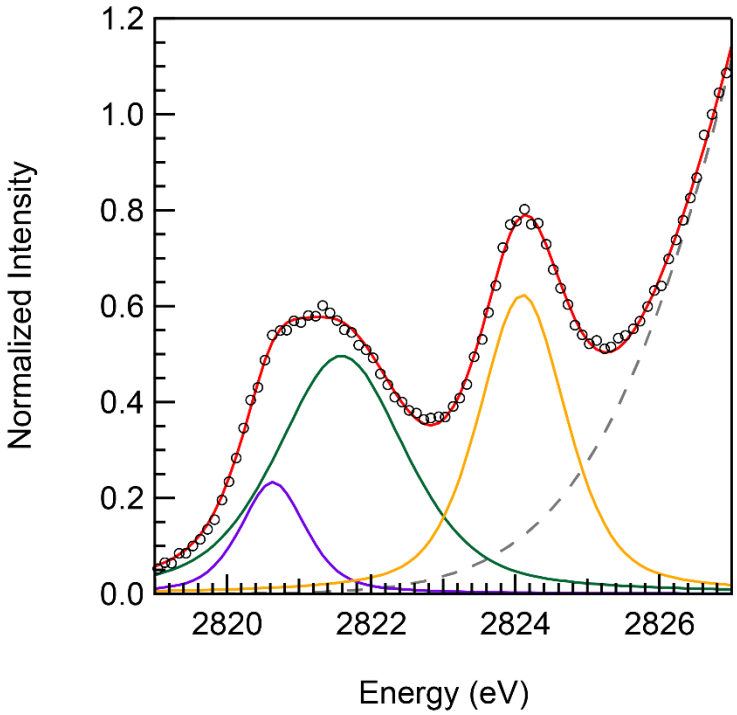

Figure 5.11. Linear least squares fits (red traces) of the Cl K-edge spectra (○) from $(PPh_4)UCl_6$. The pseudo-Voigt functions used to model the pre-edge features were shown as blue, green, and yellow traces and the function used to model the edge was represented as a gray dashed trace.

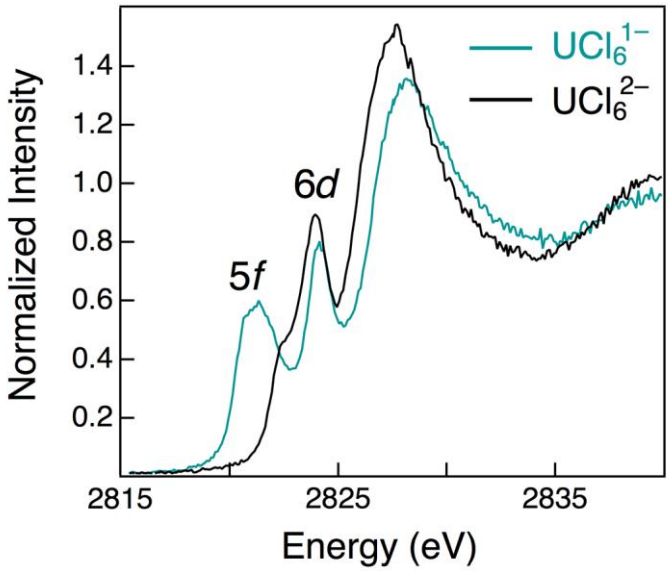

Figure 5.12. The background subtracted and normalized Cl K-edge spectra from $(PPh_4)UCl_6$ and $(PPh_4)_2UCl_6$ collected at ambient temperature. The data for $(PPh_4)_2UCl_6$ were taken from reference[28,55].

Table 5.2. A comparison of the experimental and calculated Cl K-edge XAS pre-edge peak energies (eV), intensities, and % Cl 3p character for $(PPh_4)UCl_6$ and $(PPh_4)_2UCl_6$.[a]

		A peak			**B peak**			**C peak**		
Compound		Energy[b]	Int[c]	% Cl 3*p*	Energy[b]	Int[c]	% Cl 3*p*	Energy[b]	Int[c]	% Cl 3*p*
Cs_2CuCl_4	Exp	2820.2	0.53(2)	7.53	–	–	–	–	–	–
$(PPh_4)UCl_6$	Exp	2824.1	0.39(7)	5.5	2821.5(1)	0.47(4)	6.7	2820.6	0.11(2)	1.6
	Calc	2824.1	0.64		2822.0	0.40		2721.1	0.38	
$(PPh_4)_2UCl_6$	Exp	2823.9	1.09(5)	15.5	2822.4	0.40(2)	5.6	-	-	-
	Calc	2823.9	0.48		2822.7	0.35				

[a]% Cl 3p was calculated based on D_{2d}-Cs_2CuCl_4 with a pre-edge intensity of 0.53 that corresponds to 7.5% Cl 3*p* character per Cu-Cl bond.[18]

[b]Listed errors correspond to uncertainties due to the fitting algorithm. Errors less than 0.1 eV are considered to be within experimental error, and were not listed.

[c]Experimental Pre-edge intensities are the full-width at half-maximum (FWHM) times the amplitude.[29] Calculated pre-edge intensities are the oscillator strength times 100

5.5.6 *Ground-State Electronic Structure*

Ground-state scalar relativistic and spin-orbit Density Functional Theory (DFT) calculations were used to guide the interpretation of the spectra of UCl_6^{1-}, UCl_6^{2-}, and $UO_2Cl_4^{2-}$. The calculations on UCl_6^{1-} and UCl_6^{2-} were interpreted in accordance with well-established group theory descriptions of octahedral complexes. For example, the molecular orbital (MO) energy levels diagram of UCl_6^{1-} is provided in Figure 5.13 with relevant MOs visualized in Figure 5.15. In Figure 5.13, the U and Cl atomic orbital energy levels are shown on the left side. An octahedral arrangement of six Cl ligands around a U center generates 6 symmetry-adapted linear combinations (SALCs) of Cl 3p atomic orbitals that have σ symmetry ($a_{1g} + e_g + t_{1u}$) and 12

(SALCs) of π symmetry ($t_{1g} + t_{2g} + t_{1u} + t_{2u}$) with respect to the U-Cl axes, respectively. The U 6d atomic orbitals (AOs) split into e_g and t_{2g} symmetries and interact with symmetry-matching SALCs of Cl 3p obtials forming U–Cl σ- and π-bonds, respectively, at a high energy level. Accordingly, the six 5f AOs of t_{1u} and t_{2u} symmetries were allowed by symmetry to form low-energy U-Cl σ+π and π-bonds, respectively. The remaining U 5f a_{2u} orbital and Cl t_{1g} orbitals are of non-bonding character. Overall the bonding pictures generated from the DFT calculations were consistent with previous theoretical studies conducted on O_h-MCl_6 systems (Figure 5.15).[28,42,55,57,88] It is the antibonding components of these U−Cl interactions shown in Figure 12 that are directly probed during the U $N_{5,4}$- and $M_{5,4}$-edge XAS and Cl K-edge XAS experiment of UCl_6^{1-} and UCl_6^{2-}. Incorporating spin−orbit coupling into the calculations decreased orbital energy degeneracy, increased the energy range spanned by the 5f- and 6d-orbitals, and hybridized the valence orbitals, which is in agreement with previous theoretical reports on O_h-$AnCl_6$ (An=Th, U, Am) systems.[28,42,89] The electronic structure picture in UCl_6^{2-} is similar to that in UCl_6^{2-} except that moving from $5f^2$-UCl_6^{2-} to $5f^1$-UCl_6^{1-} had a marked influence on the relative energy levels of U 5f and Cl 3p orbitals shown in Figure 5.14. The U 5f orbitals are closer to Cl 3p orbitals in energy in UCl_6^{1-} than in UCl_6^{2-}.

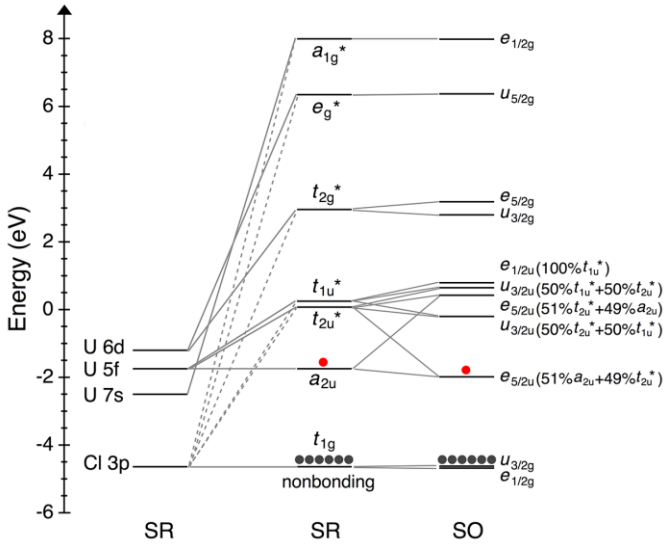

Figure 5.13. Qualitative energy level diagram from DFT ground-state calculations for UCl_6^{1-}. Left: atomic orbitals from scalar relativistic (SR) calculations. Center: orbitals for UCl_6^{1-} from SR calculations. Right: orbitals for UCl_6^{1-} from spin-orbit (SO) calculations. The electrons occupied on 5f character a_{2u} and Cl-3p character t_{1g} non-bonding orbitals are indicated by red and blue dots, respectively.

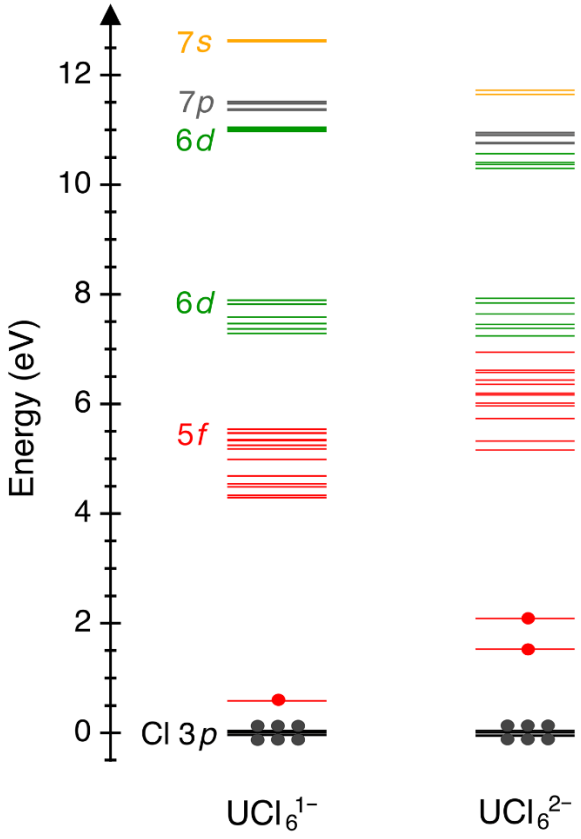

Figure 5.14. Energy level diagram from DFT ground-state calculations that incorporate spin-orbit coupling showing the change from UCl_6^{2-} to UCl_6^{1-}. The geometries of UCl_6^{1-} and UCl_6^{2-} are from experimental crystal structures of $(PPh_4)UCl_6$ and $(PPh_4)_2UCl_6$, respectively. A constant energy shift of xx eV was applied to UCl_6^{1-} to align the energy levels of the highest occupied Cl 3p orbitals of non-bonding character in UCl_6^{1-} and UCl_6^{2-} to aid visual comparison.

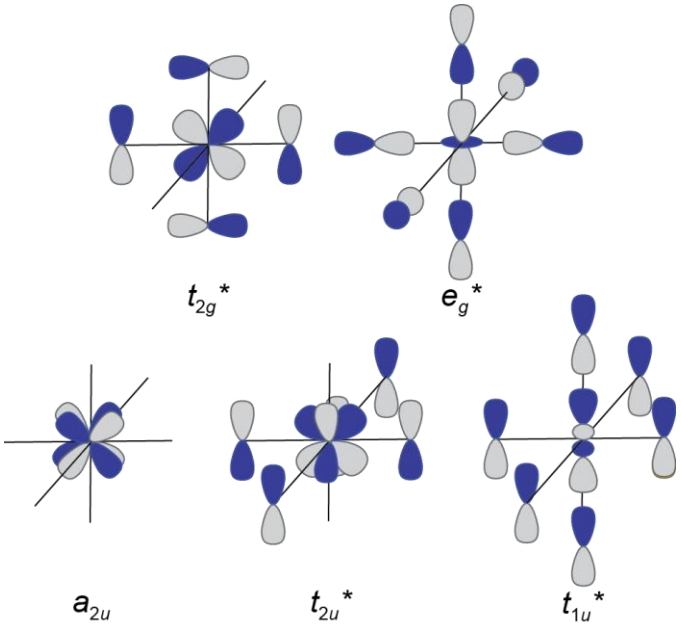

Figure 5.15. A cartoon showing the σ- and π-antibonding combinations for ligand p-orbitals interacting with f-orbitals (bottom) and d-orbitals (top).

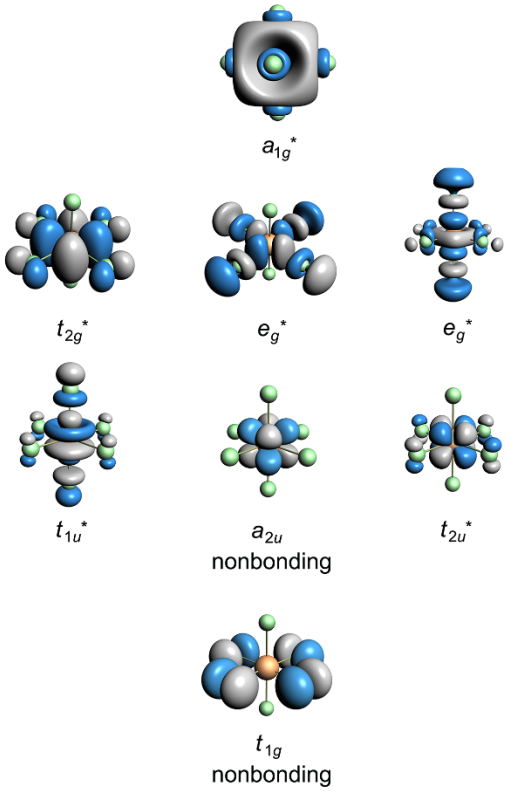

Figure 5.16. (SI) A diagram showing the σ- and π-antibonding combinations for ligand p-orbitals interacting with f-orbitals (bottom) and d-orbitals (top).

The ground-state electronic structure calculations on UO_2Cl_4 were performed at D_{4h}-symmetry geometry with experimental averaged U-O and U-Cl bond distances of 1.776 and 2.670 Å, respectively, in $Cs_2UO_2Cl_4$ compound (Table 5.3). As a typical uranyl compound, $UO_2Cl_4^{2-}$ maintain the electronic structure and chemical bonding of the bare UO_2^{2+} ion, and Cl^- coordination can be seen as a small perturbation of ligand field to the UO_2^{2+} ion.[90,91] Therefore, calculations on D_{4h}-$UO_2Cl_4^{2-}$ were interpreted mainly based on the bonding picture of the $D_{\infty h}$-UO_2^{2+} ion. The schematic energy level diagram showing the correlation between UO_2^{2+} and $UO_2Cl_4^{2-}$ is presented in Figure 5.17 with the 5f-character unoccupied MOs of $UO_2Cl_4^{2-}$ shown in Figure 5.18. Under $D_{\infty h}$ symmetry, the U-5f AOs split into σ_u and pairs of π_u, δ_u, and ϕ_u, and the U-6d AOs into σ_u and pairs of π_u and δ_g. The O 2p lone-pair shells give rise to group orbitals of dative σ_u, σ_g and

pairs of π_u and π_g bonding type, which are stabilized by the U 5fσ_u, π_u and U 6dσ_g, π_g AOs, corresponding to U≡O triple bonding. On the other hand, the U 5f and 6d AOs of σ and π-type mix into MOs and generate antibonding orbitals σ_u*, π_u*, σ_g* and π_g*. The localized 5fδ_u, ϕ_u- and 6dδ_g-type MOs are of nonbonding character. The energy levels of these U 6d-character MOs in UO_2^{2+}, i.e., δ_g, σ_g* and π_g*, are not shown in Figure 5.17, because only U 5f-related MOs are involved in the U $N_{5,4}$- and $M_{5,4}$-edge XAS experiment. From $D_{\infty h}$-UO_2^{2+} to D_{4h}-$UO_2Cl_4^{2-}$, symmetry lowering transforms the σ_u/σ_g-, π_u/π_g-, δ_u- and ϕ_u-type MOs as a_{2u}/a_{1g}, e_u/e_g, $b_{1u,2u}$ and e_u ones, and four Cl^- coordinations slightly affect the relative energy levels. Reduced symmetry allows a mixing of these uranyl orbitals with Cl 3p orbitals to a certain degree. However, the uranyl 5f-orbital character remain unchanged upon Cl^- coordination (Figre S2). Therefore, the MO notations of UO_2^{2+} are used in the presentaion of $UO_2Cl_4^{2-}$ calculation results. Besides, similar to the case in UCl_6^{1-} system, spin-orbit coupling results in 5f orbital energy degeneracy decrease and energy range increase in $UO_2Cl_4^{2-}$.

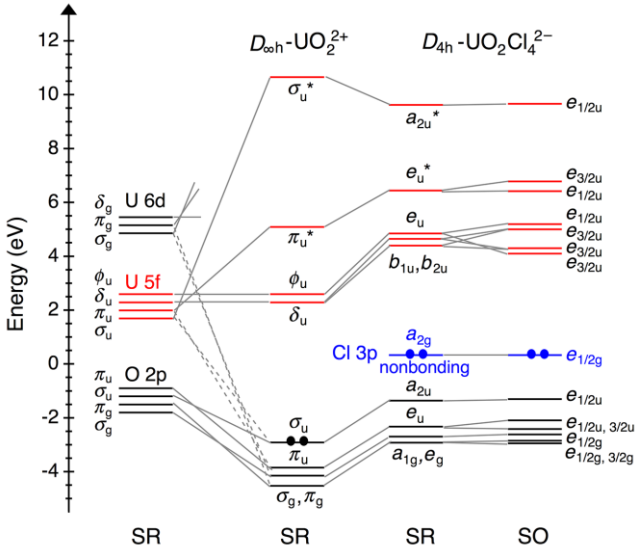

Figure 5.17. Schematic energy level diagram showing the correlation between UO_2^{2+} and $UO_2Cl_4^{2-}$ from DFT ground-state calculations. From Left to right: atomic orbitals from scalar relativisitic (SR) calculations, orbitals for UO_2^{2+} from SR calculations, orbitals for $UO_2Cl_4^{2-}$ from SR calculations, and orbitals for $UO_2Cl_4^{2-}$ from spin-orbit (SO) calculations. A constant energy shift of 20.3 eV was applied for UO_2^{2+} orbitals to increase visual convenience in correlation analysis. The electrons occupied on HOMO in UO_2^{2+} and $UO_2Cl_4^{2-}$ are indicated by black and blue dots, respectively.

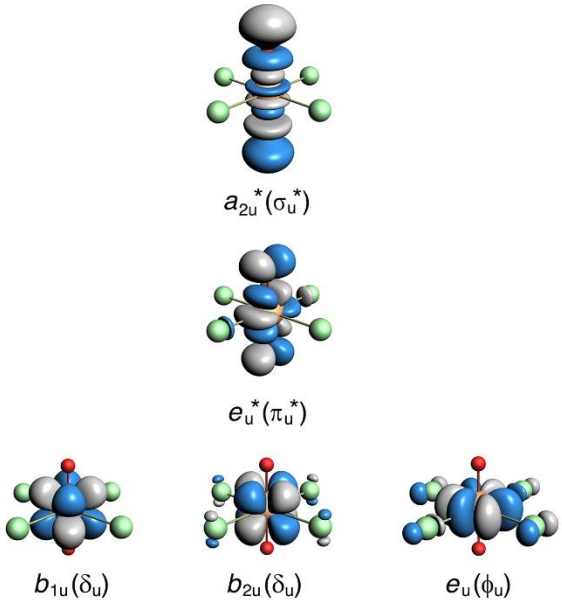

Figure 5.18. Unoccupied 5f character orbitals of D_{4h}-$UO_2Cl_4^{2-}$ from scalar relativistic DFT calculations, and the orbital notations of the corresponding ones of $D_{\infty h}$-UO_2^{2+} are in the parentheses for a convenient reference.

5.5.7 *Spectral Interpretations*

The ground-state DFT transition-dipole calculations with inclusion of spin-orbit coupling effects was carried out on $UO_2Cl_4^{2-}$, UCl_6^{-} and UCl_6^{2-} anions at their respective experimental geometries (Table 5.3) to model their U $N_{5,4}$- and $M_{5,4}$-edge XAS, U M_4-edge HERFD and Cl K-edge XAS spectra as well as U Mβ XES spectra. For a core electron excitation, the oscillator strength was calculated using the transition-dipole approximation between the occupied MO and the virtual MOs involved in the excitation, and the excitation energies were obtained from the occupied and unoccupied orbital energies. As both U Mβ resonant and non-resonant emission spectra were dominated by an intense 4f → 3d transition, we only calculated the non-resonant emission. The emission oscillator strength was calculated in the same way as the absorption one and the emission energies were the energy difference between the occupied U 4f and 3d orbitals. This transition-dipole SO-DFT method has been demonstrated to give good agreement with XAS and XES spectra from transition metal,[53,92–94] lanthanide[43] and actinide[28,42] containing analytes. See more computational details in the Experimental Section.

Table 5.3. Geometry symmetry of $UO_2Cl_4^{2-}$, UCl_6^{1-} and UCl_6^{2-} unit and U-O and U-Cl bond distances (R_{U-O} and R_{U-Cl}) in the experimental crystal structures of $Cs_2UO_2Cl_4$, $(PPh_4)UCl_6$ and $(PPh_4)_2UCl_6$ compounds.

Compound	Symmetry of anion unit	R_{U-O} (Å)	R_{An-Cl} (Å)	Averaged R_{An-Cl}(Å)
$Cs_2UO_2Cl_4$	C_{2h}	1.7763	2.6670, 2.6699	2.670
$(PPh_4)UCl_6$	C_i		2.5048(5), 2.5141(4), 2.5146(4)	2.511
$(PPh_4)_2UCl_6$	C_i		2.6326(6), 2.6087(5), 2.6224(6)	2.621

The simulated U $N_{5,4}$- and $M_{5,4}$-edge XAS spectra of $UO_2Cl_4^{2-}$, UCl_6^{-} and UCl_6^{2-} anions alongside the experimental data, which respectively correspond to 4d $\rightarrow$ 5f and 3d $\rightarrow$ 5f transitions, were shown in Figure 5.19 and Figure 5.20, respectively. The overall agreement with experiment is satisfactory. Besides the dominant contributions from 4d/3d $\rightarrow$ 5f transitions, calculations also reveal a very small contribution from 4d/3d $\rightarrow$ 7p transitions to the spectra. The calculated energy splitting between N_5 and N_4 transitions and that between M_5 and M_4 transitions are 40.9 and 176.5 eV, respectively, in good agreement with the respective experimental results of 41.3 and 174.3 eV, which reflects the spin-orbit coupling splitting of U 4d and 3d core holes. Comparing the calculated $N_{5,4}$- and $M_{5,4}$-edge energies among $UO_2Cl_4^{2-}$, UCl_6^{-} and UCl_6^{2-} anions shows a decrease of 0.2–0.3 eV from U(VI) to U(V) and a further decrease of 0.9–1.1 eV to U(IV), consistent with the observed experimental trend. This good correlation between transition energy and oxidation state provided the theoretical basis for identifying uranium oxidation state using U $N_{5,4}$- and $M_{5,4}$-edge XAS. The calculated branching ratio $A_5/(A_5+A_4)$ for both $N_{5,4}$- and $M_{5,4}$-edge XAS shows an increase trend from $UO_2Cl_4^{2-}$ to UCl_6^{-} to UCl_6^{2-}, i.e., 0.61, 0.68 and 0.72 for the former one and 0.57, 0.64, 0.68 for the latter one, which agrees well with the increased f-orbital occupancy and experimental trend.

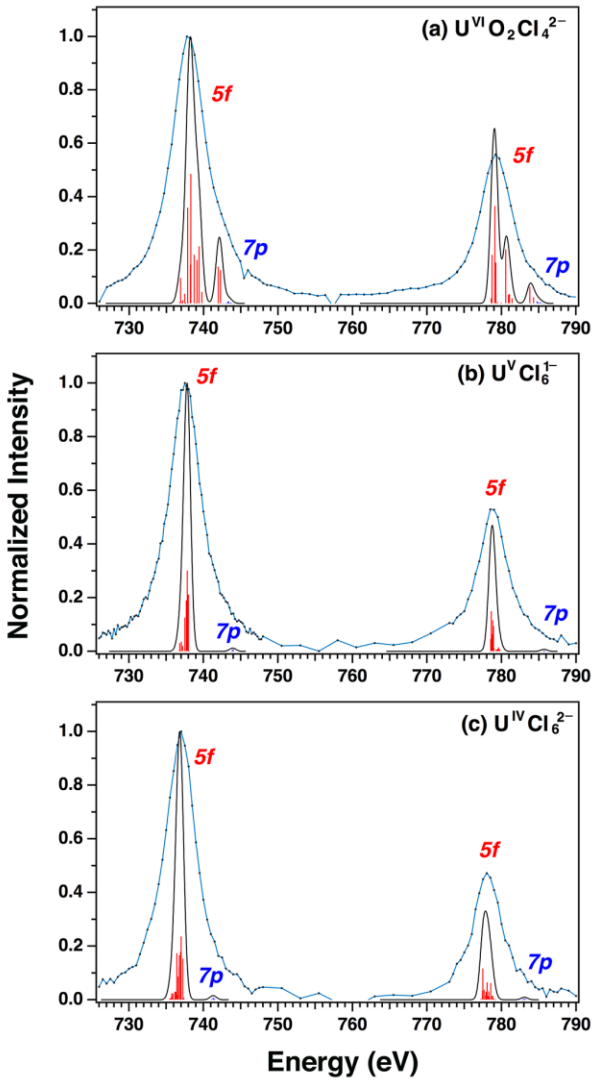

Figure 5.19. Comparison between experimental $N_{5,4}$-edge XAS spectra (•) and results from the spin−orbit coupled DFT transition dipole moment calculations (black trace) for $UO_2Cl_4^{2-}$ and UCl_6^{1-} and UCl_6^{2-} anions. The red and blue bars represent the energy and oscillator strength for the calculated transitions involving 5f- and 7p-final states, respectively.

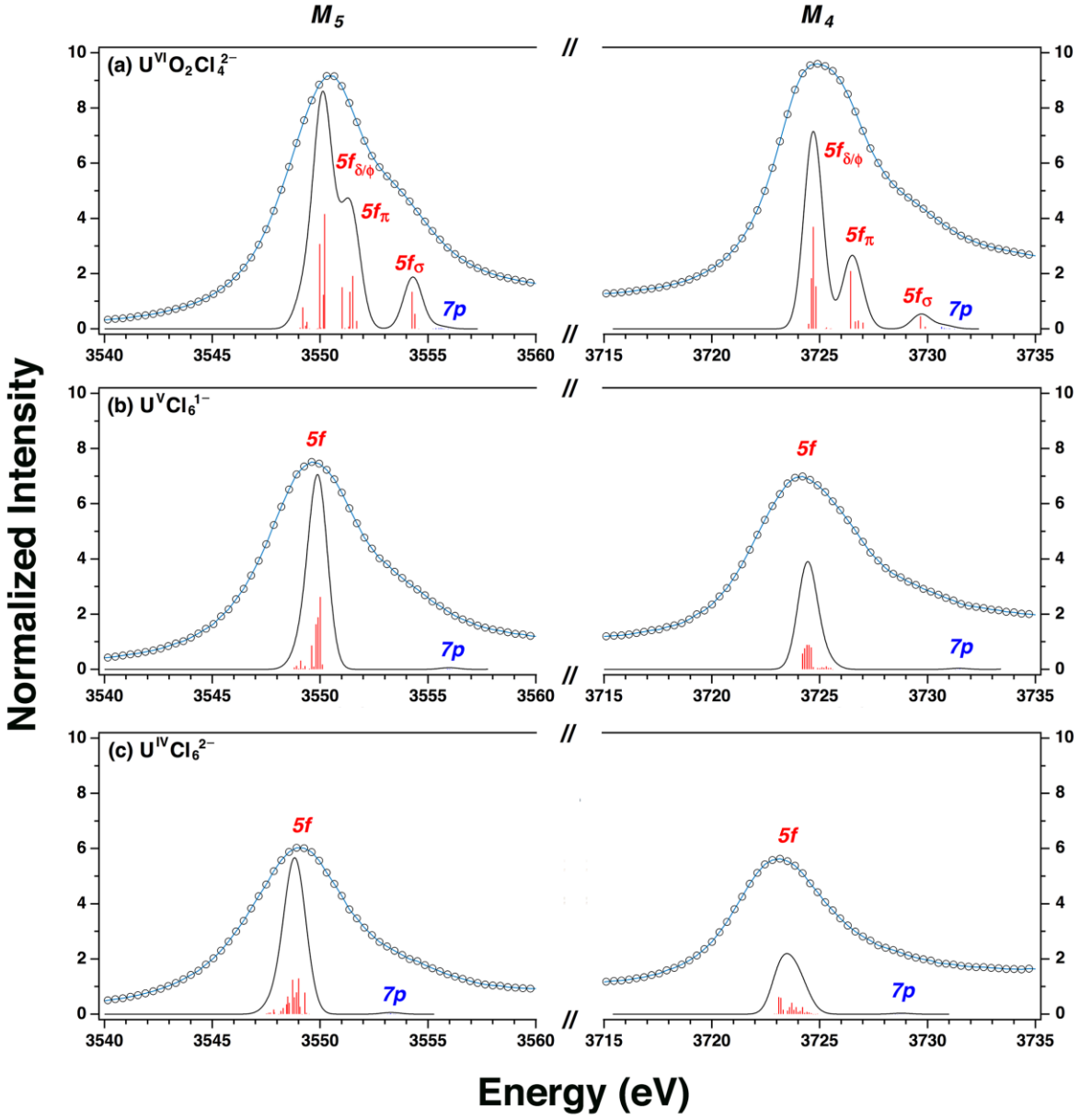

Figure 5.20. Comparison between experimental $M_{5,4}$-edge XAS spectra (•) and results from the spin−orbit coupled DFT transition dipole moment calculations (black trace) for $UO_2Cl_4^{2-}$ and UCl_6^{1-} and UCl_6^{2-} anions. The red and blue bars represent the energy and oscillator strength for the calculated transitions involving 5f- and 7p-final states, respectively.

The simulated M_4-edge HERFD spectra of $UO_2Cl_4^{2-}$, UCl_6^{-} and UCl_6^{2-} anions as well as the experimental data were shown in Figure 5.21. The calculated HERFD data were essentially

equivalent to the calculated U M_4-edge XAS data shown above in Figure 5.20 but with a smaller peak width. Calculations show that the U M_4-edge HERFD spectra are dominated by 3d $\rightarrow$ 5f transitions with a very small contribution from 3d $\rightarrow$ 7p transitions. As shown in Figure 17(a), simulated $UO_2Cl_4^{2-}$ spectrum well reproduces experimentally observed three absorption features and was consistent with the MO energy level analysis in Figure 5.14. These features are attributed to the transitions to the unoccupied 5fδ/ϕ, 5fπ and 5fσ orbitals (i.e., δ_u/ϕ_u, π_u* and σ_u* in the scalar calculations in Figure 5.14), respectively. The calculated absorption energies are 3724.3, 3726.1 and 3729.3 eV, respectively, in good agreement with experimental data with averaged difference of 0.47 eV. As for UCl_6^- and UCl_6^{2-} anions, calculations give two absorption features related with transitions to 5f orbitals, which also well reproduces the experimental two intense peaks as shown in Figure 5.21. Besides, the two intense absorption features in UCl_6^- is 1.3 –1.5 eV lower in energy than those in UCl_6^{2-}, and the peak splitting is 0.82 eV in the former one and 0.57 eV in the latter one. This is again consistent with the experimental observation that lowering the oxidation state from +5 to +4 moved absorption peaks lower in energy and closer together.

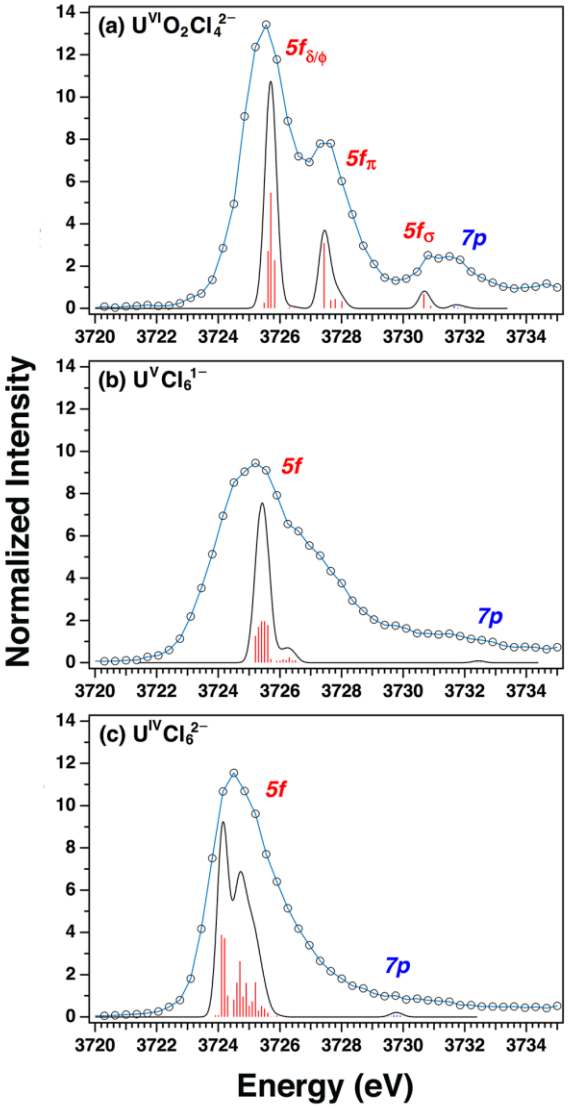

Figure 5.21. Comparison between experimental HERFD XAS spectra (•) and results from the spin−orbit coupled DFT transition dipole moment calculations (black trace) for $UO_2Cl_4^{2-}$ and UCl_6^{1-} and UCl_6^{2-} anions. The red and blue bars represent the energy and oscillator strength for the calculated transitions involving 5f- and 7p-final states, respectively.

The simulated U Mβ resonant XES spectra of $UO_2Cl_4^{2-}$, UCl_6^{-} and UCl_6^{2-} anions together with the experimental data were shown in Figure 5.22. The calculated emission spectra were dominated by an intense dipole-allowed $4f_{5/2} \rightarrow 3d_{3/2}$ transtion at 3340 eV (red peak) consistent with experiment. The dipole-forbidden $4f_{7/2} \rightarrow 3d_{3/2}$ emission at ~3350 eV (yellow peak) was

calculated to be 1000 times weaker and did not substantially affect the spectra. The ~10 eV difference corresponds to spin-orbit coupling splitting of U 4f shell, slightly smaller than the 11.6 eV splitting of the Pu 4f shell from the the 3d4f RIXS data of PuO_2.[21] The experimentally observed high-energy satellites near 3346 eV in Mβ resonant XES were not found by DFT calculations, and although we do not currently have an explanation for the source of the satellite emission, we suspect it is due to a multi-electron effect, much like the high-energy satellites of the Kα emission line.[95]

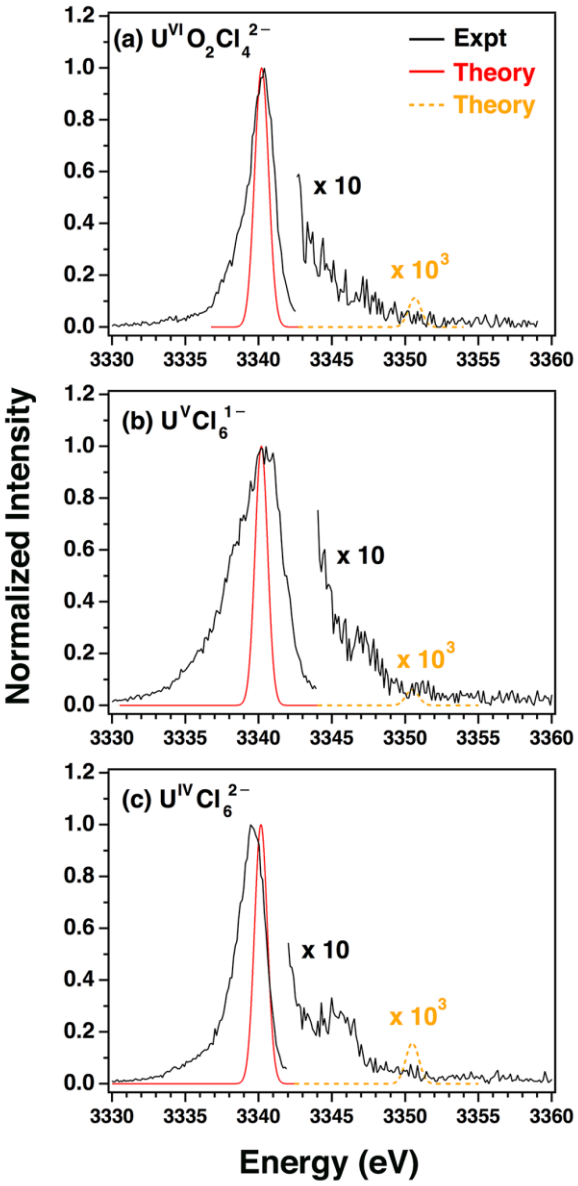

Figure 5.22. Comparison between experimental resonant x-ray emission spectra (black line) and results from the spin−orbit coupled DFT transition dipole moment calculations (red and yellow trace) for $UO_2Cl_4^{2-}$ and UCl_6^{1-} and UCl_6^{2-} anions. The red intense peak is from dipole-allowed $4f_{5/2} \rightarrow 3d_{3/2}$ transition and the yellow weak peak is due to dipole-forbidden $4f_{7/2} \rightarrow 3d_{3/2}$ transition. The high-energy side of experimental and theoretical spectra is expanded 10 and 1000 times, respectively, to highlight the high-energy M beta satellite at 3346 – 3352 eV.

The simulated and experimental Cl K-edge XAS spectra of UCl_6^- and UCl_6^{2-} anions were shown in Figure 5.23. Excellent agreement between SO-DFT transition dipole calculations with

the experimental data leads to an electronic-structure-based interpretation of the Cl K-edge XAS spectra of UCl_6^- and UCl_6^{2-}. The simulated spectra reproduced the pre-edge features in the experimental spectra and were consistent with group theoretical analyses. The calculations suggested that the pre-edge peaks stemmed from electronic excitations between Cl 1s-orbitals and unoccupied orbitals that derived from Cl 3p- orbital mixing with U(V/IV) 5f- and 6d-orbitals. The calculations revealed the high-energy A peaks (2824 eV) were almost exclusively attributed to Cl 1s-electronic excitations to low-lying 6d-orbitals (t_{2g}* in the scalar calculations). The calculations also suggested that transitions to higher lying 6d-orbitals (e_g* in the scalar calculations) were beyond the rising edge. Computational results suggested that the B and C peak in UCl_6^- and B peak in UCl_6^{2-} were associated with electronic excitations from Cl 1s-orbitals to the antibonding 5f- orbitals (those of t_{1u}* and t_{2u}* parentage in the scalar calculations). The calculations additionally reveal that moving from UCl_6^{2-} to UCl_6^{1-} shifted the 5f-transitions to lower energy, which was consistent with experiment.

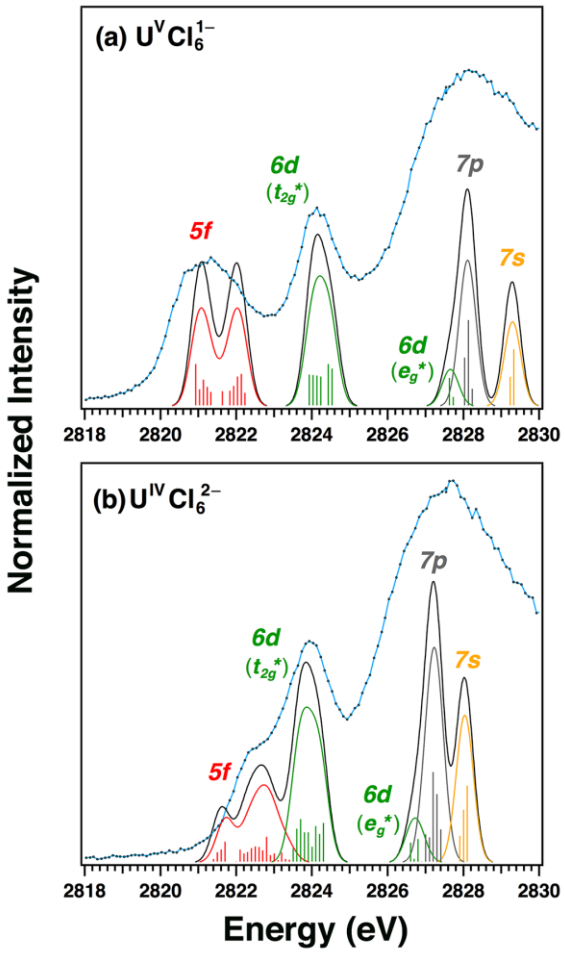

Figure 5.23. Comparison between experimental Cl K-edge XAS spectra (•) and results from the spin−orbit coupled DFT transition dipole moment calculations (black trace) for UCl_6^{1-} and UCl_6^{2-} anions. The red, green, yellow, and gray bars and dashed traces represent the energy and oscillator strength for the calculated transitions involving 5f-, 6d-, 7s-, and 7p-final states, respectively.

The calculated Cl K-edge XAS pre-edge intensities of UCl_6^{1-} showed 5f orbital mixing is larger than 6d t_{2g}, which is different from the dominant 6d t_{2g} participation in bonding in UCl_6^{2-}. This prediction is consistent with experiment (Table 5.2). This observation can be rationalized by perturbation theory. Remember that the orbital mixing coefficient (λ) is directly related to the coupling matrix element between metal and ligand (H_{ML}) and inversely related to the energy difference between the metal and ligand valence orbitals ($E_{0M} - E_{0L}$).[55]

$$\lambda = \frac{H_{ML}}{E_M^0 - E_L^0} \quad (1)$$

Consistent with the distribution of radial densities of U 5f-, 6d-, and Cl 3p-orbitals (Figure 5.24) and the corresponding orbital overlap integral (Table 5.3) our results suggested that the overlap integral between U 5f-, 6d-orbitals and Cl 3p-orbitals are notably enhanced particularly for U 5f – Cl 3p orbital overlap from UCl_6^{2-} to UCl_6^{1-} due to a decrease of 0.11 Å for U-Cl bond distance. Hence, the coupling term (H_{ML}), which relates to the orbital overlap integral, directly advances the U 5f-, 6d-orbital mixing with Cl 3p-orbitals. These observations were consistent with many accounts suggesting that increasing uranium oxidation state strengthens 5f-, 6d-orbital participation in covalent bonding.[23,89,96–100]

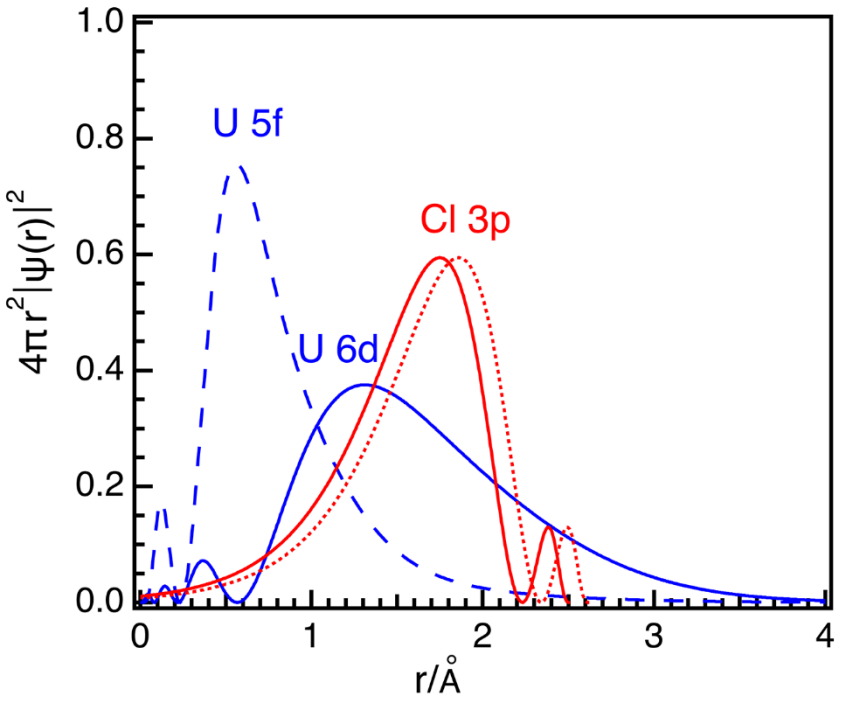

Figure 5.24. Atomic valence-orbital radial densities ($4\pi r^2|\Psi(r)|^2$) from the 5f- (blue dashed line) and 6d- (blue solid line) orbitals of U atom from DFT/B3LYP calculations. The overlap of the radial orbital density from Cl 3p-orbitals (red line) is centered at the experimental average of the U−Cl bond distance of 2.511 (red solid) and 2.621 Å (red dotted).

From UCl_6^{2-} to UCl_6^{1-} the shortening of U-Cl bond length results in an increase of the H_{ML} term. Meanwhile, increasing the oxidation state from +4 to +5 moved the 5f orbitals to a lower energy and closer to Cl 3p nonbonding orbitals (t_{1g}) as shown in Figure 5.14. Energy level diagram from DFT ground-state calculations that incorporate spin-orbit coupling showing the change from UCl_6^{2-} to UCl_6^{1-}. The geometries of UCl_6^{1-} and UCl_6^{2-} are from experimental crystal structures of $(PPh_4)UCl_6$ and $(PPh_4)_2UCl_6$, respectively. A constant energy shift of xx eV was applied to UCl_6^{1-} to align the energy levels of the highest occupied Cl 3p orbitals of non-bonding character in UCl_6^{1-} and UCl_6^{2-} to aid visual comparison.. However, the low-lying 6d orbitals (t_{2g}* in the scalar calculations), which are involved in the pre-edge feature (A peak), remain unchanged in energy. The end result is a more favorable energy degeneracy orbital term ($E^0_M - E^0_M$) for the U 5f- and Cl 3p-orbitals but not for the U 6d and Cl 3p-orbitals. In this case, the positive effects from both H_{ML} and ($E^0_M - E^0_L$) jointly enhance the 5f orbital mixing with Cl 3p from UCl_6^{2-} to UCl_6^{1-}, instead that only H_{ML} term improves the 6d orbital participation. This provides a mechanism to explain that increasing uranium oxidation state increases 5f-covalency more prominently than 6d covalency.

5.6 Outlook and Implications on Orbital Mixing

Herein, we have used XAS, XES, and DFT to evaluate propositions that U^V forms highly covalent bonds in UCl_6^{1-}. By comparison with common impurities $UO_2Cl_4^{2-}$ and UCl_6^{2-}, the U $N_{5,4}$- and $M_{5,4}$-edge XAS spectroscopic tools and DFT calculations have demonstrated good correlation between spectral features and the ground-state electronic structure in these three anions with uranium of different oxidation states. The M_4-edge HERFD spectra from U Mβ RIXS

measurement give a weakening trend of U 5f-shell splitting from $UO_2Cl_4^{2-}$ to UCl_6^{1-} to UCl_6^{2-}, which seems to indicate a trend of increasing 5f covalency with oxidation state. However, it is difficult to extract direct information of U–Cl bonding. It is our opinion that with continual improvements in instrumentation and computation, U M-edge RIXS will provide an important probe of 5*f* electronic structure. The Cl K-edge XAS results provided unambiguous evidence for significant U–Cl mixing in UCl_6^{1-}. The unique U^V ($5f^1$ $6d^0$) electronic configuration and the highly symmetric octahedral coordination environment enabled Cl 3*p*-orbital mixing with U^V 5*f*- and 6*d*-orbitals to be independently evaluated. SO-DFT transition dipole calculations suggest that on the low energy side, the spectrum contained Cl 1s electronic excitations to both U–Cl π* and σ*-orbitals that resulted from significant Cl 3p and U 5f-orbital mixing. At higher energy was a feature best described as resulting from transitions of a Cl 1s electron to the empty U 6d orbitals of t_{2g}-symmetery (π*).

Obtaining a robust interpretation of the UCl_6^{1-} Cl K-edge XAS spectrum enabled us to evaluate previous claims that both 5*f*- and 6*d*- orbitals need to be considered when evaluating the frontier orbital interactions in U–Cl bonding. As an example, the Cl K-edge XAS spectrum from UCl_6^{1-}, reported here for the first time, was overlaid with the previously published spectrum from UCl_6^{2-}.[25,28] This comparison highlighted many important changes in U–Cl electronic structure and bonding as a function of metal oxidation state. For example, moving from the tetravalent UCl_6^{2-} to the pentavalent UCl_6^{1-} caused the pre-edge feature associated with the 5*f*-orbitals to decrease in energy (Figure 5.23). In contrast, features associated with the 6*d*-orbitals remained relatively constant in energy. These observations were consistent with theoretical results of the relative final state energies, indicating that increasing the uranium oxidation state influence the less shielded U 5*f*-manifold to a greater extent than the U 6*d*-manifold.

Another dramatic difference between the UCl_6^{2-} and UCl_6^{1-} Cl K-edge spectra was the increase in intensity of the 5*f*-feature from 0.40(2) in U^{IV} to 0.58(4) for U^{V}. This increase in pre-edge peak intensity highlights a substantial increase in U 5*f*- and Cl 3*p*-orbital mixing; e.g. 5.7(3)% in UCl_6^{2-} to 8.3% for UCl_6^{1-}. Increased covalency was rationalized using first-order perturbation theory, as described previously.[28,55,101] Briefly, the theory suggests that orbital mixing is directly proportional to spatial overlap of the atomic orbitals and is inversely proportional to the energy difference between the two atomic orbitals involved in the bond. The orbital radial distributions and energy levels of U 5f- and Cl 3p-orbitals from DFT calculations show that in the UCl_6^{2-} and UCl_6^{1-} the increase in oxidation state of the central uranium ion from U^{IV} to U^{V} and concomitant decrease in U-Cl bond lengths and 5*f*-orbital energies lead to an enhancement in orbital overlap integral and the energy degeneracy between the U 5*f*- and Cl 3*p*-orbitals, thereby increasing the U–Cl orbital-mixing. Similar increases in M–Cl orbital have been correlated with increased oxidation state for $CeCl_6^{3-}$ vs. $CeCl_6^{2-}$. In that situation, the increased Ce 4*f*- and Cl 3*p*-oribtial mixing was mainly attributed to an improvement in valence orbital energy degeneracy. Instead of these concerted effects on U 5f mixing with Cl 3*p*-orbitals, only the orbital overlap driven covalency was indicated for U 6d orbital.

Overall, the U−Cl bonding results in UCl_6^{1-} provide important insight in the actinide covalency, which can be driven by both orbital overlap and energy degeneracy. This unique bonding property is closely related with actinide electronic structure, not typical for other elements on the periodic table. This work serves as an inspiration to evaluate more complicated ligand systems and a basis for exploring covalency in bonding in other actinide elements.

5.7 REFERENCES

1. La Pierre, H. S., Scheurer, A., Heinemann, F. W., Hieringer, W. & Meyer, K. Synthesis and Characterization of a Uranium(II) Monoarene Complex Supported by δ Backbonding. *Angew. Chemie Int. Ed.* **53**, 7158–7162 (2014).

2. MacDonald, M. R. *et al.* Identification of the +2 Oxidation State for Uranium in a Crystalline Molecular Complex, [K(2.2.2-Cryptand)][($C_5H_4SiMe_3)_3U$]. *J. Am. Chem. Soc.* **135**, 13310–13313 (2013).

3. Windorff, C. J. *et al.* Expanding the Chemistry of Molecular U^{2+} Complexes: Synthesis, Characterization, and Reactivity of the $\{[C_5H_3(SiMe_3)_2]_3U\}^-$ Anion. *Chem. - A Eur. J.* **22**, 772–782 (2016).

4. Huh, D. N., Ziller, J. W. & Evans, W. J. Chelate-Free Synthesis of the U(II) Complex, $[(C_5H_3(SiMe_3)_2)_3U]^{1-}$, Using Li and Cs Reductants and Comparative Studies of La(II) and Ce(II) Analogs. *Inorg. Chem.* **57**, 11809–11814 (2018).

5. Billow, B. S. *et al.* Synthesis and Characterization of a Neutral U(II) Arene Sandwich Complex. *J. Am. Chem. Soc.* **140**, 17369–17373 (2018).

6. Ryan, A. J., Angadol, M. A., Ziller, J. W. & Evans, W. J. Isolation of U(ii) compounds using strong donor ligands, C_5Me_4H and $N(SiMe_3)_2$, including a three-coordinate U(ii) complex. *Chem. Commun.* **55**, 2325–2327 (2019).

7. Joanna C. Renshaw, †,‡ *et al.* Bioreduction of Uranium: Environmental Implications of a Pentavalent Intermediate. (2005). doi:10.1021/ES048232B

8. Yuan, K. *et al.* Electrochemical and Spectroscopic Evidence on the One-Electron Reduction of U(VI) to U(V) on Magnetite. *Environ. Sci. Technol.* **49**, 6206–6213 (2015).

9. Eugene S. Ilton, *,†, Anca Haiduc, ‡, Christopher L. Cahill, § and & Felmy†, A. R. Mica Surfaces Stabilize Pentavalent Uranium. (2005). doi:10.1021/IC0487272

10. Arnold, P. L., Love, J. B. & Patel, D. Pentavalent uranyl complexes. *Coord. Chem. Rev.* **253**, 1973–1978 (2009).

11. Jones, M. B. & Gaunt, A. J. Recent Developments in Synthesis and Structural Chemistry of Nonaqueous Actinide Complexes. *Chem. Rev.* **113**, 1137–1198 (2013).

12. Natrajan, L. S., Swinburne, A. N., Andrews, M. B., Randall, S. & Heath, S. L. Redox and environmentally relevant aspects of actinide(IV) coordination chemistry. *Coord. Chem. Rev.* **266**–**267**, 171–193 (2014).

13. Warner, B. P., Scott, B. L. & Burns, C. J. A Simple Preparative Route to Bis(imido)uranium(VI) Complexes by the Direct Reductions of Diazenes and Azides. *Angew. Chemie Int. Ed.* **37**, 959–960 (1998).

14. Halter, D. P., Heinemann, F. W., Maron, L. & Meyer, K. The role of uranium–arene bonding in H2O reduction catalysis. *Nat. Chem.* **10**, 259–267 (2018).

15. Heitler, W. & London, F. Wechselwirkung neutraler Atome und hom�opolare Bindung nach der Quantenmechanik. *Zeitschrift f�r Phys.* **44**, 455–472 (1927).

16. HEDMAN, B., HODGSON, K. O. & SOLOMON, E. I. ChemInform Abstract: X-Ray Absorption Edge Spectroscopy of Ligands Bound to Open-Shell Metal Ions: Chlorine K-Edge Studies of Covalency in CuCl2- 4. *ChemInform* **21**, no-no (1990).

17. Shadle, S. E., Hedman, B., Hodgson, K. O. & Solomon, E. I. Ligand K-edge x-ray absorption spectroscopic studies: metal-ligand covalency in a series of transition metal tetrachlorides. *J. Am. Chem. Soc.* **117**, 2259–2272 (1995).

18. Solomon, E. I., Hedman, B., Hodgson, K. O., Dey, A. & Szilagyi, R. K. Ligand K-edge X-ray absorption spectroscopy: covalency of ligand–metal bonds. *Coord. Chem. Rev.* **249**, 97–129 (2005).

19. Lundberg, M. *et al.* Metal–Ligand Covalency of Iron Complexes from High-Resolution Resonant Inelastic X-ray Scattering. *J. Am. Chem. Soc.* **135**, 17121–17134 (2013).

20. Jay, R. M. *et al.* Disentangling Transient Charge Density and Metal–Ligand Covalency in Photoexcited Ferricyanide with Femtosecond Resonant Inelastic Soft X-ray Scattering. *J. Phys. Chem. Lett.* **9**, 3538–3543 (2018).

21. Baker, M. L. *et al.* K- and L-edge X-ray absorption spectroscopy (XAS) and resonant inelastic X-ray scattering (RIXS) determination of differential orbital covalency (DOC) of transition metal sites. *Coord. Chem. Rev.* **345**, 182–208 (2017).

22. Kunnus, K. *et al.* Quantifying covalent interactions with resonant inelastic soft X-ray scattering: Case study of Ni2+ aqua complex. *Chem. Phys. Lett.* **669**, 196–201 (2017).

23. Vitova, T. *et al.* The role of the 5f valence orbitals of early actinides in chemical bonding. *Nat. Commun.* **8**, 16053 (2017).

24. Gel'mukhanov, F. & Ågren, H. Resonant X-ray Raman scattering. *Phys. Rep.* **312**, 87–330 (1999).

25. Kotani, A. & Shin, S. Resonant inelastic x-ray scattering spectra for electrons in solids. *Rev. Mod. Phys.* **73**, 203–246 (2001).

26. Hermann, J. A., Suttle, J. F. & Hoekstra, H. R. Uranium(IV) Chloride. in 143–145 (John Wiley & Sons, Ltd, 2007). doi:10.1002/9780470132364.ch39

27. Minasian, S. G. *et al.* New evidence for 5f covalency in actinocenes determined from carbon K-edge XAS and electronic structure theory. *Chem. Sci.* **5**, 351–359 (2014).

28. Su, J. *et al.* Energy-Degeneracy-Driven Covalency in Actinide Bonding. *J. Am. Chem.*

Soc. **140**, 17977–17984 (2018).

29. Tami E. Westre, † *et al.* A Multiplet Analysis of Fe K-Edge 1s → 3d Pre-Edge Features of Iron Complexes. (1997). doi:10.1021/JA964352A

30. Minasian, S. G. *et al.* A Comparison of 4 *f vs* 5 *f* Metal−Metal Bonds in (CpSiMe $_3$) $_3$ M−ECp* (M = Nd, U; E = Al, Ga; Cp* = C $_5$ Me $_5$): Synthesis, Thermodynamics, Magnetism, and Electronic Structure. *J. Am. Chem. Soc.* **131**, 13767–13783 (2009).

31. Minasian, S. G. *et al.* Carbon K-Edge X-ray Absorption Spectroscopy and Time-Dependent Density Functional Theory Examination of Metal–Carbon Bonding in Metallocene Dichlorides. *J. Am. Chem. Soc.* **135**, 14731–14740 (2013).

32. Bugaris, D. E., Copping, R., Tyliszczak, T., Shuh, D. K. & Ibers, J. A. La $_2$ U $_2$ Se $_9$: An Ordered Lanthanide/Actinide Chalcogenide with a Novel Structure Type. *Inorg. Chem.* **49**, 2568–2575 (2010).

33. Gianetti, T. L. *et al.* Diniobium Inverted Sandwich Complexes with μ-η ^{6} :η ^{6} -Arene Ligands: Synthesis, Kinetics of Formation, and Electronic Structure. *J. Am. Chem. Soc.* **135**, 3224–3236 (2013).

34. Bluhm, H. *et al.* Soft X-ray microscopy and spectroscopy at the molecular environmental science beamline at the Advanced Light Source. *J. Electron Spectros. Relat. Phenomena* **150**, 86–104 (2006).

35. Holden, W. M. *et al.* A compact dispersive refocusing Rowland circle X-ray emission spectrometer for laboratory, synchrotron, and XFEL applications. *Rev. Sci. Instrum.* **88**, 073904 (2017).

36. Becke, A. D. Density-functional exchange-energy approximation with correct asymptotic behavior. *Phys. Rev. A* **38**, 3098–3100 (1988).

37. Lee, C., Yang, W. & Parr, R. G. Development of the Colle-Salvetti correlation-energy formula into a functional of the electron density. *Phys. Rev. B* **37**, 785–789 (1988).

38. te Velde, G. *et al.* Chemistry with ADF. *J. Comput. Chem.* **22**, 931–967 (2001).

39. Fonseca Guerra, C., Snijders, J. G., te Velde, G. & Baerends, E. J. Towards an order- N DFT method. *Theor. Chem. Accounts Theory, Comput. Model. (Theoretica Chim. Acta)* **99**, 391–403 (1998).

40. Van Lenthe, E. & Baerends, E. J. Optimized Slater-type basis sets for the elements 1-118. *J. Comput. Chem.* **24**, 1142–1156 (2003).

41. Lenthe, E. van, Baerends, E. J. & Snijders, J. G. Relativistic regular two-component Hamiltonians. *J. Chem. Phys.* **99**, 4597–4610 (1993).

42. Cross, J. N. *et al.* Covalency in Americium(III) Hexachloride. *J. Am. Chem. Soc.* **139**,

8667–8677 (2017).

43. Fieser, M. E. *et al.* Evaluating the electronic structure of formal LnII ions in LnII(C5H4SiMe3)31- using XANES spectroscopy and DFT calculations. *Chem. Sci.* **8**, 6076–6091 (2017).

44. Neese, F. The ORCA program system. *Wiley Interdiscip. Rev. Comput. Mol. Sci.* **2**, 73–78 (2012).

45. Nakajima, T. & Hirao, K. The Douglas–Kroll–Hess Approach. *Chem. Rev.* **112**, 385–402 (2012).

46. Reiher, M. Relativistic Douglas-Kroll-Hess theory. *Wiley Interdiscip. Rev. Comput. Mol. Sci.* **2**, 139–149 (2012).

47. Neese, F. Efficient and accurate approximations to the molecular spin-orbit coupling operator and their use in molecular g-tensor calculations. *J. Chem. Phys.* **122**, 034107 (2005).

48. Pantazis, D. A. & Neese, F. All-Electron Scalar Relativistic Basis Sets for the Actinides. *J. Chem. Theory Comput.* **7**, 677–684 (2011).

49. Weigend, F., Furche, F. & Ahlrichs, R. Gaussian basis sets of quadruple zeta valence quality for atoms H–Kr. *J. Chem. Phys.* **119**, 12753–12762 (2003).

50. Weigend, F. & Ahlrichs, R. Balanced basis sets of split valence, triple zeta valence and quadruple zeta valence quality for H to Rn: Design and assessment of accuracy. *Phys. Chem. Chem. Phys.* **7**, 3297 (2005).

51. Stoychev, G. L., Auer, A. A. & Neese, F. Automatic Generation of Auxiliary Basis Sets. *J. Chem. Theory Comput.* **13**, 554–562 (2017).

52. Neese, F. An improvement of the resolution of the identity approximation for the formation of the Coulomb matrix. *J. Comput. Chem.* **24**, 1740–1747 (2003).

53. Lee, N., Petrenko, T., Bergmann, U., Neese, F. & DeBeer, S. Probing Valence Orbital Composition with Iron Kβ X-ray Emission Spectroscopy. *J. Am. Chem. Soc.* **132**, 9715–9727 (2010).

54. DeBeer George, S. & Neese, F. Calibration of Scalar Relativistic Density Functional Theory for the Calculation of Sulfur K-Edge X-ray Absorption Spectra. *Inorg. Chem.* **49**, 1849–1853 (2010).

55. Minasian, S. G. *et al.* Determining Relative f and d Orbital Contributions to M–Cl Covalency in MCl_6^{2-} (M = Ti, Zr, Hf, U) and $UOCl_5^-$ Using Cl K-Edge X-ray Absorption Spectroscopy and Time-Dependent Density Functional Theory. *J. Am. Chem. Soc.* **134**, 5586–5597 (2012).

56. Minasian, S. G. *et al.* Synthesis and Structure of $(Ph_4P)_2MCl_6$ (M = Ti, Zr, Hf, Th, U, Np, Pu). *Inorg. Chem.* **51**, 5728–5736 (2012).

57. Löble, M. W. *et al.* Covalency in Lanthanides. An X-ray Absorption Spectroscopy and Density Functional Theory Study of $LnCl_6^{x-}$ (x = 3, 2). *J. Am. Chem. Soc.* **137**, 2506–2523 (2015).

58. Shannon, R. D. & IUCr. Revised effective ionic radii and systematic studies of interatomic distances in halides and chalcogenides. *Acta Crystallogr. Sect. A* **32**, 751–767 (1976).

59. Selbin, J. & Ortego, J. D. Chemistry of uranium (V). *Chem. Rev.* **69**, 657–671 (1969).

60. Graves, C. R. & Kiplinger, J. L. Pentavalent uranium chemistry—synthetic pursuit of a rare oxidation state. *Chem. Commun.* 3831 (2009). doi:10.1039/b902969a

61. Liddle, S. T. The Renaissance of Non-Aqueous Uranium Chemistry. *Angew. Chemie Int. Ed.* **54**, 8604–8641 (2015).

62. Bugaris, D. E. *et al.* Pentavalent and Tetravalent Uranium Selenides, $Tl_3Cu_4USe_6$ and $Tl_2Ag_2USe_4$: Syntheses, Characterization, and Structural Comparison to Other Layered Actinide Chalcogenide Compounds. *Inorg. Chem.* **50**, 6656–6666 (2011).

63. Nilsson, H. J., Tyliszczak, T., Wilson, R. E., Werme, L. & Shuh, D. K. Soft X-ray scanning transmission X-ray microscopy (STXM) of actinide particles. *Anal. Bioanal. Chem.* **383**, 41–47 (2005).

64. Moore, K. T., van der Laan, G., Haire, R. G., Wall, M. A. & Schwartz, A. J. Oxidation and aging in U and Pu probed by spin-orbit sum rule analysis: Indications for covalent metal-oxide bonds. *Phys. Rev. B* **73**, 033109 (2006).

65. Moore, K. T. & van der Laan, G. Nature of the 5 f states in actinide metals. *Rev. Mod. Phys.* **81**, 235–298 (2009).

66. van der Laan, G. *et al.* Applicability of the Spin-Orbit Sum Rule for the Actinide 5 f States. *Phys. Rev. Lett.* **93**, 097401 (2004).

67. Tobin, J. G. *et al.* Competition between delocalization and spin-orbit splitting in the actinide 5 f states. *Phys. Rev. B* **72**, 085109 (2005).

68. Moore, K. T. *et al.* Probing the population of the spin–orbit split levels in the actinide 5f states. *Ultramicroscopy* **106**, 261–268 (2006).

69. Tobin, J. G. *et al.* Oxidation and crystal field effects in uranium. *Phys. Rev. B* **92**, 035111 (2015).

70. Tobin, J. G. & Shuh, D. K. Electron spectroscopy of the oxidation and aging of U and Pu. *J. Electron Spectros. Relat. Phenomena* **205**, 83–91 (2015).

71. Kraft, S. J. *et al.* Synthesis, Characterization, and Multielectron Reduction Chemistry of Uranium Supported by Redox-Active α-Diimine Ligands. *Inorg. Chem.* **50**, 9838–9848 (2011).

72. Butorin, S. M., Modin, A., Vegelius, J. R., Kvashnina, K. O. & Shuh, D. K. Probing Chemical Bonding in Uranium Dioxide by Means of High-Resolution X-ray Absorption Spectroscopy. *J. Phys. Chem. C* **120**, 29397–29404 (2016).

73. Bès, R. *et al.* Use of HERFD–XANES at the U L_3 - and M_4 -Edges To Determine the Uranium Valence State on $[Ni(H_2O)_4]_3[U(OH,H_2O)(UO_2)_8O_{12}(OH)_3]$. *Inorg. Chem.* **55**, 4260–4270 (2016).

74. Pidchenko, I. *et al.* Uranium Redox Transformations after U(VI) Coprecipitation with Magnetite Nanoparticles. *Environ. Sci. Technol.* **51**, 2217–2225 (2017).

75. Kvashnina, K. O., Walker, H. C., Magnani, N., Lander, G. H. & Caciuffo, R. Resonant x-ray spectroscopy of uranium intermetallics at the $M_{4,5}$ edges of uranium. *Phys. Rev. B* **95**, 245103 (2017).

76. Butorin, S. M., Kvashnina, K. O., Prieur, D., Rivenet, M. & Martin, P. M. Characteristics of chemical bonding of pentavalent uranium in La-doped UO_2. *Chem. Commun.* **53**, 115–118 (2017).

77. Bès, R. *et al.* New insight in the uranium valence state determination in UyNd1−yO2±x. *J. Nucl. Mater.* **507**, 145–150 (2018).

78. Colella, M., Lumpkin, G. R., Zhang, Z., Buck, E. C. & Smith, K. L. Determination of the uranium valence state in the brannerite structure using EELS, XPS, and EDX. *Phys. Chem. Miner.* **32**, 52–64 (2005).

79. Manoubi, T., Colliex, C. & Rez, P. Quantitative electron energy loss spectroscopy on M45 edges in rare earth oxides. *J. Electron Spectros. Relat. Phenomena* **50**, 1–18 (1990).

80. Thole, B. T. *et al. 3d* x-ray-absorption lines and the $3d^9 4f^{n+1}$ multiplets of the lanthanides. *Phys. Rev. B* **32**, 5107–5118 (1985).

81. Jo, T. & Kotani, A. MULTIPLET STRUCTURES IN 4d-XAS OF CeO_2 AND $CeRh_3$. *Le J. Phys. Colloq.* **49**, C8-739-C8-740 (1988).

82. Meihaus, K. R. *et al.* Influence of Pyrazolate vs *N* -Heterocyclic Carbene Ligands on the Slow Magnetic Relaxation of Homoleptic Trischelate Lanthanide(III) and Uranium(III) Complexes. *J. Am. Chem. Soc.* **136**, 6056–6068 (2014).

83. Butorin, S. M. *et al.* Resonant X-Ray Fluorescence Spectroscopy of Correlated Systems: A Probe of Charge-Transfer Excitations. *Phys. Rev. Lett.* **77**, 574–577 (1996).

84. Kvashnina, K. O., Butorin, S. M., Martin, P. & Glatzel, P. Chemical State of Complex Uranium Oxides. *Phys. Rev. Lett.* **111**, 253002 (2013).

85. Butorin, S. M., Kvashnina, K. O., Vegelius, J. R., Meyer, D. & Shuh, D. K. High-resolution X-ray absorption spectroscopy as a probe of crystal-field and covalency effects in actinide compounds. *Proc. Natl. Acad. Sci. U. S. A.* **113**, 8093–7 (2016).

86. Schülke, W. *Electron dynamics by inelastic X-ray scattering*. (Oxford University Press, 2007).

87. Solomon, E. I., Hedman, B., Hodgson, K. O., Dey, A. & Szilagyi, R. K. Ligand K-edge X-ray absorption spectroscopy: Covalency of ligand-metal bonds. *Coord. Chem. Rev.* **249**, 97–129 (2005).

88. Figgis, B. N. & Hitchman, M. A. *Ligand field theory and its applications*. *Ligand field theory and its applications* (Wiley-VCH, 2000). doi:10.1002/1099-0739(200008)14:8<449::AID-AOC14>3.0.CO;2-6

89. Su, J. *et al.* Photoelectron spectroscopy and theoretical studies of gaseous uranium hexachlorides in different oxidation states: UCl6q− (q = 0–2). *J. Chem. Phys.* **142**, 134308 (2015).

90. Su, J., Wang, Y.-L., Wei, F., Schwarz, W. H. E. & Li, J. Theoretical Study of the Luminescent States and Electronic Spectra of UO_2Cl_2 in an Argon Matrix. *J. Chem. Theory Comput.* **7**, 3293–3303 (2011).

91. Dau, P. D. *et al.* Photoelectron spectroscopy and the electronic structure of the uranyl tetrachloride dianion: $UO_2Cl_4^{2-}$. *J. Chem. Phys.* **137**, 064315 (2012).

92. Hall, E. R. *et al.* Valence-to-Core-Detected X-ray Absorption Spectroscopy: Targeting Ligand Selectivity. *J. Am. Chem. Soc.* **136**, 10076–10084 (2014).

93. MacMillan, S. N., Walroth, R. C., Perry, D. M., Morsing, T. J. & Lancaster, K. M. Ligand-Sensitive But Not Ligand-Diagnostic: Evaluating Cr Valence-to-Core X-ray Emission Spectroscopy as a Probe of Inner-Sphere Coordination. *Inorg. Chem.* **54**, 205–214 (2015).

94. Martin-Diaconescu, V. *et al.* Kβ Valence to Core X-ray Emission Studies of Cu(I) Binding Proteins with Mixed Methionine – Histidine Coordination. Relevance to the Reactivity of the M- and H-sites of Peptidylglycine Monooxygenase. *Inorg. Chem.* **55**, 3431–3439 (2016).

95. Nigam, A. N. & Soni, S. N. Kα satellite energies in x-ray spectra. *Phys. B+C* **132**, 407–415 (1985).

96. Dau, P. D. *et al.* Photoelectron spectroscopy and theoretical studies of UF_5^- and UF_6^-. *J. Chem. Phys.* **136**, 194304 (2012).

97. Beekmeyer, R., Kerridge, A., Beekmeyer, R. & Kerridge, A. Assessing Covalency in Cerium and Uranium Hexachlorides: A Correlated Wavefunction and Density Functional Theory Study. *Inorganics* **3**, 482–499 (2015).

98. Kerridge, A. Quantification of f-element covalency through analysis of the electron density: insights from simulation. *Chem. Commun.* **53**, 6685–6695 (2017).

99. Hu, H.-S., Qiu, Y.-H., Xiong, X.-G., Schwarz, W. H. E. & Li, J. On the maximum bond multiplicity of carbon: unusual C≣U quadruple bonding in molecular CUO. *Chem. Sci.* **3**, 2786 (2012).

100. King, D. M. *et al.* Isolation and characterization of a uranium(VI)–nitride triple bond. *Nat. Chem.* **5**, 482–488 (2013).

101. Neidig, M. L., Clark, D. L. & Martin, R. L. Covalency in f-element complexes. *Coord. Chem. Rev.* **257**, 394–406 (2013).

Chapter 6. A MAIL-IN AND USER FACILITY FOR X-RAY ABSORPTION NEAR EDGE STRUCTURE: THE CEI-XANES LABORATORY X-RAY SPECTROMETER AT THE UNIVERSITY OF WASHINGTON

6.1 PREFACE

This is a paper submitted to the Journal of Synchrotron Radiation. It is formatted in the style of this journal. In this work, I describe the CEI-XANES facility at the Molecular Analysis Facility. I led the development and commissioning of the CEI-XANES facility. I did the majority of the writing, experimentation, and data analysis for this paper.

Authors Alexander S. Ditter[a], Evan P. Jahrman[a], Liam R. Bradshaw[b], Xiaojing Xia[c], Peter J. Pauzauskie[de] and Gerald T. Seidler[a]*

[a]Department of Physics, University of Washington, PO Box 351650, Seattle, Washington, 98195-1560, USA
[b]Molecular Analysis Facility, University of Washington, 4000 15th Ave NE, Seattle, Washington, 98195, USA
[c]Department of Molecular Science and Engineering, University of Washington, Seattle, Washington, 98195, USA
[d]Department of Materials Science and Engineering, University of Washington, 3920 E. Stevens Way NE, Seattle, Washington, 98195, USA
[e]Physical & Computational Sciences Directorate, Pacific Northwest National Laboratory, 902 Battelle Blvd, Richland, Washington, 99352

6.2 ABSTRACT

There are more than 100 beamlines or endstations worldwide that frequently support x-ray absorption fine structure (XAFS) measurements, thus providing critical enabling capability for research across numerous scientific disciplines. However, the absence of a supporting tier of more readily accessible, lower-performing options has caused systemic inefficiencies, resulting in high oversubscription and the omission of many scientifically and socially valuable XAFS applications that are incompatible with the synchrotron access model. To this end, we describe the design, performance, and uses of the Clean Energy Institute x-ray absorption near edge structure (CEI-XANES) laboratory spectrometer and its use as both a user-present and mail-in facility. Such new additions to the XAFS infrastructure landscape raise important questions about the most productive interactions between synchrotron and lab-based capabilities. We propose that this can be discussed in the framework of five categories, only one of which is competitive. The categories are: independent operation on independent problems, use dictated by convenience, pre-synchrotron preparatory use of lab capability, post-synchrotron follow-up use of lab capability, and parallel use of both synchrotron and laboratory systems.

6.3 INTRODUCTION

X-ray absorption spectroscopies (XAS) exhibit a global intellectual reach, with more than 100 endstations or beamlines at synchrotron or free electron laser facilities world-wide. This has led to continuing scientific impact across numerous disciplines[1,2], with XAS playing an especially central role in research in catalysis[3,4], electrical energy storage[5–8], environmental science[9], fundamental chemistry and physics[10], biochemistry[11–13], and heavy-element chemistry[14,15]. Much of the highest profile contemporary research does require the full brilliance, time resolution, or

other extreme performance metric of these light sources, but a considerable fraction of ongoing excellent work does not. Hence, while the history of XAS at synchrotron facilities is an undisputed scientific success, the recent reinvigoration of laboratory based XAS after several quiescent decades has been spawned by four observations: (1) the improved spectrometer performance seen with modern components; (2) the fact that the synchrotron facilities cannot support the full range of existing demand for XAS; (3) light source operations could benefit from a supporting tier of higher-access, if lower-performing, XAS capability; and (4) drawing analogy to x-ray diffraction, there is a large range of 'routine analytical' use of XAS that is largely incompatible with synchrotron facility priorities.

The observation of the possible synergies and mutual benefits from the coexistence of synchrotron facilities and laboratory-based systems is not new, and was recently summarized by Seidler, et al.[16] Key unmet opportunities include: the broad inclusion of XAS in education, sample validation prior to synchrotron beamtime, decreased synchrotron oversubscription by providing an alternative venue for experiments not requiring the full beamline performance (e.g., many transmission mode studies), rapid-turnaround studies for iterative improvement of new materials synthesis or for industrial process control, and even regulatory applications.

We discuss here a staffed, modern laboratory spectrometer facility for x-ray absorption near edge structure (XANES) studies in the hard x-ray range. This Clean Energy Institute X-ray Absorption Near-Edge Structure (CEI-XANES) facility is located in the Molecular Analysis Facility (MAF) at the University of Washington (https://www.moles.washington.edu/maf). CEI-XANES supports education and academic research at the University Washington in addition to accepting outside in-person users and providing mail-in measurement service for academic, national lab, and industrial studies. Placing this XANES capability in the MAF leads to interesting

multi-mode characterization via the other capabilities in the MAF, such as x-ray diffraction, various static and dynamic optical wavelength spectroscopies, and surface characterization techniques.

An outline of the CEI-XANES technical design was presented a few years ago[17] and the system has been operating since 2016. However, with the full opening of CEI-XANES to outside in-person and mail-in users, we take this opportunity to give a more detailed technical description, to present representative results, and to seed a broad discussion of the evolving XAFS infrastructure landscape. Specifically, with the growing number of investigator-owned laboratory spectrometers and also systems run as user facilities, it is time to categorize the different interactions between synchrotron and lab-based capabilities. This discussion finds that competition between the two modes is minimal, and that the most prominent interaction between synchrotron and lab-based x-ray spectroscopy will likely be disjoint, independent use or else truly synergistic benefits from use of both.

6.4 Instrument Design and Operation

The CEI-XANES spectrometer utilizes a Rowland circle monochromator with a fixed source, i.e., the so-called 'linear spectrometer' design, well known in the 1970's[18], to produce the tunable monochromatic x-rays needed for XANES measurements. A similar design has recently been implemented in Helsinki[19], and has seen good use for studies of actinide compounds[20] and for a demonstration study for *in situ* catalysis investigations[21]. The relative positioning of key components, i.e., source, analyzer, and detector, is shown in Figure 1. The description of the spectrometer then requires two paths: the key components themselves and the supporting components used for motion control. We begin with the former.

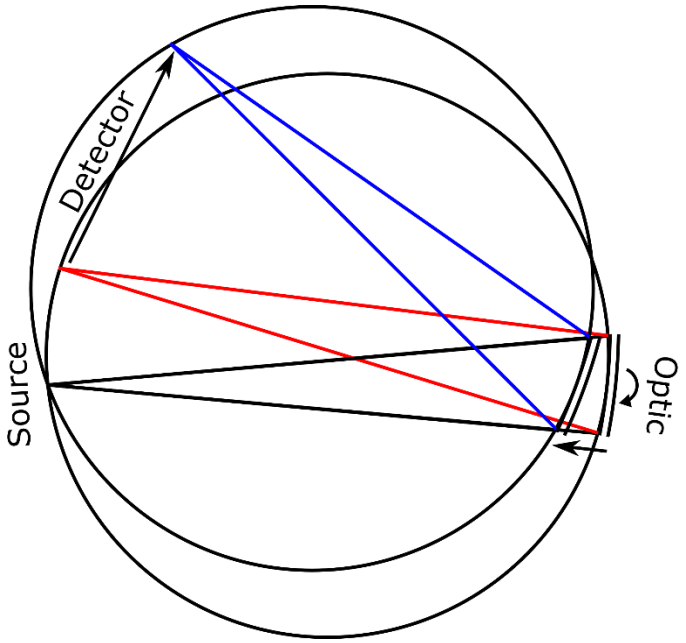

Figure 6.1. Diagram showing the movement of the Detector and the SBCA in a fixed-source Rowland circle in the direction of low (red) to high (blue) energy. Note that both the source position and the direction from the source to the optic are fixed due to the stationary source.

The computer aided design (CAD) rendering in Figure 2 now provides important context. The x-ray source used in CEI-XANES is re-purposed from a powder x-ray diffractometer. Specifically, it is a Siemens XFFAg4k system capable of using either a 1.5kW Ag-anode tube or a 3 kW W-anode tube, just as are used in many powder or single crystal diffractometers. Two different anode materials are needed to avoid strong fluorescence line contamination such as occurs with the unfortunate position of the W Lα2 (8335 eV) emission line in the XANES of Ni (K-edge 8333 eV). The x-ray tubes are used in 'point focus' configuration with a ~ 0.5 mm (vertical) x 1 mm (in-Rowland-plane) size at a median 6° angle take-off angle. The combination of limited shutter dimension and stronger absorption inside the anode at lower take-off angles results in a beam that slightly 'underfills' the horizontal extent of the spherically bent crystal analyzers (SBCA's, from XRS Tech or else home-made[22]), which have the required 1-m radius of curvature in the Johann geometry and whose constituent diffracting wafers have 10-cm diameter.

A welded aluminum helium space with polyimide windows reduces air absorption on the transit from source to SBCA, and from SBCA to detector. A lead-covered, aluminum divider inside the helium box helps to further reduce stray scatter into the line of sight of the detector.

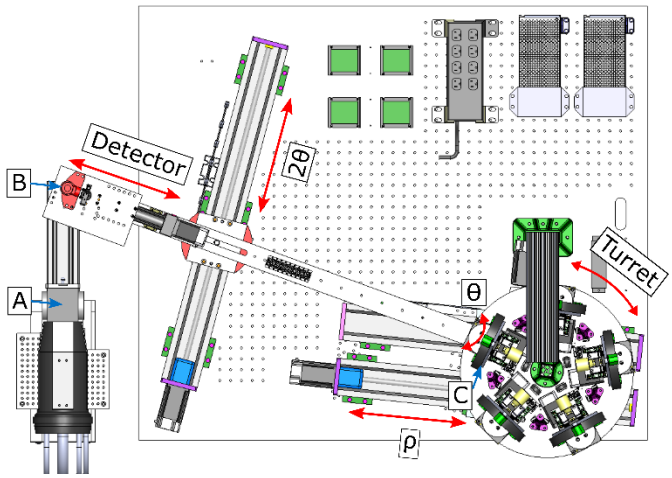

Figure 6.2. CAD Rendering of CEI-XANES (top view). Labelled with red arrows are the 4 motors used in a scan (Detector, θ, 2θ, and ρ), and the turret motor which switches between optics. The key components are labelled with blue arrows and letters: A) the x-ray source, B) the detector, and C) the optic. Not shown is the helium box to reduce air absorption.

The choice of detector poses particular problems for this generation of high-powered laboratory XAFS system. First, the peak flux on a sufficiently tall detector can reach 500,000/s to 10^6/s and, depending on the choice of SBCA crystal and (hkl) orientation, can be accompanied by strong, unwanted harmonics. Second, while toroidal optics useful for lab-based XAFS have recently been demonstrated[22], we still use (spherical) SBCA's whose sagittal focusing errors result in vertical stretching of the analyzed beam to 25 mm at a Bragg angle of 70 degrees. Hence, a relatively large detector with good energy resolution and high saturation rates would be ideal. We primarily use a silicon drift detector (SDD, Amptek Inc. with XIA Mercury digital processing hardware). Our SDD has an energy resolution of about 150 eV which easily rejects any harmonics and most background fluorescence, a necessary property to get an accurate measurement.

However, the SDD has a collimated area which is just 17 mm^2 and is unable to capture the whole vertical extent of the analyzed beam at lower Bragg angles. In addition, the saturation of this SDD above a few hundred thousand counts per second (broadband) sometimes requires beam attenuation to avoid saturation on analyser harmonics. These limitations could be improved upon with use of larger, commercially available SDD, and also with use of the latest generation of very high speed processing electronics. All results reported here use the Amptek SDD. We have also investigated use of a gas proportional counter (GPC, from LND, Inc.). The GPC has a large active area (1.5 cm x 4 cm) but an energy resolution $\Delta E \sim 2$ keV at E = 7 keV and so must only be used with low-symmetry optics where the harmonics are well separated, and also requires much greater care in rejecting stray scatter and, e.g., fluorescence from the radiation enclosure walls. Using the GPC typically adds to the measurement overhead, as it requires additional background scans with the spectrometer slightly mis-tuned. We note that Hokannen *et al.*[19] found similar concerns when using a large scintillation detector in their spectrometer.

The final important component of the CEI-XANES instrument is the radiation enclosure. This was fabricated from a welded aluminum frame with leaded-plywood walls. The total dimensions of the radiation enclosure are quite large (2.5 m x 1.2 m) to allocate space to use the second, opposite shutter on the x-ray tube source for a duplicate but independent spectrometer[17]. While the 'B-side' spectrometer is assembled, we have not yet commissioned it for operations.

Regarding spectrometer motions, a total of four motorized degrees of freedom are needed for energy scanning. We note that we use the 'clock angle' orientation scheme of Mortensen[23] to remove the need for motorizing the SBCA tilt perpendicular to the Rowland plane; that tilt axis is instead adjusted manually *once* with a micrometer and a diverging laser, then is unchanged for any and all SBCA installed onto that apparatus. The remaining four degrees of freedom are the

scattering angle of the analyzer as seen by the source (θ, Velmex B59 rotary stage, equipped with a 10:1 gear reducer), the distance from the source to the analyzer (ρ, Velmex tandem BiSlide), a linear translation of the detector assembly to put the detector into the specular reflection condition from the analyzer (2θ, Velmex BiSlide), and a final stage immediately underneath the detector + sample sub-assembly (detector, Velmex XSlide) that moves the sample onto the focal point of the monochromatized radiation. Including the effect of the reducing gearbox for the "θ" motor, a single full motor step of the stepper motor results in an angular rotation of 0.004°. For example, near the iron K edge at 7112 eV using a Ge 620 optic, the minimum step size is approximately 0.1eV. While microstepping would, in principal, be able to achieve the same performance, in practice this is not the case: microsteps are highly reproducible across full step cycles but have irregular spacing within the full-step. In addition to energy scanning, the SBCA turret (see Fig. 2) requires an additional motorized degree of freedom. This turret was included in the 2016 design to allow rapid change of energy ranges.

Measurements in CEI-XANES are performed by scanning the monochromator over a range of Bragg angles twice, once with the sample in the beam (measuring the transmitted flux) and once without the sample in the beam (measuring the incident flux). The absorption is then calculated according to the Beer-Lambert Law. The x-ray tube is set to 20 kV accelerating potential and the current is varied (up to 50 mA) so that the flux on the detector is kept near 50,000 counts per second to avoid detector dead time. Data collected here are processed by subtracting a polynomial fit to the pre-edge of the data and normalizing the edge-step to 1 using the Demeter package[24].

6.5 EXPERIMENTAL

Lepidocrocite and abiotic magnetite samples were ground to fine powders using a mortar and pestle and then spread over 25-μm thick polyimide tape. This tape was layered 8 times, resulting in a sample with an absorption edge step of approximately 0.5. Synchrotron measurements were performed at beamline 20-BM of the Advanced Photon Source. The spectra were calibrated to an iron foil (EXAFS Materials Inc.). The vanadium reference foil was also from EXAFS Materials Inc.

Single layer xx3450 pouch cell batteries were manufactured at the Cell Analysis, Modeling, and Prototyping (CAMP) Facility at Argonne National Laboratory. The anode used in these cells was Superior Graphite SCL1506T (graphite) and the cathode used was Toda NCM-04ST ($Li(Ni_{0.5}Mn_{0.3}Co_{0.2})O_2$ or NMC532). The anode was coated onto a 10-μm thick copper foil for a final electrode loading of 6.38 mg/cm^2 (coating only). The cathode was coated onto a 20-μm thick aluminum foil for a final electrode loading of 11.40 mg/cm^2 (coating only). Other standard pouch cell components included the separator (Celgard 2320), the pouch material (Cellpack-153PL from Youlchon Chemical), and the electrolyte and solvent (1.2M $LiPF_6$ in EC/EMC 3:7 wt%, respectively). Wetting and formation cycles were performed prior to x-ray analysis. The cell exhibited a nominal capacity of 20 mAh. Further cell details can be found in an upcoming manuscript[25].

Yb_2O_3 was purchased from Sigma Aldrich. This powders were mixed with BN powder (boron nitride, Alfa Aesar) and ground in a mortar and pestle, then packed into an aluminum washer between two layers of 25-μm thick polymide tape. Bulk Yb:$LiYF_4$ was synthesized by the Czochralski process at the University of New Mexico. A piece of a large single crystal was broken off, ground into a fine powder and used to fill the same type of sample holder. Nano-phase

Yb:$LiYF_4$ was synthesized at the University of Washington using previously described methods[26]. The resulting solid was mixed with BN and ground in a mortar and pestle and again put into the same type of sample holder as for the other two Yb-rich samples.

6.6 RESULTS

Here we describe measurements on several transition metal and rare-earth compounds to demonstrate the utility of CEI-XANES as a user facility. These measurements show both that CEI-XANES is able to reproduce synchrotron results and illustrate several "typical" use-cases for measurements.

To make a direct comparison with synchrotron data, lepidocrocite and aboitic magnetite were measured in transmission mode at both CEI-XANES and beamline 20-BM of the Advanced Photon Source (APS), shown in Figure 3. The CEI-XANES measurements were performed at 20 kV and 10 mA tube power for approximately two hours each using a Ge (620) optic. Measurement time would have been proportionally increased with higher tube current (we used only ~20% of maximum power) but we wished to avoid detector saturation. We can see that CEI-XANES reproduces the synchrotron results well, with no discernible difference between the spectra, showing that CEI-XANES is capable of producing sufficient quality spectra for many applications. Similar results for Rowland circle spectrometers using SBCA have been reported elsewhere.[16,19,27]

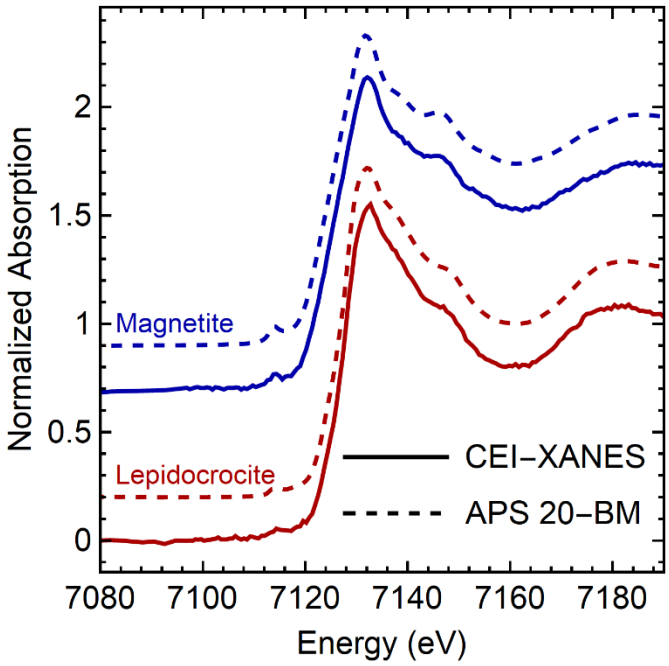

Figure 6.3. Comparison of CEI-XANES (solid) and synchrotron (dashed, collected at APS 20-BM) data for both abiotic magnetite (blue) and lepidocrocite (red). Spectra are offset for clarity.

Figure 4 shows the measurement of an V foil as well as comparison with data taken at Beamline 13-ID of APS, as per an online XAFS database[28]. In this figure, the APS spectrum is shown both as measured and convolved with a Gaussian with FWHM of 0.8 eV. The broadening of 0.8 eV matches the CEI spectrum, so taking into account the energy resolution of the initial spectrum (0.6 eV), we estimate the energy resolution of CEI-XANES at the Fe K-edge to be 1.0 eV. This is similar to previous instruments[27], and given that the 1s core-hole lifetime broadening for transition metals is on the order of 1 eV, this energy resolution is sufficient for many applications. The broadening is likely dominated by the source size in the Rowland plane.

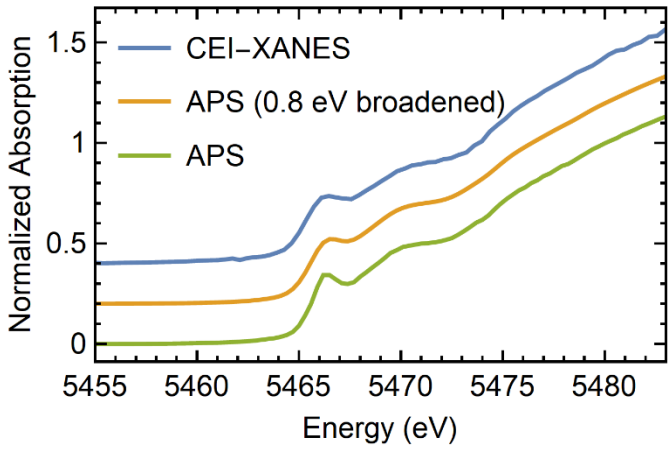

Figure 6.4. Comparison of V Foil XANES spectra taken with CEI-XANES (blue) and at APS (green). Broadening the APS spectrum by 0.8 eV (orange) aligns it well with the CEI-XANES spectrum. Assuming an energy resolution 0.6 eV for the APS data, we estimate an energy resolution of 1.0 eV for CEI-XANES at the V k-edge. Spectra are offset for clarity.

CEI-XANES has its highest flux between 5-11 keV, so quick measurements of ideal samples at these x-ray energies are possible. We demonstrate this here with a few 2-minute scans of the Ni K-edge XANES scans of a NMC pouch cell battery, see Figure 5. A careful I_0 scan was taken before the study and a longer transmission scan (30 minutes) was used to normalize the edge step for the quicker 2-minute scans. These results will be expanded upon elsewhere in a complete *in operando* study of pouch cell charging and discharging.[25]

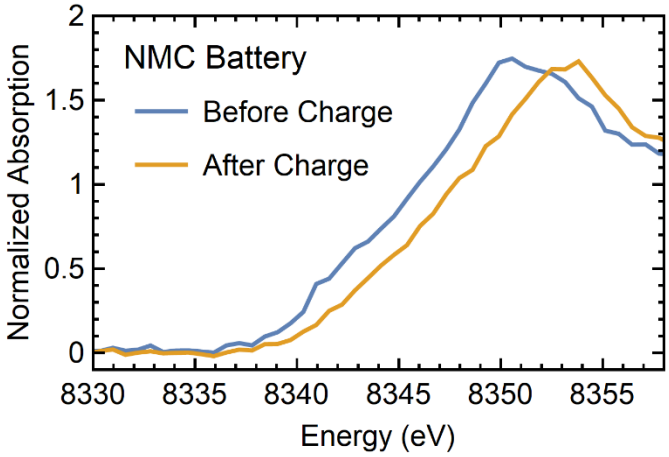

Figure 6.5. Ni XANES spectra of an NMC pouch cell battery before and after charging. Not shown is a scan over a longer range used to normalize these data. Measurement time was 2 minutes for each spectrum. See the text for discussion.

Finally, we report on a 'routine' material characterization example. Ytterbium doped $LiYF_4$ is an important laser cooling material[29], however, when using the Czochralski synthesis, some product crystals could not be cooled upon laser excitation, generating heat instead. One hypothesis is some Yb atoms are reduced to the 2+ oxidation state due to the inclusion of HF in the synthesis, where the strong background absorption by Yb(II) causes the failure of laser cooling. Hence, it is important to learn whether the hydrothermally synthesized, nanophase Yb:$LiYF_4$, in which no HF is used, contains Yb(II).

In Figure 6, bulk and nano-phase Yb:$LiYF_4$ were measured alongside a Yb_2O_3 standard, and are presented alongside a previously measured Yb doped CaF_2 crystal[30]. Previous XANES studies have shown that Yb impurities in calcite and fluorite crystals can be partially in the 2+ oxidation state, and when they are, a pre-edge peak at 8040 eV is present.[30–34] This peak is not present for Yb in the 3+ oxidation state and so the absence of these peaks in both the bulk and nanocrystals indicate Yb is solely in the 3+ oxidation state. This type of routine oxidation-state

identification is a common use-case for the CEI-XANES facility, and one that can be easily performed without the brilliance of a synchrotron beamline.

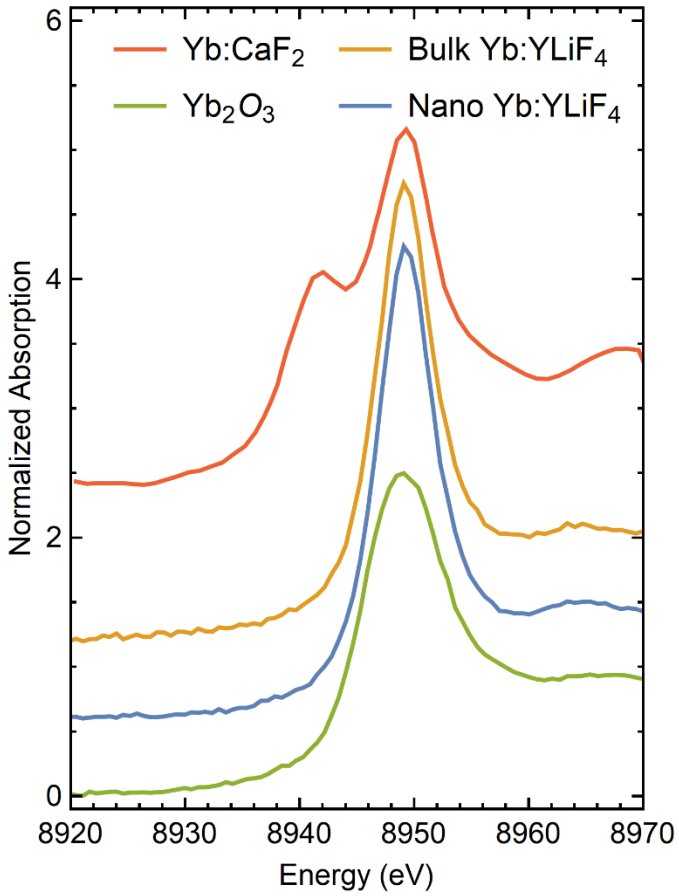

Figure 6.6. Comparison of Nano Yb:$YLiF_4$ crystals (blue) with bulk crystals (yellow), and Yb^{III} standard Yb_2O_3 (green) measured at UW and $Yb^{II/III}$ mixed-valent Yb:CaF_2 (red) reproduced from Yoshida, et al (2005). Spectra offset for clarity.

6.7 Use Landscapes in a Future with Ubiquitous Laboratory XAFS and XES

In addition to the present work, there is a growing body of laboratory spectrometers for XAFS and XES in the hard x-ray[16,18,27,35,36,36–46] and tender x-ray ranges[47–54]. These systems have seen quite varied use, showing an impressive flexibility to address problems in many different fields. For example, the previously mentioned tender x-ray spectrometers have been used to

characterize the phosphorous oxidation state in InP quantum dots[55] and to look at sulfur speciation in biochars[56]. The various hard x-ray instruments have been used to look at oxygen vacancies in V_2O_5[57], to work towards creating a standardized regulatory measurement for Cr oxidation state[58], to look at actinide oxidation state[20], and for a long-duration study of Co/TiO_2 catalysts[21].

These earliest uses in what appears to be an ongoing rebirth of lab XAFS together with the rapidly growing number of lab XAFS systems causes us to wonder about the future. We can realistically imagine a time, perhaps 10 years hence, when the availability of lab XAFS and XES compared to synchrotron XAS has reached a 'sensible' level similar to the relative availabilities of, e.g., lab-based x-ray diffraction (XRD) compared to synchrotron XRD. In such a world, how should we think about the interplay between lab-based and synchrotron capabilities and facilities? Will they compete, be disconnected, or be synergistic? Will the synchrotron XAFS demand decrease because of lab-based capability, or will it instead greatly increase due to a likely new inclusion of XAFS in University education, with possible discovery of new research applications of XAFS?

While any detailed answers to the above questions would be speculative, we can still identify several important categories of interaction between lab and synchrotron XAS, and give exemplars for each. Hence, in Figure 7, we present five schema, which we now discuss in order. First, there is the situation of Fig. 7(a) where the two access paths are fully independent. Independence of lab XAS from the synchrotron is not due to any lack of technical capability at the synchrotron but is instead due to a fundamental mismatch between the character of the desired study and the scientific mission of the synchrotron light sources. Rapid feedback studies during new materials synthesis[55] and, more hypothetically, industrial quality control testing of, e.g., Li-ion battery transition metal oxide electrodes simply do not fit the synchrotron access model: they

require a high level of on-demand measurement. On the other hand, the extreme performance characteristics of synchrotron beamlines support a plethora of studies that are impractical or impossible in the laboratory.

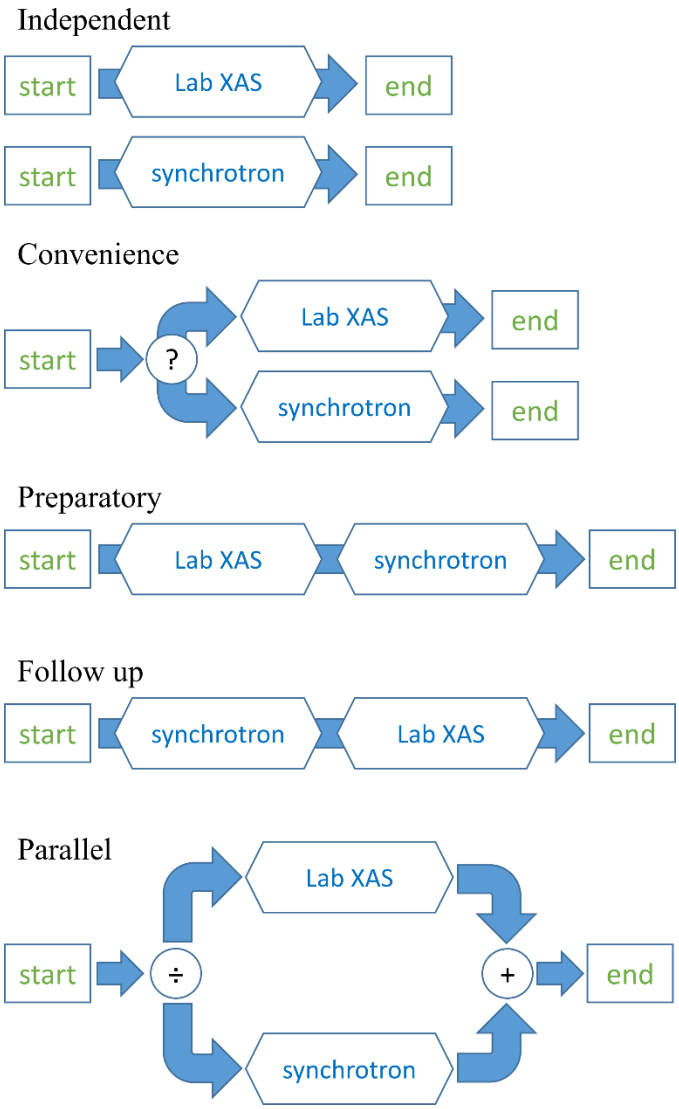

Figure 6.7. Schema outlining the different ways that synchrotron and laboratory XAS interact. See text for further details.

Second, there is the category of user convenience, as in Fig. 7(b). It is only in this access pattern that there is competition between laboratory and synchrotron facilities. The user in this case has a project that meets the scientific standards of the synchrotron so as to pass, for example,

peer review by a general user proposal review panel, but the study could be successfully be performed with a laboratory spectrometer. At present, the question is one of convenience. As modern laboratory XAS systems and lab XAS user and mail-in facilities become more common, it is fair to ask whether the 'question' of operation in this use case may not be in the control of the user, but instead in the hands of the synchrotron review panel. Some years hence, if there is generically high access to lab XAS then it is fair to expect that synchrotron facilities might be able to decline studies that could be performed with lab-based systems.

Third, there are clear benefits from decreasing some of the common inefficiencies ubiquitous in synchrotron XAS beamtime usage. Education of new users is an obvious starting point. Although tutorials and workshops have undeniable value, hands-on lab-based measurement with iteration in demonstration or pedagogical studies would give a rich training that would immediately increase efficiency for future synchrotron beamtime. Further, even experienced users often spend a nontrivial fraction of beamtime refining their sample preparation. Much of this work can be done in the lab, or at least users can become very highly expert in calculating and executing sample preparation outside of beamtime. Finally, the issue of sample and/or experiment design validation must be considered distinct from sample preparation. By validation, we mean any of: at least qualitative confirmation of the synthesis of the desired phase; supporting evidence that the intended physical phenomena will indeed have an effect on the to-be measured spectrum; determination of the efficacy of special sample containers for, e.g., air-sensitive samples; or evaluation of signal levels to better estimate final beamtime needs. This latter case where one seeks more accurate estimation of beamtime needs is one where there is considerable ongoing effort [59].

Fourth, during post-synchrotron beamtime data analysis, users frequently find that some modest additional work would greatly benefit the project, if not in fact be necessary for its

completion. If the measurement demands synchrotron flux or brilliance, then there is no alternative but to wait for repeat beamtime. However, there are at least two obvious cases where lab XAS can serve in this regard. First, when XAFS data on additional reference standards is needed, the studies can typically be performed on concentrated samples. Second, XES can often serve to provide added context to aid with interpretation of XANES, in particular. This same synergy plays a likely role below, in the final use case.

Finally, there are likely cases where lab-based spectroscopy will strictly enhance synchrotron work at an equal level of scientific merit, rather than merely augmenting in support. The most obvious example is using lab-based nonresonant XES to provide direct context for better interpretations of synchrotron-based XANES results. Valence-to-core XES can clearly improve understanding of bonding character without need to address the subtleties of core-hole effects, and Kα XES can sometimes give a cleaner fingerprint of classical oxidation state of the species of interest than can XANES, as the former is less sensitive to local environment than the latter.[56]

6.8 CONCLUSION

We have demonstrated the capabilities of the CEI-XANES instrument as the first mail-in XANES user facility using lab-based instrumentation, and shown the capability to produce synchrotron-quality spectra in the 5-11 keV range. We have also outlined a number of ways that laboratory systems interact with synchrotron x-ray spectroscopies, and argue that laboratory spectrometers are best seen not as a direct competitor with synchrotron operations, but rather as an expansion of the existing XAFS access landscape to become more similar to those of the overwhelming majority of other analytical method. This will expand the user base especially in the emerging field of ‘analytical’ applications of XAFS but will also lead to better prepared and, we can hope, high impact synchrotron XAFS studies in disciplines where XAFS has not yet made

entry. Therefore, the continuing development of laboratory instruments, including user-facility class instruments like the one described here are a promising sign for increased access and an expansion in the utilization of x-ray absorption spectroscopy.

6.9 Acknowledgements

We gratefully acknowledge the help of Maxim I. Boyanov and Kenneth M. Kemmer in providing the iron reference standards and synchrotron measurements at APS 20-ID. We would also like to thank Bryant J. Polzin, Steven E. Trask, and Allison R. Dunlop of Argonne for helping to produce the NMC battery.

6.10 Funding Information

This material is based in part upon work supported by the State of Washington through the University of Washington Clean Energy Institute and via funding from the Washington Research Foundation. EPJ was supported in part by the Joint Center for Energy Storage Research (JCESR), an Energy Innovation Hub funded by the U.S. Department of Energy, Office of Science, and Basic Energy Sciences. Part of this work was conducted at the Molecular Analysis Facility, a National Nanotechnology Coordinated Infrastructure site at the University of Washington which is supported in part by the National Science Foundation (grant NNCI-1542101), the University of Washington, the Molecular Engineering & Sciences Institute, and the Clean Energy Institute. X.X., and P.J.P. gratefully acknowledge financial support from the MURI:MARBLe project under the auspices of the Air Force Office of Scientific Research (Award No. FA9550-16-1-0362). This research used resources of the Advanced Photon Source, an Office of Science User Facility operated for the U.S. Department of Energy (DOE) Office of Science by Argonne National

Laboratory, and was supported by the U.S. DOE under Contract No. DE-AC02-06CH11357, and the Canadian Light Source and its funding partners.

6.11 REFERENCES

1. Bunker, G. *Introduction to XAFS*. (Cambridge University Press, 2010). doi:10.1017/CBO9780511809194

2. de Groot, F., Kotani, A. & Kotani, A. *Core Level Spectroscopy of Solids*. (CRC Press, 2008). doi:10.1201/9781420008425

3. Caudillo-Flores, U., Muñoz-Batista, M. J., Kubacka, A. & Fernández-García, M. Operando Spectroscopy in Photocatalysis. *ChemPhotoChem* **2**, 777–785 (2018).

4. John Meurig Thomas*, †,‡ and & Gopinathan Sankar*, †. The Role of Synchrotron-Based Studies in the Elucidation and Design of Active Sites in Titanium−Silica Epoxidation Catalysts. (2001). doi:10.1021/AR010003W

5. McBreen, J., O'Grady, W. E. & Pandya, K. I. EXAFS: A new tool for the study of battery and fuel cell materials. *J. Power Sources* (1988). doi:10.1016/0378-7753(88)80027-2

6. McBreen, J. The application of synchrotron techniques to the study of lithium-ion batteries. *J. Solid State Electrochem.* **13**, 1051–1061 (2009).

7. Cheng, H. *et al.* Synchrotron radiation X-ray powder diffraction techniques applied in hydrogen storage materials - A review. *Prog. Nat. Sci. Mater. Int.* **27**, 66–73 (2017).

8. Li, W. *et al.* Synchrotron-Based X-ray Absorption Fine Structures, X-ray Diffraction, and X-ray Microscopy Techniques Applied in the Study of Lithium Secondary Batteries. *Small Methods* **2**, 1700341 (2018).

9. Ma, B., Charlet, L., Fernandez-Martinez, A., Kang, M. & Madé, B. A review of the retention mechanisms of redox-sensitive radionuclides in multi-barrier systems. *Appl. Geochemistry* **100**, 414–431 (2019).

10. Young, N. A. The application of synchrotron radiation and in particular X-ray absorption spectroscopy to matrix isolated species. *Coord. Chem. Rev.* **277**–**278**, 224–274 (2014).

11. Sarangi, R. X-ray absorption near-edge spectroscopy in bioinorganic chemistry: Application to M–O2 systems. *Coord. Chem. Rev.* **257**, 459–472 (2013).

12. Porcaro, F., Roudeau, S., Carmona, A. & Ortega, R. Advances in element speciation analysis of biomedical samples using synchrotron-based techniques. *TrAC Trends Anal. Chem.* **104**, 22–41 (2018).

13. Kowalska, J. & DeBeer, S. The role of X-ray spectroscopy in understanding the geometric and electronic structure of nitrogenase. *Biochim. Biophys. Acta - Mol. Cell Res.* **1853**, 1406–1415 (2015).

14. Kosog, B., La Pierre, H. S., Denecke, M. A., Heinemann, F. W. & Meyer, K. Oxidation State Delineation via U L_{III} -Edge XANES in a Series of Isostructural Uranium Coordination Complexes. *Inorg. Chem.* **51**, 7940–7944 (2012).

15. Shi, W.-Q. *et al.* Exploring Actinide Materials Through Synchrotron Radiation Techniques. *Adv. Mater.* **26**, 7807–7848 (2014).

16. Seidler, G. T. *et al.* A laboratory-based hard x-ray monochromator for high-resolution x-ray emission spectroscopy and x-ray absorption near edge structure measurements. *Rev. Sci. Instrum.* **85**, 113906 (2014).

17. Seidler, G., Mortensen, D., Ditter, A., Ball, N. & Remesnik, A. A Modern Laboratory XAFS Cookbook. *J. Phys. Conf. Ser.* **712**, 012015 (2016).

18. Knapp, G. S., Chen, H. & Klippert, T. E. Development of a laboratory EXAFS facility. *Rev. Sci. Instrum.* **49**, 1658–1666 (1978).

19. Honkanen, A.-P. *et al.* Johann-type laboratory-scale x-ray absorption spectrometer with versatile detection modes. *Rev. Sci. Instrum.* **90**, 033107 (2019).

20. Bès, R. *et al.* Laboratory-scale X-ray absorption spectroscopy approach for actinide research: Experiment at the uranium L3-edge. *J. Nucl. Mater.* **507**, 50–53 (2018).

21. Moya-Cancino, J. G. *et al. In-situ* X-Ray Absorption Near Edge Structure Spectroscopy of a Solid Catalyst using a Laboratory-Based Set-up. *ChemCatChem* **11**, 1039–1044 (2019).

22. Jahrman, E. P. *et al.* Vacuum formed temporary spherically and toroidally bent crystal analyzers for x-ray absorption and x-ray emission spectroscopy. *Rev. Sci. Instrum.* **90**, 013106 (2019).

23. Mortensen, D. R. & Seidler, G. T. Robust optic alignment in a tilt-free implementation of the Rowland circle spectrometer. *J. Electron Spectros. Relat. Phenomena* **215**, 8–15 (2017).

24. Ravel, B. & Newville, M. ATHENA , ARTEMIS , HEPHAESTUS : data analysis for X-ray absorption spectroscopy using IFEFFIT. *J. Synchrotron Radiat.* **12**, 537–541 (2005).

25. Jahrman, E. P. *et al.* Laboratory-based X-ray Absorption Spectroscopy on a Working Pouch Cell Battery. (2019).

26. Roder, P. B., Smith, B. E., Zhou, X., Crane, M. J. & Pauzauskie, P. J. Laser refrigeration of hydrothermal nanocrystals in physiological media. *Proc. Natl. Acad. Sci. U. S. A.* **112**, 15024–9 (2015).

27. Jahrman, E. P. *et al.* An improved laboratory-based x-ray absorption fine structure and x-ray emission spectrometer for analytical applications in materials chemistry research. *Rev. Sci. Instrum.* **90**, 024106 (2019).

28. GSE-CARS XAFS Spectra Library (beta). Available at: http://cars.uchicago.edu/xaslib/search. (Accessed: 28th May 2019)

29. Cittadino, G., Volpi, A., Di Lieto, A. & Tonelli, M. Co-doping of $LiYF_4$ crystal: a virtuous effect of cooling efficiency. *J. Phys. D. Appl. Phys.* **51**, 145302 (2018).

30. Yoshida, T., Kagi, H., Tsuno, H., Ohta, A. & Nomura, M. Oxidation States of Ytterbium Incorporated in Calcium Carbonate and Calcium Fluoride. *Chem. Lett.* **34**, 852–853 (2005).

31. Iyer, A. K. & Peter, S. C. EuLiGe2 and YbLiGe2 - A Divalent and an Intermediate-Valent Compound with CaLiSi2-Type Structures. *Eur. J. Inorg. Chem.* **2012**, 1790–1794 (2012).

32. Peter, S. C., Disseler, S. M., Niclas Svensson, J., Carretta, P. & Graf, M. J. Yb4LiGe4 – A Yb mixed valent Zintl phase with strong electronic correlations. *J. Alloys Compd.* **516**, 126–133 (2012).

33. Rao, C. N. R. *et al.* Valence fluctuation in some Yb intermetallics by X-ray photoemission and X-ray absorption. *Chem. Phys. Lett.* **76**, 413–415 (1980).

34. Hatwar, T. K. *et al.* X-ray absorption spectroscopic study of mixed valence systems EuCu2Si2, YbCu2Si2 and Sm4Bi3. *Solid State Commun.* **34**, 617–620 (1980).

35. Hoszowska, J., Dousse, J.-C., Kern, J. & Rhême, C. High-resolution von Hamos crystal X-ray spectrometer. *Nucl. Instruments Methods Phys. Res. Sect. A Accel. Spectrometers, Detect. Assoc. Equip.* **376**, 129–138 (1996).

36. Németh, Z., Szlachetko, J., Bajnóczi, É. G. & Vankó, G. Laboratory von Hámos X-ray spectroscopy for routine sample characterization. *Rev. Sci. Instrum.* **87**, 103105 (2016).

37. Kayser, Y. *et al.* Laboratory-based micro-X-ray fluorescence setup using a von Hamos crystal spectrometer and a focused beam X-ray tube. *Rev. Sci. Instrum.* **85**, 043101 (2014).

38. Malzer, W. *et al.* A laboratory spectrometer for high throughput X-ray emission spectroscopy in catalysis research. *Rev. Sci. Instrum.* **89**, 113111 (2018).

39. Schlesiger, C., Anklamm, L., Stiel, H., Malzer, W. & Kanngießer, B. XAFS spectroscopy by an X-ray tube based spectrometer using a novel type of HOPG mosaic crystal and optimized image processing. *J. Anal. At. Spectrom.* **30**, 1080–1085 (2015).

40. Szlachetko, M., Berset, M., Dousse, J.-C., Hoszowska, J. & Szlachetko, J. High-resolution Laue-type DuMond curved crystal spectrometer. *Rev. Sci. Instrum.* **84**, 093104 (2013).

41. Cohen, G. G., Fischer, D. A., Colbert, J. & Shevchik, N. J. Tunable laboratory extended x-

ray absorption fine structure system. *Rev. Sci. Instrum.* **51**, 273–277 (1980).

42. Thulke, W., Haensel, R. & Rabe, P. Versatile curved crystal spectrometer for laboratory extended x-ray absorption fine structure measurements. *Rev. Sci. Instrum.* **54**, 277–283 (1983).

43. Tohji, K., Udagawa, Y., Kawasaki, T. & Masuda, K. Laboratory EXAFS spectrometer with a bent crystal, a solid-state detector, and a fast detection system. *Rev. Sci. Instrum.* **54**, 1482–1487 (1983).

44. Williams, A. Laboratory x-ray spectrometer for EXAFS and XANES measurements. *Rev. Sci. Instrum.* **54**, 193–197 (1983).

45. Yuryev, Y. N. *et al.* Variable Rowland radius laboratory vacuum surface-sensitive x-ray absorption fine structure spectrometer. *Rev. Sci. Instrum.* **78**, 025108 (2007).

46. Anklamm, L. *et al.* A novel von Hamos spectrometer for efficient X-ray emission spectroscopy in the laboratory. *Rev. Sci. Instrum.* **85**, 053110 (2014).

47. Dolgih, V. E. *et al.* X-ray fluorescent spectrometer with linear position sensitive detector. *Nucl. Instruments Methods Phys. Res.* **224**, 117–119 (1984).

48. Yarmoshenko, Y. M. *et al.* Possibility of sulphur-oxygen substitution in YBa2Cu3O6+xSy analyzed by means of X-ray emission spectroscopy. *J. Phys. Chem. Solids* **54**, 1211–1214 (1993).

49. Yarmoshenko, Y. M., Trofimova, V. A., Kurmaev, E. Z., Slater, P. R. & Greaves, C. X-ray emission spectra of YSr2Cu3O7−δ containing sulphate and phosphate groups. *Phys. C Supercond.* **224**, 317–320 (1994).

50. Yarmoshenko, Y. M. *et al.* X-ray emission spectra and valence state of sulphur atoms of $YBa_2((CuO)_{1-x}(NiS)_x)_3O_{4-delta}$. *J. Phys. Condens. Matter* **7**, 213–218 (1995).

51. Sugiura, C., Gohshi, Y. & Suzuki, I. Sulfur K β x-ray emission spectra and electronic structures of some metal sulfides. *Phys. Rev. B* **10**, 338–343 (1974).

52. Sugiura, C., Gohshi, Y. & Suzuki, I. Kβ Emission and *K* Absorption Spectra of Sulfur in MnS. *Jpn. J. Appl. Phys.* **11**, 911–912 (1972).

53. Kavčič, M. *et al.* Design and performance of a versatile curved-crystal spectrometer for high-resolution spectroscopy in the tender x-ray range. *Rev. Sci. Instrum.* **83**, (2012).

54. Holden, W. M. *et al.* A compact dispersive refocusing Rowland circle X-ray emission spectrometer for laboratory, synchrotron, and XFEL applications. *Rev. Sci. Instrum.* **88**, 073904 (2017).

55. Stein, J. L. *et al.* Probing Surface Defects of InP Quantum Dots Using Phosphorus Kα and Kβ X-ray Emission Spectroscopy. *Chem. Mater.* **30**, 6377–6388 (2018).

56. Holden, W. M., Seidler, G. T. & Cheah, S. Sulfur Speciation in Biochars by Very High Resolution Benchtop Kα X-ray Emission Spectroscopy. *J. Phys. Chem. A* **122**, 5153–5161 (2018).

57. Bi, W. *et al.* Tailoring Energy and Power Density through Controlling the Concentration of Oxygen Vacancies in V_2O_5 /PEDOT Nanocable-Based Supercapacitors. *ACS Appl. Mater. Interfaces* **11**, 16647–16655 (2019).

58. Jahrman, E. P., Seidler, G. T. & Sieber, J. R. Determination of Hexavalent Chromium Fractions in Plastics Using Laboratory-Based, High-Resolution X-ray Emission Spectroscopy. *Anal. Chem.* **90**, 6587–6593 (2018).

59. Abe, H. *et al.* Improving the quality of XAFS data. *J. Synchrotron Radiat.* **25**, 972–980 (2018).

Chapter 7. RESONANT INELASTIC X-RAY SCATTERING USING A MINIATURE DISPERSIVE X-RAY SPECTROMETER

7.1 PREFACE

This is a paper submitted to the Journal of Synchrotron Radiation. It is formatted in the style of this journal. This paper demonstrates the use of the tender x-ray spectrometer developed by Holden *et al.* for resonant inelastic x-ray spectroscopy. I led this experiment, from writing the beamtime proposal to make this study possible, to integrating the instrument with beamline facilities and performing the measurements, to writing the paper. This paper is a more complete description of the types of measurements which are the subject of chapter 5.

Authors

Alexander S. Ditter[ab], William M. Holden[a], Samantha Cary[b], Veronika Mocko[b], Matthew T. Latimer[c], Erik Nelson[c], Stosh A. Kozimor[b]* and Gerald T. Seidler[a]*
[a]Department of Physics, University of Washington, PO Box 351650, Seattle, Washington, 98195-1560, USA
[b]C-IIAC, Los Alamos National Laboratory, PO Box 1663, Los Alamos, New Mexico, 87545, USA
[c]Stanford Synchrotron Radiation Lightsource, SLAC National Accelerator Laboratory, 2575 Sand Hill Rd, Menlo Park, CA, 94025, USA

7.2 ABSTRACT

X-ray absorption spectroscopy (XAS) beamlines worldwide are steadily increasing their emphasis on full photon-in / photon-out spectroscopies, such as resonant inelastic x-ray scattering (RIXS), resonant x-ray emission spectroscopy (RXES), and high energy resolution fluorescence detection XAS (HERFD-XAS). In such cases, each beamline must match the choice of emission spectrometer to the scientific mission of its users. Previous work has recently reported a miniature

tender x-ray spectrometer using a dispersive Rowland refocusing (DRR) geometry that functions with high energy resolution even with a large x-ray spot size on the sample [1]. This instrument has been used in the laboratory in multiple studies of non-resonant x-ray emission spectroscopy (XES) using a conventional x-ray tube, but only for preliminary measurements at a low-intensity, microfocus synchrotron beamline. Here we report an extensive study of the performance of the miniature DRR spectrometer at an unfocused wiggler beamline, where the incident monochromatic flux allows for resonant studies, which are impossible in the laboratory. These results support the broader use of the present design and also suggest the DRR method with an unfocused beam could have important application for materials having low radiation damage thresholds and that therefore would not survive analysis on focused beam lines.

7.3 INTRODUCTION

The more complete utilization of fully photon-in / photon-out x-ray spectroscopies in the tender x-ray regime (2 – 5 keV) shows great scientific promise[2–8]. Despite the demonstrated high impact for these spectroscopic studies, the tasks of expanding material type compatibility and experimental access throughout the scientific community faces numerous challenges. There exist both logistical barriers in the relatively small number of high flux beamlines operating in the tender x-ray range (e.g., ESRF 12-ID, 26-ID, SSRL 4-3, 6-2, NSLSII 7-ID) and also technical barriers in the design and operation of the needed x-ray emission spectrometers[9–12]. Key technical considerations include compatibility with beamline design and vacuum systems, mitigation of beam damage, and the complexity and cost of spectrometer development.

For these reasons, recent work in laboratory-based x-ray emission spectroscopy provides an interesting development[1]. Those authors developed an extremely compact tender x-ray emission spectrometer using the dispersive Rowland refocusing (DRR) geometry that largely removes

source size effects on spectrometer energy resolution. While the removal of source-size effects has enabled steady application of that instrument in the laboratory environment with only a conventional, unfocused x-ray tube source[13,14], the small size and compatibility of the equipment with either helium or vacuum environments suggested the versatility for synchrotron application. Nonetheless, the study by Holden *et al.* gave only a preliminary investigation at a low-flux beamline. Here, we give a broader assessment of the miniature DRR spectrometer in synchrotron applications, where we use an unfocused wiggler beamline at the Stanford Synchrotron Radiation Laboratory (SSRL) on beam line (BL) 4-3 to perform resonant inelastic x-ray scattering (RIXS) studies in the tender x-ray regime; sulfur (S) Kα, S Kβ, and uranium (U) Mβ RIXS. The instrument performance was successful and shows good potential use at other high-flux tender x-ray beamlines, especially for studies of materials having low radiation damage thresholds.

7.4 EXPERIMENTAL

7.4.1 *DRR Spectrometer and Installation at Beamline 4-3*

The tender x-ray emission spectrometer operates in a DRR geometry. As shown in Figure 7.1a, a point source on the Rowland circle ray-traces symmetrically to a point on the detection arc of the Rowland circle. In Figure 7.1b, a large source that is positioned significantly interior to the Rowland circle is seen by the analyzer as equivalent to a superposition of discrete source points of varying energy, resulting in spectral refocusing onto each point on a corresponding detector arc but without any imaging of sample location, i.e., the detected spectrum is at least significantly a spatial average, loosening sample preparation homogeneity constraints. Operation of a Rowland circle spectrometer with an extended source on the Rowland circle has seen discussion by[15], and commonly in plasma physics research[16–29], where combined imaging and spectroscopy is achieved.

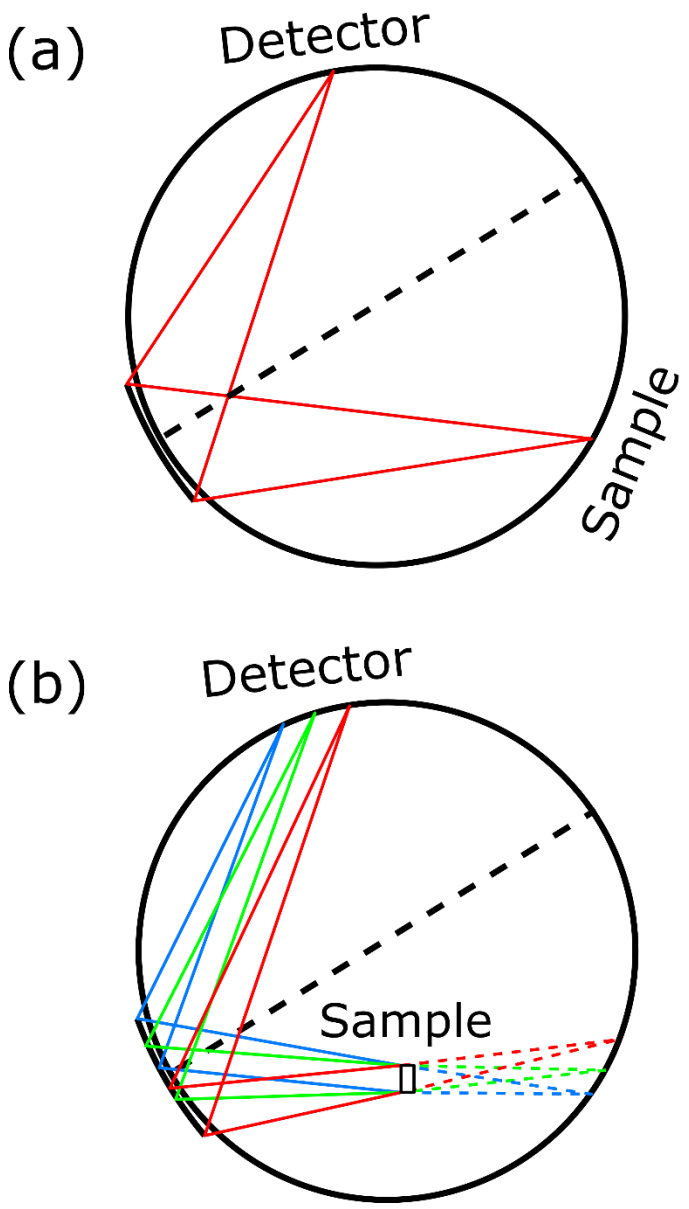

Figure 7.1. Rowland circle diagram of a point-focusing spectrometer design (a) and a dispersive Rowland refocusing (DRR) design (b). In the point-focusing case, the sample and detector must be scanned across the circle to measure the spectrum, but in the DRR case, the entire spectrum is collected at once with a position-sensitive detector. Placing the detector tangent to the Rowland circle removes source-size broadening effects.

Complete instrument details are given in the previous work[1]. Here we only briefly survey the instrument design before carefully addressing the installation and use at the synchrotron. All studies were performed at beamline 4-3 of the Stanford Synchrotron Radiation Laboratory (SSRL).

This is a wiggler beamline with a double Si(111) monochromator. The incident flux at the S K-edge and the U M_4 edge were approximately ~5 x 10^{11}/s and 1 x 10^{12}/s, respectively, as measured by upstream gas ionization chambers. The beam size was approximately 10 mm (horizontal) by 0.5 mm (vertical). A photograph of the installed spectrometer at BL 4-3 is given in Figure 7.2a and shows an interesting constraint: BL 4-3 is a side-station with only ~7 cm clearance between the beam and the hutch wall. The small size of the DRR spectrometer's helium/vacuum chamber fortuitously accommodates this tight clearance when rotated so that the optic was in the preferred horizontal direction to suppress elastic scattering. The spectrometer was directly attached to the helium-filled beampipe using a flexible bellows without any intervening window. A slow flow of helium was used to continually flush the system.

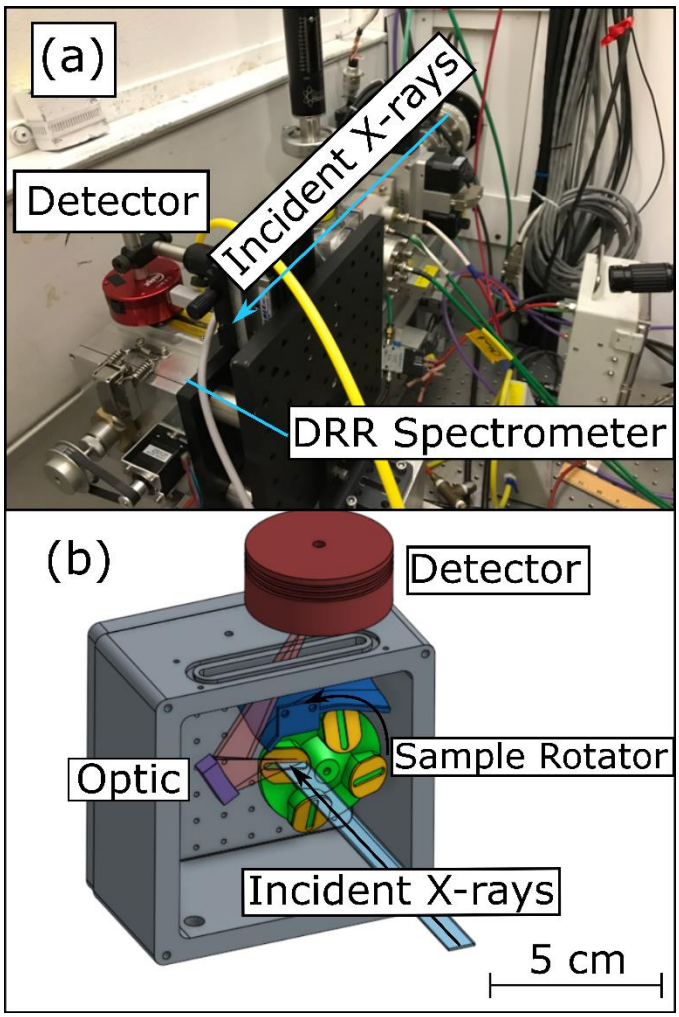

Figure 7.2. a) – Picture of the DRR x-ray spectrometer mounted at beamline 4-3 of SSRL. b) – A computer aided design (CAD) rendering of the spectrometer's interior, showing the incident beam (blue), sample holder (yellow), sample rotator (green), focusing optic (purple), and sample emission (red). Note that the orientation changes between the two subfigures.

A rendering of the spectrometer in the as-installed orientation is given in Figure 7.2b. As shown, the sample footprint (preparation described below) was designed to match the unfocused beam spot. Fluorescence from the sample illuminates the 10-cm radius Si (111) cylindrical analyzer crystal (XRSTech) and is detected by a home-made spectroscopic x-ray camera [1,30] that is positioned on the Rowland circle defined by the analyzer. The spectroscopic nature of the camera allows energy-windowing of each detected event to reject stray scatter backgrounds at energies far

from the anticipated fluorescence line. However, the camera also limits the upper energy range of the spectrometer, as the quantum efficiency of the detector decreases with increasing energy. The efficiency is approximately 50% near sulfur Kβ (2.5 keV), 35% near uranium Mβ (3.7 keV), and drops to <10% above 6 keV[30]. The x-ray camera, sample turret motor, and camera motors were run using a user laptop. Coordination between the user laptop and the beamline software was straightforward, using a TTL gate signal to trigger the camera software on the laptop, just as is typically used for other detectors.

Fine alignment of the spectrometer was performed at the beamline. First, the energy of the incident x-rays is tuned to the maximum of the white line of the absorption spectrum of the sample (e.g., incident energy 2472 eV for $Na_2S_2O_3$). The position of the spectrometer perpendicular to the beam was adjusted by motorized stages to achieve maximal count rates. Then the camera position is optimized to focus the emission spectrum in the center of the camera. When complete, this alignment finds a full-width half-maximum of 0.81 eV for the elastic scattering peak at 2472 eV, see section 8.5 for more discussion of performance.

7.4.2 *Sample Preparation*

The $(PPh_4)_2WS_4$ and $Na_2S_2O_3$ compounds were prepared on the benchtop for S K-edge spectroscopic analyses and analyzed at beamline 4-3 of SSRL. Samples intended for x-ray absorption spectroscopy (XAS) were prepared so that total fluorescence measurements (TFY) on the samples could be obtained for comparison with subsequent RIXS measurements. These samples were mounted in an aluminum sample holders consisting of a simple 1-mm thick aluminum plates with 5 mm × 20 mm slots. Single-sided tape (40 mm) that had been confirmed by x-ray fluorescence spectroscopy to contain low concentrations of sulfur was fixed to the downstream side of the holder. Analytes were prepared by finely grinding the sample for 2 min in

polystyrene canisters with Teflon pestles using an automatic grinder to obtain a homogeneous fine powder. The sample canisters and pestles showed no detectable S by x-ray fluorescence analysis. The finely divided powder was then uniformly dispersed onto the single-sided tape using a Winsor & Newton paintbrush, which did not contain significant amounts of S as determined by independent S K-edge XAS analysis. The sample holder was sealed by adhering a 4-mm thick polypropylene window (SPEX CertiPrep 3525 Ultralene) to the aluminum plate double-sided tape, the latter slotted to match the front side of the sample holder. The x-ray absorption spectra (XAS) samples were inserted into a sample chamber flushed continuously with helium gas.

RIXS samples were prepared by loading the finely ground samples (appx. 60 mg) into RIXS sample holders. These were 1-mm thick aluminum plates with a 5 mm × 20 mm slots, i.e., similar to the XAS holder. They differ in that the downstream side of the plates were sealed with five layers of single-sided low-S content tape. This thick backing prevented transmission to (and subsequent fluorescence of) the sample turret, thus decreasing potential backgrounds. The upstream side of the holder was equipped with a polypropylene window (4 μm) that was secured to the holder with double-sided tape. Sample holders were fixed to the sample rotator with double-sided tape.

The $Cs_2UO_2Cl_4$ compound was prepared as previously described[31]. It should be emphasized that uranium is radioactive and represents a hazard to human health. These experiments should only be performed in facilities with the proper controls in place to handle radioactive material. The sample was prepared in an argon-filled glovebox and finely ground for 2 min in polystyrene canisters with plexiglass pestles using a Wig-L-Bug grinder. A 5 mm x 20 mm x 1 mm aluminum well was filled with the sample (appx. 50 mg). The back of the sample holder was sealed with a single layer of 1 mil thick Kapton tape. The front of the holder was sealed

with a piece of polypropylene (4 µm thick). The entire sample holder was covered with a second layer of containment, which consisted of a single layer of 1 mil thick Kapton tape on the back and a second layer of polypropylene (4 µm thick) on the front. This envelope provided a second layer of containment. The sample assembly was then shipped to SSRL.

7.4.3 *Data Collection and Operating Conditions*

Sulfur K-edge x-ray absorption spectra (XAS) were collected within the LANL Tender X-ray Chamber at BL 4-3 under dedicated operating conditions (3.0 GeV, 500 mA) for normalization of the S RIXS spectra. This chamber and incident flux (I_0) gas ionization detector were separated from the beam pipe by a beryllium window. Sample fluorescence was monitored using a partially depleted series charged particle detector with a 5000 mm^2 active area (Mirion Technologies, model PD5000-75-500AM). The energy scale was calibrated by setting the energy of the pre-edge maximum of a thin $Na_2S_2O_3$ sample to 2742.02 eV[32]. Measurement times were 5 minutes total per incident energy point with a total RIXS plane measurement time of 5 hours. We ruled out beam damage (in this and other spectra in this paper) by observing no changes during several scans over the incident energy range.

All RIXS measurements were done under dedicated operating conditions (3.0 GeV, 500 mA) at beamline 4-3 of SSRL. Sulfur x-ray emission measurements used a cylindrically-bent Si (111) optic at median Bragg angles of 58.9° (Kα) and 54.5° (Kβ), respectively. Uranium Mβ RIXS measurements used a cylindrically-bent Ge (220) optic at a median Bragg angle of 68.0°. Incident energy scales were calibrated to the pre-edge maximum of a thin $Na_2S_2O_3$ sample at 2472.02 eV and a thin KCl sample at 3608.4 eV for sulfur and uranium samples, respectively. Emission energy scales of sulfur were calibrated to the highest energy peak of non-resonant $Na_2S_2O_3$ emission at 2309.12 eV, which corresponds to the $K\alpha_1$ of the S^{6+} atom. We expect this to be similar to S^{6+}

compounds measured previously, which showed little variation, and matched this peak to the 2309.12 eV S $K\alpha_1$ of Na_2SO_4[33]. For S Kβ RIXS, we used the elastic scatter peak of $Na_2S_2O_3$ at 2472 eV (with incident x-ray energy of 2472 eV) for calibration, and for U Mβ, we used the non-resonant $UO_2Cl_4^{2-}$ emission at 3339.8 eV[34].

7.4.4 *Data Processing and Self-Absorption Corrections*

Because the samples were thick, and we wished to take cuts in the RIXS plane to obtain HERFD spectra, self-absorption corrections are needed. First, we define an effective absorption coefficient $\mu_{RIXS}(E_i)$ as the sum over emitted energy of the measured RIXS intensity, i.e., a partial fluorescence yield (PFY) measurement of the x-ray absorption for the particular fluorescence energy range being studied,

$$\mu_{RIXS}(E_i) = \sum_{E_e} I_{RIXS}(E_i, E_e) \quad (1)$$

where $I_{RIXS}(E_i, E_e)$ is the intensity of the measured RIXS spectrum at emitted energy, E_e and incident energy E_i. Under the assumption that the PFY signal on the thick RIXS sample is roughly proportional to a total fluorescence yield (TFY) signal on the same (thick) sample, we then see that the sample self-absorption can be corrected by the ratio of a TFY measurement on a thin sample (i.e., not exhibiting self-absorption) and the measured PFY signal integrated from the RIXS,

$$I_{Corrected}(E_i, E_e) = I_{RIXS}(E_i, E_e)\frac{\mu_{TFY}(E_i)}{\mu_{RIXS}(E_i)}, \quad (2)$$

where $I_{Corrected}(E_i, E_e)$ is the final corrected RIXS spectrum and $\mu_{TFY}(E_i)$ is the XAS spectrum collected on a thin sample in fluorescence mode. We can see that summing over the emitted energy of the corrected RIXS spectrum yields the TFY absorption spectrum on a thin sample, as desired.

This self-absorption correction was applied to all RIXS datasets, and results in corrections of less than 20%.

Other data processing was minimal. Several of the collected spectra had hot pixels which were filtered. Each emission spectrum was normalized to the time-integrated incident x-ray intensity measured at the I_0 ion chamber. XAS data was normalized to an edge-step of unity using the `Athena` and the `Demeter` packages[35].

7.5 Results and Discussion

It is useful to briefly describe the underlying physics of the S Kα RIXS experiment. A naïve description involves two-steps. There is an excitation to an intermediate excited state followed by characterization of the relaxation process to a final excited state. Using orbital descriptions (Figure 7.3), the excitation involves bound-state transitions between S 1*s*-orbitals and virtual (unoccupied) orbitals that contain, e.g., some degree of S 3*p*-character, for excitations near the S K-edge. The emission involves electronic relaxation from the S 2*p*-orbitals to the S 1*s*-orbitals. Hence, for a free S^{6+} ion (no ligand field), the experiment involves electronic excitation of the $1s^2\ 2s^2\ 2p^6\ 3p^0$ ground-state to the intermediate $1s^1\ 2s^2\ 2p^6\ 3p^1$ excited electronic state followed by relaxation to the $1s^2\ 2s^2\ 2p^5\ 3p^1$ final excited state.

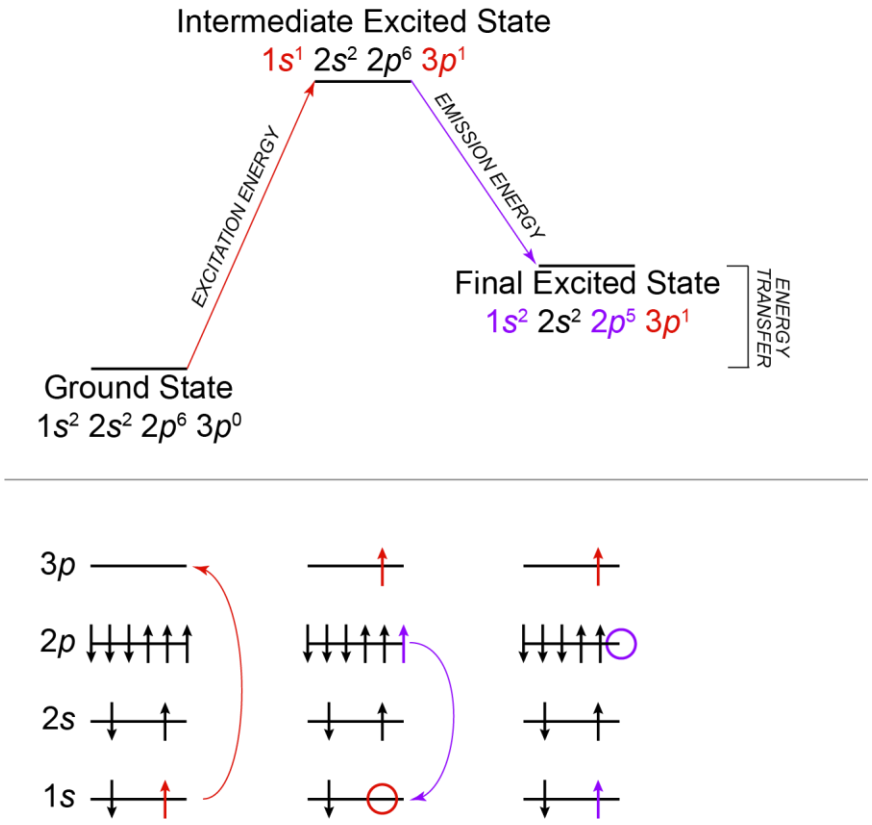

Figure 7.3. A general description for electron transfer processes for a free S^{6+} ion during the S Kα RIXS spectroscopy experiment.

Figure 7.4 shows experimental S Kα RIXS data from two compounds, $(PPh_4)_2WS_4$ and $Na_2S_2O_3$, with the intensity is plotted as a function of incident energy and energy transfer (incident energy minus emitted energy, Figure 7.3). Plotting versus energy transfer makes it clear that the broadening of the final and intermediate states are independent, and that a diagonal cut across the RIXS plane at constant emission energy can yield an XAS-like spectrum where the core-hole lifetime broadening is suppressed[36]; this is the basis of so-called high energy resolution fluorescence detection (HERFD).

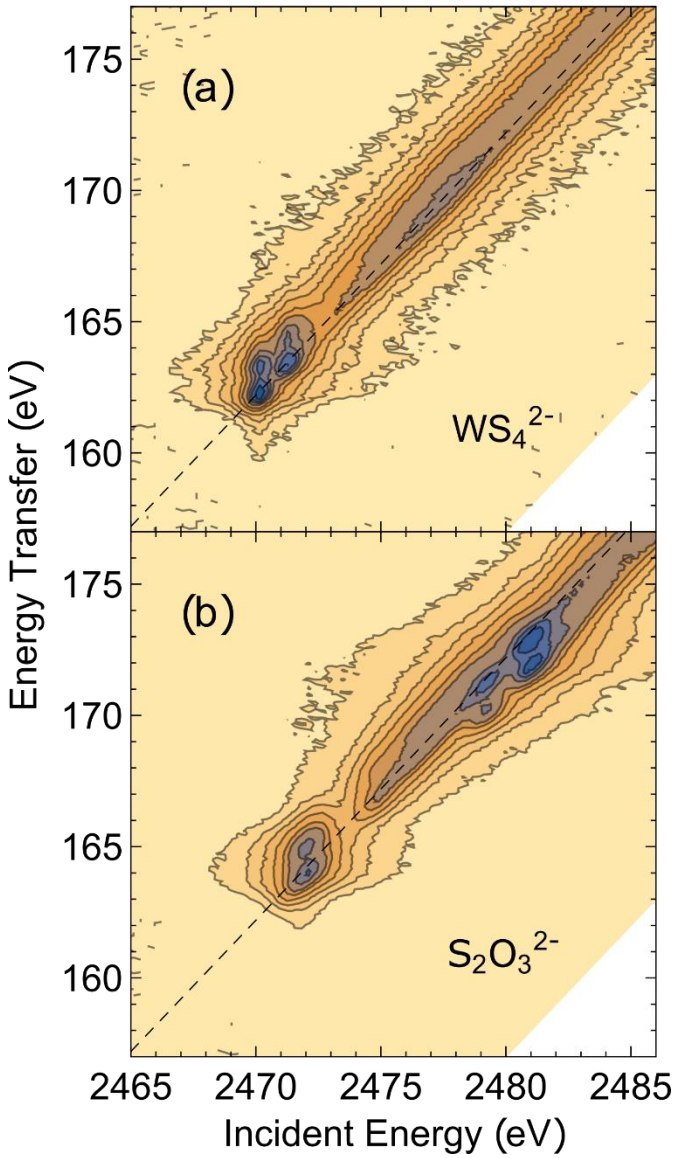

Figure 7.4. Contour plots showing the resonant inelastic x-ray scattering (RIXS) measurements from $(PPh_4)_2WS_4$ (a) and $Na_2S_2O_3$ (b). Each plot shows energy transfer (S K-edge x-ray absorption energies minus the $K\alpha_1$, $K\alpha_2$, x-ray emission energies) versus the S K-edge x-ray absorption energy. The dotted line corresponds to a constant emission energy cut at 2307.8 eV.

WS_4^{2-} is a well-studied system in XANES, with a pair of pre-edge features due to excitation into unoccupied molecular orbitals which split into e and t_2[37–40]. The RIXS spectrum obtained here contains a quartet of low energy peaks whose final excited states (energy transfer) are approximately 163 eV above the ground state incident energies near 2473 eV). The four features are best described as a set of pairs, one with incident energies near 2470 eV and a second set with

excitation energies near 2472 eV. Within each pair, a 1 eV difference in energy transfer distinguishes the two peaks and is the expected $K\alpha_{1,2}$ spin-orbit splitting.

Moving to $Na_2S_2O_3$, thiosulfate has two distinct sulfur sites, one sulfate-like (S^{6+}) and one sulfide-like (S^{2-}). These different oxidation states have XANES spectra with edge-steps at 2482 eV and 2470-2473 eV respectively, and XES spectra with $K\alpha_1$ peak locations at 2309.1 eV and 2307.8 eV respectively[33]. We see one pair of low energy features was identified at an incident energy of 2472 eV and an energy transfer of ~164 eV corresponding to the $K\alpha_{1,2}$ peaks of the sulfide-like site. At higher energy (2482 eV incident and 170 eV energy transfer), the sulfate-like site can also be excited and two additional pairs of peaks were observed. The emission energy of these peaks is higher, and so these peaks fall below the dotted line corresponding to a constant S^{2+} $K\alpha_1$ emission energy of 2307.8 eV. While RIXS of these compounds has not previously been reported, the quality of signal above background of our results compare favorably with prior work on other sulfur compounds[2,3,9,41].

In Fig. 4, we present $K\alpha$ HERFD cuts (emission energy 2307.8 eV) through the RIXS plane for both compounds and compare those spectra to the total fluorescence yield (TFY) results collected for normalization. The dotted line in Fig. 3 shows the constant emission energy (2307.8 eV) cuts taken to obtain the HERFD spectra. In both cases, there is a modest improvement in energy resolution over the XANES data, similar to previous results[3] on SO_3^{2-}. The magnitude of the energy resolution improvement can be estimated as shown in deGroot, et al.,[42], yielding a HERFD energy resolution of 0.43 eV, only a bit smaller than the S 1*s* lifetime broadening of 0.53 eV.

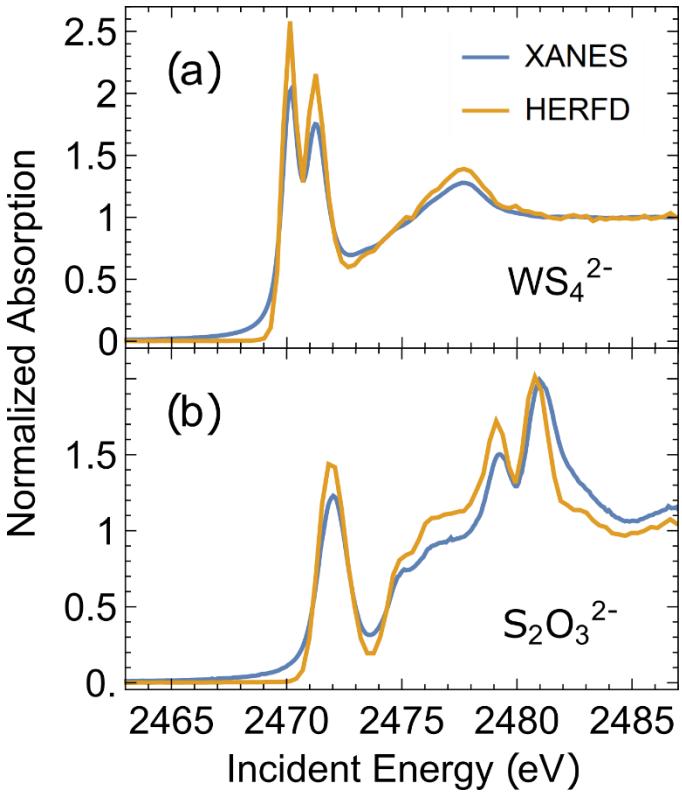

Figure 7.5. HERFD (orange) and XANES (blue) spectra for both $(PPh_4)_2WS4$ (a) and Na2S2O3 (b). In both cases, the HERFD spectrum shows modestly improved energy resolution with respect to the XAS spectrum.

As a more stringent test of the sensitivity of the spectrometer at BL 4-3, we also measured S Kβ RIXS of NaS_2O_3, shown in Fig. 5. The S Kβ RIXS experiment is similar to the S Kα RIXS process described above (Scheme 1) in that it also involves an initial electronic excitation from the 1*s*-orbital to an intermediate excited state that involves the S 3*p* valence orbitals, see Scheme 2. It differs in that progression to the final excited state involves a higher energy $3p \rightarrow 1s$ transition, rather than the $2p \rightarrow 1s$ process in S Kα RIXS. As a result, the S Kβ RIXS technique directly probes the occupied valence orbitals and the S Kβ RIXS spectra is more heavily influenced by the sulfur chemical environment than the Kα RIXS spectra. Another difference is associated with emission intensity. For each 1s core hole created, S Kβ x-ray emission is more than 10 times less

likely than the Kα emission[43,44], so count rates are low (appx. 50 total counts/second). Fortunately, the detected background is also correspondingly low.

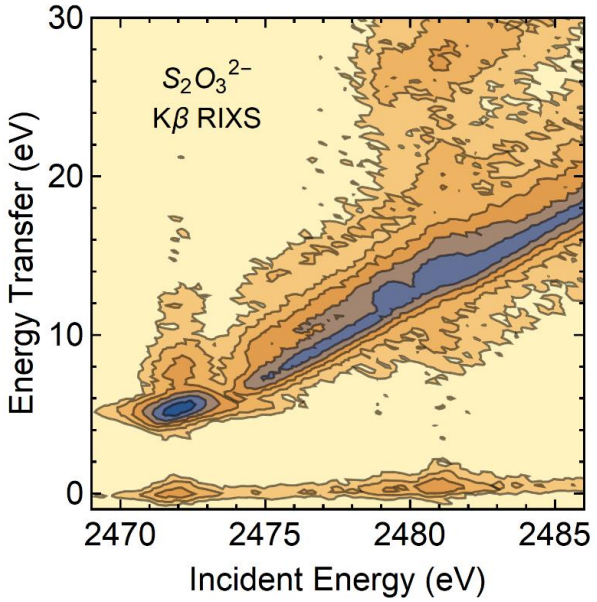

Figure 7.6. Contour plot of S Kβ RIXS collected on $Na_2S_2O_3$. As in Fig. 3, x-ray intensity is plotted against incident energy and energy transfer (incident – emitted energy).

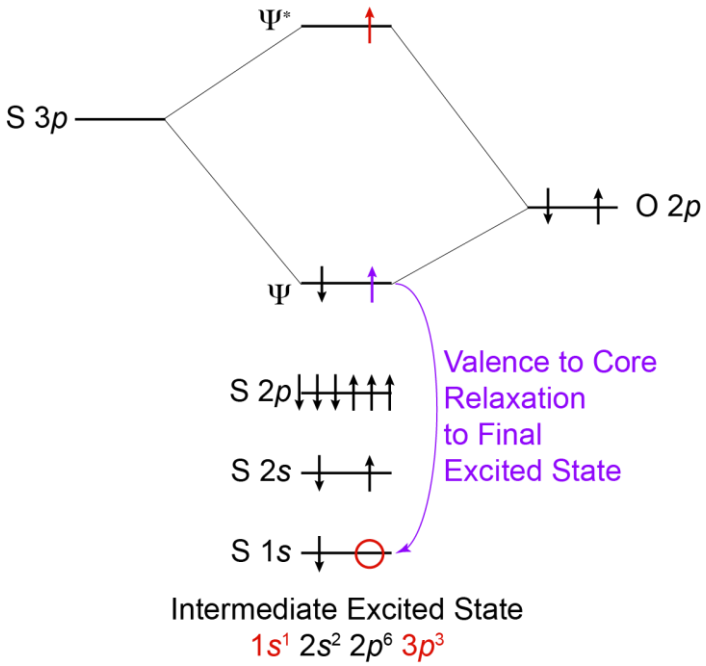

Figure 7.7. A general description for the valence-to-core relaxation process that occurs during the S Kβ RIXS spectroscopy experiment.

The $S_2O_3^{2-}$ S Kβ RIXS spectrum is shown in Fig. 5 and RXES spectra are shown in Fig. 6. The RIXS spectrum contains a strong feature with an incident energy of 2472 eV and 6 eV in energy transfer, the latter of which tails to approximately 12 eV. At higher incident energy, there are a series of peaks that also tail in energy transfer by about 6 eV. The RXES cuts shown are split into two groups: ones with an excitation energy below the sulfate-like edge of 2482 eV (A, B) and those with an excitation energy above that edge (C, D). The main difference is that spectra A and B show no Kβ' peak, but spectra C and D do at approximately 2453 eV emission energy. This peak is due to a molecular orbital of primarily oxygen character [45], so because only the sulfate-like site is bonded to oxygen, there is no satellite present in the sulfide-like spectra (A, B). The elastic scattering present in the Kβ RIXS measurement (highest energy peak of Fig. 6(b) in each case) provides an opportunity to measure the energy resolution of the spectrometer, as this peak should only be broadened by the energy resolution of the beamline monochromator. With an incident energy of 2472 eV, the elastic scattering peak in the S Kβ RIXS study showed a full-width half maximum of 0.81 eV. Allowing for the ~0.3 eV energy resolution of the monochromator, we infer a spectrometer energy resolution of ~0.75 eV. While slightly inferior to that of other spectrometers in this energy range[9], the results below indicate that this resolution suffices for a broad range of future applications.

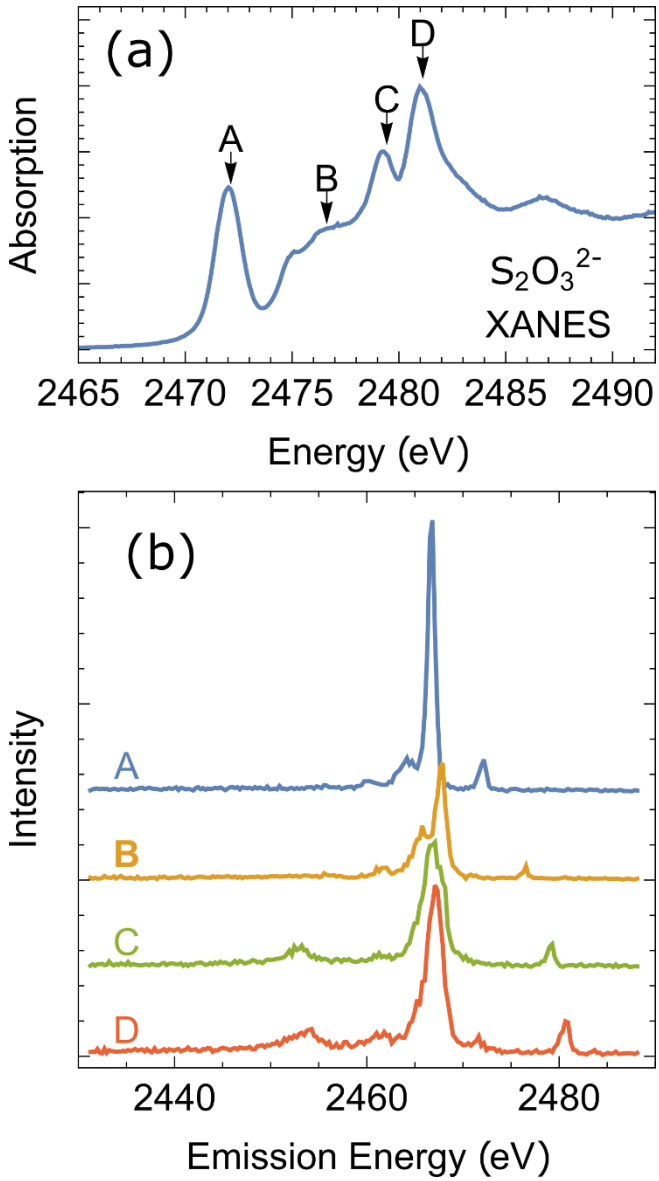

Figure 7.8. Resonant XES (constant incident energy) cuts of the $Na_2S_2O_3$ Kβ RIXS plane. Spectra (b) correspond to the incident energies selected in (a). The highest energy emission peak is elastic scatter at emission energy equal to the incident energy.

This energy resolution, however, is extremely effective for the slightly higher energy study of the U Mβ emission from $Cs_2UO_2Cl_4$, see Fig. 7. The study of actinide M-edge XAS has been stymied by the large (3.5 eV) core-hole broadening of the 3*d* electrons which limits the ability of x-ray absorption to distinguish features. Therefore, RIXS of actinide materials has great promise

as it resolves features at energy scales less than the core-hole lifetime broadening. This was done to great effect in UO_2^{2+},[34,46,47] which revealed several previously unresolved $3d \rightarrow 5f$ transitions.

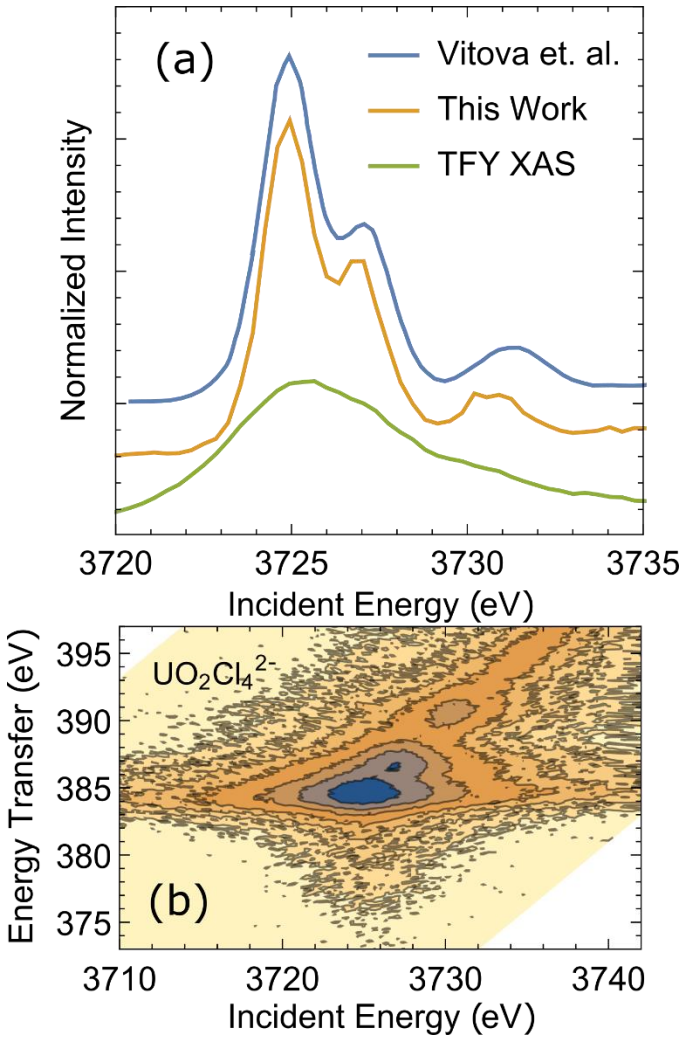

Figure 7.9. a) U M_4 edge HERFD cut of $UO_2Cl_4^{2-}$ collected using both the DRR spectrometer (orange) and measurements by Vitova et. al. (blue) at ANKA-INE[34], and a TFY XANES measurement on a thin sample (green). Spectra are offset for clarity. b) U Mβ RIXS plane collected using the DRR spectrometer.

Of particular significance – especially for the experiments reported herein – is the study by Vitova *et al.* of using U Mβ RIXS to study uranium electronic structure. The experiment involves core-to-core electron transitions involving a U $3d \rightarrow$ U $5f$ excitation followed by relaxation of a core U $4f$-electron (Scheme 3). Using our spectrometer, we were able to obtain a spectrum in 2 h

on 60 mg of $Cs_2UO_2Cl_4$ sample using the unfocused beam line at SSRL (4-3) that reproduces Vitova's spectrum collected with a scanning, point-focusing Rowland spectrometer at the INE actinide beamline of Angströmquelle Karlsruhe (ANKA)[48,49]. The spectrum contains three primary peaks with incident energies of approximately 3723, 3728, and 3730 eV that are separated by about 2 eV in energy transfer energy, corresponding to the splitting of the unoccupied 5f states into δ/φ non-bonding and σ- and π-antibonding orbitals. The data of Fig. 7 has been shifted by 1.8 eV to align the two spectra at the energy of the first peak. We attribute the difference in energy scales to the difference in calibration methods between the two experiments. To better align with other previous M-edge studies[50], our $UO_2Cl_4^{2-}$ spectra was calibrated to the pre-edge maximum of a KCl XAS spectrum at 3608.4 eV and Vitova *et. al.* calibrated to the inflection point of a titanium foil at 4966.0 eV [47]. Other than the energy scale mismatch, the results collected here agree well with those of Vitova *et al*. In comparing the two experiments, one major difference is that to collect a HERFD spectrum, the focusing Rowland spectrometer only collects at the peak emission energy of the U Mβ and so the HERFD spectrum was collected in 1 second per point. By contrast, the experiment described here required 80 seconds per point collection time, but the whole RIXS plane was collected.

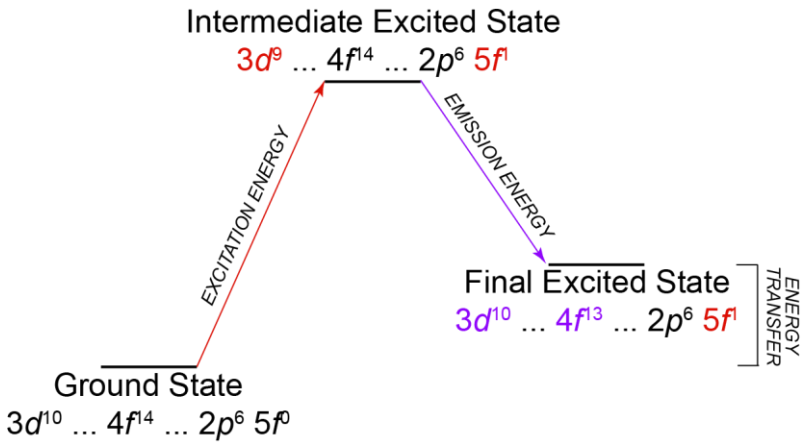

Figure 7.10. A general description for the core-to-core processes occurring during the U Mβ RIXS spectroscopy experiment.

Looking to the future, there are several directions for improved performance or broader range of application. First, finer energy resolution or improved solid angle of collection can be achieved with a Johansson (bent and ground) optic; this crystal motif eliminates the Johann error resulting from the edges of the optic not sitting on the Rowland circle[51], especially when working at Bragg angles farther from backscatter. Second, as pointed out previously, the spectrometer's compact design suggests its installation in a glovebox at an end-station[1]. In this way, RIXS measurements could be performed on air-sensitive samples without the samples ever leaving a controlled atmosphere. This also has particular relevance for actinide chemistry, where the glovebox could act as a layer of containment, allowing for more complex experiments and easier facilitation of on-site chemistry. Finally, the DRR design could be modified to use larger radii optics. Although this would increase the footprint of the instrument, it could allow for doubly-focusing optics which would improve efficiency and count rates.

7.6 CONCLUSION

We have demonstrated that the miniature dispersive Rowland refocusing spectrometer offers an opportunity to perform advanced photon-in, photon-out x-ray spectroscopies (XES, RIXS, HERFD) using a portable instrument which is suitable for use with unfocused beamlines and large beam spots. The compatibility of this spectrometer with large beam spots permits intentionally increasing spot size to reduce radiation dose and subsequent damage to sensitive samples. Collection times are manageable (several hours for a RIXS plane) and low background allows for the measurement of low intensity x-ray emission lines. Results compared favorably with previous sulfur RIXS measurements made with a dispersive spectrometer design and also reproduced prior measurements on $UO_2Cl_4^{2-}$ made with a focusing spectrometer. As such, we anticipate that this spectrometer design will expand the availability of these advanced spectroscopies, especially in this energy range, which is presently only possible at a small number of beamlines.

7.7 REFERENCES

1. Holden, W. M. *et al.* A compact dispersive refocusing Rowland circle X-ray emission spectrometer for laboratory, synchrotron, and XFEL applications. *Rev. Sci. Instrum.* **88**, 073904 (2017).

2. Robba, A. *et al.* Mechanistic Study of Magnesium-Sulfur Batteries. *Chem. Mater.* **29**, 9555–9564 (2017).

3. Kavčič, M. *et al.* Operando Resonant Inelastic X-ray Scattering: An Appropriate Tool to Characterize Sulfur in Li-S Batteries. *J. Phys. Chem. C* **120**, 24568–24576 (2016).

4. Kvashnina, K. O., Kvashnin, Y. O. & Butorin, S. M. Role of resonant inelastic X-ray scattering in high-resolution core-level spectroscopy of actinide materials. *J. Electron Spectros. Relat. Phenomena* **194**, 27–36 (2014).

5. Butorin, S. M. Resonant inelastic X-ray scattering as a probe of optical scale excitations in strongly electron-correlated systems: quasi-localized view. *J. Electron Spectros. Relat. Phenomena* **110**, 213–233 (2000).

6. de Groot, F. & Kotani, A. (Akio). *Core level spectroscopy of solids*. (CRC Press, 2008).

7. Glatzel, P. & Bergmann, U. High resolution 1s core hole X-ray spectroscopy in 3d transition metal complexes—electronic and structural information. *Coord. Chem. Rev.* **249**, 65–95 (2005).

8. Schülke, W. *Electron dynamics by inelastic X-ray scattering*. (Oxford University Press, 2007).

9. Kavčič, M. *et al.* Design and performance of a versatile curved-crystal spectrometer for high-resolution spectroscopy in the tender x-ray range. *Rev. Sci. Instrum.* **83**, (2012).

10. Welter, E., Machek, P., Dräger, G., Brüggmann, U. & Fröba, M. A new X-ray spectrometer with large focusing crystal analyzer. *J. Synchrotron Radiat.* **12**, 448–454 (2005).

11. Hudson, A. C., Stolte, W. C., Lindle, D. W. & Guillemin, R. Design and performance of a curved-crystal x-ray emission spectrometer. *Rev. Sci. Instruments* **78**, 53101 (2007).

12. Dolgih, V. E. *et al.* X-ray fluorescent spectrometer with linear position sensitive detector. *Nucl. Instruments Methods Phys. Res.* **224**, 117–119 (1984).

13. Stein, J. L. *et al.* Probing Surface Defects of InP Quantum Dots Using Phosphorus Kα and Kβ X-ray Emission Spectroscopy. *Chem. Mater.* **30**, 6377–6388 (2018).

14. Holden, W. M., Seidler, G. T. & Cheah, S. Sulfur Speciation in Biochars by Very High Resolution Benchtop Kα X-ray Emission Spectroscopy. *J. Phys. Chem. A* **122**, 5153–5161 (2018).

15. Huotari, S., Pylkkänen, T., Verbeni, R., Monaco, G. & Hämäläinen, K. Direct tomography with chemical-bond contrast. *Nat. Mater.* **10**, 489–493 (2011).

16. Labate, L., Köster, P., Levato, T. & Gizzi, L. A. A novel technique for single-shot energy-resolved 2D x-ray imaging of plasmas relevant for the inertial confinement fusion. *Rev. Sci. Instrum.* **83**, 103504 (2012).

17. Hudson, L. T. *et al.* A high-energy x-ray spectrometer diagnostic for the OMEGA laser. *Rev. Sci. Instrum.* **73**, 2270–2275 (2002).

18. Valdivia, M. P., Stutman, D. & Finkenthal, M. Single-shot Z_eff dense plasma diagnostic through simultaneous refraction and attenuation measurements with a Talbot–Lau x-ray moiré deflectometer. *Appl. Opt.* **54**, 2577 (2015).

19. Glenzer, S. H. & Redmer, R. X-ray Thomson scattering in high energy density plasmas. *Rev. Mod. Phys.* **81**, 1625–1663 (2009).

20. Matlis, N. H. *et al.* Snapshots of laser wakefields. *Nat. Phys.* **2**, 749–753 (2006).

21. Gamboa, E. J. *et al.* Imaging x-ray Thomson scattering spectrometer design and demonstration (invited). *Rev. Sci. Instrum.* **83**, 10E108 (2012).

22. Woolsey, N. C. *et al.* Precision X-ray spectroscopy of intense laser-plasma interactions. *High Energy Density Phys.* **7**, 105–109 (2011).

23. Kritcher, A. L. *et al.* Development of X-ray Thomson scattering for implosion target characterization. *High Energy Density Phys.* **7**, 271–276 (2011).

24. Glenzer, S. H. *et al.* Demonstration of Spectrally Resolved X-Ray Scattering in Dense Plasmas. *Phys. Rev. Lett.* **90**, 175002 (2003).

25. Hoidn, O. R. & Seidler, G. T. Photometric study of single-shot energy-dispersive x-ray diffraction at a laser plasma facility. *Phys. Plasmas* **21**, 012707 (2014).

26. Mao, J. Y. *et al.* Application of a transmission crystal x-ray spectrometer to moderate-intensity laser driven sources. *Rev. Sci. Instrum.* **83**, 043104 (2012).

27. Suggit, M. *et al.* Nanosecond x-ray Laue diffraction apparatus suitable for laser shock compression experiments. *Rev. Sci. Instrum.* **81**, 083902 (2010).

28. Plateau, G. R. *et al.* Low-Emittance Electron Bunches from a Laser-Plasma Accelerator Measured using Single-Shot X-Ray Spectroscopy. *Phys. Rev. Lett.* **109**, 064802 (2012).

29. Valdivia, M. P. *et al.* Talbot–Lau x-ray deflectometry phase-retrieval methods for electron density diagnostics in high-energy density experiments. *Appl. Opt.* **57**, 138 (2018).

30. Holden, W. M., Hoidn, O. R., Seidler, G. T. & DiChiara, A. D. A color x-ray camera for 2–6 keV using a mass produced back illuminated complementary metal oxide semiconductor sensor. *Rev. Sci. Instrum.* **89**, 093111 (2018).

31. Watkin, D. J., Denning, R. G. & Prout, K. Structure of dicaesium tetrachlorodioxouranium(VI). *Acta Crystallogr. Sect. C Cryst. Struct. Commun.* **47**, 2517–2519 (1991).

32. Solomon, E. I., Hedman, B., Hodgson, K. O., Dey, A. & Szilagyi, R. K. Ligand K-edge X-ray absorption spectroscopy: Covalency of ligand-metal bonds. *Coord. Chem. Rev.* **249**, 97–129 (2005).

33. Alonso-Mori, R. *et al.* Electronic Structure of Sulfur Studied by X-ray Absorption and Emission Spectroscopy. *Anal. Chem.* **81**, 6516–6525 (2009).

34. Vitova, T. *et al.* The role of the 5f valence orbitals of early actinides in chemical bonding. *Nat. Commun.* **8**, 1–9 (2017).

35. Ravel, B. & Newville, M. ATHENA , ARTEMIS , HEPHAESTUS : data analysis for X-ray absorption spectroscopy using IFEFFIT. *J. Synchrotron Radiat.* **12**, 537–541 (2005).

36. Glatzel, P. & Bergmann, U. High resolution 1s core hole X-ray spectroscopy in 3d transition metal complexes—electronic and structural information. *Coord. Chem. Rev.* **249**, 65–95 (2005).

37. Olson, A. C. *et al.* Using solution- and solid-state S K-edge X-ray absorption spectroscopy with density functional theory to evaluate M–S bonding for MS_4^{2-} (M = Cr, Mo, W) dianions. *Dalt. Trans.* **43**, 17283–17295 (2014).

38. Müller, A., Wittneben, V., Diemann, E., Hormes, J. & Kuetgens, U. Electronic structure of thiometalates [MS4]n− (M=Mo, W, Re). XANES spectra and SCF-Xα-SW calculations. *Chem. Phys. Lett.* **225**, 359–363 (1994).

39. Wittneben, V. *et al.* Sulfur-edge X-ray absorption near edge spectra (XANES) of some thiometallates and thiometallato complexes. *J. Mol. Struct.* **198**, 525–529 (1989).

40. Frank, P. *et al.* A large reservoir of sulfate and sulfonate resides within plasma cells from ascidia ceratodes, revealed by x-ray absorption near-edge structure spectroscopy. *Biochemistry* **26**, 4975–4979 (1987).

41. Marchenko, T. *et al.* Electron Dynamics in the Core-Excited CS_2 Molecule Revealed through Resonant Inelastic X-Ray Scattering Spectroscopy. *Phys. Rev. X* **5**, 031021 (2015).

42. De Groot, F. M. F., Krisch, M. H. & Vogel, J. Spectral sharpening of the Pt L edges by high-resolution x-ray emission. *Phys. Rev. B - Condens. Matter Mater. Phys.* **66**, 1–7 (2002).

43. Ertuğral, B., Apaydın, G., Çevik, U., Ertuğrul, M. & Kobya, A. İ. Kβ/Kα X-ray intensity ratios for elements in the range $16 \leqslant Z \leqslant 92$ excited by 5.9, 59.5 and 123.6 keV photons. *Radiat. Phys. Chem.* **76**, 15–22 (2007).

44. Salem, S. I., Panossian, S. L. & Krause, R. A. Experimental K and L relative x-ray emission ratess. *At. Data Nucl. Data Tables* **14**, 91–109 (1974).

45. Mori, R. A. *et al.* Sulfur-Metal Orbital Hybridization in Sulfur-Bearing Compounds Studied by X-ray Emission Spectroscopy. **129**, 6468–6473 (2010).

46. Kvashnina, K. O., Butorin, S. M. & Glatzel, P. Direct study of the f-electron configuration in lanthanide systems. *J. Anal. At. Spectrom.* **26**, 1265 (2011).

47. Vitova, T. *et al.* Polarization Dependent High Energy Resolution X-ray Absorption Study of Dicesium Uranyl Tetrachloride. *Inorg. Chem.* **54**, 174–182 (2015).

48. Kleymenov, E. *et al.* Five-element Johann-type x-ray emission spectrometer with a single-photon-counting pixel detector. *Rev. Sci. Instruments* **82**, 65107 (2011).

49. Rothe, J. *et al.* The INE-Beamline for actinide science at ANKA. *Rev. Sci. Instruments* **83**, 43105 (2012).

50. Kraft, S. J. *et al.* Synthesis, Characterization, and Multielectron Reduction Chemistry of Uranium Supported by Redox-Active α-Diimine Ligands. *Inorg. Chem.* **50**, 9838–9848 (2011).

51. Bergmann, U. & Cramer, S. P. High-resolution large-acceptance analyzer for x-ray fluorescence and Raman spectroscopy. in (eds. Macrander, A. T., Freund, A. K., Ishikawa, T. & Mills, D. M.) **3448**, 198 (International Society for Optics and Photonics, 1998).

Chapter 8. VACUUM FORMED TEMPORARY SPHERICAL AND TOROIDAL BENT CRYSTAL ANALYZERS FOR X-RAY ABSORPTION AND EMISSION SPECTROSCOPY

8.1 PREFACE

This work has been published in the journal Review of Scientific Instruments. It is a demonstration of the use of a vacuum mold to create the bent optics necessary to run an x-ray spectrometer. My main contribution to this work was the ray-tracing simulations and the writing about the same.

Authors

Evan P. Jahrman[1] (§), William M. Holden[1] (§), Alexander S. Ditter[1,2], Stosh A. Kozimor[2], Scott L. Kihara[1], Gerald T. Seidler[1] (*).

[1]Physics Department, University of Washington, Seattle WA 98195

[2]Chemistry Division, Los Alamos National Laboratory, Los Alamos, NM 87545

(§) These authors contributed equally to this work.

8.2 ABSTRACT

We demonstrate that vacuum forming of 10-cm diameter silicon wafers of various crystallographic orientations under an x-ray permeable, flexible window can easily generate spherically bent crystal analyzers (SBCA) and toroidally bent crystal analyzers (TBCA) with ~1-eV energy resolution and a 1-m major radius of curvature. In applications at synchrotron light sources, x-ray free electron lasers, and laboratory spectrometers these characteristics are generally sufficient for many x-ray absorption fine structure (XAFS), x-ray emission spectroscopy (XES),

and resonant inelastic x-ray scattering (RIXS) applications in the chemical sciences. Unlike existing optics manufacturing methods using epoxy or anodic bonding, vacuum forming without adhesive is temporary in the sense that the bent wafer can be removed when vacuum is released and exchanged for a different orientation wafer. Therefore, the combination of an x-ray compatible vacuum-forming chamber, a library of thin wafers, and a small number of forms having different secondary curvatures can give extreme flexibility in spectrometer energy range. As proof of this method we determine the energy resolution and reflectivity for several such vacuum-formed bent crystal analyzers (VF-BCA) in laboratory based XAFS and XES studies using a conventional x-ray tube. For completeness we also show x-ray images collected on the detector plane to characterize the resulting focal spots and optical aberrations.

8.3 INTRODUCTION

Doubly-curved Bragg optics see extensive use in advanced x-ray spectroscopies at x-ray free electron lasers, synchrotron x-ray light sources, laser plasma facilities, and laboratories performing in-house x-ray absorption fine structure and x-ray emission spectroscopy. This has been made possible by a large body of work aimed at characterizing and evaluating the properties of doubly-curved optics.[1-7] These optics are available commercially; the traditional production methods use glue or anodic bonding to affix crystal wafers after pressing into precision glass or metallic substrates.[8-11] Other production techniques such as vacuum-bent analyzers[12] and hot plastic deformation techniques[13] have also been explored. Another approach is to use a spherical bending apparatus that allows the curvature to be characterized before fixing to a permanent shape.[14]

Even with a variety of available production techniques, acquiring a large number of such optics for multi-analyzer systems can be challenging. Synchrotron endstations for x-ray emission

spectroscopy (XES), high energy resolution fluorescence detection (HERFD) of x-ray absorption fine structure (XAFS), or nonresonant inelastic x-ray scattering (NRIXS) now often use from five to as many as ~100 such optics.[15-22] In addition to cost issues, for XES there is a pragmatic issue: different synchrotron users may come with experiments requiring acquisition of an entirely new set of optics for some energy range that has not previously been explored at that facility. The same issue arises with the increasing use of laboratory-based spectrometers,[23-31] where again the elements and energy ranges that are capable of being studied depend on the availability of analyzers having a variety of crystal cuts to achieve the necessary Bragg angles and energy resolutions. As an additional issue, when used in a Rowland circle spectrometer the most common doubly-curved optics, spherically bent crystal analyzers (SBCA) in the Johann configuration[32], sagittal bending error results in large spot sizes out of the Rowland plane when far from backscatter. Toroidally bent crystal analyzers (TBCA) are needed for a truer point-to-point focus, but are far less common and their secondary curvature must be tuned to match a chosen Bragg angle.

The purpose of this paper is to address the above concerns, at least for applications requiring only the 'modest' energy resolution of ~1-eV, such as is frequently sufficient in the chemical sciences.[33] Specifically, we demonstrate a simple method to make temporary SBCA's and TBCA's with good performance and very high ease of use. Unlike methods using epoxy or anodic bonding, vacuum forming without adhesive is temporary in the sense that the bent wafer can be removed when vacuum is released and exchanged for a different orientation wafer. While vacuum formed bent crystal analyzers have been utilized before in other applications, this work demonstrates the efficacy of these analyzers in x-ray absorption and emission spectroscopy. The combination of an x-ray compatible vacuum-forming chamber, a suitable library of thin single-

crystal wafers, and a small number of forms having different secondary curvatures can give extreme flexibility in spectrometer or monochromator energy range at low cost and with great flexibility for addition of new energy ranges, as needed.

8.4 METHODS

The overall concept and resulting design of the vacuum-formed bent crystal analyzer (VF-BCA) is presented in Figure 8.1. Front-view and section-view computer aided design (CAD) renderings are shown in Figure 8.1(a) and (b), respectively. The key point is that an x-ray transparent, flexible polyimide window serves to seal the volume containing the wafer and the machined aluminum alloy or glass lens form from the outside atmosphere. When pumping on the VF-BCA, outside air pressure forces the polyimide window to collapse inward, pressing the wafer firmly onto the underlying form. A photograph of a VF-BCA is shown in Figure 8.1(c), and for comparison, a commercial, anodically-bonded analyzer (XRS TECH LLC) is shown in Figure 8.1(d).

Several different supporting forms were used, all with the 1-m major radius of curvature required by the laboratory spectrometer[27] that served as an extremely convenient testbed for this project. Table 8.1 defines the character of the different forms. The lens form was a plano-concave spherical lens made of BK7 glass from Esco Optics with 125 mm diameter, 1-meter ± 1% radius of curvature, and thickness 10 mm. When the forming contact surface was machined from aluminum 6061 alloy, a Mitsubishi M-V5Cn-L vertical machining center was used. The necessary cutting paths were generated under the target scallop deviation of 5 μm with a ball end mill having a ball-end radius of ~7.14 mm. The resulting surfaces were cleaned with solvents but otherwise not modified by, e.g., polishing or lapping.

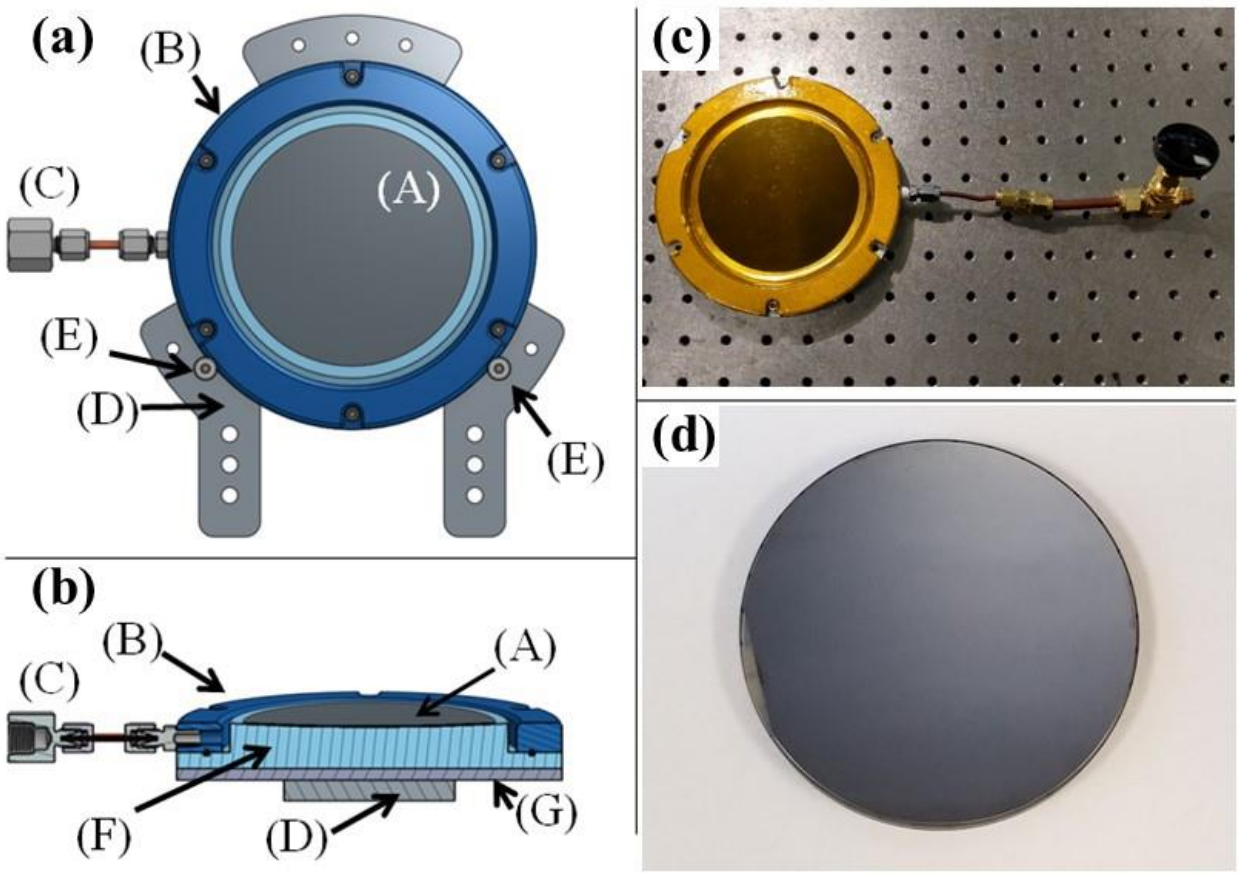

Figure 8.1. **(a)** CAD rendering front view of the vacuum formed bent crystal analyzer (VF-BCA). (A) bent wafer; (B) front flange with polyimide film (not shown); (C) pumping line; (D) aluminum alloy vertical support plate; (E) support bolts to define the position of the outer diameter of the VF-BCA body. **(b)** CAD rendering section view of the VF-BCA. (F) CNC-machined vacuum form; (G) steel backing plate for magnetic mounting, where magnets (not shown) are attached to part (D). **(c)** Photograph of the VF-BCA, note the flexible orange polyimide film that allows air pressure to force the wafer into the shape of the form machined into part (F). A second, similar VF-BCA instead has a simple recess in part (F) to accept a 1-m radius of curvature concave glass lens. **(d)** Photograph of a commercial, anodically-bonded 10-cm diameter SBCA with 1-m radius of curvature.

Table 8.1. List of all bent crystal analyzers and analyzer forms used in this study.

Optic name	Major radius (cm)	Perpendicular radius (cm)	Vacuum form surface
SBCA	100.0	100.0	Wafer anodically bonded to glass
VF-BCA-1	100.0	100.0	Glass lens
VF-BCA-2	100.0	100.0	Al6061 spherical recess
VF-BCA-3	100.0	88.3	Al6061 torus, $\theta^* = 70$ °

Table 8.2. List of experiments performed, commercial SBCA or wafers used in the VF-BCA, and nominal Bragg angle for the absorption edge or fluorescence line from the indicated crystal reflection.

Study	Commercial SBCA	Wafer for VF-BCA	Bragg angle (deg)
Ni XAFS	Si (551)	Si (711)	78.0
Ni XAFS	Si (444)	Si (444)	71.6
Cu Kα XES	Si (444)	Si (444)	79.3

The wafers used in the VF-BCA were standard 10-cm diameter double side polished Si wafers of various orientations, all nominally 400-μm thick. Different crystal orientations yield different energy ranges over the useful Bragg angle range. A list of absorption edges or fluorescence lines studied and the corresponding commercial SBCA or wafer used in a VF-BCA is given in Table 8.2.

The laboratory spectrometer used here[27] is a 1-m diameter Rowland circle spectrometer based on the approach of Seidler, et al.,[23] as modified by tilt-free alignment[34] and by the use of a higher-powered x-ray tube and longer translation stages to give a wider range in Bragg angle (θ_B). Across several instrument generations this overall approach using a conventional x-ray tube and a 'scissors' monochromator has been used in several studies with ~1-eV energy resolution for either transmission-mode XAFS or XES[24, 26, 29, 34-36] and the present instrument and its performance have been described in detail in Jahrman, et al.[27]

Measurements were performed with a Varex VF-80 x-ray tube with Pd-anode operating at 35 kV accelerating potential and 100 W total electron beam power. A silicon drift diode (Amptek X-123 SDD) with ~4.6-mm diameter active region was the final detector for all XAFS and XES scans. In Fig. 2 we show a schematic of the Rowland circle implementation for this spectrometer, a photograph of the spectrometer in an XAFS configuration, and a photograph of the VF-BCA installed at the optic location.

Under the protocol for tilt-free alignment,[34] spherical analyzers are rotated about their circular symmetry axis until the wafer's miscut is in the Rowland plane. For a toroidal VF-BCA, the wafer orientation must be determined in a spherical VF-BCA prior to installation into the toroidal vacuum form holder with the miscut oriented in the Rowland plane, i.e., in the plane of the 1-m major radius of curvature. The use of a sliding magnet mount (Fig. 2(c)) makes it particularly convenient to rotate about the necessary axis in the Rowland plane.

Imaging of the x-ray intensity on the detector plane was performed using a small home-built CMOS x-ray camera. This is an updated version[37] of an earlier camera[38] that has seen good use in a lower-energy XES instrument.[39-42] The camera has a 3.2×5.6 mm^2 field of view. It was mounted on a micrometer-driven vertical translation stage and manually repositioned to achieve mosaic coverage of the x-ray intensity's spatial distribution. Furthermore, the camera's ability to identify both the location and energy of individual x-ray photons allowed the rejection of stray fluorescence by energy-windowing.

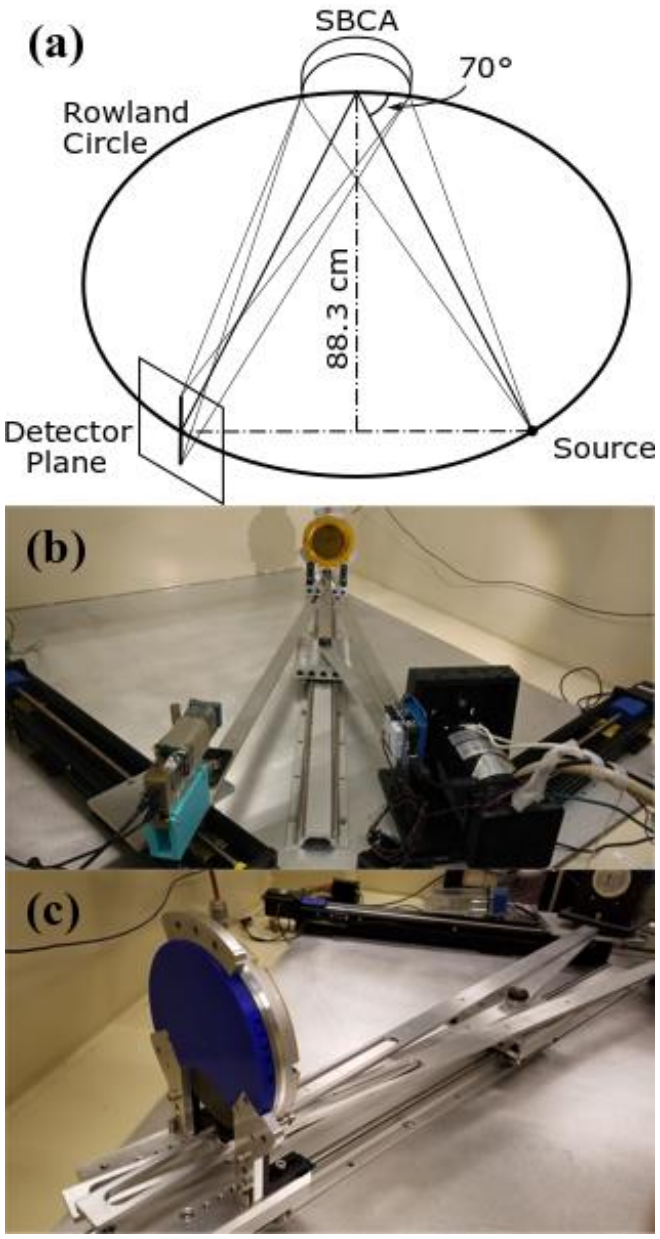

Figure 8.2. **(a)** The Rowland circle implementation for the laboratory spectrometer, shown for a 70 ° Bragg angle. Note the definition of the detector plane. Also note that perfect point-to-point focusing by the optic would require that its radius of curvature out of the Rowland plane be equal to the normal distance from the source-detector arc to the optic, i.e., the sagitta of the reflexive arc from the source point on the Rowland circle to the detector point, indicated as 88.3cm on the diagram above. This motivates the use of toroidally curved forms, as discussed in the text. (**b**) Photograph of the laboratory spectrometer. **(c)** Photograph from the reverse side of a vacuum-formed bent crystal analyzer installed into the spectrometer. Note the use of small magnets inside the plastic 3D-printed part coupled to the steel mounting plate (part (G) in Fig. 1) to hold the analyzer in location but allow easy rotation about the azimuthal angle.

Ray tracing software written in Mathematica was used to assess Johann error and beam spreading perpendicular to the Rowland plane due to sagittal error, i.e., the use of optics whose second radius of curvature is not equal to the perpendicular distance from the optic center to the line connecting the source and detector points on the Rowland circle (the sagitta). Unlike recent work aiming to give an advanced treatment of the interplay between strain effects and, e.g., dynamical diffraction in SBCAs,[43, 44] here we only seek purely geometric optics effects on slightly sub-mm length scales. Consequently, the Monte-Carlo ray tracing code generated x-rays from a 1-mm diameter source spot, reflected them from the bent optic using simple, specular Bragg reflection assuming zero wafer miscut, and then recorded the position of the intersection of those rays with the detector plane.

Transmission-mode XAFS measurements were performed on a 6-μm thick Ni foil from EXAFS Materials. XES measurements were performed on a 75-μm thick sheet of commercial Cu foil. All measurements were performed with the sample in air under ambient conditions, and a helium space was used to reduce air-absorption. In some cases, small corrections for slow leaks in the helium space have been made to ensure that all comparisons are on a common efficiency basis. All XAFS spectra were dead time corrected and subsequently processed in Athena where standard background removal and normalization procedures were followed.[45] For XES, all spectra are dead time corrected and approximately aligned to a common energy scale.

8.5 RESULTS

Optic performance encompasses both its focal properties, as this is crucial for coupling to the final detector, and also its energy resolution. We begin with focal properties. In Figure 8.3 we present the x-ray intensity in the detector plane for the commercial, anodically bonded Si (551) SBCA and for a Si (711) wafer in VF-BCA-1, VF-BCA-2, and VF-BCA-3 (see Table 8.1 for the

definitions of these terms). Note that these two crystal orientations have the same *d*-spacing, and consequently are identical for present purposes, giving the same energy range over the same span of Bragg angles. The qualitative agreement is very good. All optics show strong in-Rowland-plane focusing and also the expected degree of out-of-Rowland-plane focusing subject to sagittal distortion. VF-BCA-2 and VF-BCA-3, which are based on machined, unpolished metal forms, have slightly inferior focal properties. As discussed below, precision polishing of machined surfaces is an obvious future direction for improvement.

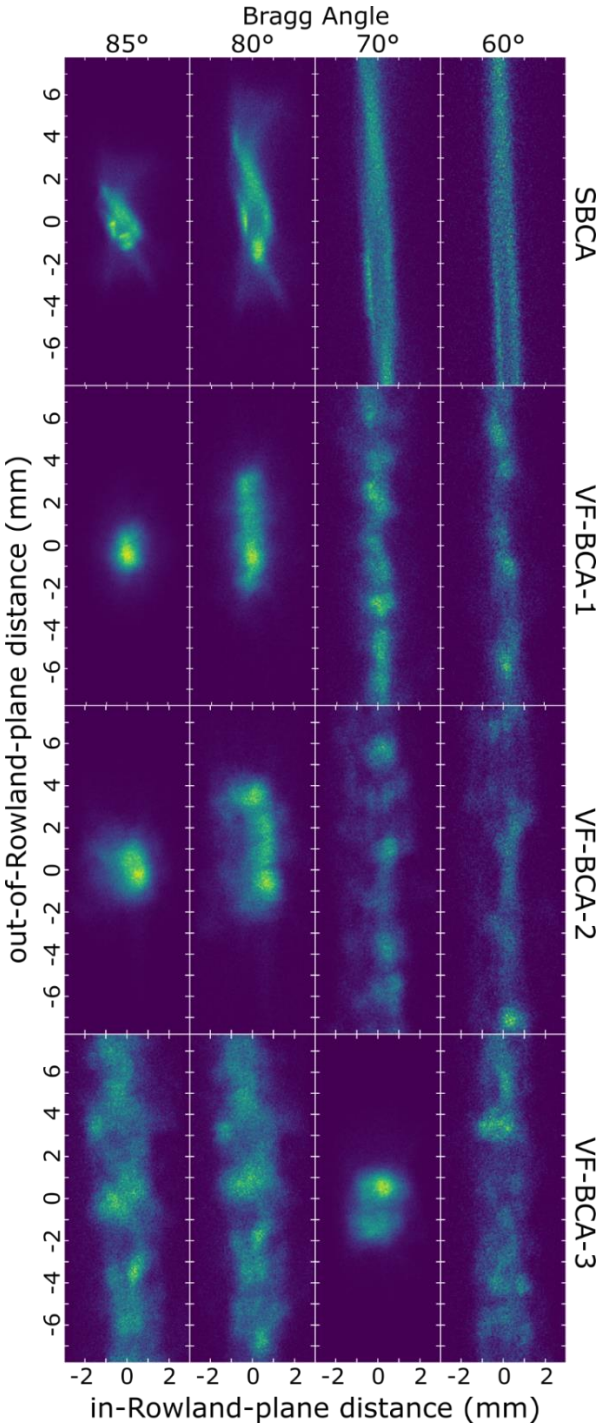

Figure 8.3. Characterization of the spatial distribution of x-ray intensity on the detector plane from **(top)** a commercial Si (551) analyzer (SBCA); **(second from top)** VF-BCA-1 with a Si (711) wafer and **(second from bottom)** VF-BCA-2 with a Si (711) wafer; **(bottom)** VF-BCA-3 with a Si (711) wafer, a torus optimized for $\theta_B = 70\,°$. The orientations are defined relative to the plane of the Rowland focusing circle. The colorscale of each frame is independently normalized; for a comparison of intensities, see Figure 8.4.

In Fig. 4(a), we show the in-Rowland-plane intensity spread across the detector plane at different Bragg angles for each of the above optics and a Si (711) or equivalent wafer. Although the in-plane focal qualities of SBCA and VF-BCA-1 are similar, the profile of VF-BCA-2 is found to be broader and skewed. The out-of-Rowland-plane intensity spread is shown in Fig. 4(b). Near backscatter, the out-of-plane focal quality of both VF-BCA-1 and VF-BCA-2 is found to be comparable to the SBCA. At lower values of θ_B, VF-BCA-1 and VF-BCA-2 demonstrate clear inhomogeneities, although the total refocused intensity remains comparable.

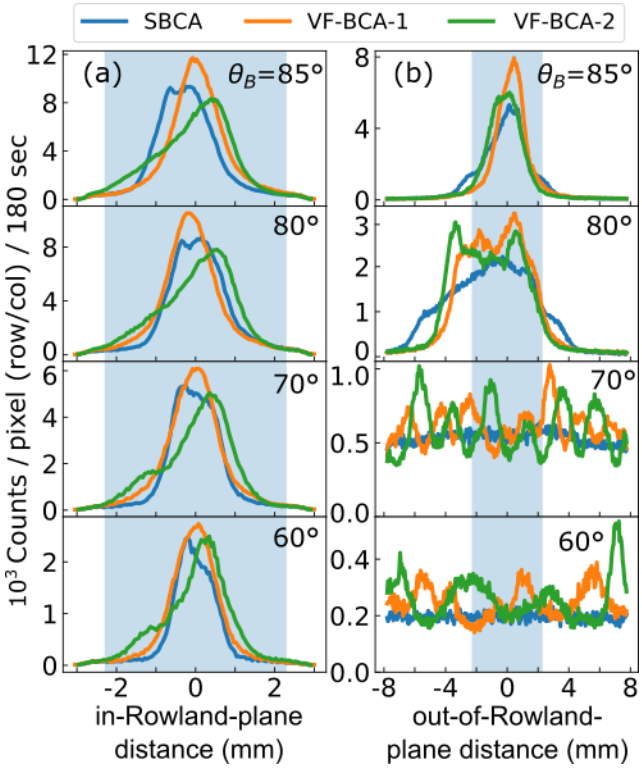

Figure 8.4. **(a)** Comparison of beam profiles in the Rowland plane for different optics. **(b)** Comparison of beam profiles in the direction perpendicular to the Rowland plane different optics. The extent of the silicon SDD's active region is represented by the shaded regions.

For the out-of-plane focal quality, it is clear that the use of a SBCA sufficiently far away from backscatter ($\theta_B = 90$ deg) results in rapid spreading of the beam in the out-of-plane direction

as expected from sagittal error. In this configuration, the out-of-Rowland-plane spread of the beam exceeds the height of the detector's active area, as shown in Figure 8.4(b). This raises the question of using toroidal optics where the primary radius of curvature is dictated by the Rowland circle diameter but where the secondary radius of curvature is chosen for ideal point-to-point focusing for a selected 'design' Bragg angle θ^*. For the Johann geometry, with a Rowland circle of radius D, the secondary radius of curvature R^* is given by $R^* = D\ \sin^2\theta_B$. Ray-tracing calculations for the out-of-plane beam height as a function of θ_B are shown in Figure 8.5(a) for TBCA's having design θ^* varying from 55 to 90°, the lattermost being simply an SBCA. These simulations strongly suggest that TBCA should give a more efficient coupling to the finite-sized detector when the secondary radius of the TBCA is chosen to eliminate sagittal error for θ^* in the middle of the angular range dictated by the energies of interest. Consequently, in the bottom panel of Figure 8.3 we show the intensity distributions on the detector plane for VF-BCA-3 with a Si (711) wafer. The out-of-plane focal properties of the TBCA are clearly much superior to the SBCA when θ_B is in the vicinity of the designed θ^*.

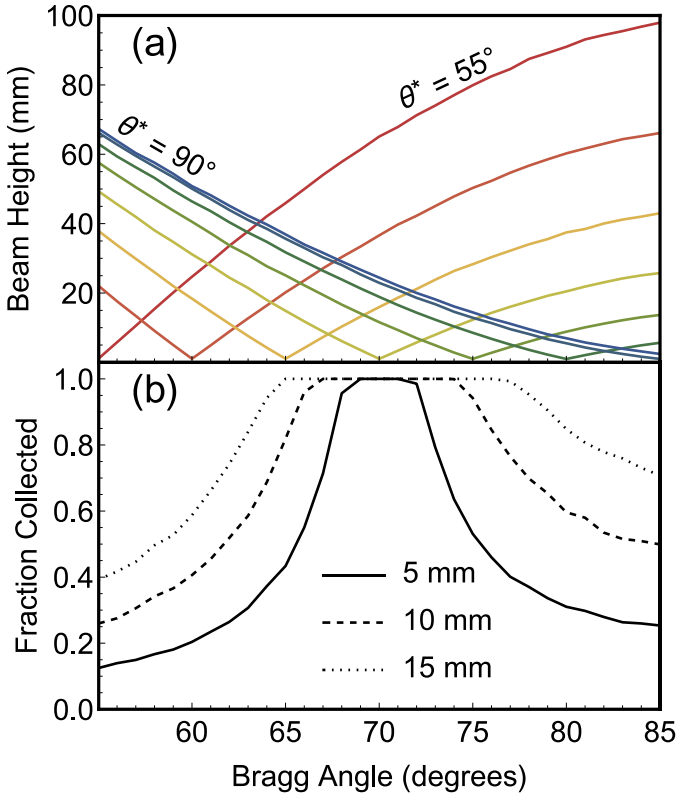

Figure 8.5. **(a)** The modeled beam height as a function of θ_B for doubly-curved optics with a 1-m principal radius of curvature but with secondary curvatures designed for point-to-point focus as design Bragg angles θ^* varying in 5° steps from 55° to 90°, the latter being for a fully spherical analyzer. **(b)** For a θ^* = 70° toroidal optic, the modeled fraction of x-rays hitting three different circular detectors with diameters of 5 mm, 10 mm, and 15 mm.

The improved spectrometer performance when using a TBCA at θ_B near the designed θ^* is demonstrated in Fig. 6. Here, the intensity of x-rays refocused at the SDD by each optic is shown across the full angular range of the instrument. The very short detectors used in the test studies (~4.6-mm active height) gives an especially high sensitivity to out-of-Rowland-plane beam spread, resulting in the narrow experimental Bragg angle range for optimum performance of the TBCA. Ray tracing calculations for TBCA simulating different detector heights are given in Fig. 5(b). In each case, there is an optimal, flat-top region of Bragg angles where all of the reflected x-rays are collected by the detector when the height of the reflected beam is smaller than the detector

diameter. This agrees well with the experimental data of Figure 8.6, which shows the same flat top near the θ^*, and a decrease in count rate far from θ^*. Further, the ray tracing demonstrates the utility of a larger detector which increases both the width of the flat-top region as well as the count rate when θ_B is far from θ^*.

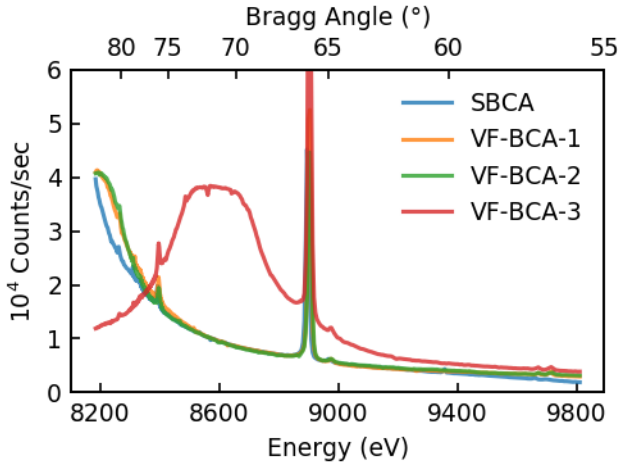

Figure 8.6. Monochromator count rate as a function of photon energy using a Si (551) or equivalent wafer. The sharp features at, e.g., ~8900 eV, are Cu Kβ fluorescence lines from the heatsink of the x-ray tube anode. The rapid roll-off for the spherical optics is due the steadily increasing out-of-plane spread upon decreasing Bragg angle, causing the beam to become taller than the 4-mm active height of the SDD. The toroidal optic shows much improved performance in the designed Bragg angle range.

The preceding discussion has only addressed focal properties. Now we report on the energy resolution using the vacuum clamped optics. The measured Ni K-edge XANES for all optics using a Si (551) or equivalent wafer are shown in Figure 8.7(a). It can be seen that all optics produced nearly identical spectra, suggesting a negligible loss in energy resolution from the commercial to vacuum clamped optics. The high quality of the XANES spectra is typical of modern laboratory based XAFS systems.[23, 24, 27, 46, 47] Similarly, Figure 8.7(b) presents again Ni K-edge XANES where the spectra are instead measured with the Si (444) reflection by several

different optics. Again, spectra are nearly identical, with only minor differences observable in the extent of the shoulder at ~8334 eV and in the magnitude of the oscillation at ~8352 eV.

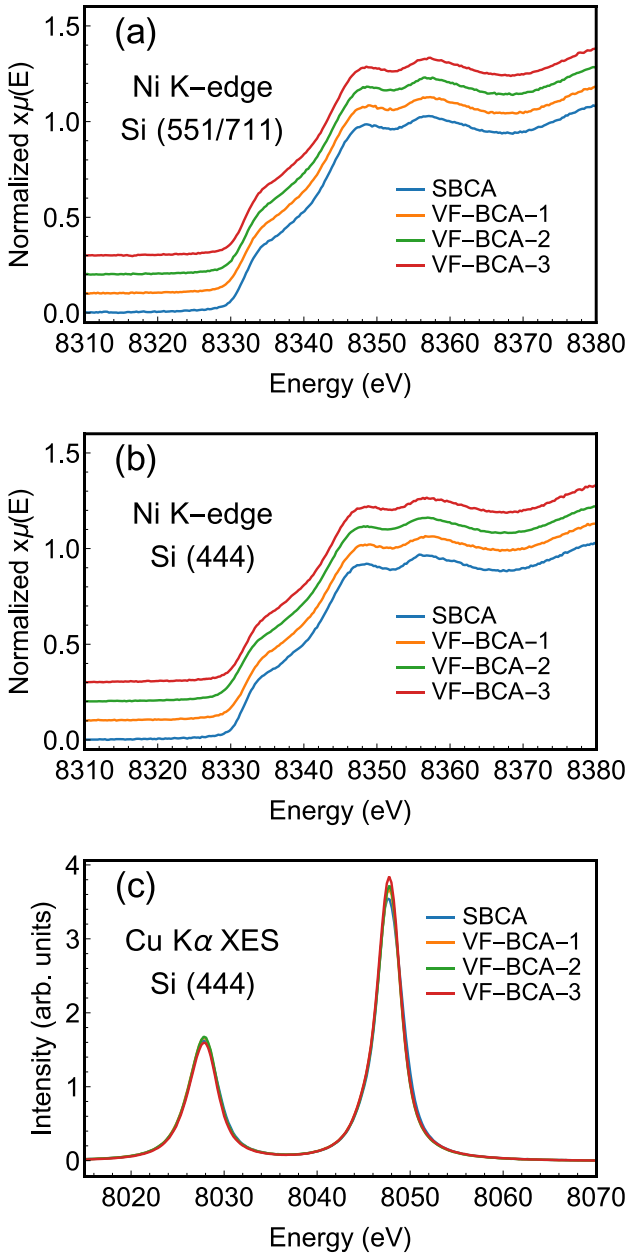

Figure 8.7. Representative spectra demonstrating the capability of the vacuum-clamped optics to perform high-resolution measurements. **(a)** comparison of Ni XANES measured with each optic using Si (551) or equivalent wafers **(b)** comparison of Ni XANES measured with each optic using Si (444) wafers (c) comparison of Cu Kα XES with each optic using Si (444) wafers.

In Figure 8.7(c), Cu Kα XES results are presented for all optics using the Si (444) reflection. Here again, spectra were found to be nearly identical, however some small differences in peak ratios can be observed in accordance with small differences in energy resolution and also small differences in the angular response functions between optics. Recall again that the analyzed radiation is being imperfectly focused in the out-of-Rowland-plane dimension, with a spread larger than the detector height. Consequently, small changes in spectrometer alignment can lead to few-percent differences in net monochromator efficiency as a function of energy.

Given the success and limitations shown in this effort to make temporary doubly-bent crystal analyzers, there are several future directions that merit comment. First, the focal quality of optics should be improved by lapping and polishing the surfaces of the machined forms, or by acquiring precision surface-ground glass forms for the toroidal case, in analogy to the high-quality lens used for the spherical case. While this is not particularly relevant for the ~1-eV resolution needed for many measurements in a point-to-point Rowland circle configuration, the same would not be true for higher-energy resolution applications or the important case of dispersive spectrometers based on spherical analyzers, as is commonly used at synchrotron light sources.[48-50] Second, the efficiency of each optic across wider angular ranges of the instrument could be improved by implementing a taller detector. Third, it would be interesting to explore forms with smaller primary radii of curvature or using wafers composed of crystalline materials besides silicon, each with the goal of obtaining higher signal levels. Fourth, although we have only used this method for intact round wafers, one should expect that the same apparatus can be used for segmented wafers, such as is used in the recent development of 0.5-m radius of curvature SBCAs,[9] or for pieces of multiple wafers integrated to obtain a larger BCA solid angle than could be

obtained with any single wafer. This lattermost opportunity is likely relevant for materials where the *de facto* standard 10-cm diameter wafers are not available.

8.6 CONCLUSIONS

We report the development and performance of spherically and toroidally bent crystal analyzers for use in x-ray absorption and emission spectroscopies. Unlike the present practice of gluing or bonding the necessary crystalline wafers to a high-precision glass lens, we instead use only air pressure to hold the wafer against the shaping form that provides the necessary profile. The specifications for the shaping form are found to be rather modest, in that modern machined metal forms suffice and high-precision, high-cost surface ground lenses are not needed. The resulting optics demonstrate resolutions and efficiencies comparable to their commercially available counterparts as determined by XANES and XES measurements using a laboratory spectrometer. These results establish a considerable convenience, simplicity, and flexibility that may prove useful for Rowland circle spectrometers in the lab for XAFS and XES studies, as well as at synchrotron and x-ray free electron laser x-ray facilities for XES, high-energy resolution fluorescence detection (HERFD), and resonant inelastic x-ray scattering (RIXS).

8.7 ACKNOWLEDGEMENTS

E. Jahrman was supported in part by the Joint Center for Energy Storage Research (JCESR), an Energy Innovation Hub funded by the U.S. Department of Energy, Office of Science, and Basic Energy Sciences, and by the U.S. Department of Energy through the Chemical Science and Engineering Division of Argonne National Laboratory. W. Holden and G. Seidler were supported by the Joint Plasma Physics Program of the National Science Foundation and the Department of Energy under Grant No. DE-SC0016251. R&D associated with the Los Alamos

National Laboratory (LANL) spectrometer was funded under the Heavy Element Chemistry Program by the Division of Chemical Sciences, Geosciences, and Biosciences, Office of Basic Energy Sciences, U.S. Department of Energy and the U.S. Department of Energy. LANL is operated by Los Alamos National Security, LLC, for the National Nuclear Security Administration of U.S. Department of Energy (contract DE-AC52-06NA25396).

8.8 REFERENCES

1. D. B. Wittry and S. Sun, J Appl Phys **71** (2), 564-568 (1992).
2. D. B. Wittry and S. Sun, J Appl Phys **69** (7), 3886-3892 (1991).
3. D. B. Wittry and S. Sun, J Appl Phys **67** (4), 1633-1638 (1990).
4. D. B. Wittry and S. Sun, J Appl Phys **68** (2), 387-391 (1990).
5. D. B. Wittry and W. Z. Chang, J Appl Phys **72** (8), 3440-3446 (1992).
6. A. Hauer, J. D. Kilkenny and O. L. Landen, Review of Scientific Instruments **56** (5), 803-805 (1985).
7. G. Askari Germi, S. J. Pestehe and A. Rastkar Ebrahimzadeh, Journal of Applied Crystallography **50** (4), 1104-1116 (2017).
8. R. Verbeni, M. Kocsis, S. Huotari, M. Krisch, G. Monaco, F. Sette and G. Vanko, Journal of Physics and Chemistry of Solids **66** (12), 2299-2305 (2005).
9. M. Rovezzi, C. Lapras, A. Manceau, P. Glatzel and R. Verbeni, Review of Scientific Instruments **88** (1), 013108 (2017).
10. M. Krämer, K. Kuzushita, S. Maeo, T. Utaka and K. Taniguchi, Spectrochimica Acta Part B: Atomic Spectroscopy **63** (12), 1408-1414 (2008).
11. E. Collart, A. Shukla, F. Gelebart, M. Morand, C. Malgrange, N. Bardou, A. Madouri and J.-L. Pelouard, Journal of Synchrotron Radiation **12** (4), 473-478 (2005).
12. P. Suortti, T. Buslaps, V. Honkimäki, N. Hiraoka and U. Lienert, Zeitschrift für Physikalische Chemie **220** (7), 831-847 (2006).
13. H. Okuda, K. Nakajima, K. Fujiwara, K. Morishita and S. Ochiai, Journal of Applied Crystallography **41** (4), 798-799 (2008).
14. A. H. Said, H. Sinn and R. Divan, Journal of Synchrotron Radiation **18** (3), 492-496

(2011).

15. S. Huotari, C. J. Sahle, C. Henriquet, A. Al-Zein, K. Martel, L. Simonelli, R. Verbeni, H. Gonzalez, M. C. Lagier, C. Ponchut, M. M. Sala, M. Krisch and G. Monaco, J. Synchrot. Radiat. **24**, 521-530 (2017).

16. R. Verbeni, T. Pylkkanen, S. Huotari, L. Simonelli, G. Vanko, K. Martel, C. Henriquet and G. Monaco, J. Synchrot. Radiat. **16**, 469-476 (2009).

17. T. T. Fister, G. T. Seidler, L. Wharton, A. R. Battle, T. B. Ellis, J. O. Cross, A. T. Macrander, W. T. Elam, T. A. Tyson and Q. Qian, Rev. Sci. Instrum. **77** (6), 063901 (2006).

18. D. Sokaras, D. Nordlund, T. C. Weng, R. A. Mori, P. Velikov, D. Wenger, A. Garachtchenko, M. George, V. Borzenets, B. Johnson, Q. Qian, T. Rabedeau and U. Bergmann, Rev. Sci. Instrum. **83** (4), 043112 (2012).

19. D. Sokaras, T. C. Weng, D. Nordlund, R. Alonso-Mori, P. Velikov, D. Wenger, A. Garachtchenko, M. George, V. Borzenets, B. Johnson, T. Rabedeau and U. Bergmann, Rev. Sci. Instrum. **84** (5), 053102 (2013).

20. I. Llorens, E. Lahera, W. Delnet, O. Proux, A. Braillard, J. L. Hazemann, A. Prat, D. Testemale, Q. Dermigny, F. Gelebart, M. Morand, A. Shukla, N. Bardou, O. Ulrich, S. Arnaud, J. F. Berar, N. Boudet, B. Caillot, P. Chaurand, J. Rose, E. Doelsch, P. Martin and P. L. Solari, Rev. Sci. Instrum. **83** (6), 063104 (2012).

21. M. M. Sala, K. Martel, C. Henriquet, A. Al Zein, L. Simonelli, C. J. Sahle, H. Gonzalez, M. C. Lagier, C. Ponchut, S. Huotari, R. Verbeni, M. Krisch and G. Monaco, J. Synchrot. Radiat. **25**, 580-591 (2018).

22. E. Kleymenov, J. A. van Bokhoven, C. David, P. Glatzel, M. Janousch, R. Alonso-Mori, M. Studer, M. Willimann, A. Bergamaschi, B. Henrich and M. Nachtegaal, Rev. Sci. Instrum. **82** (6), 065107 (2011).

23. G. T. Seidler, D. R. Mortensen, A. J. Remesnik, J. I. Pacold, N. A. Ball, N. Barry, M. Styczinski and O. R. Hoidn, Review of Scientific Instruments **85** (11), 113906 (2014).

24. G. T. Seidler, D. R. Mortensen, A. S. Ditter, N. A. Ball and A. J. Remesnik, Journal of Physics: Conference Series **712** (1), 012015 (2016).

25. D. R. Mortensen, G. T. Seidler, J. J. Kas, N. Govind, C. P. Schwartz, S. Pemmaraju and D. G. Prendergast, Physical Review B **96** (12), 125136 (2017).

26. D. R. Mortensen, G. T. Seidler, A. S. Ditter and P. Glatzel, Journal of Physics: Conference Series **712** (1), 012036 (2016).

27. E. P. Jahrman, W. M. Holden, A. S. Ditter, D. R. Mortensen, G. T. Seidler, T. T. Fister, S. A. Kozimor, L. F. J. Piper, J. Rana, N. C. Hyatt and M. C. Stennett, Review of Scientific

Instruments **90** (2), 024106 (2019).

28. W. M. Holden, O. R. Hoidn, A. S. Ditter, G. T. Seidler, J. Kas, J. L. Stein, B. M. Cossairt, S. A. Kozimor, J. Guo, Y. Ye, M. A. Marcus and S. Fakra, Review of Scientific Instruments **88** (7), 073904 (2017).

29. R. A. Valenza, E. P. Jahrman, J. J. Kas and G. T. Seidler, Phys Rev A **96** (3), 032504 (2017).

30. M. E. Mundy, D. Ung, N. L. Lai, E. P. Jahrman, G. T. Seidler and B. M. Cossairt, Chem Mater **30** (15), 5373-5379 (2018).

31. W. M. Holden, G. T. Seidler and S. Cheah, The Journal of Physical Chemistry A **122** (23), 5153-5161 (2018).

32. H. H. Johann, Zeitschrift Fur Physik **69** (3-4), 185-206 (1931).

33. P. Glatzel and U. Bergmann, Coord. Chem. Rev. **249** (1-2), 65-95 (2005).

34. D. R. Mortensen and G. T. Seidler, J Electron Spec **215**, 8-15 (2017).

35. M. E. Mundy, D. Ung, N. L. Lai, E. P. Jahrman, G. T. Seidler and B. M. Cossairt, Chem Mater (2018).

36. E. P. Jahrman, G. T. Seidler and J. R. Sieber, Analytical Chemistry **90** (11), 6587-6593 (2018).

37. W. M. Holden, O. R. Hoidn, G. T. Seidler and A. D. DiChiara, Rev. Sci. Instrum. **89** (9), 093111 (2018).

38. O. R. Hoidn and G. T. Seidler, Review of Scientific Instruments **86** (8), 086107 (2015).

39. W. M. Holden, O. R. Hoidn, A. A. Ditter, G. T. Seidler, J. Kas, J. Stein, C. B.M., S. A. Kozimor, J. Guo, Y. Ye, M. A. Marcus and S. Fakra, Rev. Sci. Instrum. **88** (7), 073904 (2017).

40. W. M. Holden, G. T. Seidler and S. Cheah, Journal of Physical Chemistry A **122** (23), 5153-5161 (2018).

41. J. L. Stein, W. M. Holden, A. Venkatesh, M. E. Mundy, A. J. Rossini, G. T. Seidler and B. M. Cossairt, Chem Mater (2018).

42. B. M. Cossairt, J. L. Stein, W. M. Holden and G. T. Seidler, SID Symposium Digest of Technical Papers **49** (1), 21-24 (2018).

43. A.-P. Honkanen, C. Ferrero, J.-P. Guigay and V. Mocella, Journal of Applied Crystallography **51** (2), 514-525 (2018).

44. A.-P. Honkanen, G. Monaco and S. Huotari, Journal of Applied Crystallography **49** (4),

1284-1289 (2016).

45. B. Ravel and M. Newville, Journal of Synchrotron Radiation **12** (4), 537-541 (2005).

46. R. Bès, T. Ahopelto, A. P. Honkanen, S. Huotari, G. Leinders, J. Pakarinen and K. Kvashnina, Journal of Nuclear Materials **507**, 50-53 (2018).

47. Z. Németh, J. Szlachetko, É. G. Bajnóczi and G. Vankó, Review of Scientific Instruments **87** (10), 103105 (2016).

48. S. Huotari, T. Pylkkänen, R. Verbeni, G. Monaco and K. Hämäläinen, Nature Materials **10**, 489 (2011).

49. S. Huotari, F. Albergamo, G. Vankó, R. Verbeni and G. Monaco, Review of Scientific Instruments **77** (5), 053102 (2006).

50. S. Huotari, G. Vankó, F. Albergamo, C. Ponchut, H. Graafsma, C. Henriquet, R. Verbeni and G. Monaco, Journal of Synchrotron Radiation **12** (4), 467-472 (2005).

Chapter 9. AN IMPROVED LABORATORY-BASED XAFS AND XES SPECTROMETER FOR ANALYTICAL APPLICATIONS IN MATERIALS CHEMISTRY RESEARCH

9.1 PREFACE

This chapter is a paper which has been published in the journal Review of Scientific Instruments. It describes an improved x-ray absorption and x-ray emission spectrometer that was led by Evan Jahrman. My contributions to this work were the uranium spectra, and as part of collecting those spectra, I installed and commissioned one of these spectrometers at Los Alamos National Laboratory.

Evan P. Jahrman[1], William M. Holden[1], Alex S. Ditter[1,2], Devon R. Mortensen[1,3], Gerald T. Seidler[1] (*), Timothy T. Fister[4], Stosh A. Kozimor[2], Louis F.J. Piper,[5] Jatinkumar Rana,[5] Neil C. Hyatt,[6] and Martin C. Stennett[6]

[1]Physics Department, University of Washington, Seattle, WA 98195-1560
[2]Chemistry Division, Los Alamos National Laboratory, Los Alamos, NM 87545
[3]easyXAFS LLC, Seattle, WA 98122
[4]Chemical Sciences and Engineering Division, Argonne National Laboratory, Lemont, IL 60439
[5] Department of Physics, Binghamton University, Binghamton, NY 13902
[6] Materials Science and Engineering Dept., The University of Sheffield, Mapping Street, Sheffield, S1 3JD, UK

LA-UR-18-26355

9.2 ABSTRACT

X-ray absorption fine structure (XAFS) and x-ray emission spectroscopy (XES) are advanced x-ray spectroscopies that impact a wide range of disciplines. However, unlike the majority of other spectroscopic methods, XAFS and XES are accompanied by an unusual access

model, wherein; the dominant use of the technique is for premier research studies at world-class facilities, i.e., synchrotron x-ray light sources. In this paper we report the design and performance of an improved XAFS and XES spectrometer based on the general conceptual design of Seidler, *et al.*, Rev. Sci. Instrum. 2014. New developments include reduced mechanical degrees of freedom, much-increased flux, and a wider Bragg angle range to enable extended x-ray absorption fine structure (EXAFS) for the first time with this type of modern laboratory XAFS configuration. This instrument enables a new class of routine applications that are incompatible with the mission and access model of the synchrotron light sources. To illustrate this, we provide numerous examples of x-ray absorption near edge structure (XANES), EXAFS, and XES results for a variety of problems and energy ranges. Highlights include XAFS and XES measurements of battery electrode materials, EXAFS of Ni with full modeling of results to validate monochromator performance, valence-to-core XES for 3d transition metal compounds, and uranium XANES and XES for different oxidation states. Taken *en masse*, these results further support the growing perspective that modern laboratory-based XAFS and XES have the potential to develop a new branch of analytical chemistry.

9.3 INTRODUCTION

X-ray absorption fine structure (XAFS) analysis is an especially capable and impactful tool for interrogating a material's local electronic and atomic structure. This element-specific technique encompasses both the x-ray absorption near edge structure (XANES), an acutely sensitive probe of a compound's oxidation state and molecular geometry, and the extended x-ray absorption fine structure (EXAFS), which is routinely used to extract multi-shell coordination

numbers and bond lengths. These techniques enable premier scientific research campaigns in catalysis,[1-2] energy storage,[3-4] actinide chemistry,[5-7] heavy metal speciation in the environment,[8-10] etc. Likewise, the partner process, x-ray emission spectroscopy (XES), has been used to assess spin and ligand character, notably in critical discoveries of magnetic phase transitions under geophysical conditions.[11-12] At present, XES continues to emerge as an important measure of valence-level (occupied) electronic state properties through improved theoretical treatment of the valence-to-core (VTC) and core-to-core (CTC) XES. However, as has been pointed out several times in the modern history of XAFS and XES, and most recently by Seidler,[13] these x-ray spectroscopies suffer from an anomalous access model. In general, XAFS and XES studies require access to synchrotron facilities with entry requirements that limit more introductory, routine, or high-throughput analytical studies that, by contrast, are common for NMR, XPS, or optical spectroscopies where high-access benchtop equipment is easily available.

Over the last several decades, the capabilities of lab-based XAFS and XES instruments have rapidly grown. Researchers now report spectrometers operating as low as the C K-edge (284 eV)[14] using a laser-produced plasma source. Other spectrometers probe the S and P K emission lines (~ 2-2.5 keV) using double crystal monochromators,[15-17] a dispersive Rowland circle geometry,[18-21] and an instrument in the von Hamos geometry.[22] A variety of von Hamos instruments exist which are intended to operate in the ~3-12 keV range needed for studies of first row transition metals and lanthanides.[23-26] Many spectrometers operating in this range can be directly integrated into synchrotron beamlines.[27] For similar energies, a large number of XAFS spectrometers employing a Rowland circle geometry exist.[28-33] Lastly, higher energies, including the Au Kβ (78 keV), are accessible via Laue-type spectrometers.[34] We focus here on the case of

Rowland circle geometries with a spherically bent crystal analyzer (SBCA), which has been extensively developed by some of the present authors.[13, 35-40]

The purpose of the present manuscript is to describe the design and performance of what is our latest-generation of improvements upon the first prototype instrument using an SBCA.[13] These are embodied in two nearly identical spectrometers, one at the University of Washington (UW) in Seattle and one at Los Alamos National Laboratory (LANL). Each of these sites is more than 1000 km away from the nearest synchrotron x-ray light source. The spectrometer improvements include several simplifications to the monochromator mechanical system that decrease its operation from five to only two motorized degrees of freedom and the selection of a ten-fold higher power x-ray tube that retains the small size and necessary anode characteristics to meet the needs of laboratory XAFS and XES.

The manuscript continues as follows: First, in section 9.4, we describe the new monochromator. Important highlights include decreased mechanical complexity of the new design and modification of the drive configuration to increase its Bragg angle range while minimizing its air-absorption path and overall footprint. Second, in Section 9.5.2 we present and discuss results for XANES and EXAFS of several materials reflecting contemporary interest in materials chemistry and other specialties. Examples include reference metal foils, battery electrode laminates of several different compositions, a family of reference Ce compounds, and uranium-rich materials. In all cases we find good agreement with prior synchrotron studies. For the recorded EXAFS spectrum of the metal foil, we further present a full Fourier-transform analysis using standard methods, and again find high quality results. Next, in Section 9.5.3 we present and discuss results for XES from a wide variety of elements, chemical systems, and emission lines. This includes both deep-shell emission lines and the VTC XES that provides direct insight into

chemical bonding. In sections 9.4.3 and 9.5, care is taken to provide measurement times, thus serving as useful benchmarks for assessing the feasibility of future studies using SBCA-based laboratory monochromators.

9.4 EXPERIMENTAL

9.4.1 *Monochromator Design*

Throughout the period between first publication[13] and this work, several advances in the spectrometer design have been made. Specifically, we have integrated a higher powered x-ray source, rotated and greatly elongated the source and detector stages, implemented passive tracking of the SBCA position (removing a motorized degree of freedom), and enacted the tiltless optic alignment introduced by Mortensen *et al*.[39] (removing two additional motorized degrees of freedom). These changes were motivated by a focus on greater count rates, instrument stability, ease-of-use, and achieving a wider useful energy range with each analyzer crystal orientation.

An overview of the new spectrometer design is given in Figure 9.1. The approach uses linear translation stages to generate fine rotations (Bragg angle steps) and ‘steering bars’ to maintain alignment between the source, detector, and SBCA. This design was based directly on our prototype system.[13] We now summarize similarities and differences of the two new instruments with respect to the prototype instrument.

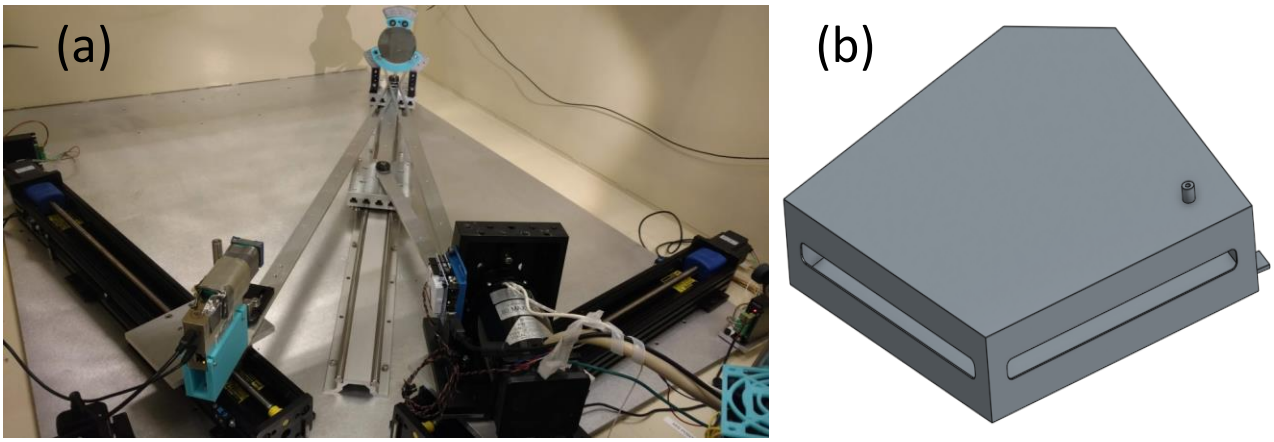

Figure 9.1. (a) Corner perspective of spectrometer in XANES configuration. The SBCA and source are mechanically coupled to the center carriage. The two-axis tilt is no longer utilized. Source and detector are at $\alpha = 40°$ (see Fig. 2). (b) CAD rendering of the helium box (removed from frame (a)) enclosing the x-ray beampath. The slots on the left and right faces are oriented at the height of source and detector, while a rectangular cutout on the far face permits transit of x-rays to the SBCA. Each slot is typically covered by a polyimide film attached to the frame of the helium box.

First, the prototype system used a motorized translation stage underneath the SBCA to maintain its position on the 1-m Rowland circle while the source and detector positions (and hence Bragg angles) were scanned. In the present instrumentation, a passive linear translation stage with two carriages is used; one carriage for the SBCA and another carriage for a pin located at the moving center of the Rowland circle. Coupling bars with lengths equal to the radius of the Rowland circle constrain the Rowland-center pin to be the correct distance (0.5 m) from pins underneath both the SBCA and the source location. This direct mechanical coupling provides exceptional scan-to-scan reproducibility and decreases instrument complexity by removing one motorized degree of freedom.

Second, the source and detector stages have been rotated and made much longer than in the earlier system. The longer travel range allows access to Bragg angles between 55 and 85 degrees, a considerable improvement over the prototype that allows a much wider energy range for each crystal orientation of SBCA. This change decreases the total number of SBCA optics

required of XAFS and XES analysis. Moreover, it extends the utility of the spectrometer beyond XANES, enabling EXAFS studies for several elements. The stage rotation requires some careful comment. The resulting stage geometry is shown in Figure 9.1 and the rotation parameter α is defined in Figure 9.2a. The issue that motivates the rotation of the stages is the desire to minimize the linear travel of the SBCA needed to maintain its position on the (traveling) 1-m Rowland circle. Long SBCA travel is not mechanically onerous, but clearance is required with respect to the helium box (Figure 9.1b) enclosing the beampath to reduce air absorption. When the SBCA has a long travel, the helium box must be made shorter which results in higher air absorption for most operations. To address this problem, a suitable value of α can be deduced from geometric considerations. As the source and detector are swept outward to smaller Bragg angles, the SBCA is necessarily displaced to ensure the source and detector remain on the Rowland circle. This displacement $d(\theta_B)$ is given by

$$d(\theta_B) = -R * sec[\alpha] * (cos[\theta_o - \alpha] + cos[\alpha + 2\theta_B]), \quad (9.1)$$

where R is the radius of the Rowland circle, θ_B is the Bragg angle, and the displacement is measured relative to the position of the SBCA when $\theta_B = 85°$, this value is denoted above as θ_o. In Figure 9.2b, Eq. 1 is plotted as a function of θ_B for various values of α. It is apparent that translation of the SBCA, and consequently attenuation due to air outside of a fixed helium enclosure, can be minimized by an appropriate choice of α. This translation is minimized when the SBCA's travel is symmetric across the angle range, which can be enforced by choosing α to be equal to 180° minus twice the midpoint of the angle range. For a θ_B range of 85° to 55° the SBCA's displacement is minimized when α = 40°, as is utilized in Figure 9.1. Moreover, an additional benefit of the stage rotations is a smaller instrument footprint.

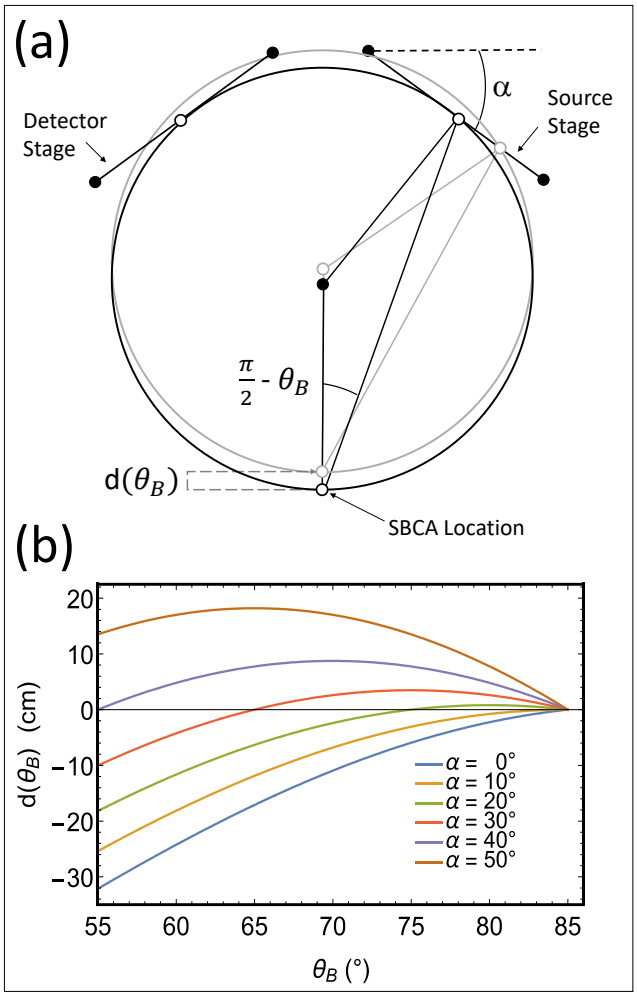

Figure 9.2. (a) Illustration depicting the parameter α and θ_B. The SBCA resides at the bottom of the Rowland circle while the carriage coupling the SBCA location and the source as represented by the hollow dot is at the center of the Rowland circle. The diagonal line represents the travel range of the source with dots at its end points. (b) The magnitude of the SBCA's displacement from its location, d(θB), at $\theta_B = 85°$ is plotted as a function of θB for various values of α.

Third, the present design discontinues the traditional two-axis tilt alignment of the SBCA in favor of orienting the crystal miscut into the plane of the source and detector and enforcing a constant angular offset of the detector, as described by Mortensen and Seidler.[39] This removes two motorized degrees of freedom and also enables easy, reproducible exchange of different SBCAs for different energy ranges. Here, SBCAs are aligned by performing repeated detector scans at different rotations of the optic about its natural cylindrical axis. This fast process gives a

permanent alignment orientation. See Figure 9.3 for representative calibration scans. Note that the highest count rates are generally observed when the crystal miscut is oriented into the Rowland plane, as the SBCA is rotated in either direction away from this orientation, the centroid of the corresponding scans move in the same direction away from the peak at optimal orientation.

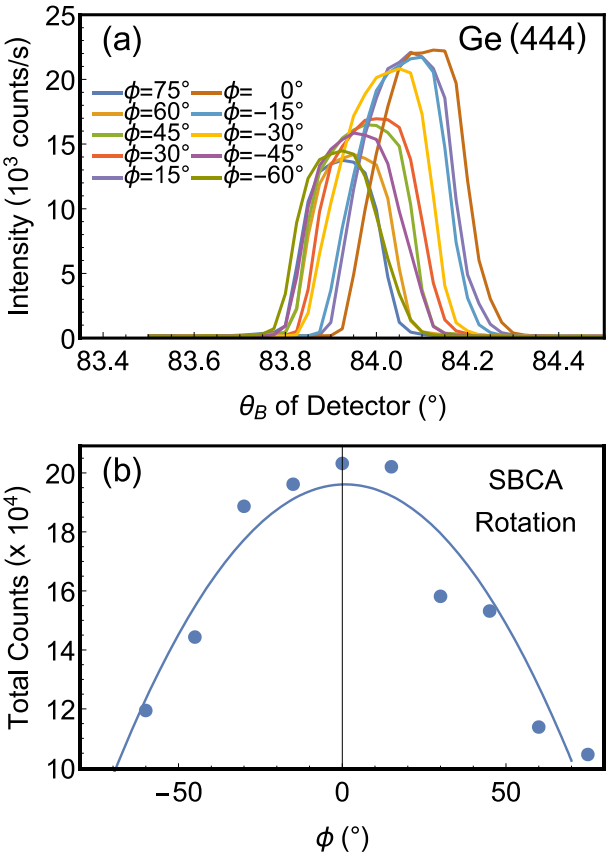

Figure 9.3. (a) While holding the source fixed at $\theta_B = 84°$, the detector was scanned from 83.5 to 84.5°. Scans were taken at various rotations of the SBCA about its center with the optimum position designated as 0°. Data was taken off the 444 harmonic of a Ge SBCA using a x-ray tube source with a Pd anode operated at 52.5 W tube power. The duration of each scan was approximately 45 seconds. (b) The total number of counts, as integrated over the range from 83.5 to 84.5° for each scan, is shown as a function of the analyzer's angular rotation. The solid line is a quadratic fit.

Fourth, from a practical standpoint, the primary benefit of a high-flux source is shorter acquisition times and thus higher potential instrument throughput. Moreover, greater flux can broaden an instrument's limit-of-detection, thus enabling studies of particularly dilute samples or

weak transition lines. Nonetheless, there exist several points of concern when utilizing a high-powered tube source. Namely, high-powered sources typically increase demands on cooling, require progressively more expensive components and high voltage supplies, and their size typically scales in a nontrivial way with increasing tube power, thus posing a challenge toward integration into the synchronous scanning motif. To balance these considerations, the Varex VF50 and VF80 x-ray tube sources are used in the present instruments. These tube sources operate at 50 and 100 W, respectively, and we use either W or Pd anodes as needed to optimize signal levels or avoid tube-source fluorescence lines. These x-ray tubes have small spot sizes (0.5 – 1 mm) and use a 90-degree take-off geometry giving especially efficient generation of x-ray flux per unit electron beam power. By comparison, the x-ray tubes used in the prototype spectrometer[13] were 5-12 W total power and used transmission-geometry anodes with ~3x lower efficiency per unit electron beam power due to absorption during transit through the anode material itself.

Fifth, the high voltage supplies (Spellman uX at LANL and both uX and uXHP at UW) are factory customized to not exceed 35 kV accelerating potential. Since the tube can still be operated at maximum power at these accelerating potentials, this has little effect on the final flux generated at useful energies but has the considerable advantage that the radiation enclosure can then be made from 3.175 mm steel. The new radiation enclosure is a welded steel box with two gas-spring loaded top-facing doors for access to the spectrometer. Two labyrinths provide pass-throughs for cables and gas flow lines.

Finally, at UW the same silicon drift detector (Amptek X-123 SDD) is used as in the prototype spectrometer, while a PIN diode is used in the spectrometer at LANL (Amptek X-123 Si-PIN). Here, however, the ~4-mm active height of each detector does prove somewhat limiting. As θ_B deviates strongly from backscatter (decreasing θ_B) the height of the refocused beam on the

detector quickly becomes taller than the active height of the detector, resulting in significant inefficiency. As discussed below, and in more detail in an upcoming manuscript,[41] this can be ameliorated by incorporation of a taller SDD or by use of a toroidal curved crystal analyzer that is tailored to the Bragg angle range of interest.

9.4.2 *Sample Preparation Details*

In the results and discussion below, we present numerous studies of both XAFS and XES for a wide range of materials. In this subsection we briefly summarize the preparation or provenance of each system. CeO_2 was prepared by thermal decomposition of cerium (IV) oxalate, $Ce(C_2O_4)_2 \cdot xH_2O$ at 800 °C, for 1h, in air, as described by Stennett *et al*.[42] $CePO_4$ (with the monazite structure) was prepared by solid state reaction of stoichiometric quantities of CeO_2 and $NH_4H_2PO_4$: an intimate mixture of these reagents, prepared by hand grinding with a mortar and pestle, was heated at 1100 °C, for 8h, in air. Analysis of the products by powder X-ray diffraction confirmed the synthesis of single phase materials. Specimens were prepared for XAS analysis by sieving to less than 63 μm before mixing with polyethylene glycol and pressing into 13-mm diameter pellets having suitable μx for transmission-mode study. ε-$VOPO_4$ investigated in the present study was prepared by hydrothermal synthesis.[43] Thin laminates for XAS investigation were prepared by mixing ε-$VOPO_4$ powder with graphene and polyvinylidene fluorine (PVDF) as binder in a weight ratio 75:15:10 using 1-methyl-2-pyrrolidinine (NMP) as the solvent. The resultant slurry was tape cast onto an aluminum foil and dried in air at 60 °C. Circular discs of about 13mm diameter were punched out of the coated aluminum foil and sealed between the adhesive-coated Kapton tapes.

Commercial nickel- manganese- cobalt- (NMC) oxide battery cathode laminates were manufactured in a 6:2:2 stoichiometric ratio between the transition metals. The cathode laminate was cast with a 5 wt % PVDF binder and carbon on a 10 µm thick aluminum current collector. Laminates were prepared in two states of charge, a pristine uncharged laminate and a charged laminate harvested from a coin cell. The latter was sealed in an aluminum-coated polyimide envelope during measurement to reduce interaction with air.

Uranium(IV) hexachloride, $(PPh_4)_2UCl_6$, was prepared as previously described.[44] Uranyl tetrachloride was prepared in a modified version of previous syntheses.[45-46] This involved addition of two equivalents of tetramethyl ammonium chloride (NMe_4Cl) to UO_2^{2+} in concentrated hydrochloric acid (HCl, 12 M). Within 1 week crystals formed and the compounds identity was then confirmed by single crystal X-ray diffraction.

Caution! *^{238}U is a low specific-activity (half-life 4.4 billion years) a-emitter, which is hazardous to human health. This type of research should only be performed in a facility equipped with appropriate controls for the safe handling of radioactive materials.*

Samples were prepared by grinding the $(PPh_4)_2UCl_6$ (20 mg) with boron nitride (BN, 40 mg) for two minutes. An aluminum spacer with interior dimensions 1 mm x 5 mm x 20 mm was filled with the resulting powder and sealed in two layers of polyimide tape.

Finally, metal foils were acquired from EXAFS Materials. These include a 6 µm Ni foil, a 5 µm V foil, a -400 mesh Mn foil, and a 25 µm Y foil. Also, the V_2O_3, VO_2, V_2O_5, $NaAsO_2$, and $Na_2HAsO_4 \cdot 7H_2O$ powders measured in XES were purchased from commercial vendors.

9.4.3 *Synchrotron XAS Measurement Details*

XAS measurements of ε-VOPO4 were carried out at the beamline 9-BM of Advanced Photon Source (APS) in USA. Data were collected in the transmission mode at the V K-edge using

the Si (111) double-crystal monochromator, which was slightly detuned to suppress higher harmonics. Absolute energy calibration of the monochromator was carried out by measuring the reference foil of pure V simultaneously with the sample. Intensities of the incident beam and the beams transmitted through the sample and the reference foil were recorded using the gas-filled ionization chambers. All spectra were energy-calibrated with respect to the first peak in the derivative spectrum of pure V. Data processing operations were carried out using ATHENA.[47]

Ce L_3 edge XAS data of CeO_2 and $CePO_4$ (with the monazite structure) were acquired on beamline X23A2 of the National Synchrotron Light Source (NSLS), Brookhaven National Laboratory (BNL), USA. The experimental configuration and details described in Hyatt et al.[48] were repeated for the present study. Here, the data were acquired in transmission mode using finely ground specimens dispersed in polyethylene glycol (PEG) to achieve a thickness of one absorption length. 0.5 eV steps were used over the absorption edge with a dwell time of 5 seconds per point.

The U L_3 XANES spectra were measured at the Stanford Synchrotron Radiation Lightsource (SSRL) on end station 11-2 according to the methods of Pattenaude et al.[49] This includes the use of a double-crystal Si (220) monochromator, along with collimating and focusing mirrors, on a 26-pole, 2.0 tesla wiggler.

9.5 XAFS AND EXAFS RESULTS AND DISCUSSION

9.5.1 *Basic Instrument Performance*

The present instrumentation was evaluated according to several performance criteria, including typical count rates. In Figure 4, the intensity of the incident beam in an absorption configuration was measured across the full angular range of the instrument. Near backscatter (θ_B

= 90 °), count rates near 50,000/s are observed at 100 W x-ray tube power with the Pd anode (this and all subsequent measurements were performed at 35 kV accelerating potential), yet the count rate quickly drops to around 15 % of this value at especially low Bragg angles. The reason for this decline is the limited size of the detector. In the present design, x-rays are refocused to a line at the detector due to sagittal error. The height of this line increases as the source and detector travel to lower Bragg angles and only a portion of this line is measured as permitted by the finite size of the detector. The decline in count rates observed in Figure 9.4 is consistent with ray tracing simulations reported elsewhere.[41] If a larger detector or toroidal optic is integrated into the design, consistent count rates could be observed across the instrument's angular range.[41]

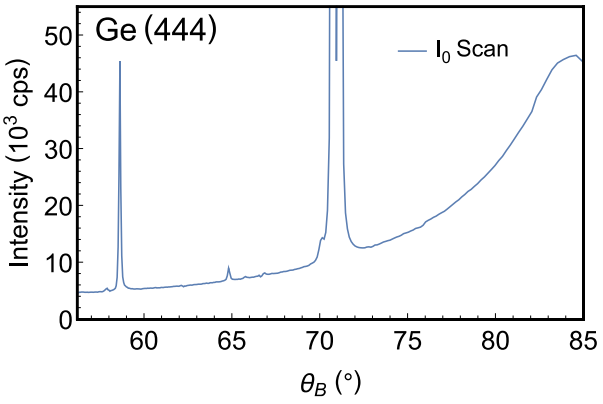

Figure 9.4. An I_0 scan spanning the entire range of the instrument. Data was collected using the 444 harmonic of a Ge SBCA. An x-ray tube source with a Pd anode was operated at 100 W power. Fluorescence lines can be seen from Cu Kα and Kβ lines as well as a small W line around 8400 eV. This last line is likely due to some small number of W atoms from the filament being deposited onto the surface of the target anode as has been discussed elsewhere.[31]

The spectrometer's reliability was assessed according to its scan-to-scan reproducibility. Figure 9.5 shows a series of consecutive scans collected in a transmission mode XANES configuration across the Mn K-edge of the Mn foil. Also shown is the residual of each scan with respect to the first and an envelope of two standard deviations as calculated from the incident flux by Poisson statistics. The residuals are well captured by Poisson statistics.

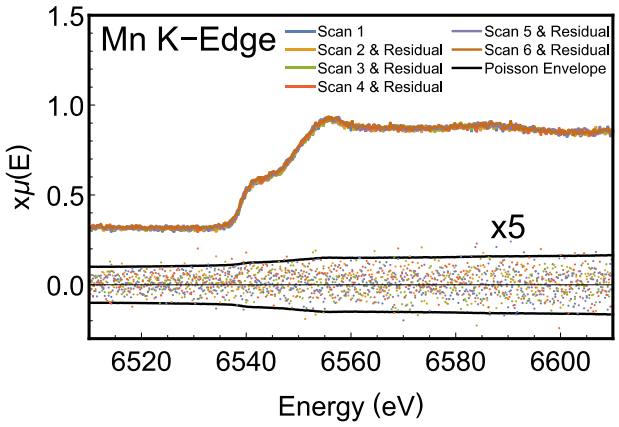

Figure 9.5. Six consecutive scans are shown of a transmission mode measurement across the K-edge of the Mn foil. Measurements were collected using a Si (440) SBCA. An x-ray tube source with a W anode was operated at 25 W with a 10 μm thick Zn foil acting as an absorber to suppress the W fluorescence line observed on the Si (660) harmonic in accordance with methods previously reported, although done here without a slit system.[107] The residuals between subsequent scans are shown at the bottom of the figure (magnified five times) with a Poisson envelope enclosing two standard deviations.

The monochromator performs well in a final, critical performance metric, its energy resolution. This parameter was assessed by measuring the XANES spectrum of a V metal foil. From Figure 9.6a, the laboratory-based instrumentation produces spectra nearly identical to those acquired at the synchrotron, however, minor changes in resolution can be observed by magnifying the especially sharp pre-edge feature found in this system. Convolving the synchrotron spectrum with a 0.4 eV FWHM Gaussian yields excellent agreement with the first set of laboratory-based measurements. One contribution to the broadening is that although the V K-edge is located at a Bragg angle of 79.2 ° for the Ge (422) optic, the spectrum will still exhibit some broadening due to Johann error. To investigate this effect, the outer portion of the SBCA was blocked with a Pb mask to produce a spectrum that is now broadened by only 0.2 eV relative to the spectrum reported by NSLS X23A2. Although the critical metric for extracting scientific inference is the ability to

resolve spectral features and not any quoted energy resolution, the question of absolute energy resolution, both for XAFS and for XES, deserves special mention.

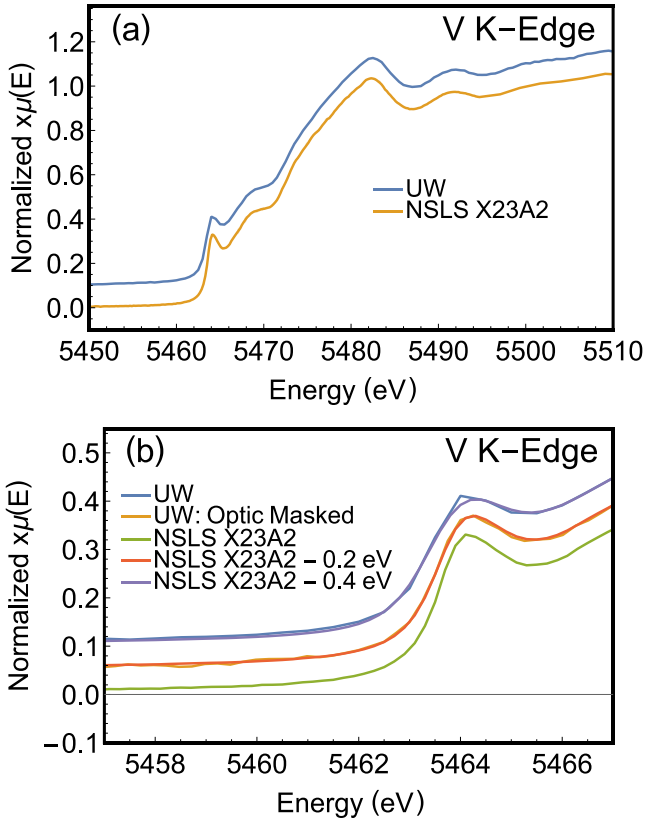

Figure 9.6. (a) XANES spectra of the V foil collected using an x-ray tube source with a W anode and operated at 50 W power. Comparison was made to synchrotron results and offset for clarity, see the text for discussion. (b) An enlarged view of the pre-edge feature at ~5464 eV including comparison with synchrotron results with the indicated Gaussian broadening. Laboratory-based measurements used either a masked or unmasked Ge (422) SBCA. Spectra are offset for clarity.

Three primary factors dictate the present instrument's energy resolution. First, the intrinsic energy resolution of the non-strain-relieved SBCA at the energy of interest is approximately 0.3 eV based on the results of Hämäläinen et al.,[50-51] which are consistent with those of Rovezzi et al. in the 6 - 11 keV energy range.[52] Second, the use of a Johann analyzer yields an energy broadening of at most 0.25 eV in the present case,[53-55] however, the severity of this error will increase at lower

Bragg angles. Third, the source size in the Rowland plane gives a purely geometric energy broadening which can be calculated from the differential form of Bragg's law.[52, 55] While this is usually set for the XAFS configuration by the 1-mm x-ray source spot size (upper bound), we note that our implementation of an entrance slit on the source side provides a means to tune this aberration.[38] Yet in the present scenario, this geometric factor contributes a maximum broadening of 1 eV. From the work of Bergmann and Cramer,[55] we can see that other geometric sources of broadening are negligible here and report a conservatively estimated nominal absolute energy resolution of 1.1 eV.

9.5.2 *XAFS Demonstration Studies*

Here, we present the results of several XAFS studies using the lab spectrometer. These include XANES of battery materials, lanthanide and actinide compounds and also EXAFS of reference metal foils. The times for scan acquisitions of all demonstration studies are summarized in Table 1. Taken *en masse*, the results strongly support the usefulness of the lab spectrometer for a very wide range of concentrated systems where transmission-mode studies are possible. We begin with XANES.

Table 9.1. Experimental details of XES and XAFS measurements performed in this work. Acquisition times spanning multiple compounds refer to the time allotted to each sample. Acquisition times reported in this table only includes the time required to span the energy range shown in the corresponding figure. XAFS acquisition times are reported only for the transmission scans.

Figure #	Anode	Power (W)	SBCA	Compound	Measurement	Acquisition Time (h)
7a	W	50	Ge (422)	ε-$VOPO_4$	XANES	3.0
7b	Pd	50	Si (444)	NMC	XANES	0.22
7c	W	50	Si (444)	NMC	XES $K\beta_{1,3}$	0.06
8a	W	50	Si (422)	CeO_2	XANES	1.0
				$CePO_4$		
8b	Pd	50	Si (12,6,6)	$(PPh_4)_2UCl_6$	XANES	44
9	Pd	100	Si (551)	Ni	EXAFS	6.9
10a	W	50	Ge (422)	ε-$VOPO_4$	XES Kβ	12.4
				V		
				V_2O_3		
				VO_2		
				V_2O_5		
10b	W	50	Ge (422)	V_2O_3	XES $K\beta_{1,3}$	4.5
				VO_2		
				V_2O_5		
11	Pd	100	Ge (555)	Zn	XES $K\beta_{2,5}$	9.6
				ZnO		8.0
				$ZnCl_2$		11.5
12a	W	50	Si (555)	$NaAsO_2$	XES Kα	1.4
				$Na_2HASO_4 \cdot 7H_2O$		0.8
12b	Pd	50	Si (12,6,6)	$(PPh_4)_2UCl_6$	XES Lβ	30
				$TBA_2UO_2Cl_4$		24

First, electrical energy storage is a particularly promising application for laboratory-based x-ray spectroscopies.[56-59] Here, XANES is already established as a useful tool for the study of electronic properties at various levels of detail. For example, a routine approach utilizes XANES to assess the redox reversibility of battery materials during cycling.[60] Similarly, many examples exist of x-ray spectroscopies addressing more complex speciation inquiries, including lithiation dynamics in nickel cobalt aluminum oxide cathode materials,[61] discernment of the soluble Mn ion

in a Li-Mn spinel electrode,[4] and evaluation of sulfide precipitation and under-utilization of active material as competing hypotheses for sub-optimal capacities in lithium sulfur batteries.[3]

Several other factors suggest lithium ion battery (LIB) cathode materials as an ideal system for laboratory-based x-ray instrumentation. Most importantly, the typical thickness of the metal oxide layer found on a cathode frequently gives edge steps $\Delta\mu \cdot x \sim 1-2$, as is desirable for XAS studies.[62] Also, the electrochemically active elements in modern LIB cathodes are often 3*d* transition metals, for which the K-edges are at energies high enough so that some air attenuation can be tolerated but low enough that the SBCA and other Bragg-based analyzers still have good efficiency.

The XANES spectra of two archetypal Li-ion battery materials, ε-$VOPO_4$ and NMC oxide laminates, are presented in Figure 9.7a and Figure 9.7b. The agreement between lab-based and synchrotron spectra in Figure 9.7a is excellent, including the details of the pre-edge feature which is important for elucidating the molecular symmetry at the metal center.[63] Figure 9.7b presents NMC electrodes at two different states of charge. The charged and uncharged laminates exhibit multiple differences, including a pronounced shift in the edge position of the two systems. Such an edge shift is traditionally attributed to a change in oxidation state[64] and, in the present case, confirms the instrument's capability for element-specific tracking of redox behavior in cathode materials.

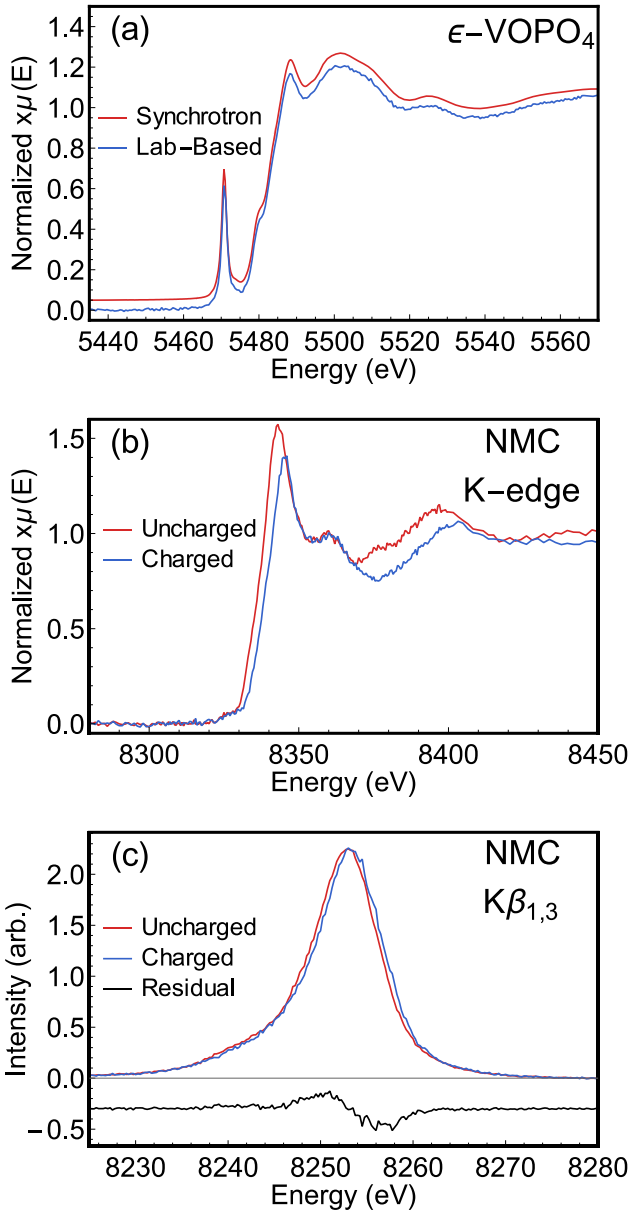

Figure 9.7. (a) The V K-edge XANES spectra of a vanadyl phosphate-based battery laminate. Spectra were acquired with the present instrumentation (Lab-Based) and at APS 9-BM (Synchrotron). The spectra are offset for clarity of presentation. The full range of scans was chosen to extend from 5390 eV out to 10 $\mathbf{Å^{-1}}$ to ensure proper normalization and background removal for comparison to the synchrotron. (b) XANES spectra of uncharged and charged battery laminates of NMC composition. Data was again acquired out to 10 $\mathbf{Å^{-1}}$ and data was collected at lower energies to aid background removal. (c) XES spectra of a charged and uncharged NMC laminate. The residual of the two spectra is displaced below the main results. Peak count rates were around 12,000 counts per second for the uncharged laminate and 6,000 for the charged laminate.

Moving away from the 3d transition metals, it is useful to next discuss lanthanide compounds. The L3-edges of the lanthanides are in a very similar energy range as the 3d transition metals, strongly suggesting good performance for our system, and there exists a large body of research using the dependence of XAFS spectral features on the speciation of lanthanide compounds.[65-67] Sample applications include high temperature, *in situ* analysis of: ceria-based oxide materials used in the activation and storage of oxygen,[68] the effect of annealing temperature on the valence state of cerium oxide nanoparticles manufactured to catalyze the oxidation of organic compounds or reduction of heavy metals in industrial waste streams,[69] and the mechanism by which cerium-containing films inhibit the corrosion of aluminum.[70]

XANES spectra of $CePO_4$ and CeO_2 taken in the lab are presented in Figure 9.8a. The lab-based spectra are energy corrected by alignment with the reference cerium dioxide spectrum found in Hephaestus.[47] In particular, note that Poisson errors observed in Figure 9.8a are far from eclipsing the shape of spectral features and that scan acquisition times, just as with the above transition metal study, are reasonable for many applications involving routine analytical characterization. This is true throughout the energy range from 6 keV to as high as the actinide L_3 edges at and above 17 keV, as we now show. The difference in height of the CeO_2 near-edge peak may be due to different preparation of the samples, as oxygen deficiency can commonly influence that feature.

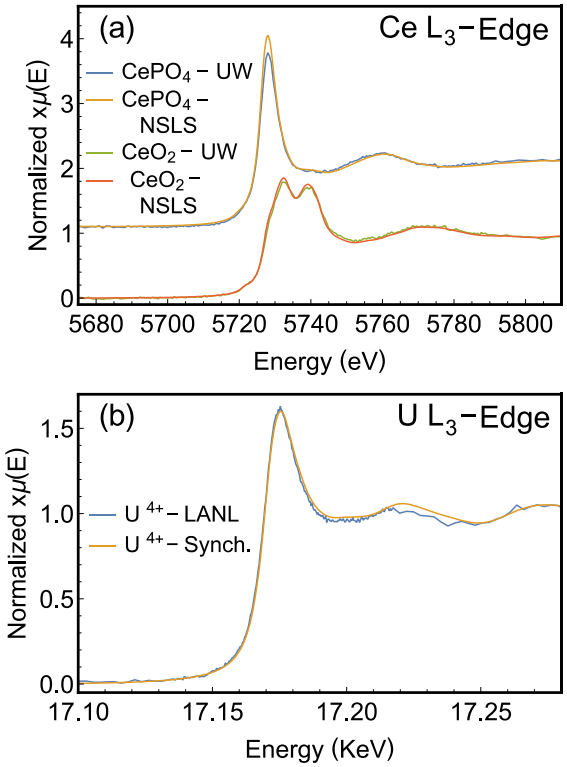

Figure 9.8. (a) XANES spectra of $CePO_4$ and CeO_2, representative Ce^{3+} and Ce^{4+} compounds, respectively. Reference spectra were acquired on beamline X23-A2 of the National Synchrotron Light Source (NSLS). (b) Comparison of synchrotron (endstation 11-2 at SSRL) and lab-based U L_3-edge XANES for $(PPh_4)_2UCl_6$, a U^{4+} reference compound. Data was calibrated to the maximum of the first derivative of the K-edge spectrum of a yttrium foil at 17038.4 eV.

Next, we address the high-energy range for applications of the laboratory spectrometer. While the present instrument design is not optimal for operation at 17 keV and beyond, it has proven quite effective. U L_3-edge XANES spectra for $(PPh_4)_2UCl_6$ is presented in Figure 9.8b and directly compared to a synchrotron-based measurement. These measurements used the older, 50 W x-ray tube in the spectrometer at LANL. Clearly, U L_3 XANES can be measured in useful study times with our spectrometer; comparable results with a spectrometer of similar design have recently been reported by Bès, *et al.*[71]

The decreased performance of the lab spectrometers at high photon energy is due to limitations in the source, Bragg optic, and detector. The bremsstrahlung spectrum from the tube

has the usual $\sim 1/E$ roll-off at high energy. This is complicated here, however, by our choice to hardware-limit the high-voltage supply to 35 kV, resulting in somewhat less proportional generation of ~17 keV photons than would be the case with a higher accelerating potential and the same total electron beam power. Combined with the narrower Darwin width of the SBCA for higher order reflections, the integral reflectivity is greatly decreased at higher photon energy.[72] There are some studies of higher-energy XAFS using laboratory-based instruments having Laue-style analyzers where the optic has much higher integral reflectivity from lower-order reflections, but where the effective solid angle is typically much reduced.[34, 73] The present detector also limits the efficiency for two reasons: it has only ~50 % quantum efficiency at these energies, and the active region of the detector used in the actinide study was only ~5-mm tall, so that ~2x flux was lost because of the vertical extent of the beam. Hence, the corresponding obvious upgrades to a 100-W x-ray tube and a taller detector with higher quantum efficiency will yield ~8x improved count rates on the same monochromator. The question of optimum lab-spectrometer design for high-energy XANES is very much an open question that could have high impact in heavy element chemistry (via L-edges) and 4*d*-chemistry (via K-edges).

The above studies demonstrate the broad versatility of the lab-based system for XANES studies. The extended oscillations pose a more stringent challenge, due to both the limitations imposed by Poisson statistics and the requirement of correct monochromator function over a wider energy range.

Face-centered cubic, metallic nickel was chosen as a model system to assess the present instrument's EXAFS capabilities relative to a synchrotron. The forward Fourier transform of Ni's EXAFS spectrum was performed for photoelectron momentum up to k = 12 **Å^{-1}**. An isotropic expansion model was used for both systems and distinct Debye-Waller (DW) factors were assigned

to the single scattering path associated with each neighboring atom. DW factors for collinear paths were calculated in the manner of Hudson *et al*.[74] while triangular paths were approximated from the single scattering path's DW factors. Fits were performed in Artemis[47] from R=1 to R=5.5 Å and included all scattering paths in that range. Resulting R-factors reveal the spectra to be well described by the fitted model. Similarly, the passive reduction factor, which is subject to inconsistencies according to individual beamline characteristics,[75] is within the range of values typically reported for robust fits. In Figure 9.9, excellent agreement is found between the lab and synchrotron-based measurements, as well as between experimental results and fitted models. Likewise, the physical quantities produced by the EXAFS fits are presented in Table 9.2. Selected EXAFS fitting parameters for Ni foil measured at APS and at UW as compared to literature fits, x-ray diffraction (XRD), and neutron PDF analysis. Uncertainties correspond to one standard deviation., revealing excellent agreement between data acquired at different instruments and with previously reported values.

Table 9.2. Selected EXAFS fitting parameters for Ni foil measured at APS and at UW as compared to literature fits, x-ray diffraction (XRD), and neutron PDF analysis. Uncertainties correspond to one standard deviation.

			Shell1		Shell2		Shell3		Shell4	
	S_o^2	R-factor	Ni-Ni (Å)	σ^2 (10^{-4} Å^2)	Ni-Ni (Å)	σ^2 (10^{-4} Å^2)	Ni-Ni (Å)	σ^2 (10^{-4} Å^2)	Ni-Ni (Å)	σ^2 (10^{-4} Å^2)
XRD[104]			2.4863		3.5161		4.3063		4.9725	
Neutron PDF[105]			2.487 (1)	64 ± 1						
XAFS Lit.[106]			2.493 (2)	65 ± 2						
XAFS Lit.[105]	0.84 (2)		2.485 (2)	64 ± 2						
APS 13-ID[47]	0.90 (6)	0.015	2.493 (4)	67 ± 6	3.525 (5)	96 ± 19	4.317 (6)	91 ± 10	4.985 (7)	79 ± 8
UW	0.81 (6)	0.016	2.490 (4)	61 ± 6	3.522 (5)	76 ± 16	4.314 (7)	92 ± 11	4.981 (8)	79 ± 9

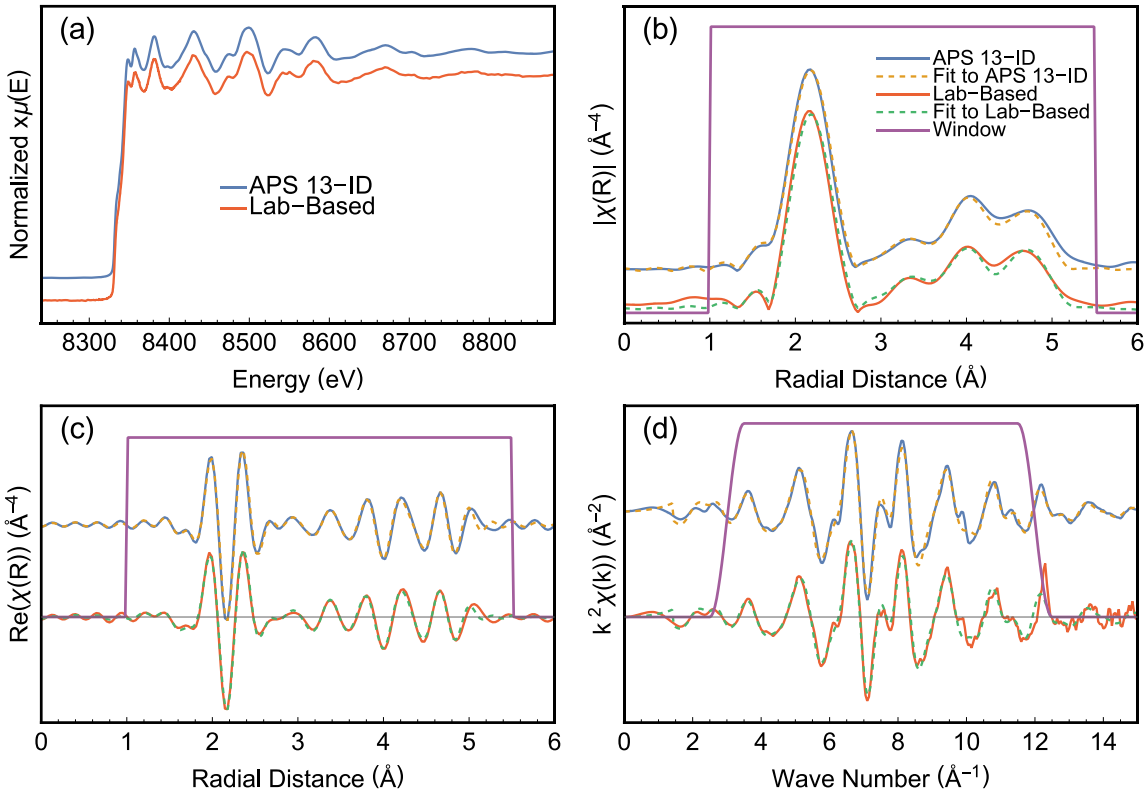

Figure 9.9. EXAFS of Ni Foil collected at UW (Lab-based) compared to synchrotron results (APS 13-ID). Results are shown in energy space (a), along with the magnitude of the EXAFS in radial space (b), the real part of the EXAFS in radial space (c), and the EXAFS with quadratic weighting in k-space (d), respectively. Also shown are the fitted models acquired from Artemis.[47] Data was collected using 100 W power for a Pd anode x-ray tube and using a Si (551) SBCA. Measurement times were 1.7 and 6.9 h for I_0 and I_T, respectively.

9.5.3 *XES Demonstration Studies*

X-ray emission spectroscopy (XES) is seeing rapid growth as both a complement to XANES and as an emergent technique in its own right. Its sensitivity to the occupied local electronic density of states can often aid in assessing the oxidation state, spin state, covalency, state of protonation, or ligand environment of a given metal atom.[76-78]

From an experimental perspective, XES benefits from several pragmatic advantages in the laboratory environment. While the simpler sample preparation for XES than for transmission-mode XAFS is often relevant, the dominant issue is the efficient use of the incident x-ray flux.

Conventional x-ray tubes are inherently broadband, showing a few strong fluorescence lines on top of a bremsstrahlung background. Monochromatizing the raw tube spectrum with a crystal analyzer selects only a modest solid angle of the total tube emission and also a tiny slice of the entire tube energy spectrum, decreasing broadband, wide-angle fluxes of ~10^{13} /s or more to only 10^4 – 10^5/s. However, direct illumination of the sample, as in non-resonant XES, utilizes a large solid angle and makes every incident photon above the relevant binding energy capable of stimulating the creation of a core-hole. Accordingly, a recent publication by the authors demonstrated lab-based XES measurements as a viable route to quantitatively assess metal speciation even in very dilute systems,[40] even with the very low powered x-ray tube of the earlier prototype spectrometer.[13]

Here, we present the results of several XES studies using the lab spectrometer. Thematically, the XES results are presented from lowest to highest energy emission lines. This begins with an overview of the Kβ lines for a collection of vanadium compounds including metallic vanadium, a suite of vanadium oxides, and vanadyl phosphate, a candidate material for energy storage applications. Similarly, routine valence-to-core (VTC) XES measurements of assorted zinc compounds sampling a variety of ligand environments are discussed. Next, arsenic Kα XES results suggest the potential of the present instrumentation for speciation studies of dilute environmental samples. Finally, less standard measurements of actinide L emission lines are presented. Note that, again, the acquisition times for all studies are summarized in Table 1 and repeated in the figure captions.

First, a range of chemical information is accessible in the V Kβ spectra in Figure 9.10a. For example, note that the wide-energy range accessible by a single scan permits careful branching ratio studies of vanadium oxide $K\beta_{1,3}$ and $K\beta_{2,5}$ features which, as can be seen in Figure 9.10a, are

exceedingly well resolved. An additional advantage of this range is the feasibility of robustly subtracting the tail of the main Kβ emission from the VTC region to aid the analysis of the latter. Furthermore, Figure 9.10b shows the $K\beta_{1,3}$ of a variety of vanadium oxide moieties, with a clear evolution in the spectrum as oxidation state changes. Likewise, the Kβ', which is split from the $K\beta_{1,3}$ by (3p,3d) exchange, can be seen to vary in intensity across the oxides. For transition metals, the intensity of this feature often correlates with the number of unpaired 3*d* electrons and thus provides a measure of the spin state of the probed atom. For some systems, the dependence of the $K\beta_{1,3}$ emission's energy on oxidation state can be muted, as is the case for Ni oxides.[79-80] However, it can be seen in Figure 9.7c that there is a small but measurable shift between the $K\beta_{1,3}$ XES of two NMC laminates at different states of charge. These spectra are also intense, allowing acquisition times on the order of minutes.

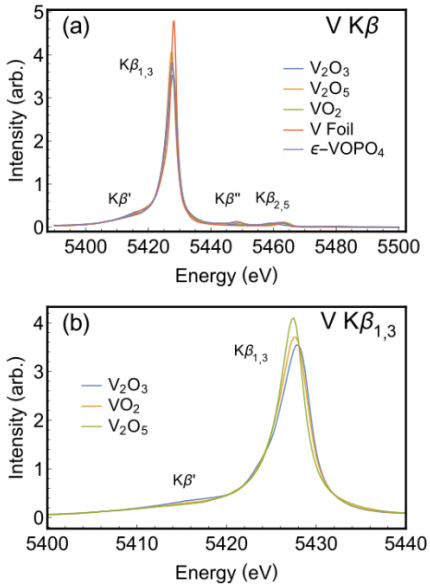

Figure 9.10. (a) The full range of V Kβ XES from a collection of V compounds measured in the lab spectrometer. Measurement times were 12.4 h for all samples. Note that the vanadyl phosphate data represents three scan ranges, with the main scans spanning 5395 eV to 5485 eV, this range was joined with supplemental data sets to span the entire range shown and permit equivalent background subtractions for all systems. (b) V $K\beta_{1,3}$ XES from a suite of oxides measured in the lab spectrometer.

The VTC region for some Zn compounds is presented in Figure 9.11. The significance of this region warrants some discussion. In recent years, VTC-XES has emerged as a highly useful tool for the interrogation of a system's local electronic structure. This method permits a direct probe of the orbitals involved in chemical bonding, and, as a result, is highly-sensitive to changes in oxidation state, covalency, state of protonation, and coordination environment. As a unique case in point, VTC-XES is sometimes able to discern which of several light elements is ligated to a central metal atom, with considerable impact. In 2002, Einsle *et al*. reported the presence of carbon, oxygen, or nitrogen as a central atom in iron-molybdenum cofactor (FeMoco), a cluster which acts as the active site of substrate binding and reduction in nitrogenase.[81] Despite intense study, the identity of this atom could not be unambiguously established until the Fe VTC-XES study of Lancaster and co-workers.[82] Likewise, the utility of this method has, on numerous occasions, been evidenced in recent catalysis research. For example, Pushkar *et al*. demonstrated the feasibility of VTC-XES for detecting and probing the oxo bridges found in the Mn_4Ca cluster of photosystem II, establishing a powerful tool for studying the O-O bond formation preceding O_2 evolution.[83] Due to its increasing popularity, much research has been conducted to develop the theoretical underpinnings of VTC-XES and to identify spectral features that can serve as measures of various chemical parameters. For example, a recent article by Pollock, *et al.*,[84] identifies a feature in the VTC-XES spectra of several Fe-N_2 complexes that can be attributed to a transition from the 2s2s σ^* antibonding-orbital to the 1s core-hole. The energy of this feature is then related to the N-N bond length and serves as a measure of the degree of activation of small molecules during catalytic reduction.[84] Finally, several review articles can be found that discuss VTC-XES in various levels of detail.[76-77, 85]

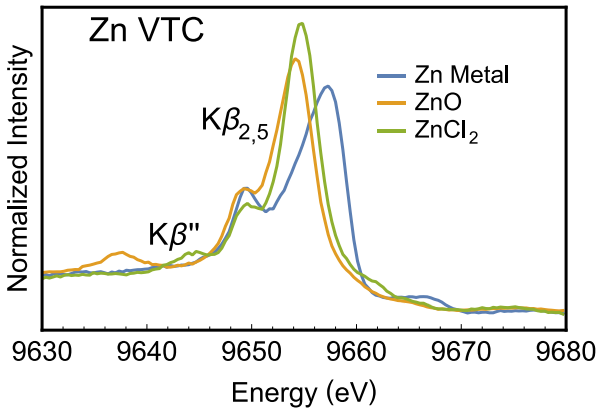

Figure 9.11. VTC-XES spectra of Zn metal, ZnO, and $ZnCl_2$ after background subtraction and integral normalization across the full VTC energy range.

Here, a system of Zn compounds comprised of Zn metal, ZnO, and $ZnCl_2$ was chosen to reflect the feasibility of VTC-XES measurements with the present instrumentation along with its sensitivity to a variety of ligand environments. A similar study using an earlier, lower powered instrument investigated similar compounds and made a critical comparison across several theoretical treatments of VTC-XES.[37] Despite the present instrument's increase in flux, background removal only required the subtraction of a constant as determined by the measured intensity at the highest energies sampled and typically five percent or less of the peak intensity in the VTC region. As can be seen in Figure 9.11, the present instrumental resolution also clearly resolves the double-peak structure of the $K\beta_{2,5}$ lines. In addition, the Kβ'' transitions indicative of the ligand environment are clearly discernible for the oxide and chloride systems, with the former ~17 eV below the main peak, in rough agreement with values reported elsewhere for the relative Kβ'' position.[86] Finally, the non-resonant excitation process utilized with a broadband source again gives rise to multielectron features that can be observed toward high energies in the spectrum of metallic zinc. We note that similar XES features have been reported for other sample matrices elsewhere.[35, 87-88] However, it is interesting to note that while multielectron features were largely suppressed in the ligated Zn-compounds due to charge-transfer effects, this is expected not to be

the case for early row transition metals whose properties are better described by the motif of Mott-insulators than charge-transfer semiconductors.[89]

Beyond investigations of the electronic details discussed so far, there exists a wealth of applications that would benefit from routine oxidation state analysis using laboratory-based XES. This has recently been demonstrated for hexavalent Cr identification using Cr Kα spectroscopy with the UW instrument,[40] and has also been used for identification of sulfur oxidation state in biochars[90] and phosphorus oxidation state in InP quantum dots[91-92] using a different very high-resolution lab-based XES system at UW. Indeed, this theme of routine access enabling XAFS and XES studies has been borne out in several fields. Of particular note, laboratory-based instrumentation has been applied to the coordination analysis of the Ni^{2+}-EDTA-CN^- ternary system,[93] oxidation state analysis of a reactive dinuclear Ni(IV) oxido complex,[94] chemical state analysis of a mesoporous perovskite proposed for energy-related applications,[71, 95] and the spin-state analysis of model Fe compounds.[96] Indeed, similar arguments which advocate for laboratory-based instrumentation as high-access tools to accelerate research have been made by Bès et al. regarding studies which address nuclear fuel development and nuclear waste disposal.[71]

Here, we consider whether benchtop XES can address the oxidation state of environmental arsenic. A pioneering work by Penrose found that of the two most common oxidation states, the trivalent species of arsenic is generally more toxic than the pentavalent.[97] XAFS techniques have emerged as essential alternatives for quantitative species fraction determinations of arsenic in solid matrices, such as in soils where the methodology can be paired with sequential extraction procedures[98] or HPLC-ICP-MS[8] to provide insights into the behavior of arsenic in ecological systems. Here, representative As(III) and As(V) compounds are presented as a demonstration study relevant for potential environmental speciation studies in a laboratory setting. For this study,

samples were obtained in powder form and directly transferred to a polyimide pouch easily positioned in front of the source. As can be seen in Fig. 12a, the As Kα XES measurements reveal several noticeable spectral differences, including an energy shift that can be used as an indicator of oxidation state. Figure 12a also highlights the high intensity of these features, suggesting the potential of this technique in studies of dilute environmental samples. This approach to As speciation requires further investigation, as would other As fluorescence lines. We note that while the As Kα does have a clear energy shift, true environmental samples with As contamination also commonly have nontrivial Pb content, and that the Pb $L_{III}M_V$ emission line at 10551.6 eV can interfere with the As Kα XES.

Finally, we address XES of actinide materials. The L emission lines in U lie between 10 and 21 keV, with most toward the latter. Similar detector, source, and analyzer inefficiencies discussed above in the context of actinide XANES are problematic in U XES studies as well. In addition, the L-shell fluorescence lines more likely to be sensitive to chemical bonding are those involving shells closer to the valence and are consequently weaker transitions, again requiring instrumentation with minimal backgrounds. Nonetheless, U XES measurements of $(PPh_4)_2UCl_6$ and $(NMe_4)_2UO_2Cl_4$ are presented in Figure 9.12b. The most prominent feature is the $L\beta_1$ ($L_{II}M_{IV}$) found around 17220 eV.[99] Other than a shift of the $(PPh_4)_2UCl_6$ emission spectrum to about 0.5 eV higher energy than that of $(NMe_4)_2UO_2Cl_4$, little sensitivity to speciation was observed. While other L emission lines are observed in this energy region their inadequate separation from the tails of these features complicates their use as fingerprints for the relevant U species.

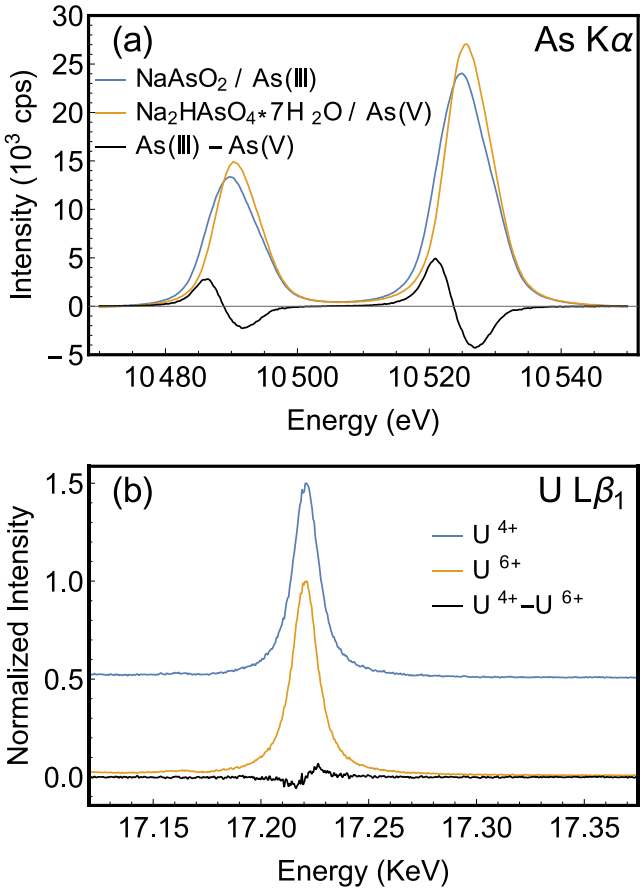

Figure 9.12. (a) The As Kα XES spectra of trivalent and pentavalent arsenic oxide species (a). The intensity scale is for the $NaAsO_2$ sample; the intensity of the Na_2HAsO_4*7H20 has been scaled upward by ~30% to give it the same integral intensity for ease of comparison for the energy shift as a function of As oxidation state. The study used a Si (555) toroidally bent crystal analyzer following an in-house design.[41] (b) Collected $L\beta_1$ XES spectra of $(PPh_4)_2UCl6$ and $(NMe_4)_2UO_2Cl_4$, which are in the U^{4+} and U^{6+} state, respectively. The most intense spectral feature is the $L\beta_1$, though less intense features can be found toward lower energies. The spectra are peak normalized here for comparison. A residual is provided and spectra are offset for clarity. No change in spectrum was observed across any of the scans, indicating no radiation damage. The data was calibrated to the maximum of the Kα of a Mo foil at 17480 eV.

9.6 Summary and Conclusions

We present the instrumentation details and a wide variety of test study results for an improved laboratory spectrometer for XAFS and XES. This includes measurements that demonstrate important extremes for lab-based capability: EXAFS, VTC XES, and higher-energy

performance. The assembled body of work using this new spectrometer, building on top of numerous studies by our research group[13, 35-41, 90-91, 100-101] and also ongoing research of several other research groups[23, 25-26, 34, 71, 102] strongly supports the position that laboratory XAFS and XES should not be judged in competition with synchrotron capability but should instead be appreciated for the new analytical capabilities that are enabled. These new capabilities hold high promise for routine materials analysis that can accelerate progress in electrical energy storage, coordination chemistry,[103] actinide chemistry,[71] and environmental and regulatory testing,[40] to name only a few prominent examples.

9.7 Acknowledgements

E. Jahrman and T. Fister were supported in part by the Joint Center for Energy Storage Research (JCESR), an Energy Innovation Hub funded by the U.S. Department of Energy, Office of Science, and Basic Energy Sciences, and by the U.S. Department of Energy through the Chemical Science and Engineering Division of Argonne National Laboratory. This material is based in part upon work supported by the State of Washington through the University of Washington Clean Energy Institute. The work of J. Rana and L. Piper was supported as part of the NorthEast Center for Chemical Energy Storage (NECCES), and Energy Frontier Research Center funded by the U.S. Department of Energy, Office of Science, Basic Energy Sciences under Award# DE-SC0012583. The work of N. Hyatt and M. Stennett was supported, in part by, the Nuclear Decommissioning Authority and EPSRC under grant numbers EP/N017617/1 and EP/R511754/1; and utilized the MIDAS facility at The University of Sheffield established with financial support from the Department for Business, Energy & Industrial Strategy. The authors would like to acknowledge the efforts of Carrie Siu and Dr. M. Stanley Whittingham in

synthesizing the phase pure epsilon-VOPO4 and the efforts of Mateusz Zuba in collecting the synchrotron XAS data of that sample. R&D associated with the Los Alamos National Laboratory (LANL) spectrometer was funded under the Heavy Element Chemistry Program by the Division of Chemical Sciences, Geosciences, and Biosciences, Office of Basic Energy Sciences, U.S. Department of Energy and the U.S. Department of Energy. LANL is operated by Los Alamos National Security, LLC, for the National Nuclear Security Administration of U.S. Department of Energy (contract DE-AC52-06NA25396). Use of the Stanford Synchrotron Radiation Lightsource, SLAC National Accelerator Laboratory, was supported by the U.S. Department of Energy, Office of Science, Office of Basic Energy Sciences under Contract No. DE-AC02-76SF00515. This research used resources of the Advanced Photon Source, a U.S. Department of Energy (DOE) Office of Science User Facility operated for the DOE Office of Science by Argonne National Laboratory under Contract No. DE-AC02-06CH11357. Finally, we note that three of the authors (W. Holden, D. Mortensen, and G. Seidler) have a significant financial interest in easyXAFS LLC, which is commercializing laboratory XAFS and XES technology. No funding from easyXAFS was used in the present work.

9.8 REFERENCES

1. Clausen, B. S.; Topsøe, H., In Situ high pressure, high temperature XAFS studies of Cu-based catalysts during methanol synthesis. *Catalysis Today* **1991,** *9* (1), 189-196.

2. Chen, Y.; Fulton, J. L.; Linehan, J. C.; Autrey, T., In Situ XAFS and NMR Study of Rhodium-Catalyzed Dehydrogenation of Dimethylamine Borane. *J Am Chem Soc* **2005,** *127* (10), 3254-3255.

3. Cuisinier, M.; Cabelguen, P. E.; Evers, S.; He, G.; Kolbeck, M.; Garsuch, A.; Bolin, T.; Balasubramanian, M.; Nazar, L. F., Sulfur Speciation in Li-S Batteries Determined by Operando X-ray Absorption Spectroscopy. *J Phys Chem Lett* **2013,** *4* (19), 3227-3232.

4. Banerjee, A.; Shilina, Y.; Ziv, B.; Ziegelbauer, J. M.; Luski, S.; Aurbach, D.; Halalay, I. C., On the Oxidation State of Manganese Ions in Li-Ion Battery Electrolyte Solutions. *J Am Chem Soc* **2017,** *139* (5), 1738-1741.

5. Schelter, E. J.; Wu, R.; Veauthier, J. M.; Bauer, E. D.; Booth, C. H.; Thomson, R. K.; Graves, C. R.; John, K. D.; Scott, B. L.; Thompson, J. D.; Morris, D. E.; Kiplinger, J. L., Comparative Study of f-Element Electronic Structure across a Series of Multimetallic Actinide and Lanthanoid-Actinide Complexes Possessing Redox-Active Bridging Ligands. *Inorg Chem* **2010,** *49* (4), 1995-2007.

6. Lind, O. C.; Salbu, B.; Janssens, K.; Proost, K.; García-León, M.; García-Tenorio, R., Characterization of U/Pu particles originating from the nuclear weapon accidents at Palomares, Spain, 1966 and Thule, Greenland, 1968. *Science of The Total Environment* **2007,** *376* (1), 294-305.

7. Le Naour, C.; Trubert, D.; Di Giandomenico, M. V.; Fillaux, C.; Den Auwer, C.; Moisy, P.; Hennig, C., First Structural Characterization of a Protactinium(V) Single Oxo Bond in Aqueous Media. *Inorg Chem* **2005,** *44* (25), 9542-9546.

8. Takahashi, Y.; Ohtaku, N.; Mitsunobu, S.; Yuita, K.; Nomura, M., Determination of the As(III)/As(V) Ratio in Soil by X-ray Absorption Near-edge Structure (XANES) and Its Application to the Arsenic Distribution between Soil and Water. *Analytical Sciences* **2003,** *19* (6), 891-896.

9. Szulczewski, M. D.; Helmke, P. A.; Bleam, W. F., Comparison of XANES analyses and extractions to determine chromium speciation in contaminated soils. *Environ Sci Technol* **1997,** *31* (10), 2954-2959.

10. Fandeur, D.; Juillot, F.; Morin, G.; Olivi, L.; Cognigni, A.; Webb, S. M.; Ambrosi, J. P.; Fritsch, E.; Guyot, F.; Brown, G. E., XANES Evidence for Oxidation of Cr(III)) to Cr(VI) by Mn-Oxides in a Lateritic Regolith Developed on Serpentinized Ultramafic Rocks of New Caledonia. *Environ Sci Technol* **2009,** *43* (19), 7384-7390.

11. Rueff, J. P.; Krisch, M.; Cai, Y. Q.; Kaprolat, A.; Hanfland, M.; Lorenzen, M.;

Masciovecchio, C.; Verbeni, R.; Sette, F., Magnetic and structural alpha-epsilon phase transition in Fe monitored by x-ray emission spectroscopy. *Physical Review B* **1999,** *60* (21), 14510-14512.

12. Nomura, R.; Tateno, H.; Tateno, S.; Hirose, K.; Hernlund, J.; Muto, S.; Ishii, H.; Hiraoka, N., *Spin crossover and iron-rich silicate melt in the Earth's deep mantle*. 2011; Vol. 473, p 199-202.

13. Seidler, G. T.; Mortensen, D. R.; Remesnik, A. J.; Pacold, J. I.; Ball, N. A.; Barry, N.; Styczinski, M.; Hoidn, O. R., A laboratory-based hard x-ray monochromator for high-resolution x-ray emission spectroscopy and x-ray absorption near edge structure measurements. *Review of Scientific Instruments* **2014,** *85* (11), 113906.

14. Mantouvalou, I.; Witte, K.; Grötzsch, D.; Neitzel, M.; Günther, S.; Baumann, J.; Jung, R.; Stiel, H.; Kanngießer, B.; Sandner, W., High average power, highly brilliant laser-produced plasma source for soft X-ray spectroscopy. *Review of Scientific Instruments* **2015,** *86* (3), 035116.

15. Sugiura, C.; Gohshi, Y.; Suzuki, I., Sulfur Kβ x-ray emission spectra and electronic structures of some metal sulfides. *Physical Review B* **1974,** *10* (2), 338-343.

16. Gohshi, Y.; Hukao, Y.; Hori, K., A wide-range, single-axis, vacuum two-crystal spectrometer for fluorescent X-ray analysis. *Spectrochimica Acta Part B: Atomic Spectroscopy* **1972,** *27* (3), 135-142.

17. Chikara, S.; Yohichi, G.; Isao, S., Kβ Emission and K Absorption Spectra of Sulfur in MnS. *Jpn J Appl Phys* **1972,** *11* (6), 911.

18. Yu, M. Y.; Trofimova, V. A.; Dolgih, V. E.; Korotin, M. A.; Kurmaev, E. Z.; Aguiar, J. A.; Ferreira, J. M.; Pavao, A. C., X-ray emission spectra and valence state of sulphur atoms of YBa 2 ((CuO) 1-x (NiS) x) 3 O 4- delta. *Journal of Physics: Condensed Matter* **1995,** *7* (1), 213.

19. Yarmoshenko, Y. M.; Trofimova, V. A.; Kurmaev, E. Z.; Slater, P. R.; Greaves, C., X-ray emission spectra of YSr2Cu3O7−δ containing sulphate and phosphate groups. *Physica C: Superconductivity* **1994,** *224* (3), 317-320.

20. Yarmoshenko, Y. M.; Trofimova, V. A.; Elokhina, L. V.; Kurmaev, E. Z.; Butorin, S.; Cloots, R.; Ausloos, M.; Aguiar, J. A.; Lobatchevskaya, N. I., Possibility of sulphur-oxygen substitution in YBa2Cu3O6+xSy analyzed by means of X-ray emission spectroscopy. *Journal of Physics and Chemistry of Solids* **1993,** *54* (10), 1211-1214.

21. Dolgih, V. E.; Cherkashenko, V. M.; Kurmaev, E. Z.; Goganov, D. A.; Ovchinnikov, E. K.; Yarmoshienko, Y. M., X-ray fluorescent spectrometer with linear position sensitive detector. *Nuclear Instruments and Methods in Physics Research* **1984,** *224* (1), 117-119.

22. Kavčič, M.; Dousse, J. C.; Szlachetko, J.; Cao, W., Chemical effects in the Kβ X-ray emission spectra of sulfur. *Nuclear Instruments and Methods in Physics Research Section*

B: Beam Interactions with Materials and Atoms **2007,** *260* (2), 642-646.

23. Németh, Z.; Szlachetko, J.; Bajnóczi, É. G.; Vankó, G., Laboratory von Hámos X-ray spectroscopy for routine sample characterization. *Review of Scientific Instruments* **2016,** *87* (10), 103105.

24. Kayser, Y.; Błachucki, W.; Dousse, J. C.; Hoszowska, J.; Neff, M.; Romano, V., Laboratory-based micro-X-ray fluorescence setup using a von Hamos crystal spectrometer and a focused beam X-ray tube. *Review of Scientific Instruments* **2014,** *85* (4), 043101.

25. Hoszowska, J.; Dousse, J. C.; Kern, J.; Rhême, C., High-resolution von Hamos crystal X-ray spectrometer. *Nuclear Instruments and Methods in Physics Research Section A: Accelerators, Spectrometers, Detectors and Associated Equipment* **1996,** *376* (1), 129-138.

26. Anklamm, L.; Schlesiger, C.; Malzer, W.; Grötzsch, D.; Neitzel, M.; Kanngießer, B., A novel von Hamos spectrometer for efficient X-ray emission spectroscopy in the laboratory. *Review of Scientific Instruments* **2014,** *85* (5), 053110.

27. Tirao, G.; Stutz, G.; Cusatis, C., An inelastic X-ray scattering spectrometer at LNLS. *Journal of Synchrotron Radiation* **2004,** *11* (4), 335-342.

28. Yuryev, Y. N.; Lee, H.-J.; Park, H.-M.; Cho, Y.-K.; Lee, M.-K.; Pogrebitsky, K. J., Variable Rowland radius laboratory vacuum surface-sensitive x-ray absorption fine structure spectrometer. *Review of Scientific Instruments* **2007,** *78* (2), 025108.

29. Williams, A., Laboratory x-ray spectrometer for EXAFS and XANES measurements. *Review of Scientific Instruments* **1983,** *54* (2), 193-197.

30. Tohji, K.; Udagawa, Y.; Kawasaki, T.; Masuda, K., Laboratory EXAFS spectrometer with a bent crystal, a solid-state detector, and a fast detection system. *Review of Scientific Instruments* **1983,** *54* (11), 1482-1487.

31. Thulke, W.; Haensel, R.; Rabe, P., Versatile curved crystal spectrometer for laboratory extended x-ray absorption fine structure measurements. *Review of Scientific Instruments* **1983,** *54* (3), 277-283.

32. Knapp, G. S.; Chen, H.; Klippert, T. E., Development of a laboratory EXAFS facility. *Review of Scientific Instruments* **1978,** *49* (12), 1658-1666.

33. Cohen, G. G.; Fischer, D. A.; Colbert, J.; Shevchik, N. J., Tunable laboratory extended x-ray absorption fine structure system. *Review of Scientific Instruments* **1980,** *51* (3), 273-277.

34. Szlachetko, M.; Berset, M.; Dousse, J. C.; Hoszowska, J.; Szlachetko, J., High-resolution Laue-type DuMond curved crystal spectrometer. *Review of Scientific Instruments* **2013,** *84* (9), 093104.

35. Valenza, R. A.; Jahrman, E. P.; Kas, J. J.; Seidler, G. T., Double-ionization satellites in the x-ray emission spectrum of Ni metal. *Phys Rev A* **2017,** *96* (3), 032504.

36. Seidler, G. T.; Mortensen, D. R.; Ditter, A. S.; Ball, N. A.; Remesnik, A. J., A Modern Laboratory XAFS Cookbook. *Journal of Physics: Conference Series* **2016,** *712* (1), 012015.

37. Mortensen, D. R.; Seidler, G. T.; Kas, J. J.; Govind, N.; Schwartz, C. P.; Pemmaraju, S.; Prendergast, D. G., Benchmark results and theoretical treatments for valence-to-core x-ray emission spectroscopy in transition metal compounds. *Physical Review B* **2017,** *96* (12), 125136.

38. Mortensen, D. R.; Seidler, G. T.; Ditter, A. S.; Glatzel, P., Benchtop Nonresonant X-ray Emission Spectroscopy: Coming Soon to Laboratories and XAS Beamlines Near You? *Journal of Physics: Conference Series* **2016,** *712* (1), 012036.

39. Mortensen, D. R.; Seidler, G. T., Robust optic alignment in a tilt-free implementation of the Rowland circle spectrometer. *J Electron Spec* **2017,** *215*, 8-15.

40. Jahrman, E. P.; Seidler, G. T.; Sieber, J. R., Determination of Hexavalent Chromium Fractions in Plastics Using Laboratory-Based, High-Resolution X-ray Emission Spectroscopy. *Analytical Chemistry* **2018,** *90* (11), 6587-6593.

41. Jahrman, E. P.; Holden, W. M.; Ditter, A. S.; Kihara, S. L.; Seidler, G. T., Vacuum Formed Temporary Spherical and Toroidal Bent Crystal Analyzers for High Resolution X-ray Spectroscopy. *In Prep* **2018**.

42. Stennett, M. C.; Corkhill, C. L.; Marshall, L. A.; Hyatt, N. C., Preparation, characterisation and dissolution of a CeO2 analogue for UO2 nuclear fuel. *Journal of Nuclear Materials* **2013,** *432* (1), 182-188.

43. Siu, C.; Seymour, I. D.; Britto, S.; Zhang, H.; Rana, J.; Feng, J.; Omenya, F. O.; Zhou, H.; Chernova, N. A.; Zhou, G.; Grey, C. P.; Piper, L. F. J.; Whittingham, M. S., Enabling multi-electron reaction of ε-VOPO4 to reach theoretical capacity for lithium-ion batteries. *Chemical Communications* **2018,** *54* (56), 7802-7805.

44. Minasian, S. G.; Boland, K. S.; Feller, R. K.; Gaunt, A. J.; Kozimor, S. A.; May, I.; Reilly, S. D.; Scott, B. L.; Shuh, D. K., Synthesis and Structure of (Ph4P)2MCl6 (M = Ti, Zr, Hf, Th, U, Np, Pu). *Inorg Chem* **2012,** *51* (10), 5728-5736.

45. Watkin, D. J.; Denning, R. G.; Prout, K., Structure of Dicesium Tetrachlorodioxouranium(Vi). *Acta Crystallogr C* **1991,** *47*, 2517-2519.

46. Spencer, L. P.; Yang, P.; Minasian, S. G.; Jilek, R. E.; Batista, E. R.; Boland, K. S.; Boncella, J. M.; Conradson, S. D.; Clark, D. L.; Hayton, T. W.; Kozimor, S. A.; Martin, R. L.; MacInnes, M. M.; Olson, A. C.; Scott, B. L.; Shuh, D. K.; Wilkerson, M. P., Tetrahalide Complexes of the [U(NR)2]2+ Ion: Synthesis, Theory, and Chlorine K-Edge X-ray Absorption Spectroscopy. *J Am Chem Soc* **2013,** *135* (6), 2279-2290.

47. Ravel, B.; Newville, M., ATHENA, ARTEMIS, HEPHAESTUS: data analysis for X-ray absorption spectroscopy using IFEFFIT. *Journal of Synchrotron Radiation* **2005,** *12* (4), 537-541.

48. Hyatt, N. C.; Schwarz, R. R.; Bingham, P. A.; Stennett, M. C.; Corkhill, C. L.; Heath, P. G.; Hand, R. J.; James, M.; Pearson, A.; Morgan, S., Thermal treatment of simulant plutonium contaminated materials from the Sellafield site by vitrification in a blast-furnace slag. *Journal of Nuclear Materials* **2014,** *444* (1), 186-199.

49. Pattenaude, S. A.; Mullane, K. C.; Schelter, E. J.; Ferrier, M. G.; Stein, B. W.; Bone, S. E.; Lezama Pacheco, J. S.; Kozimor, S. A.; Fanwick, P. E.; Zeller, M.; Bart, S. C., Redox-Active vs Redox-Innocent: A Comparison of Uranium Complexes Containing Diamine Ligands. *Inorg Chem* **2018,** *57* (11), 6530-6539.

50. Hämäläinen, K.; Siddons, D. P.; Hastings, J. B.; Berman, L. E., Elimination of the inner-shell lifetime broadening in x-ray-absorption spectroscopy. *Phys Rev Lett* **1991,** *67* (20), 2850-2853.

51. Hämäläinen, K.; Kao, C. C.; Hastings, J. B.; Siddons, D. P.; Berman, L. E.; Stojanoff, V.; Cramer, S. P., Spin-dependent x-ray absorption of MnO and MnF2. *Physical Review B* **1992,** *46* (21), 14274-14277.

52. Rovezzi, M.; Lapras, C.; Manceau, A.; Glatzel, P.; Verbeni, R., High energy-resolution x-ray spectroscopy at ultra-high dilution with spherically bent crystal analyzers of 0.5 m radius. *Review of Scientific Instruments* **2017,** *88* (1), 013108.

53. Suortti, P.; Buslaps, T.; Fajardo, P.; Honkimaki, V.; Kretzschmer, M.; Lienert, U.; McCarthy, J. E.; Renier, M.; Shukla, A.; Tschentscher, T.; Meinander, T., Scanning X-ray spectrometer for high-resolution Compton profile measurements at ESRF. *Journal of Synchrotron Radiation* **1999,** *6* (2), 69-80.

54. Lu, K. Q.; Stern, E. A., Johann and Johansson focussing arrangements Analytical analysis. 1980; Vol. 64, pp 104-108.

55. Bergmann, U.; Cramer, S. P. In *High-resolution large-acceptance analyzer for x-ray fluorescence and Raman spectroscopy*, SPIE's International Symposium on Optical Science, Engineering, and Instrumentation, SPIE: 1998; p 12.

56. Tabuchi, M.; Nakashima, A.; Shigemura, H.; Ado, K.; Kobayashi, H.; Sakaebe, H.; Kageyama, H.; Nakamura, T.; Kohzaki, M.; Hirano, A.; Kanno, R., Synthesis, Cation Distribution, and Electrochemical Properties of Fe-Substituted Li2MnO3 as a Novel 4 V Positive Electrode Material. *Journal of The Electrochemical Society* **2002,** *149* (5), A509-A524.

57. Shigemura, H.; Sakaebe, H.; Kageyama, H.; Kobayashi, H.; West, A. R.; Kanno, R.; Morimoto, S.; Nasu, S.; Tabuchi, M., Structure and Electrochemical Properties of LiFe x Mn2 − x O 4 (0 ⩽ x ⩽ 0.5) Spinel as 5 V Electrode Material for Lithium Batteries. *Journal of The Electrochemical Society* **2001,** *148* (7), A730-A736.

58. McLaren, V. L.; West, A. R.; Tabuchi, M.; Nakashima, A.; Takahara, H.; Kobayashi, H.; Sakaebe, H.; Kageyama, H.; Hirano, A.; Takeda, Y., Study of the Capacity Fading Mechanism for Fe-Substituted LiCoO2 Positive Electrode. *Journal of The Electrochemical Society* **2004,** *151* (5), A672-A681.

59. Kageyama, H.; Shigemura, H.; Tabuchi, M.; Ado, K.; Kobayashi, H., XAFS study of LiCo1-xFexO2 cathode for rechargeable lithium battery by laboratory XAFS spectrometer. *Journal of Synchrotron Radiation* **2001,** *8* (2), 863-865.

60. Talaie, E.; Bonnick, P.; Sun, X. Q.; Pang, Q.; Liang, X.; Nazar, L. F., Methods and Protocols for Electrochemical Energy Storage Materials Research. *Chem Mater* **2017,** *29* (1), 90-105.

61. Nowack, L.; Grolimund, D.; Samson, V.; Marone, F.; Wood, V., Rapid Mapping of Lithiation Dynamics in Transition Metal Oxide Particles with Operando X-ray Absorption Spectroscopy. *Scientific Reports* **2016,** *6*.

62. Jaklevic, J.; Kirby, J. A.; Klein, M. P.; Robertson, A. S.; Brown, G. S.; Eisenberger, P., Fluorescence detection of exafs: Sensitivity enhancement for dilute species and thin films. *Solid State Communications* **1977,** *23* (9), 679-682.

63. Gaur, A.; Shrivastava, B. D., Speciation using X-ray absorption fine structure (XAFS). *Review Journal of Chemistry* **2015,** *5* (4), 361-398.

64. Agarwal, B. K. V., V. P., A rule for chemical shifts of x-ray absorption edges. *Journal of Physics C: Solid State Physics* **1970,** *3* (3), 535-537.

65. Allen, P. G.; Bucher, J. J.; Shuh, D. K.; Edelstein, N. M.; Craig, I., Coordination Chemistry of Trivalent Lanthanide and Actinide Ions in Dilute and Concentrated Chloride Solutions. *Inorg Chem* **2000,** *39* (3), 595-601.

66. Asakura, H.; Shishido, T.; Teramura, K.; Tanaka, T., Local Structure and L1- and L3-Edge X-ray Absorption Near Edge Structure of Late Lanthanide Elements (Ho, Er, Yb) in Their Complex Oxides. *The Journal of Physical Chemistry C* **2015,** *119* (15), 8070-8077.

67. Upadhyaya, G. K.; Shah, G.; Gupta, S. N., XANES studies of rare earth metals and compounds. *Physica B: Condensed Matter* **1995,** *208-209*, 297-299.

68. Rothensteiner, M.; Sala, S.; Bonk, A.; Vogt, U.; Emerich, H.; Van Bokhoven, J. A., Ce K edge XAS of ceria-based redox materials under realistic conditions for the two-step solar thermochemical dissociation of water and/or CO 2. *Phys. Chem. Chem. Phys.* **2015,** *17* (40), 26988-26996.

69. Zhang, J.; Wu, Z.; Liu, T.; Hu, T.; Wu, Z.; Ju, X., XANES study on the valence transitions in cerium oxide nanoparticles. *J. Synchrot. Radiat.* **2001,** *8*, 531-532.

70. Davenport, A. J.; Isaacs, H. S.; Kendig, M. W., XANES investigation of the role of cerium compounds as corrosion inhibitors for aluminum. *Corrosion Science* **1991,** *32* (5), 653-

663.

71. Bès, R.; Ahopelto, T.; Honkanen, A. P.; Huotari, S.; Leinders, G.; Pakarinen, J.; Kvashnina, K., Laboratory-scale X-ray absorption spectroscopy approach for actinide research: Experiment at the uranium L3-edge. *Journal of Nuclear Materials* **2018,** *507*, 50-53.

72. Gog, T.; Casa, D. M.; Said, A. H.; Upton, M. H.; Kim, J.; Kuzmenko, I.; Huang, X.; Khachatryan, R., Spherical analyzers and monochromators for resonant inelastic hard X-ray scattering: a compilation of crystals and reflections. *Journal of Synchrotron Radiation* **2013,** *20* (1), 74-79.

73. Lecante, P.; Jaud, J.; Mosset, A.; Galy, J.; Burian, A., A laboratory EXAFS spectrometer in transmission dispersive mode. *Review of Scientific Instruments* **1994,** *65* (4), 845-849.

74. Hudson, E. A.; G. Allen, P.; Terminello, L.; Denecke, M.; Reich, T., *Polarized x-ray-absorption spectroscopy of the uranyl ion: Comparison of experiment and theory*. 1996; Vol. 54, p 156-165.

75. Kelly, S. D.; Bare, S. R.; Greenlay, N.; Azevedo, G.; Balasubramanian, M.; Barton, D.; Chattopadhyay, S.; Fakra, S.; Johannessen, B.; Newville, M.; Pena, J.; Pokrovski, G. S.; Proux, O.; Priolkar, K.; Ravel, B.; Webb, S. M., Comparison of EXAFS foil spectra from around the world. *Journal of Physics: Conference Series* **2009,** *190* (1), 012032.

76. Glatzel, P.; Bergmann, U., High resolution 1s core hole X-ray spectroscopy in 3d transition metal complexes - electronic and structural information. *Coordin Chem Rev* **2005,** *249* (1-2), 65-95.

77. Gallo, E.; Glatzel, P., Valence to Core X-ray Emission Spectroscopy. *Advanced Materials* **2014,** *26* (46), 7730-7746.

78. Pollock, C. J.; DeBeer, S., Valence-to-Core X-ray Emission Spectroscopy: A Sensitive Probe of the Nature of a Bound Ligand. *J Am Chem Soc* **2011,** *133* (14), 5594-5601.

79. Kawai, J.; Ohta, M.; Konishi, T., Chemical Effects in High-Resolution Nickel Kα X-Ray Fluorescence Spectra. *Analytical Sciences* **2005,** *21* (7), 865-868.

80. Gul, S.; Ng, J. W. D.; Alonso-Mori, R.; Kern, J.; Sokaras, D.; Anzenberg, E.; Lassalle-Kaiser, B.; Gorlin, Y.; Weng, T.-C.; Zwart, P. H.; Zhang, J. Z.; Bergmann, U.; Yachandra, V. K.; Jaramillo, T. F.; Yano, J., Simultaneous detection of electronic structure changes from two elements of a bifunctional catalyst using wavelength-dispersive X-ray emission spectroscopy and in situ electrochemistry. *Physical Chemistry Chemical Physics* **2015,** *17* (14), 8901-8912.

81. Einsle, O.; Tezcan, F. A.; Andrade, S. L. A.; Schmid, B.; Yoshida, M.; Howard, J. B.; Rees, D. C., Nitrogenase MoFe-Protein at 1.16 Å Resolution: A Central Ligand in the FeMo-Cofactor. *Science* **2002,** *297* (5587), 1696.

82. Lancaster, K. M.; Roemelt, M.; Ettenhuber, P.; Hu, Y.; Ribbe, M. W.; Neese, F.; Bergmann, U.; DeBeer, S., X-ray Emission Spectroscopy Evidences a Central Carbon in the Nitrogenase Iron-Molybdenum Cofactor. *Science* **2011,** *334* (6058), 974.

83. Pushkar, Y.; Long, X.; Glatzel, P.; Brudvig, G. W.; Dismukes, G. C.; Collins, T. J.; Yachandra, V. K.; Yano, J.; Bergmann, U., Direct Detection of Oxygen Ligation to the Mn4Ca Cluster of Photosystem II by X-ray Emission Spectroscopy. *Angewandte Chemie International Edition* **2010,** *49* (4), 800-803.

84. Pollock, C. J.; Grubel, K.; Holland, P. L.; DeBeer, S., Experimentally Quantifying Small-Molecule Bond Activation Using Valence-to-Core X-ray Emission Spectroscopy. *J Am Chem Soc* **2013,** *135* (32), 11803-11808.

85. Rovezzi, M.; Glatzel, P., *Hard x-ray emission spectroscopy: A powerful tool for the characterization of magnetic semiconductors*. 2013; Vol. 29.

86. Bergmann, U.; Horne, C. R.; Collins, T. J.; Workman, J. M.; Cramer, S. P., Chemical dependence of interatomic X-ray transition energies and intensities – a study of Mn Kβ″ and Kβ2,5 spectra. *Chem Phys Lett* **1999,** *302* (1), 119-124.

87. Enkisch, H.; Sternemann, C.; Paulus, M.; Volmer, M.; Schulke, W., 3d spectator hole satellites of the CuK beta(1,3) and K beta(2,5) emission spectrum. *Phys Rev A* **2004,** *70* (2), 022508.

88. Sternemann, C.; Kaprolat, A.; Krisch, M. H.; Schulke, W., Evolution of the germanium K beta '" X-ray satellites from threshold to saturation. *Phys Rev A* **2000,** *61* (2), 205011-205014.

89. Kawai, J.; Takami, M.; Satoko, C., Multiplet Structure in Ni K-Beta X-Ray-Fluorescence Spectra of Nickel Compounds. *Phys Rev Lett* **1990,** *65* (17), 2193-2196.

90. Holden, W. M.; Seidler, G. T.; Cheah, S., Sulfur Speciation in Biochars by Very High Resolution Benchtop Kα X-ray Emission Spectroscopy. *The Journal of Physical Chemistry A* **2018**.

91. Stein, J. L.; Holden, W. M.; Venkatesh, A.; Mundy, M. E.; Rossini, A. J.; T., S. G.; Cossairt, B. M., *Chem Mater* **2018,** *Submitted*.

92. Stein, J. L.; Holden, W. M.; Cossairt, B. M.; Seidler, G. T., Something something InP. *In Prep* **2018**.

93. Bajnóczi, É. G.; Németh, Z.; Vankó, G., Simultaneous Speciation, Structure, and Equilibrium Constant Determination in the Ni2+–EDTA–CN– Ternary System via High-Resolution Laboratory X-ray Absorption Fine Structure Spectroscopy and Theoretical Calculations. *Inorg Chem* **2017,** *56* (22), 14220-14226.

94. Padamati, S. K.; Angelone, D.; Draksharapu, A.; Primi, G.; Martin, D. J.; Tromp, M.; Swart, M.; Browne, W. R., Transient Formation and Reactivity of a High-Valent

Nickel(IV) Oxido Complex. *J Am Chem Soc* **2017,** *139* (25), 8718-8724.

95. Kuai, L.; Kan, E.; Cao, W.; Huttula, M.; Ollikkala, S.; Ahopelto, T.; Honkanen, A.-P.; Huotari, S.; Wang, W.; Geng, B., Mesoporous LaMnO3+δ perovskite from spray−pyrolysis with superior performance for oxygen reduction reaction and Zn−air battery. *Nano Energy* **2018,** *43*, 81-90.

96. Joe, Y. I.; O'Neil, G. C.; Miaja-Avila, L.; Fowler, J. W.; Jimenez, R.; Silverman, K. L.; Swetz, D. S.; Ullom, J. N., Observation of iron spin-states using tabletop x-ray emission spectroscopy and microcalorimeter sensors. *Journal of Physics B: Atomic, Molecular and Optical Physics* **2016,** *49* (2), 024003.

97. Penrose, W. R.; Woolson, E. A., Arsenic in the marine and aquatic environments: Analysis, occurrence, and significance. *C R C Critical Reviews in Environmental Control* **1974,** *4* (1-4), 465-482.

98. Niazi, N. K.; Singh, B.; Shah, P., Arsenic Speciation and Phytoavailability in Contaminated Soils Using a Sequential Extraction Procedure and XANES Spectroscopy. *Environ Sci Technol* **2011,** *45* (17), 7135-7142.

99. Bearden, J. A., X-ray wavelengths. *Reviews of Modern Physics* **1967,** *39* (1), 78-124.

100. Mundy, M. E.; Ung, D.; Lai, N. L.; Jahrman, E. P.; Seidler, G. T.; Cossairt, B. M., Aminophosphines as Versatile Precursors for the Synthesis of Metal Phosphide Nanocrystals. *Chem Mater* **2018,** *30* (15), 5373-5379.

101. Holden, W. M.; Hoidn, O. R.; Ditter, A. S.; Seidler, G. T.; Kas, J.; Stein, J. L.; Cossairt, B. M.; Kozimor, S. A.; Guo, J.; Ye, Y.; Marcus, M. A.; Fakra, S., A compact dispersive refocusing Rowland circle X-ray emission spectrometer for laboratory, synchrotron, and XFEL applications. *Review of Scientific Instruments* **2017,** *88* (7), 073904.

102. Schlesiger, C.; Anklamm, L.; Stiel, H.; Malzer, W.; Kanngießer, B., XAFS spectroscopy by an X-ray tube based spectrometer using a novel type of HOPG mosaic crystal and optimized image processing. *Journal of Analytical Atomic Spectrometry* **2015,** *30* (5), 1080-1085.

103. Haldrup, K.; Gawelda, W.; Abela, R.; Alonso-Mori, R.; Bergmann, U.; Bordage, A.; Cammarata, M.; Canton, S. E.; Dohn, A. O.; van Driel, T. B.; Fritz, D. M.; Galler, A.; Glatzel, P.; Harlang, T.; Kjaer, K. S.; Lemke, H. T.; Moller, K. B.; Nemeth, Z.; Papai, M.; Sas, N.; Uhlig, J.; Zhu, D. L.; Vanko, G.; Sundstrom, V.; Nielsen, M. M.; Bressler, C., Observing Solvation Dynamics with Simultaneous Femtosecond X-ray Emission Spectroscopy and X-ray Scattering. *J Phys Chem B* **2016,** *120* (6), 1158-1168.

104. Li, G.; Bridges, F.; H. Booth, C., *X-ray-absorption fine-structure standards: A comparison of experiment and theory*. 1995; Vol. 52, p 6332-6348.

105. Krayzman, V.; Levin, I.; Woicik, J. C.; Proffen, T.; Vanderah, T. A.; Tucker, M. G., A combined fit of total scattering and extended X-ray absorption fine structure data for local-

structure determination in crystalline materials. *Journal of Applied Crystallography* **2009,** *42* (5), 867-877.

106. Karolewski, M. A.; Cavell, R. G.; Gordon, R. A.; Glover, C. J.; Cheah, M.; Ridgway, M. C., Predicting XAFS scattering path cumulants and XAFS spectra for metals (Cu, Ni, Fe, Ti, Au) using molecular dynamics simulations. *Journal of Synchrotron Radiation* **2013,** *20* (4), 555-566.

107. Stern, E. A.; Heald, S. M., X-ray filter assembly for fluorescence measurements of x-ray absorption fine structure. *Review of Scientific Instruments* **1979,** *50* (12), 1579-1582.